Engineering Materials

Volume 35

For further volumes:
http://www.springer.com/series/4288

Ricardo H. R. Castro · Klaus van Benthem
Editors

Sintering

Mechanisms of Convention Nanodensification and Field Assisted Processes

Springer

Editors
Ricardo H. R. Castro
Department of Chemical Engineering and Materials Science
University of California
Davis, CA
USA

Klaus van Benthem
Department of Chemical Engineering and Materials Science
University of California
Davis, CA
USA

ISSN 1612-1317 ISSN 1868-1212 (electronic)
ISBN 978-3-642-31008-9 ISBN 978-3-642-31009-6 (eBook)
DOI 10.1007/978-3-642-31009-6
Springer Heidelberg New York Dordrecht London

Library of Congress Control Number: 2012945736

© Springer-Verlag Berlin Heidelberg 2013
This work is subject to copyright. All rights are reserved by the Publisher, whether the whole or part of the material is concerned, specifically the rights of translation, reprinting, reuse of illustrations, recitation, broadcasting, reproduction on microfilms or in any other physical way, and transmission or information storage and retrieval, electronic adaptation, computer software, or by similar or dissimilar methodology now known or hereafter developed. Exempted from this legal reservation are brief excerpts in connection with reviews or scholarly analysis or material supplied specifically for the purpose of being entered and executed on a computer system, for exclusive use by the purchaser of the work. Duplication of this publication or parts thereof is permitted only under the provisions of the Copyright Law of the Publisher's location, in its current version, and permission for use must always be obtained from Springer. Permissions for use may be obtained through RightsLink at the Copyright Clearance Center. Violations are liable to prosecution under the respective Copyright Law.
The use of general descriptive names, registered names, trademarks, service marks, etc. in this publication does not imply, even in the absence of a specific statement, that such names are exempt from the relevant protective laws and regulations and therefore free for general use.
While the advice and information in this book are believed to be true and accurate at the date of publication, neither the authors nor the editors nor the publisher can accept any legal responsibility for any errors or omissions that may be made. The publisher makes no warranty, express or implied, with respect to the material contained herein.

Printed on acid-free paper

Springer is part of Springer Science+Business Media (www.springer.com)

Preface

Technologies based on nanostructured materials are present and has become increasingly important in our daily lives. Nanomaterials can be found in many applications, such as catalytic processes, ultra-violet filters, pigments, electronics, etc. It has long been recognized that nanostructured materials can have significantly altered properties when compared to their larger scale counterparts. A high level of control over the microstructure evolution of such materials is necessary during processing to ensure the development and synthesis of more stable high performance nanomaterials. Studies of stability and processing of nanomaterials typically involve concepts of sintering. That is, due to the large interface areas, nanomaterials tend to transform into their microscale counterparts if enough diffusion is provided. Therefore, a fundamental understanding of the sintering process is of critical importance to maintain reasonable control over the evolution nano- and microstructures. This understanding is provided through sintering theories, developed many years ago for the processing of powders in both metallurgy and ceramic industries. However, stability concepts are not the only connections between nanomaterials and sintering. Nanograined structures, that show outstanding mechanical and electrical properties, can only be obtained using either a refined control of sintering parameters, or assisted processing, such as field-assisted sintering. In this book, we present an organized collection of contributions from outstanding leading researchers in the field of (assisted) sintering technologies. The objective is to provide the reader with a useful overview of sintering concepts, followed by a detailed description of the particularities of nanosintering, and an up-to-date description and review of the current understanding of densification mechanisms that occur during electric field assisted sintering.

This book is intended to be both a teaching and consulting text. Although the individual chapters represent independent contributions from the respective authors, the editors made a great effort to communicate with all of the authors during the preparation of the texts to assure a logical order in the book. The final editorial review was conducted in a way to generate a text suitable for graduate level courses in field assisted-sintering. Some redundancies between individual chapters are by intention to improve the book's educational value and make it appealing as a compendium for researchers and industrial users throughout their career.

As an experimental approach, this book has been used during the editing process as the textbook for a Field-Assisted Sintering graduate course offered in Fall of 2011 at the University of California, Davis. The course was taught by the Editors to a class of seven Materials Science and Chemical Engineering graduate and undergraduate students in a reading and discussion format. The students' comments were used as guidelines to improve the educational value during the editing of the individual chapters. With the assistance of the authors, this process helped this book to become a clear and didactic introduction to the field of assisted sintering. The following students are therefore greatly acknowledged as contributing reviewers to this book: Chi-Hsiu Chang, Hasan Ghadialy, Tammy Harrell, Seong Kim, Binzhi Li, Eskin Murat, and Jorgen F. Rufner.

The first chapter of this book provides a short overview of sintering and competitive processes, such as grain growth and coalescence. The driving forces are described in detail, as well as the relevant kinetic mechanisms. The following chapter, by Li and Pan (University of Leicester, UK) introduces nanoeffects in sintering and describes that nanoparticles should have different sintering behavior than their larger counterparts. This chapter also addresses simulations of two-particle sintering by molecular dynamics, and discusses how the simulated results relate to the classical models for sintering. The third chapter, by Liu and Gong (Northwestern Polytechnical University, China) presents nanoscale effects related to grain growth. As retaining grain growth is a common goal during sintering, the chapter addresses the problem from both the kinetics and thermodynamics points of view. Available models to control the grain growth using dopants are presented and discussed.

In the following topic, Kelly and Graeve (Alfred University, USA) add a more realistic perspective to sintering considering agglomerations and aggregations of nanoparticles as precursors. In addition, the authors discuss influences of processing parameters during nanoparticle synthesis. In a more "simulation" perspective, the Chapter by Wonisch, Rasp, Kraft, and Riedel (Fraunhofer Institute for Mechanics of Materials, Germany) provides a different perspective through simulations of sintering when exploiting to manufacture parts. The authors use finite element approaches to simulate sintering of large bodies and investigate effects of particle rearrangement during densification.

In another experimental oriented chapter, Lu, Li, and Chen (Virginia Polytechnic Institute and State University, USA) discuss the synthesis of porous materials, where sintering concepts are used to achieve porosity control. Several different methods of achieving and controlling such microstructures are described with the aid of examples.

From the second half on, this book turns its focus toward field assisted sintering processes and a review of heavily debated mechanisms. Munir and Quach (University of California, Davis, USA) and Ohyanagi (Ryukoku University, Japan) introduce electrical field assisted sintering concepts to set the bases for the following chapters, and show concrete examples of products that can be obtained using this technique. The authors briefly introduce some of the relevant mechanisms and focus particularly on Spark Plasma Sintering. In the following chapter, Anselmi-Tamburini, Holland, Spinolo, Maglia, Tredici, and Mukherjee (University of Pavia, Italy and University of California, Davis, USA) present a more quantitative description of the effects of currents and fields on mass transport phenomena during sintering.

With a different point of view, Guillon (Friedrich-Schiller-Universität Jena, Germany) describes the role of pressure and heating rates during the SPS process in the next chapter. That is, most of the advantageous effects related to the SPS process can be attributed to the applied pressure and high heating rates. Guillon shows this by using model systems and comparing hot pressing sintering with the field assisted process. Finally, the final chapter of the book by van Benthem (University of California, Davis, USA) reviews characterization techniques suitable to obtain a deeper understanding of the relevant mechanisms during sintering. The chapter concentrates on electron microscopy methods for the atomic resolution characterization of as-sintered microstructures, and discusses new avenues for in situ investigations that will shed light on defect evolutions during densification.

Davis, CA, USA

Ricardo H. R. Castro
Klaus van Benthem

Contents

Overview of Conventional Sintering

Ricardo H. R. Castro

Abstract This introductory chapter addresses an overview of the main processes taking place during the so-called Sintering phenomenon. The driving forces and mechanisms for the competitive processes, coalescence and grain growth, are also briefly discussed. The goal is not to provide and exhaustive review of the field, but to give the reader a concise perspective of the commonly accepted concepts of sintering, pathing the way for the next chapters of this book to address the specifics of nanosintering and field assisted processes.

1 Introduction

Sintering is typically recognized as an old field in materials sciences, where most of the scientific questions are well understood, and the process can be easily optimized. Unfortunately, this is not true yet, and though we have a very good knowledge of the sintering parameters, there are still many open questions. These questions become more critical when dealing with the sintering of nanoparticles, where the increased surface area seems to significantly affect the densification process. It is not clear, though, whether the problems found at the nanoscale are related to experimental issues (such as sample contamination, aggregations, etc.) or due to the inadequacy of the current sintering theories. Hence, revisiting the basis of those theories and data is important to clearly understand the real novelties of nanosintering.

R. H. R. Castro (✉)
Peter A. Rock Thermochemistry Laboratory and Department of Chemical Engineering and Materials Science, University of California, Davis, CA, USA
e-mail: rhrcastro@ucdavis.edu

R. H. R. Castro and K. van Benthem (eds.), *Sintering*, Engineering Materials 35,
DOI: 10.1007/978-3-642-31009-6_1, © Springer-Verlag Berlin Heidelberg 2013

Many different definitions have been given to sintering depending on the field where it is used or studied. That is, sintering can be described in many different scenarios, the most common being powder processing, where sintering is exploited to consolidate particles with controlled porosity by heating a compact at around 2/3 of its melting point (this temperature would allow significant atomic mobility and typically serves as a reference to establish sintering conditions). However, sintering is also a serious matter on the stability of catalysts, where the concept is used to avoid collapsing of nanostructures upon operation, pore elimination is not the goal, and the temperatures are much lower than the melting point. Regardless of the field, what can unequivocally define sintering is its driving force: surface elimination. That is, the goal of this process is to decrease the surface area, leading to a decrease in the total free energy (as surfaces always bring extra, or excess, energy). Therefore, the higher the surface energy is, the higher the potential for sintering to happen is. This is what is so-called the 'global' driving force of sintering, but without a 'local' driving force, sintering will not occur. The local driving force is typically given by the curvature potential, which will drive local diffusion of atoms (we will see more of this ahead).

At this point, one may raise the valid questions: Actually, surface energy and curvature are also driving forces for other processes commonly discussed in the literature of powder processing, such as coalescence of particles and grain growth. So, what is the difference between these processes? What is coarsening? What is grain growth? What is sintering? Well, in a real system, all these processes are happening at the same time, but they do have different dependences on their driving forces. In order to understand these dependences, we have to first remember a few concepts and build the scenarios where these processes take place.

2 Global Driving Forces

Consider a soap bubble toy. Yes, a simple round wire with a soap film. If you blow it strongly, you will create a funny soap bubble sphere. However, if you only blow weakly, the film will only be distorted. If you then stop blowing, it will come back as a flat surface. This is illustrated in Fig. 1 and can clearly show the concept of surface tension. That is, you are providing work by blowing the toy, and the energy you give is being used to create a new surface area.

The new 'extended' film area is unstable, such that when there is no energy to create it, it will disappear. With this, one can mathematically describe the surface tension as the reversible work needed to increase the surface of a unit area by stretching it:

$$\gamma = \frac{dw_R}{dA} \tag{1}$$

Surface tension is responsible for many phenomena in the nature, and explains why when you join two droplets of water sitting on a table they spontaneously become one (decreasing the total surface area). The concept of surface tension is

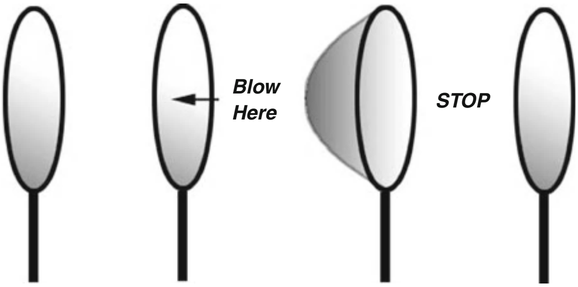

Fig. 1 Schematic representation of a soap film formed in an arc and expanded by blowing

however slightly different from surface energy. Surface energy is the energy required to create a new unit of surface area, and not to 'stretch' it. While in liquids there is no difference between them (because the high mobility of the molecules will always relax the surface bonds), in solids they are typically different due to the limited diffusion. Hence, the surface energy can be expressed as the extra energy caused by the presence of a new interface in a system with a constant number of atoms at certain temperature and pressure:

$$\gamma_S = \left(\frac{dE}{dA}\right)_{T,P,n_i} \tag{2}$$

Similarly to surface tension, the surface energy will always make particles unstable. Therefore, a surface elimination will take place to decrease the total free energy (eliminate excess energy) whenever diffusion of the atoms allows. This process happens throughout the combination of two or more particles, as seen in Fig. 2 (*top*). Note that this combination of particles happens via formation of 'necks' between them. While in liquids those necks are very stable and mobile, as with two droplets of water becoming one immediately when they are joined, however, in crystalline materials the necks are solid–solid interfaces that may have a non-negligible energy associated to it. During this particles fusion (generally called coalescence), the newly created interface will bring an energy cost to the surface elimination process. That is, to better understand this we have to define the variables influencing the total free energy change of the system. The energetic evolution during coalescence of crystalline materials is described by:

$$\delta G_{sys} = \delta \int \gamma_S dA_S + \delta \int \gamma_{SS} dA_{SS} \tag{3}$$

where G_{sys} is the total interfacial energy of the system, A_S is the specific free surface area, A_{SS} is the area of the newly created interface, and γ_{SS} is its energy. Looking from a thermodynamic perspective, there is a competition between the interfaces. The decreasing of A_S is always favorable along the process (since the system wants to decrease its energy by removing excesses), and the decreased energy is calculated from the area change times the surface energy. However, to eliminate A_S, A_{SS} must be formed. While the product $A_S.\gamma_S$ is larger than $A_{SS}.\gamma_{SS}$,

Fig. 2 Energy change as a function of contact angle evolution for an assembly of three particles for different ratios between interface energies (modified from Lange et al. [1]). *The dots along the curves* represent the minimum, i.e. the dihedral angle

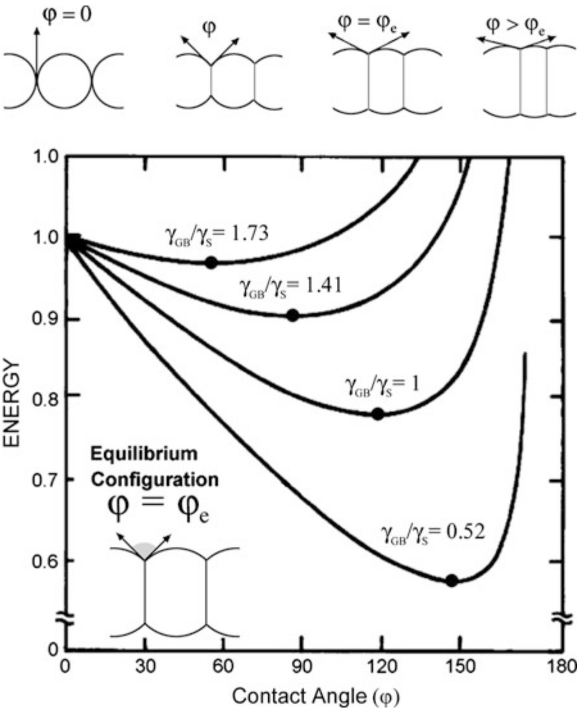

Fig. 3 Schematic 2D representation of the relationship between the interface energies and the dihedral angle

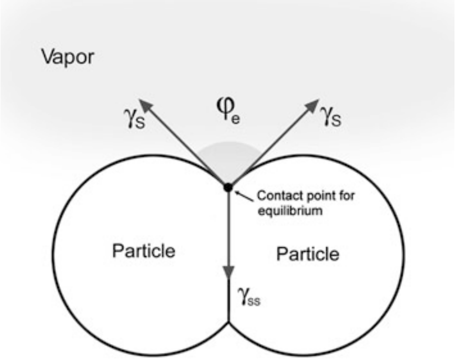

the process is spontaneous. But when A_S becomes small, the formation of A_{SS} will be costly, and the coalescence process will become non-spontaneous. This can be seen in Fig. 2, as demonstrated by Lange simulations on the interface energy during coarsening of a particle array.

One can see that the total energy of a system of particles of the same size decreases when necks start to form. The system finds a minimum at certain relationship between A_{SS} and A_S. This relationship can be easily translated to a 2D projection of the problem, which will tell us that the system has a minimum of

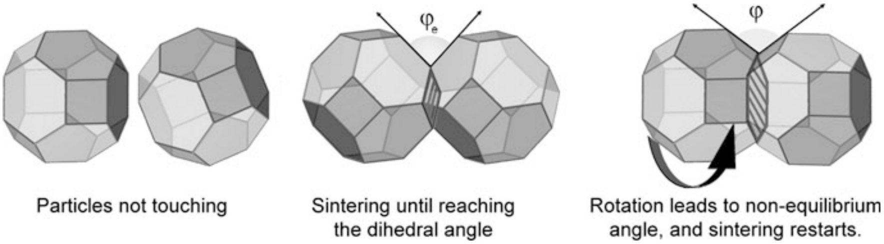

Fig. 4 Schematic representation of the non-spherical particles being sintered. Different interface energies can lead to rotation or rearrangement of grains to decrease the total free energy

energy when it reaches the equilibrium angle, the so-called the *dihedral angle* (φ_e). The dihedral angle has been extensively described in the literature, and is basically given by a relationship between the energies at the contact point between particles, as shown in Fig. 3.

At equilibrium, the energies have to be balanced at the point where the interfaces touch each other, as shown in Fig. 3. Considering that the energies work as forces, their equilibrium will provide an angle defined by:

$$\frac{\gamma_{SS}}{\gamma_S} = 2\cos\left(\frac{\varphi_e}{2}\right) \tag{4}$$

Though φ_e is commonly called 'equilibrium' angle, this is more likely a metastable equilibrium configuration, since mass can still be transferred between particles to reduce further the total free energy and the global and local driving forces are still present. However, the system is in an energy 'valley', as indicated in Fig. 2. To move the system out from this minimum, coarsening or grain rotation should take place. But why can grain rotation disturb the metastable state?

Crystalline particles are not typically perfect spheres as the ones we have used to describe the process. Indeed they have faceted surfaces, with distinct exposed surface planes and energies. Hence, any rotation of a particle will actually create a different solid–solid energy, breaking the stability of the dihedral angle, and moving the system towards a new lower energy metastable equilibrium state. Fig. 4 shows a schematic representation of this mechanism.

Another phenomenon moving the system from the minimum is the movement of the just formed solid–solid interface. As we mentioned, this interface has an excess energy associated to it. In order to decrease the total energy of the system, the interface can move through the grain, changing the contact angles, and promoting re-start of sintering. In fact, thinking about the movement of an interface, one should agree that if the interface is flat, it is very unlike that it will move. This is because, locally, the atoms from both sides from an interface are similar, having no 'will' to exchange places (which atomically describes the movement of the interface). For this movement to happen, local driving forces must exist.

3 Local Driving Forces

The excess surface energy is a necessary but not a sufficient condition for sintering. Diffusion promoted by thermal energy and local driving forces are also necessary conditions. The local driving forces are those pushing the atoms to certain directions at the microscale. While diffusion is basically related to the 'jumping' of an atom within the structure, pure diffusion will cause the atom to walk around the same average position. With the local driving forces, a preferential direction is given. Though the interface energetics can be related to the local chemical potentials, it is typically accepted that the local driving forces are mainly caused by the 'curvatures' present in the system.

Consider a cup full of a viscous liquid (like oil), and that you are blowing through a straw dipped into it (see Fig. 5). By blowing, you are providing work to expand a bubble of air inside the liquid. If you are creating a new surface area, energy is required for that, and the work provided in the form of pressure and volume should be equal to the energy of the newly created surface:

$$\Delta P dV = \gamma dA \tag{5}$$

That is, work is equal to the total bubble surface energy, given by γdA, where A is the surface area. If the bubble is spherical, the volume change is given by $4\pi r^2 dr$, where r is the radius of the bubble as shown in Fig. 5a. Hence, the area variation will be $8\pi r dr$, then, re-writing the above equation:

$$\Delta P = \gamma \frac{dA}{dV} = \gamma \frac{8\pi r dr}{4\pi r^2 dr} = \gamma \frac{2}{r} \tag{6}$$

This equation tells us that the smaller the radius, the higher the pressure needed to expand the bubble, and vice versa. As expansion is a reversible process, this means also that smaller bubbles are more prone to disappear than the big ones. Therefore, a bubble with 5 nm will be less mechanically stable than a bubble with 100 nm. This can be translated into a solid particle, with $r > 0$ (Fig. 5b), and suggests that the small particles are less stable than the large ones. If the radius is infinite, like in a flat surface, it will be even more stable, as ΔP will be very small. What happens then if the radius is negative? This is the case for a concave shape, as shown in Fig. 5d. As the surface energy in Eq. (6) cannot be negative, the negative radius induces a negative ΔP, suggesting no pressure is required to form it, but the contrary, pressure assists its formation, indicating a highly stable shape.

In fact, in addition to the mechanical pressure effect described by ΔP, the vapor pressure and the solubility of the particles are significantly affected by the curvature as well. That is, the vapor pressure is related to the chemical potential by the equation:

$$\mu = RT \ln p \tag{7}$$

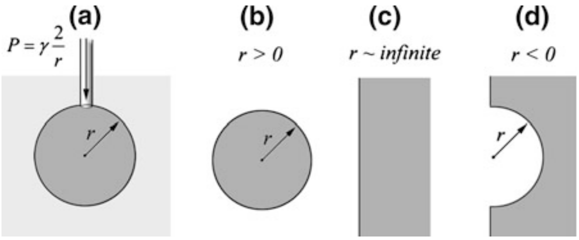

Fig. 5 Schematic representation of the relationship between the interface energies and the dihedral angle

where μ is the chemical potential, R is the gas constant, T the temperature, and p the vapor pressure. The difference of the chemical potentials for an atom sitting on a curved surface (p) and on a flat surface (p_0), if only curvature is acting, is then given by:

$$\Delta\mu = (RT\ln p - RT\ln p_0) \tag{8}$$

From the energetic perspective, the only difference between an atom on a flat surface and a curved surface is the area that is multiplying the surface energy. Hence, re-writing the equation assuming a spherical shape we have:

$$\Delta\mu = \left(RT\ln\frac{p}{p_0}\right) = \gamma dA = \gamma 8\pi r dr \tag{9}$$

Thence, for a molar volume V_M, we have:

$$p = p_0\exp\left(\frac{\gamma V_M}{RT}\frac{2}{r}\right) \tag{10}$$

This equation suggests that the vapor pressure and solubility are strongly dependent on the particle size, and that small particles are expected to dissolve/evaporate and re-precipitate in areas of smaller or negative curvatures. Those areas can be either a negative radius or simply larger particles. But how this will relate to the movement of atoms during a coarsening process?

4 Sintering, Coalescence and Grain Growth

Local and global driving forces are acting together on the atoms in a particulate system. When diffusion is high enough, concomitant processes start to happen, and they can be didactically divided into: sintering, coalescence, and grain growth (all commonly refereed to with the generic term ‘coarsening’). The difference among these processes lies on how the driving forces are acting. For instance, coalescence is the process by which smaller particles are dragged by larger ones. The driving force is surface elimination and, certainly, the higher curvature of the smaller particles. If the solubility of the particles is ruled by Eq. (10), and assuming that the size of a particle only varies if mass is diffusing into it, we can use a Fick’s law concept to write:

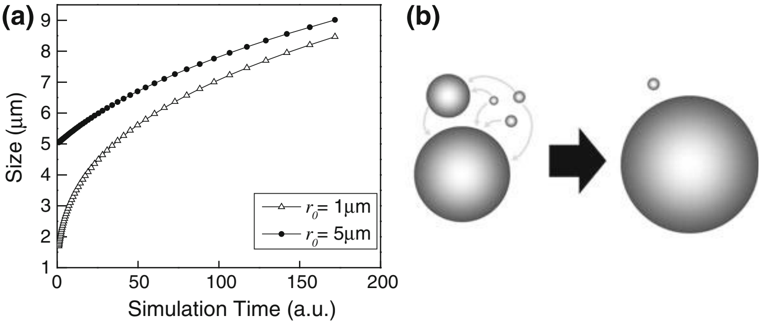

Fig. 6 Coalescence: **a** Simulation of ripening using Eq. (12) for Al_2O_3 at 1293 K and two different initial particle sizes. **b** Schematic representation of the process, where small particles disappear by evaporation and condensation of atoms on larger particles

$$J = \frac{dr}{dt} = D\frac{dp}{dr} \tag{11}$$

where J is the flux of atoms, D is the diffusion coefficient and dp/dr gives the driving force for movement of the atoms. We can solve Eq. (11) using Eq. (10) to give a common expression known as Ostwald ripening model [2]:

$$r^3 - r_0^3 = \frac{Dp_0\gamma M}{\rho^2 RT}t \tag{12}$$

In this equation, ρ is the density, and M is the molar weight. This equation shows that the average particle size of a system will increase as a function of time as shown in a simulation in Fig. 6a for Al_2O_3 coalescence. Certainly, the diffusion coefficient, surface energy and temperature will be critical parameters controlling the growth; however, if we fix these parameters, the interesting consequence of this equation is the effect of the initial particle size (r_0). That is, if the average particle size starts with relatively small particles (e.g. 1 µm), the coalescence is very intense, and the average radius increases rapidly (Fig. 6a). If, however, r_0 is large (e.g. 5 µm), the coalescence will be much slower. Since any real system is composed of both small and large sizes due to the natural size distribution, the equation predicts that the smaller ones will 'disappear' faster. This is the fundament of coalescence process. Moreover, for long processing times, all the particles will tend to have similar sizes, sharpening the size distribution (note how the simulated curves approach each other for long simulation times) in Fig. 6a.

This process will happen whenever there is a difference between radius, and mass will be evaporated (or dissolved) and condensed (or precipitated) from the smaller particles on the larger ones. Figure 6b shows a schematic representation of this phenomenon.

Sintering has the same basic driving forces of coalescence, but the sources and sinks of materials are different. The local driving force is actually the presence of a neck between two particles. This creates a negative curvature, as shown in Fig. 7,

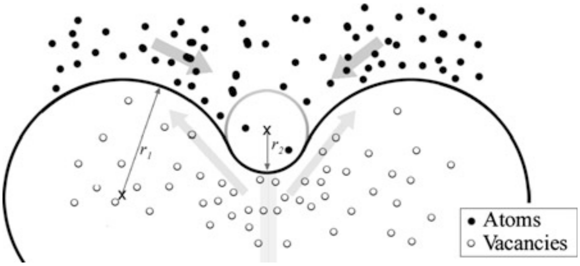

Fig. 7 Negative curvature formed in between two particles (r_2) will cause atoms to move in this direction from the positive curvature r_1. The opposite happens with vacancies

which will drag material from all over the particle surface (that has a positive curvature) to the neck area.

So, sintering can potentially happen between two particles of same size.[1] The different sources of materials will define the sintering mechanisms, that we will be discussing latter on this chapter. But as sintering progresses, the grain boundary (neck) is formed and grows, decreasing pore volume until they become isolated. In a ‘two particles’ model of sintering, it is hard to see a decreasing pore area as sintering progresses. This is more clearly observed in a ‘three particles’ model, as we will see ahead in Fig. 13.

The microstructure evolution considering pore elimination defines a well known didactic division of sintering into: *early stage*, *intermediate stage* and *final stage*. These stages are related to the relative density of the body as shown in Fig. 8. It is important to say that this is only a didactic division, and the process has always the same form of driving forces acting from the beginning to the end. The microstructure will have an effect on the contribution of each driving force though, giving rise to this division.

As soon as the neck is formed, another concomitant process takes place, *grain growth*. Again, the driving forces are the same (interface energy and curvature), but in this process the newly created grain boundary migrates through the grain. This process occurs as soon as boundaries are formed, but becomes more important in the final stages of sintering, where large amounts of boundaries exist. While grain boundary energy is the driving force, the movement of the boundary happens due to the curvature that pushes them towards the curvature center. The presence of a curvature in between two grains is not an obvious concept, and to explain this we need to remind that the contact angles between particles are moving towards the dihedral angle.

For instance, consider two particles of different sizes touching each other, as shown in Fig. 9. As the necks start to form, the microstructure evolves to satisfy the energy ‘equilibrium’ predicted by Eq. (4). This energy balance is only governed by the interface energetics, so it will be specific for each system and composition. Considering that the surface energy of a particular system is 1 J·m^{-2},

---

[1] There is still some discussion in the community arguing that sintering is only happening if a large number of particles in a compact is subjected to thermal treatment. However, the description based on the driving allows easier and distinguishable classification of the processes.

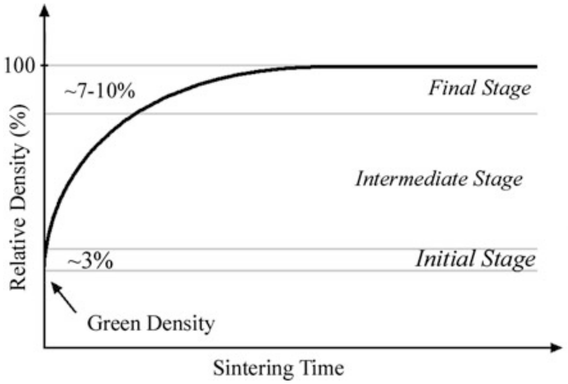

Fig. 8 Generic densification curve as a function of sintering time illustrating the stages of sintering. Green density represents the density of a compact before sintering starts

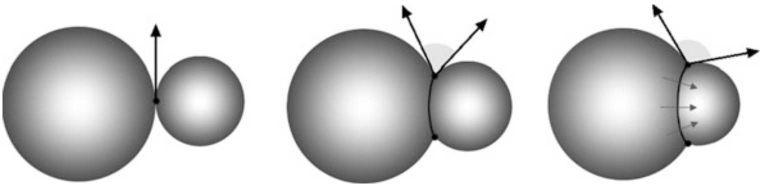

Fig. 9 Schematic representation of two particles of different sizes under sintering conditions showing the contact angle and curvatures are affected by the relative sizes. *Small gray arrows* describe the movement of the boundary

and the grain boundary energy is 0.75 J·m^{-2}, the predicted dihedral angle is 136 degrees. Assuming that the surfaces of the small and the larger particles in Fig. 9 are the same (same energy), the dihedral angle will have to be formed tilted as shown. As in each point of contact between the particles the same angle has to be respected, a curved boundary has to be formed. In a two dimensional analysis, this is represented by a curved line, in a real three dimensional analysis, there will be actually a curved surface, like a spherical cap. If this curve exists, the atoms in one side of the surface will be on a convex position, and in the other will be on a concave position. Considering the stability concepts described previously, we may say that the atoms will move such that the boundary interface itself will move towards the concave direction.

Therefore, the stability of a grain with relation to grain growth can be related to the curvature of the interfaces, which is related to the interface energies and to the number of grains surrounding it. While the interface energy dependence is clear from the previous example, the dependence on the number of grains is geometrical. For instance, consider a final stage of sintering, where A_S is significantly small. In this case, all the interfaces meeting at a triple point (point where three interfaces meet) will have similar energies (γ_{gb}). Using a 2D analogy of the

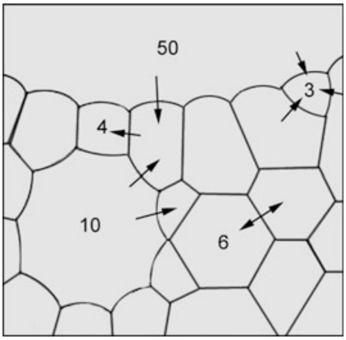

Fig. 10 Two dimensional schematics of grains in a dense material. The numbers represent the number of neighbors of each grain and the arrows the direction of movement of the interfaces

problem, each of the triple points would have to form a 120° angle (since all associated 'forces' would be pulling with the same strength).

However, this is only possible if exactly six grains are surrounding a particular grain. If more than six are there, the angles will be forced to be smaller, geometrically forcing a distortion of the boundary, and creating a concave interface with relation to the central grain. This creates a driving force for movement of the interfaces away from the central grain, provoking grain growth. If the contrary happens, i.e. a small number of grains surrounds it, the convex boundary will induce grain shrinkage. A schematic representation of this phenomenon is shown in Fig. 10. Note that for a 3D system, the idea is the same, but a little more critical, since it is impossible to geometrically accommodate 120° angles in all boundaries of a 3D grain. The closest one can get to it is the grains having the shape of a tetrakaidecahedron (shape shown in Fig. 4), that has 24 vertices, each having two 120° angles and one with 90°.

The growth of the grain is then determined by the movement of the interface, and mathematically we can write:

$$\frac{dr}{dt} = k \cdot J \cdot V_M \tag{13}$$

where k is a constant. Writing J in terms of diffusion and curvature potential:

$$\frac{dr}{dt} = k \cdot \frac{D_{gb}}{kT}(\Delta P) \cdot V_M \tag{14}$$

$$\frac{dr}{dt} = k \cdot \frac{D_{gb}}{RT}\frac{2\gamma_{gb}}{r_0}\frac{V_M}{w} \tag{15}$$

where D_{gb} is the grain boundary diffusion, γ_{gb} is its energy, w is the boundary thickness, and r_o is the initial radius. Integrating and condensing constants, we have:

$$r^2 - r_0^2 = k \cdot \frac{4D_{gb}\gamma_{gb}V_M}{RTw}t \tag{16}$$

This equation looks very similar to the one describing coalescence (Eq. 12), but r is elevated to two, and obviously the driving forces and diffusion being those for the grain boundary. The square of the final grain size will be proportional to these last two variables, and inversely proportional to the boundary thickness. The inverse dependence on the boundary thickness comes from the fact that a coherent movement of atoms must take place for a boundary to move. That is, the migration of the whole boundary depends on the combined movement of one atom and its neighbor (along the boundary), and the other neighbor, and so on. The thicker the boundary is, more coherent movements are required, retarding grain growth.

Although we give a different description of each of these phenomena: sintering, coarsening and grain growth, they are all happening at the same time during a regular thermal treatment. Because of the different driving forces, it is possible to evaluate which will have a more pronounced effect depending on the microstructure of the sample, and conditions of the treatment.

5 Pore Stability

During the first stages of sintering, necking takes place and the empty areas in between the particles decreases, promoting densification. At this stage, the particles become attached to each other, and the remaining free space is then called pores. The pores become an interconnected entity at the intermediate stage of sintering, where some grain growth is taking place and necking continues. At the final stage of sintering, pores become isolated on the grain boundaries, and at this point a description of its stability becomes very useful. That is, while the pores evolution is certainly a consequence of coarsening, one may look exclusively at the stability conditions of the pores to see what are the parameters affecting it, enabling a better control of pore elimination or pore stabilization (for catalysis purposes, for instance).

Pores are basically vapor phases that create solid–vapor interfaces with the grains. Similar to grain growth, the stability of a pore will be strongly dependent on the number of grains that can be surrounding it. This is because the solid–vapor interface will induce the formation of a dihedral angle with the grain boundary energy of the grains. Since the dihedral angle is defined by Eq. (4), only at certain specific number of surrounding grains it is possible to satisfy that angle. For all others, a curved pore-grain interface will be formed (to force the angles), providing local driving force for growth or shrinkage of pores.

Bringing up the 2D projection one more time, as shown in Fig. 11, the concept of the stability of a pore with relation to the number surrounding grains becomes clearer. If the dihedral angle is 120°, only when exactly six grains surround the pore it can be satisfied with flat interfaces. For a smaller number of grains, a concave interface (with relation to the pore) is formed, promotes movement of the interface towards the pore (by curvature potential), and shrinks the pore. On the other hand, if a larger number of grains surround the pore, a convex interface

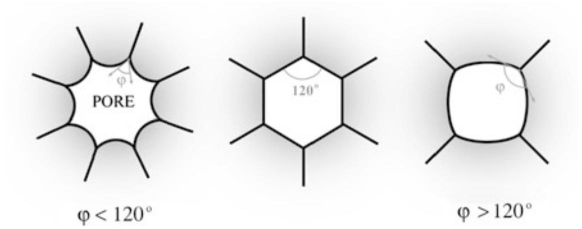

Fig. 11 Two dimensional schematics of pores surrounded by grains. The number of grains around a pore will define the internal angle, and hence the curvature that drives the movement of the interface to eliminate or grow the pores

Fig. 12 Relationship between the stability of pores, dihedral angle and number of grains surrounding the pore in a three dimension array

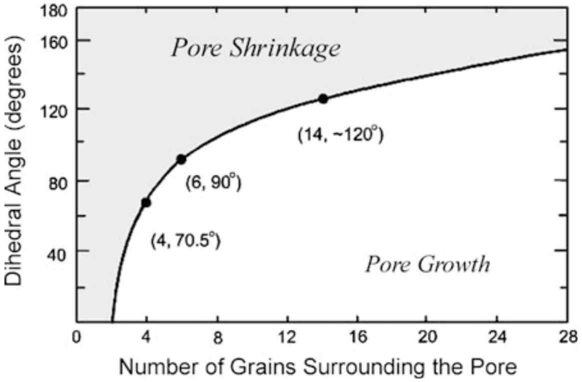

exists, and leads to pore growth if enough diffusion is provided. Since the dihedral angle can have different values, there is a balance of the effect of the number of grains surrounding the pores and the dihedral angle that controls the pore stability. In a 3D analysis, the picture is similar, but the geometry certainly more complex. A summary of the pore stability diagram in a 3D system is shown in Fig. 12, where it is clear that high dihedral angles will always lead to pore shrinkage, while for smaller dihedral angles the number of surrounding grains is very important to define the pore stability.

6 Sintering Mechanisms: Kinetic Control

We have described the driving forces for sintering of particles, which provide the directions of the flow of atoms in a system with enough mobility. However, another important concept on sintering is ‘how’ the atomic movement happens. The kinetics of sintering will tell us how fast sintering happens, what is the path the atoms go for, and consequently what is the final microstructure. Certainly

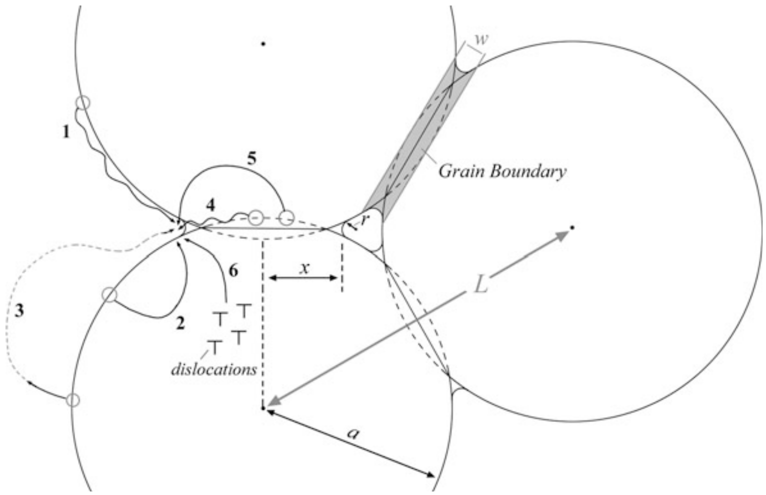

Fig. 13 Illustration of the sintering mechanisms in a three particles array. The *numbers* represent the different mechanisms and sources of material. (1) from surface by surface diffusion; (2) from surface by bulk diffusion; (3) from surface by evaporation/condensation; (4) from grain boundary by boundary diffusion; (5) from grain boundary by bulk diffusion; (6) from bulk by bulk diffusion (through dislocations)

thermodynamics is closely related to the kinetics, and both will control the final microstructure of the sintered body.

Looking at an assembly of three particles (Fig. 13), one can visualize the driving forces for the phenomena described above. In the initial stages of sintering the neck is considered to be the sink for the atoms. Therefore, atoms from the surface, from the grain boundary, or from the bulk, can move using different paths towards the neck. Analyzing Fig. 13, one can establish the following transport mechanisms: (1) Lattice diffusion; (2) Grain boundary diffusion; (3) Surface diffusion; (4) Gas phase transport by evaporation/condensation or gas diffusion; and (5) Viscous flow. The atoms' source can be the surface of the grain, the grain boundary, and the bulk.

The theory establishes a clear relationship between the source of material and the density of the compact in a simplistic way. If material is moving from the grain boundary or bulk to the neck, one should see high densification during sintering (pore elimination). If material is moving from the surface to the neck, densification will be limited. The explanation is given based on the distance between the particles' center. Imagine two particles touching each other, if material is being removed from the area in between the particles, they are expected to become closer by increasing neck area (with consequent centers approach). On the other hand, if material is being removed from the surface of the particle to the neck, the neck area increases, but can lead solely to a particle elongation and not to centers approach, resulting in low densification.

A quantitative description of the mechanisms can be done based on a two spherical particles model. The description is simple, and considers that the driving force of sintering is only the curvature potential, assuming that the grain boundary energy is negligible. Each description is exclusive for a certain mechanism, though. For instance, let us describe here the sintering with lattice diffusion from grain boundary. Considering two particles touching each other, the volume change as a function of time is given by:

$$\frac{dV_n}{dt} = JA_n V_M \tag{17}$$

where A_n is the neck area and V_n is the neck volume. Since the particles are spherical, we can write:

$$\frac{\pi x^3 dx}{a\ dt} = \frac{D_l}{RT}\left(\frac{\gamma_s}{r}\frac{1}{x}\right)A_n V_M \tag{18}$$

and hence,

$$x^4 = \frac{16 D_l V_M \gamma_s a}{RT} t \tag{19}$$

Where x is the radius of the circle forming the neck when two particles are touching, r is the radius of the negative curvature formed between the particles (as shown in Fig. 13), and a is the particle radius. From this, one can determine an equation for shrinkage:

$$\frac{\Delta L}{L} = \frac{r}{a} = \frac{x^2}{4a^2} = \left(\frac{D_l \gamma_s V_M}{RTa^3}\right)^{1/2} t^{1/2} \tag{20}$$

where L is the distance between the centers of the particles. This equation suggests that the shrinkage in a system governed by lattice diffusion from grain boundary is dependent on $t^{1/2}$. Hence, experimentally one is capable of fitting shrinkage curves to say if certain system is or not controlled by this transport mechanism. A similar derivation can be done for all other mechanisms, and they should have different dependences on the time (for a detailed derivation of each case, please refer to S-J. Kang's book [3]).

7 An Unfinished Story

The present description of sintering has been extensively used to explain the sintering behaviors of different materials with relative success. However, this theory cannot *predict* if a system will have pore elimination or not during sintering, as it is only a descriptive analysis of the process. To improve the model, some works have proposed that the reason why some materials are more prone to densification lies mainly on the interface energetics. Materials with grain boundary energy significantly lower than the surface energy would be more likely to get dense, while those with high grain boundary energy would have a thermodynamic barrier to overcome in order to eliminate pores. As you have noticed, this term is not considered in the above sintering description, which assumes the grain boundary energy is negligible with relation to the surface energy, which is not always the reality in most cases. J.L. Shi has reported on the improvement [4], but the community is debating novel approaches still without consensus.

8 Summary

The present chapter was designed to introduce the reader to the largely accepted theories of sintering, coalescence and grain growth. We have identified the phenomenological differences between these processes, and seen that though they share similar driving forces (interface energies and curvatures), the interfaces and local curvatures are located in different places, and are therefore responsible for different mass movements. One should remember that they are expected to happen at the same time during a real processing, and certainly interfere in one another. The presented equations describe the individual processes though, and should be used with some criteria, as they have serious limitations.

As an initial chapter of the book, we have also established a 'common language' so the reader will be familiar with the next chapters that will address more specifically some aspects of these processes.

Acknowledgments This chapter was written with support from the National Science Foundation under grant DMR 1055504.

References

1. Lange, F.F.: J. Eur. Ceram. Soc. **28**, 1509–1516 (2008)
2. Chiang, Y.M, Birnie, D.P, Kingery, W.D *Physical Ceramics.* Wiley, New York p. xiv, p. 522 (1997)
3. Kang, S.J.L.: Sintering: Densification, grain growth and microstructure. Elsevier Butterwirth-Heinemann, Oxford (2005)
4. Shi, J.L.: J. Mater. Res. **14**(4), 1378–1388, 1398–1408 (1998)

Modelling "Nano-Effects" in Sintering

Fan Li and Jingzhe Pan

Abstract Materials at the nanoscale typically show distinct behavior from their microsized counter parts. This is not different in sintering, and this chapter collects some previous studies on nano effects on this important phenomenon. It is constantly argued by researchers that classical continuum sintering model requires re-examination in the context of nanosintering. A possible way of doing this is by incorporating multiple mechanisms which may cause nano effects into the modeling. In this chapter we introduce both analytical and computational approaches. Analytical method is used to provide a guidance and first insight into nanosintering. Various computational models are then constructed using techniques such as Finite Difference (FD), Finite Element (FE), and Molecular Dynamics (MD), in order to capture the coupled features.

1 Introduction

The evaluation of the nanoscale effects on sintering can be done on an analytical basis by writing a more generic equation for its atomic movement. That is, solid state sintering is conventionally modeled using a diffusive flux, j, representing the number of atoms passing through a unit area per second (we are disregarding liquid phase sintering for now). Thanks to the understanding of sintering at the atomic level, this flux can be represented by an atomic driving force F, which equals to the spatial gradient of the chemical potential μ. The total flux of atoms in a general sintering process can then be related to the atomic concentration (C) and

---

F. Li · J. Pan (✉)
Department of Engineering, University of Leicester, LE1 7RH, Leicester, UK
e-mail: jp165@leicester.ac.uk

R. H. R. Castro and K. van Benthem (eds.), *Sintering*, Engineering Materials 35,
DOI: 10.1007/978-3-642-31009-6_2, © Springer-Verlag Berlin Heidelberg 2013

Fig. 1 Geometry of particle contact with two diffusion mechanisms

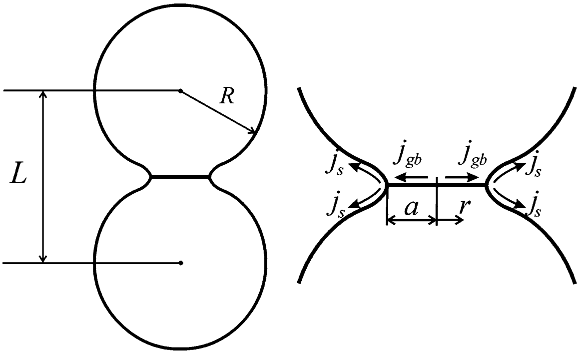

the atomic drift velocity (*V*) by $J = CV$. Since V is the product of the atomic jumping frequency (*f*) and the atomic spacing (*a*), we can write: $J = Caf$.

Since diffusion is driven by F, and the jumping frequency is dependent on the hyperbolic sine of F [1], we have:

$$j = \frac{2D}{a\Omega}\sinh\left(\frac{aF}{2kT}\right) = \frac{2D}{a\Omega}\sinh\left(-\frac{a}{2kT}\nabla\mu\right) \tag{1}$$

in which D is the diffusion coefficient depending on material constants and temperature, a and Ω are atomic spacing and volume, respectively, k is the Boltzmann constant, and T is the temperature in Kelvin.

The classical sintering theory assumes $aF \leq kT$, which leads to the linearization: $\sinh(aF/2kT) \approx (aF/2kT)$. A simplified linear diffusion law is therefore recovered:

$$j_{linear} = \frac{DF}{\Omega kT} = -\frac{D}{\Omega kT}\nabla\mu \tag{2}$$

Solving Eqs. (1) and (2) requires an explicit expression for the chemical potentials, μ. The gradient of μ along the diffusion route will be the driving force for mass movement. The chemical potential is a measure of the energy difference when one atom is added to a particular location. So, in absence of a concentration gradient, local excess energies will affect the chemical potential and lead diffusion.

Figure 1 shows two types of diffusions which are believed to play roles during the sintering process: grain boundary diffusion with flux j_{gb} and surface diffusion with flux j_s. The corresponding chemical potentials for these locations are [2]:

$$\mu = -\Omega\sigma \tag{3}$$

for the grain boundary (where σ is the stress normal to the grain boundary), and

$$\mu = -\Omega\gamma_s\kappa \tag{4}$$

for the free surface, where γ_s is the specific surface energy and κ the principal curvature of the free surface. As shown in Fig. 1, assuming a circular shape of

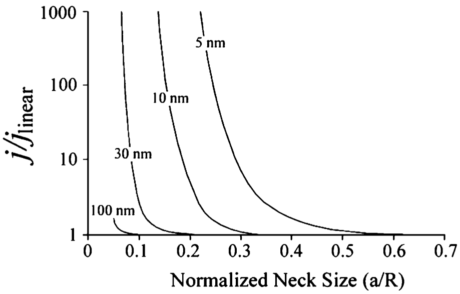

Fig. 2 Comparisons between linear diffusion law and non-linear diffusion law, for a typical set of sintering parameter of alumina. The sizes along the plots represent ‘R’. Modified from Ref. [1]

grain boundary, the main curvature at the tip of the contact area can be described as [3]:

$$\kappa_{(r=a)} = 1/\rho - 1/a = 4R/a^2 - 1/a \tag{5}$$

in which r is the radial coordinate of the circular grain boundary, κ is the curvature of the particle profile, a the radius of grain boundary, and R the radius of the particle. The driving force at the edge of grain boundary can be estimated as:

$$F = \nabla\mu = \frac{\Delta\mu}{\Delta r} \approx -\frac{\mu_{(r=a)} - \mu_{(r=0)}}{a/2} = 2\gamma_s(4R - a)\frac{\Omega}{a^3} \tag{6}$$

A simple rearrange of Eq. (6) yields:

$$F = 2\gamma_s(4 - a/R)\frac{\Omega}{(a/R)^3}\frac{1}{R^2} \tag{7}$$

in which a/R is the normalized half neck size. Given a normalized neck size, the level of matter redistribution is determined for particles of any size. It can be then observed from Eq. (7) that the diffusion driving force F increases by the power of two with the decreasing of particle radius R. Therefore, there is potentially a huge driving force for the sintering of nanoparticles, i.e. particles with small values of R. If this is true, the approximation $aF \leq kT$ may not hold at these conditions and the linearization in Eq. (2) may have to be re-examined.

For the sintering of alumina with material parameters $a = 0.5$ nm, $\gamma_s = 1$ J/m^2, $\Omega = 0.02$ nm^3, at temperature T = 1160 K, Eqs. (1) and (2) can be solved separately through Eq. (6). The comparisons are shown in Fig. 2, where j obtained by the nonlinear law over that by the linear law is plotted against the normalized particle neck size. From the figure, it is evident that the linearization causes more error in calculating the driving force when both particle size R and neck size a/R are small. For particles of $R \geq 100$ nm however, the linearization is generally acceptable.

2 Densification Law

In the classical sintering theory, densification is believed to happen by the approaching motion of the particles, i.e., the change in the center to center distance, L, as shown in Fig. 1. Variational calculus is a convenient tool to solve this sort of problem [4–6].

Defining a total potential energy rate, Π, of a material under sintering as the summation of the power of the driving force over all migrating atoms and the changing rate of the total free energy E, we have:

$$\Pi = \sum_{all\_atoms} F V_{atom}(hdA/\Omega) + \dot{E} \tag{8}$$

in which V_{atom} is the atomic migration velocity, h is the thickness of the layer within which diffusion takes place, A is the area of the particle surface or grain boundary, and dot denotes the time derivative. Noticing that the diffusive flux $j = V_{atom}\, h\Omega$ and assuming linear diffusion law, Eq. (8) becomes:

$$\Pi = \int_S \frac{kT}{2\Omega D_s} j \cdot j dA + \int_{GB} \frac{kT}{2\Omega D_{GB}} j \cdot j dA + \dot{E} \tag{9}$$

in which D_{GB} and D_s are the diffusion coefficients at grain boundary and particle surface, respectively. The total free energy is reduced when two free surfaces turn into a grain boundary at a particle contact, i.e. we have $\dot{E} = -4\pi a\ \dot{a}\gamma_s$. $\delta\Pi = 0$ leads to [3]:

$$\left(\frac{\Delta L}{R}\right)^3 = 3\frac{\gamma_s D_{GB} h\Omega}{kTR^4} t \tag{10}$$

Equation (10) was first obtained by Coble [7] using the linear flux in equation (2) (Note that this is basically the same sort of derivation shown in the introductory chapter of this book for the lattice diffusion case). However, for the sintering of nanoparticles, the nonlinear flux in Eq. (1) may become important. Following Coble's [7] protocol, Eqs. (1) and (9) can be solved through numerical iterations. The results are plotted in Fig. 3. Interestingly, despite the huge error of flux using linear diffusion law for nanoparticles as shown in Fig. 2, the densification law is very similar, even for particle size as small as 5 nm. The figure shows densification as a function of time, hence the derivative (slope) represents the densification rate. The linear diffusion law yields the largest error at the beginning of the sintering and quickly catches up the nonlinear law, indicating a similar densification rate. It can be concluded that even for nanosized particles, the accuracy of classical linear diffusion law is acceptable, with a slight under-prediction of the sintering rate at the early stages.

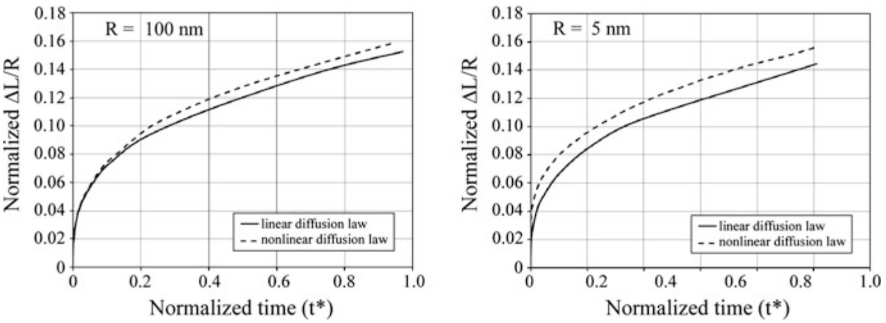

Fig. 3 Comparison between the linear solution (*solid lines*) and the nonlinear solutions (*dashed lines*) for the shrinkage between two spherical particles as functions of time, for different particle sizes

3 Nonlinear Relation Between Stress and Strain Rate

The densification equation can be further developed into a constitutive equation. For micron-sized particles, linear constitutive laws are often used to calculate sintering deformation. By considering a representative volume of a particle compact, the macroscopic stress–strain rate relationship in compact under sintering can be estimated from the total potential energy Π of the representative volume [8]:

$$\Pi = \dot{E}_{ij}\Sigma_{ij} - \frac{1}{v}\int_{GB}\frac{1}{2D_{GB}}j\cdot j dA - \frac{1}{v}\dot{E} \tag{11}$$

in which $\dot{E}_{ij}$ and Σ_{ij} are the macroscopic strain rate and stress, i and j are direction indices, and v is the volume of the macroscopic representative unit of the particle compact. Note that this equation does not include the surface diffusion term, as it can be generally assumed that surface diffusion is faster than grain boundary diffusion which controls the densification rate [9]. By relating the representative volume of the sintered body v to the relative density λ, Eq. (11) leads to a *viscous constitutive law* for solid state sintering [10, 11]:

$$\dot{E}_{ij} = \frac{36\Omega D_{GB}}{kTR^3}\Sigma_{ij}f(\lambda) + \dot{E}_{\text{exp}} = \dot{E}_{0d}\frac{\Sigma_{ij}}{\Sigma_0}f(\lambda) + \dot{E}_{\text{exp}} \tag{12}$$

where $\dot{E}_{\text{exp}}$ is the free sintering strain rate, $\dot{E}_{0d}$ is a reference strain rate for the fully dense material under a reference stress Σ_0, $f(\lambda)$ is a non-dimensional function of the relative density λ, and the numeric parameter comes from assuming that the particles are of spherical shape.

For sintering processes under a large external force (such as in hot isostatic pressure assisted sintering, HIPing), the free sintering term in Eq. (12) can be ignored and a linear relationship between the strain rate and applied stress is predicted. Such constitutive law is therefore generally referred to be linear viscous and widely used. On the other hand, it has been shown that in nanosintering with fine grains, the grain boundaries may not be the perfect sinks for vacancies (because they may have well defined structures) [12]. Hence atoms or vacancies can only be added to or removed from those sites as dislocations, resulting in climb of the dislocations in the boundary plane. In these cases, mechanisms at atomic level, such as viscous drag, or the action of friction and pinning forces may slow down the solid diffusion or even control the whole sintering process. Such mechanisms are referred to as "interface reaction" [12]. In the existence of interface reaction, the total chemical potential available to drive diffusion is reduced by an interface stress σ_r, and Eq. (3) becomes:

$$\mu = -\Omega(\sigma - \sigma_r) \tag{13}$$

By fitting existing experimental data, Cocks [13] suggested that the interface reaction stress follows a power law function of the separation rate $\Delta\dot{L}$ of particles:

$$\sigma_r = \frac{\sigma_0}{v_0^2}\Delta\dot{L}^2 \tag{14}$$

in which σ_0 is a reference stress, v_0 is the characteristic rate related to the interface reaction. If the diffusion is completely dominated by interface reaction, Cocks obtained the following constitutive law [12]:

$$\dot{E}_{ij} = 0.772\frac{v_0}{R}\left(\frac{\Sigma_{ij}}{\Sigma_0}\right)^2 g(\lambda) + \dot{E}_{\mathrm{exp}} = \dot{E}_{0i}\left(\frac{\Sigma_{ij}}{\Sigma_0}\right)^2 g(\lambda) + \dot{E}_{\mathrm{exp}} \tag{15}$$

in which g(λ) is a non-dimensional function different from $f(\lambda)$, $\dot{E}_{0i}$ is a reference strain rate for the interface reaction controlled process. As indicated by Eq. (15), if $\dot{E}_{\mathrm{exp}}$ is ignored, the stress–strain rate relationship follows a power law of exponent 2, rather than being linear in the diffusion controlled densification [Eq. (12)]. The ratio between the reference strain rates of the two mechanisms is given by:

$$\frac{\dot{E}_{0d}}{\dot{E}_{0i}} = \frac{46.5D_{GB}V_M}{kTR^2v_0}\Sigma_0 \tag{16}$$

which can be used as an indicator for the relative importance of the two mechanisms. When $\dot{E}_{0d}/\dot{E}_{0i}$ is large, the interface reaction consumes more energy than the diffusion process. The interface reaction therefore controls the sintering rate. Judging from Eq. (16), for small grain-size and lower temperature, the sintering process is more likely to be dominated by interface reaction. The experimental data in Ref. [14] (see Fig. 3 in Ref. [14]) shows that the power exponent in the stress-strain rate relation changes from 1 to 2, indicating a switch of mechanism in the half way of sintering. For nano-powder compacts, the stress–strain rate relationship may become nonlinear due to the dominance of interface reaction.

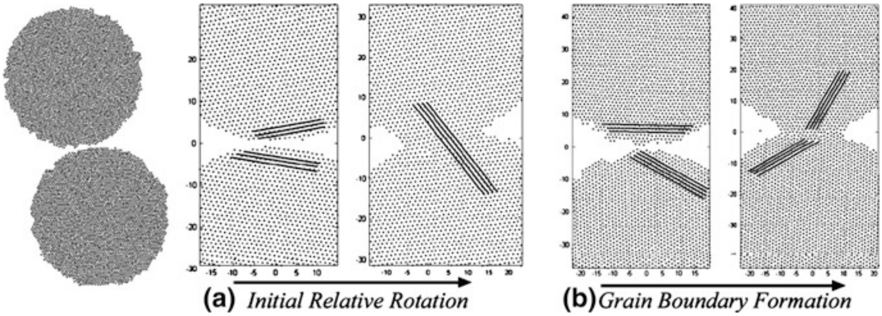

Fig. 4 Two kinds of contact formed between nanoparticles in sintering **a** a low energy perfect atomic alignment and **b** a high energy ‘miss oriented’ grain boundary

4 A Molecular Dynamics Study of Sintering

The diffusion law expressed by Eq. (1) and the densification law expressed by Eq. (11) are based on the assumption that grain boundary diffusion and surface diffusion are the two mechanisms controlling the whole diffusion process. This continuum treatment of the atomic migration can be naturally assessed by molecular dynamics (MD) studies [15]. The MD model of particles in sintering is illustrated in Fig. 4. The particle diameter is about 16 nm. An interesting observation from these MD simulations is that the contact area between the two particles can reach a low energy state in the very beginning of the sintering process and form a perfectly aligned interface. As shown in Fig. 4a, for particles with different initial crystalline orientations, a quick adjustment in the atomic orientations can occur at the very beginning of the sintering. The particles then remain in the adjusted orientations throughout the rest of the sintering process (Fig. 5a). This reorientation has been also observed in nanosintering experiments [16]. In some other cases, a non-coherent grain boundary is formed after the initial adjustment, as shown in Fig. 4b. It is observed that three factors can help the formation of a grain boundary: (i) large initial misalignment angle between particles, (ii) relatively large particle size, and (iii) high sintering temperatures.

Snapshots of the simulated sintering process are presented in Fig. 5. The following colouring scheme is used: the bulk atoms are always coloured as blue, any atom that has been on either the particle surface or the particle interface is colored as red, and any atom that has ever been into the vapor is colored as cyan. The coloring scheme therefore provides a rough picture of the matter redistribution during the sintering process. For Fig. 5a, since the crystalline structures of both particles are aligned at the very beginning of the sintering process, there exists no fast diffusion route between the two particles, as detailed in Fig. 4a. The sintering process started with a quick neck formation followed by neck growth firstly by surface diffusion and then by vapor condensation. However these matter redistribution mechanisms do not make the two particles to approach each other. For the second case there is a grain boundary acting as the fast diffusion route between two

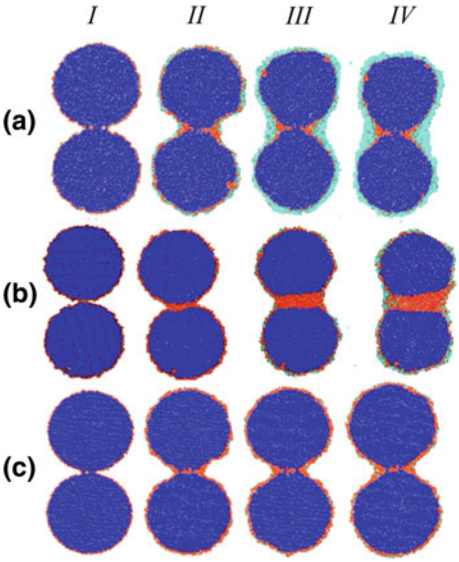

Fig. 5 MD simulation of two nanoparticles in sintering **a** high temperature without grain boundary, **b** high temperature with grain boundary and **c** low temperature (73 % to that of (**a**) and (**b**)) without grain boundary. (I–IV) shows different sintering times (same times for all the three cases); see text for the coloring scheme. Adapted from Ref. [15]

the contacting particles (Fig. 5b), the neck is filled up dominantly by atoms coming from the particle interface. Grain boundary diffusion is the controlling mechanism and the two particles approach each other. A case of lower sintering temperature is shown in Fig. 5c, where it is difficult to form a grain boundary between the two particles and vapor evaporation is also much weaker. Surface diffusion is the dominant mechanism of material redistribution. Further measurements confirm that if the atomic orientations of the two particles are perfectly aligned, such as that shown in Figs. 5a, c, the distance between the two particles remains unchanged during the sintering process. This is consistent with the established continuum theory that densification is only observed by grain boundary diffusion [9]. However, what the continuum theory cannot predict is the crystalline orientation of the particles and therefore unable to predict the sintering behavior of the nano-particles. These three cases shown in Fig. 5 therefore highlight the difference between the MD models and the continuum models for sintering of nanoparticles.

For nanoparticles, the sintering behavior observed in the MD simulations is therefore beyond the predictability of the continuum theory. If the assumed mechanism of matter redistribution in a continuum model does occur in a MD simulation, then it would be interesting to see if the two models agree with each other. Figure 6 compares the neck growth as a function of time predicted by continuum and MD models respectively. Figure 6a shows a case where matter redistribution is controlled by grain boundary diffusion, corresponding to Fig. 5b. Figure 6b shows a case controlled by surface diffusion corresponding to Fig. 5c. The straight lines are the continuum models while the discrete dots were obtained from several independent MD simulations. It is remarkable to see that the continuum models work reasonably well for nanoparticles, though it is clear that there is a change in the slopes of MD calculation that cannot be fitted by the continuum models.

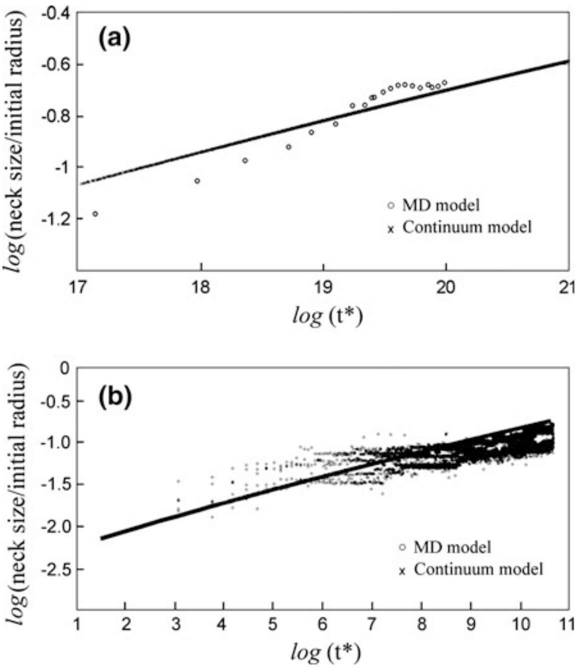

Fig. 6 Normalized neck size as a function of normalized time calculated by the MD model (*discrete dots*) and continuum model (*solid line*) for the sintering of two particles **a** high temperature sintering controlled by grain boundary diffusion and **b** low temperature sintering controlled by surface diffusion. Adapted from Ref. [15]

5 Coarsening Law

Particle/grain coarsening is another important phenomenon in nanosintering. It is important to maintain the nano-size of the particles to obtain a nanostructure for the sintered material. Practically the sizes of the particles are not as uniform as illustrated in Figs. 1 and 4. When a large particle meets a smaller one, classical sintering theory predicts that the grain boundary migrates towards the small particle and the size of large particle increases [17–19]. Nano-effect may also play a key role in the particle coarsening process.

According to Ref. [20], energy dissipation by grain-boundary migration can be reflected by an additional term in the variational functional in Eq. (9):

$$\begin{aligned}\Pi &= \int_S \frac{1}{2D_s} j \cdot j dA + \int_{GB} \frac{1}{2D_{GB}} j \cdot j dA \\ &\quad + \int_{GB} \frac{h}{2\tilde{M}} v_\perp \cdot v_\perp dA + \dot{E}\end{aligned} \tag{17}$$

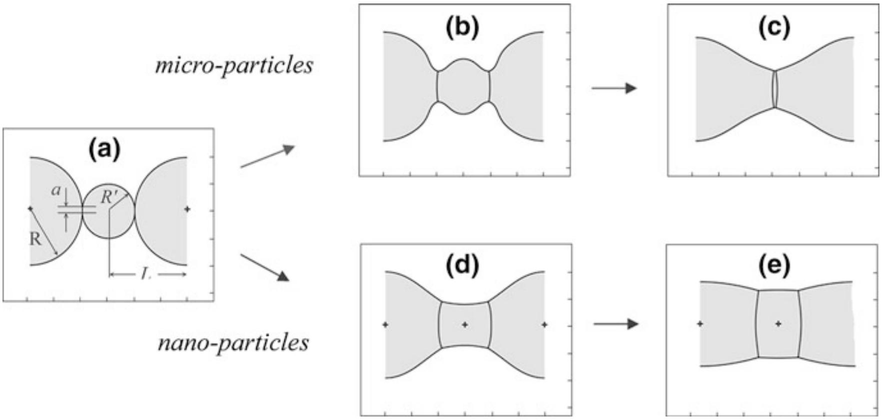

Fig. 7 Computer simulated shape evolutions of nano-sized particles of different sizes. **a** initial configuration, **b**, **c** micron size particles at different sintering stages, **d**, **e**, nano size particles at different sintering stages. Adapted from Ref. [20]

in which $v_\perp$ is the atomic migration velocity normal to the particle interface which leads to grain boundary migration and $\tilde{M}$ is the grain boundary mobility. A non-dimensionalisation analysis leads to [20]

$$\begin{aligned} \Pi^* = & \int_S \frac{1}{2D_s^*} j \cdot j dA + \int_{GB} j \cdot j dA \\ & + \int_{GB} \frac{1}{2\tilde{M}^*} v_\perp \cdot v_\perp dA + \dot{E}^* \end{aligned} \tag{18}$$

in which

$$D_s^* = D_s / D_{GB}^*,\ \tilde{M}^* = \tilde{M} R^2 / h D_{GB} = (R/h)^2,\ E^* = E / D_{GB} \tag{19}$$

In Eq. (18), $\tilde{M}^*$ serves as an indicator for a size effect during particle coarsening. For grain boundary migration, atoms only have to move slightly normal to the grain boundary in the range of the grain-boundary thickness h, which is in the order of a few nanometers. For the grain boundary diffusion, on the other hand, atoms have to move along the grain boundary in a tangential direction, which has the length scale of the particle size, $a^2 \approx \Delta L/R$ (see Fig. 1). Reducing the particle size therefore has a huge effect on grain boundary diffusion but almost no effect on grain-boundary migration. Reference [20] derived a numerical scheme to solve Eq. (18). Their results are shown in Fig. 7.

Coarsening was simulated using a model of a small particle located in the middle of two large neighboring particles. The radius of the large particles is twice the small one. Two different particle sizes are used in Fig. 7 to illustrate the size effect. For the large particles with sizes equal 1 μm, it can be seen from Fig. 7b, c that the grain boundary continually moves towards the small particle. The large particles invade into the small one and finally only a small fraction of the small particle remains. This is consistent with classical particle coarsening theory during sintering. For the nanoparticles shown in Fig. 7d, e, however, the coarsening behavior is more complicated. The small nanoparticle shows certain resistance to invasion. The curvature of the surface of the small particle changes direction from Fig. 7d, e, indicating that the small particle was taking materials from the surfaces of the large particles through surface diffusion up to certain stage. This occurs only in the nanoparticles because of the short diffusion distance (the actual size of the particles in Fig. 7d, e is three order of magnitude smaller than that in the Figures above them). The small particle then grows, rather than shrinks, at the expense of the two large particles. At the final stage, the small particle eventually decreases in size, leading to the coarsening of two large particles.

This interesting phenomenon of resistance to coarsening by nanoparticles can be seen more clearly in Fig. 8, which compares the coarsening behaviors for particles of different sizes of two different particle arrangements. A log plot is used in order to include all particle sizes in one figure. The points *b*, and *c* in Fig. 8 correspond to Fig. 7b, c. For the particle arrangement shown in Fig. 7a, the small particle can increase its size rather than decreasing it. It can be seen from Fig. 8 that the smaller the particle size is, the larger resistance it has to coarsening. However, if a different particle arrangement is assumed, such as one large particle in contact with one small particle, there is no resistance to coarsening at all as shown by the broken lines in Fig. 8. A parallel study of densification law [20] (which is not shown here) in the existence of coarsening also suggests that densification law may be very different when assuming different particle contact, such as in Fig. 8. These numerical studies suggest that densification law and coarsening law cannot be considered separately, which has been a standard practice in the existing sintering theory.

6 Pre-Sintering Agglomeration

The numerical simulation above shows that the nanoparticle exerts certain degree of resistance to coarsening. This has also been reported in experiments [21]. However at the same time, it has been also reported that there is severe coarsening of nanoparticles [22]. Such contradiction can be attributed to the agglomeration state in the pre-sintering powder. As the size of particles gets smaller, the surface interaction between fine particles makes them very ‘sticky’ and difficult to separate.

As shown in Fig. 9, the agglomeration can be modelled using two particle contact, which is very similar to the diffusion model in Fig. 1. Size effect is studied by assigning a kinetic energy to the particles about to contact each other. Whenever the particles meet each other, that kinetic energy is converted into neck formation. A neck is formed by either elastic or plastic deformation and total free energy associated with the surface energy is reduced. Continuum theory predicted that the force required to separate adhered particles is in between $-2\pi R\ \gamma_s$ and

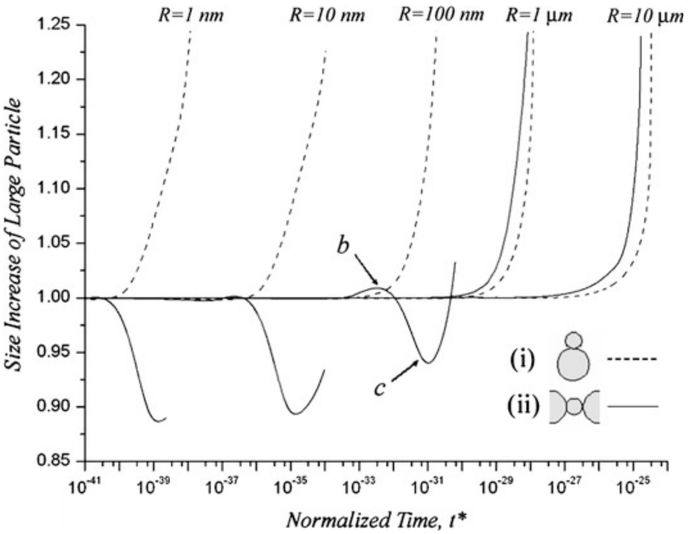

Fig. 8 Particle size (normalized by its original size) versus normalized sintering time. The solid lines were obtained using a model of one small particle placed between two large ones and the *dashed lines* were obtained using a model of one large particle in contact with a small one model. **b** and **c** correspond to the stages of the particle evolution shown in Fig. 7b, c. Adapted from Ref. [20]

$-1.5\pi R\ \gamma_s$ [23–26], recalling that γ_s represents the specific surface energy. If we ignore the effect of the surface energy, the particles will always rebound after impact. However a smaller particle has a higher proportion of surface energy comparing to the elastic strain energy. The surface energy effect becomes more important for small particles and is responsible for the sticking and agglomeration between small particles.

The coupled problem of particle interaction under the combined effects of surface energy and elastic deformation energy can be solved numerically using the Finite Element method [27, 28]. The force–displacement curve is plotted in Fig. 9a–c for different particle sizes using a common value for the specific surface energy of $\gamma_s = 0.11$ J/m^2. The results are normalized by the particle size. The surface energy and deformation energy can be measured as the area under the contact force–displacement curves. It can be seen from Fig. 9 that the work done by surface energy is more important for smaller particles, explaining the higher agglomeration of the nanoparticles.

The Maugis contact law that takes into account of particle adhesion is also plotted in Fig. 9 [28]. It appears that the analytical model works fairly well for nanoparticles. However, particle surfaces are never atomically smooth. It is therefore important to understand the effect of surface roughness on the particle adhesion. As shown in Fig. 10, the contact between rough surfaces can be modeled as contact between the asperities of the surfaces. The effect of roughness is here considered using two identical particles of 50 nm in the enveloping radius with

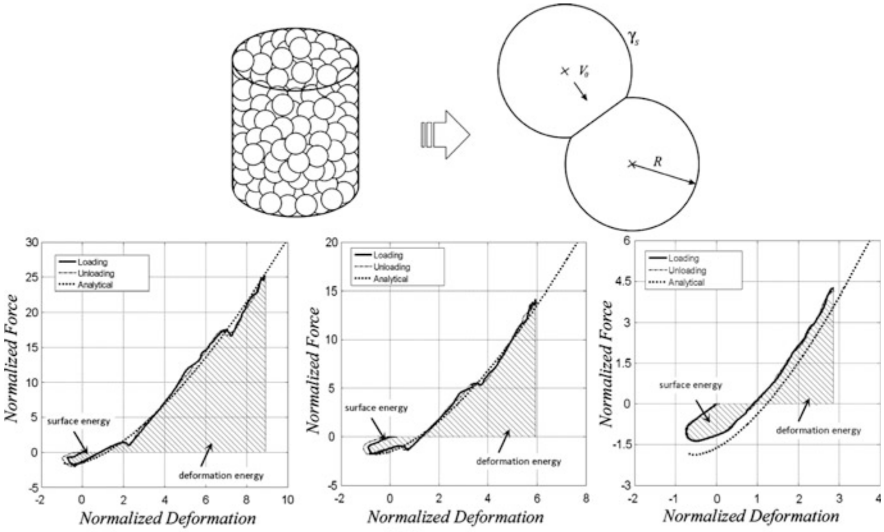

(a) $R = 500$ nm (b) $R = 250$ nm (c) $R = 50$ nm

Fig. 9 Contact force versus particle deformation for adhesive contact between particles of different sizes: **a** $R = 500$ nm, **b** $R = 250$ nm and **c** $R = 50$ nm. Shaded areas represent kinetic energy (positive) and surface energy (negative)

sinusoidal asperities of about 1 nm in height of two different periods [28]. The specific surface energy is taken as $\gamma_s = 1.17$ J/m^{2,} which is roughly the nominal value for metallic particles such as copper. The shape of the force–displacement curve in Fig. 10a is very similar to the one in Fig. 10c. The whole kinetic energy is fully recovered at the end of contact, represented by a zero deformation at the end of unloading curve. For the Fig. 10b, on the other hand, the final unloading deformation is not zero, indicating particle adhesion. This is a typical adhesive behaviour in which the kinetic energy is not large enough to overcome the surface energy. The two cases are designed to demonstrate that a slight difference in surface roughness can change the behaviour of the particles from non-sticking (Fig. 10a) to sticking (Fig. 10b). The particles with more asperities (Fig. 10a), i.e. a rougher surface, behave like particles with smaller specific surface energy as those shown in Fig. 9c. Using an effective value of specific surface energy it is possible to fit the numerical results with the Maugis contact law. This is shown in Fig. 10a, b by taking $\gamma_{eff} = 0.19$ J/m^2 and $\gamma_{eff} = 0.26$ J/m^2 respectively. The analytical solution would work well if a relation between the surface roughness and the effective specific surface energy can be established.

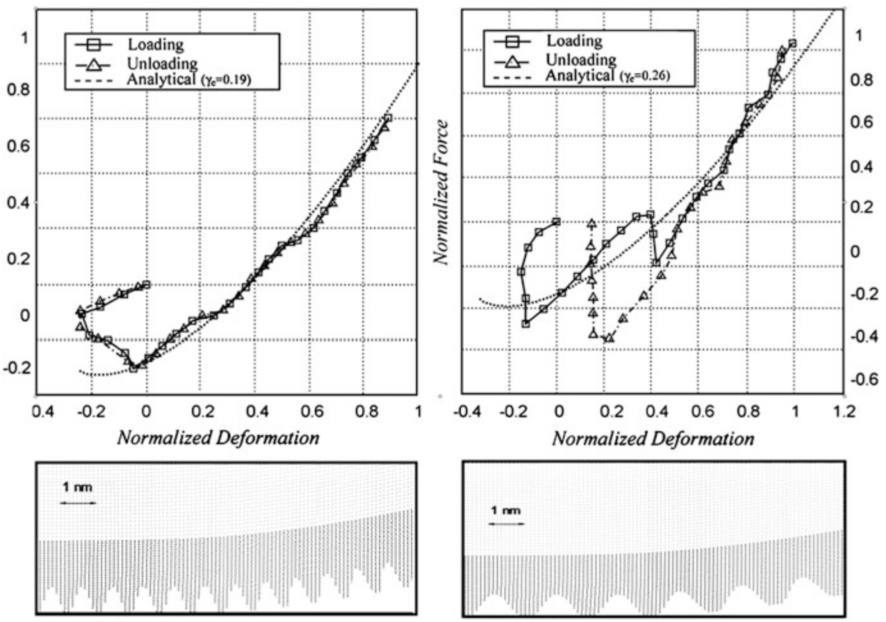

(a) Profile = -5 cos(240π)/12

(b) Profile = -5 cos(120π)/12

Fig. 10 Force plotted again deformation for particles ($R = 50$ nm) with a rough surface near the contact area with different degrees of roughness. **a** a rougher surface, and **b** less rough surface. Analytical solution using an effective surface energy is also plotted for comparisons

7 Closing of Large Pores

A consequence of agglomeration is that it is difficult to achieve dense packing for a pre-sintering nanoparticle system. During the sintering process, a common problem is that large pores are left behind the sintering of which requires long time and destroys the nanostructure by grain-coarsening. Sintering kinetics of the large pores could be a key concern for controlling the densification behaviour of all granulated powders [29]. A text book theory of sintering of large pores can be explained using the configuration in Fig. 11 of the previous chapter. If we refer to the number of grains surrounding a pore, i.e. the coordination number, as n, a pore is said to be large if n is large. For a small change in pore radius referred to as Δr, the total free energy change will be the difference between the increase in the interface energy associated with the grain boundaries and the decrease of the total surface energy:

$$\delta E = n\delta r\gamma_{gb} - 2\pi\delta r\gamma_s \tag{20}$$

Pore shrinkage requires the reduction of total energy $\Delta E < 0$, which leads to

$$n < 2\pi\gamma_s/\gamma_{gb} \tag{21}$$

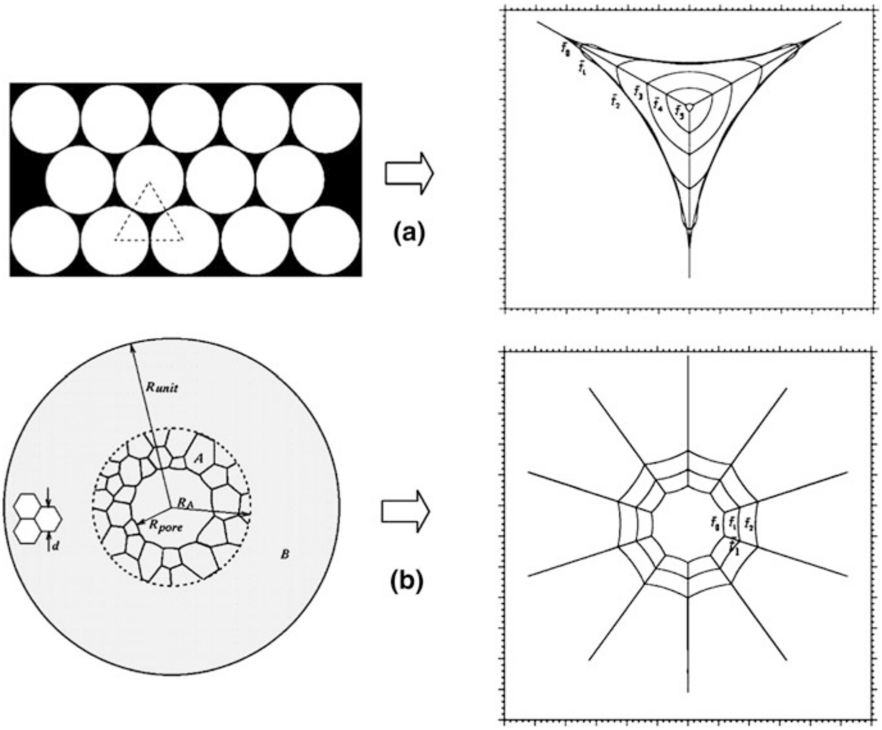

Fig. 11 Computer simulated evolutions of pores surrounded by symmetrical grains with two different coordination numbers. $\bar{t}_i$(i = 0, 1, …) indicates time sequence. **a** Pore with a coordination number of three shrinks and **b** pore with a coordination number of ten grows

A parallel argument is that only if the surface of the grains surrounding the large pore is "concave" does the pore shrink. It is therefore predicted that there exists a critical coordination number, which depends on the dihedral angle of the material. A pore will shrink only if its coordination number is less than the critical value Eq. (21). For a powder compact, the critical coordinate number is predicted according to the dihedral angle, which is a material constant. It follows that a large pore can only be eliminated after sufficient grain-growth, which reduces the coordination number to be under the critical value. There are two simplifications in the critical coordination number theory: (i) the large pore is surrounded by identical grains, and (ii) the grains move simultaneously during size changing of a large pore. It turns out that these simplifications are one step too far in understanding the behavior of any real powder compact.

In the past decades, increasing experimental evidence contradicts the critical coordination theory [30–32]. Pan and coworkers used their numerical methods described previously and studied what occurs if these simplifications are dropped [33, 34]. As shown in Fig. 11, two different initial configurations of pores with different coordination numbers are constructed. Grain boundary diffusion, surface

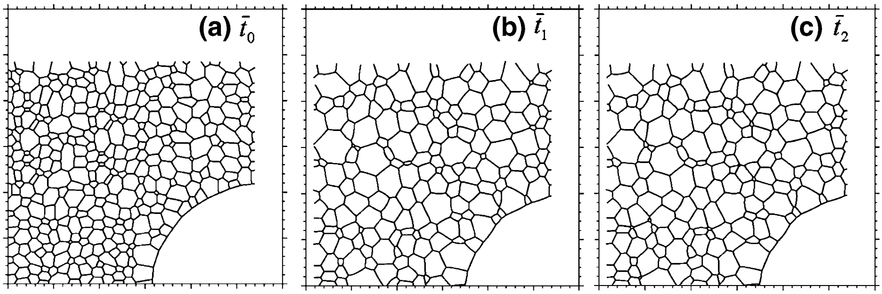

Fig. 12 Computer simulated evolutions of pore surrounded by a random arrayed grains: **a** initial configuration at time $\bar{t}_0$, **b** configuration at time $\bar{t}_1$, and **c** configuration at time $\bar{t}_2$. Taken from Ref. [34]

diffusion, and grain boundary migration are considered by solving Eq. (18). It is clearly shown in Fig. 11 that if the grains surrounding the pore are symmetrically arranged, the critical coordination number works well: the pore with small coordination number shrinks while the pore with large coordination number grows.

For a real powder compact, it is unrealistic to model the pore-grain matrix as shown in Fig. 11, i.e., there is no such symmetrical condition. For a network of random grains with roughly equiaxed shape, the strong symmetrical assumption is relaxed in Fig. 12. With time sequence from Fig. 12a–c, it is clear that the large pore shrinks despite its very large coordination number. A continuum version of the large pore model is shown in Fig. 13. The sintering stress σ_s exists due to the tendency for the large pore to reduce its surface and hence associated free energy. Material containing a large pore can be modeled by a hollow sphere [34]. The initial grain-size in Fig. 13b is 250 nm and the pore size varies from 20 to 125 μm. Figure 13c compares the analytical solution with the experimental data [32].

These studies conclude that large pores always shrink because there is always a thermodynamic driving force to eliminate the pores regardless of its coordination number. This does not mean that one can expect to eliminate the large pores through extended sintering. The time required for eliminating these large pores can be unrealistically long during which other events, such as coarsening, can take over. It does mean, however, that promoting grain-growth during sintering is always counter-productive if one wants to achieve densification.

8 Concluding Remarks

Modelling sintering of nanopowders is a challenging task where many text book theories need to be re-examined. The studies presented in this chapter are certainly far from a complete understanding. In terms of the validity of existing sintering theory for nano-particles, a somewhat obvious conclusion emerged from these previous studies, that is, the behavior of nanoparticles during the sintering process

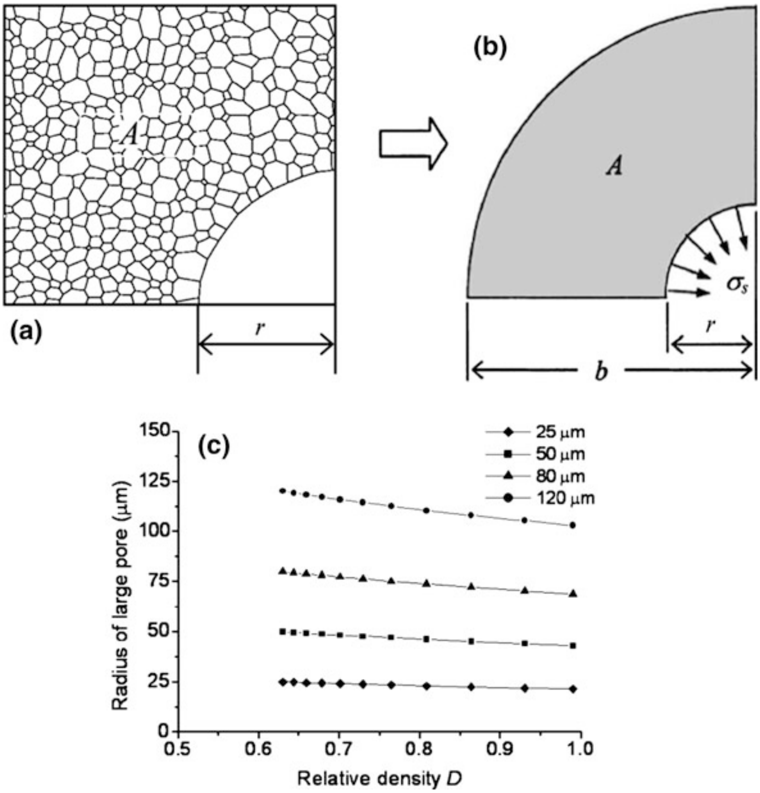

Fig. 13 An analytical model for the sintering of large pore: **a** discrete model, **b** continuum hollow sphere model, and **c** comparison with experiments showing the shrinkage of large pores for different pore sizes (with initial grain-size 250 nm), From Ref. [34]

is a lot more diverse than that the classical sintering theory could capture. For example, a classical sintering model, such as Coble’s sintering law, has to be based on an assumed sintering mechanism. It is widely believed that a dominating sintering mechanism exists which depends on the powder material, the particle size and the sintering temperature. For nano-particles however, different contact necks in a same powder compact could form different inter-particle boundaries and therefore sinter by different mechanisms. Specific surface energy is an important parameter because it is the total surface energy that drives sintering. For nano-powder however the specific surface energy of the powder material should include a term considering the atomic structure (roughness) of the particle surface, as it plays a major role. An encouraging result is that the classical framework of solid state physics appears being valid for nano-particles if one can capture the diversity, i.e. if one knows that a contact sinters by grain-boundary diffusion, then Coble’s theory applies. The issue is how to predict which contact (or how many of them) sinters by which mechanism.

References

1. Pan, J.: Philos. Mag. Lett. **84**, 303–310 (2004)
2. Herring, C.: The Physics of powder metallurgy. Kingston, W.E. (eds.) McGraw-Hill Book Company Inc., New York (1951)
3. Bouvard D., McMeeking, R.: J. Am. Ceram. Soc. 79, 666–672 (1996)
4. Suo, Z.: Adv. Appl. Mech. **33**, 193–294 (1997)
5. Pan, J., Cocks, A.C.F., Kucherenko, S.: Proc. R. Soc. Lond. A **453**, 2161–2184 (1997)
6. Cocks, A., Gill, S., Pan, J.: Adv. Appl. Mech. **36**, 81–162 (1999)
7. Coble, R.L.: J. Appl. Phys. **41**, 4798–4807 (1970)
8. Pan, J., Cocks, A.C.F.: Acta Mater. **42**, 1223–1230 (1994)
9. Pan, J., Cocks, A.C.F.: Acta Metall. Mater. **43**, 1395–1406 (1995)
10. Mcmeeking, R., Kuhn, L.: Acta Metall. Mater. **40**, 961–969 (1992)
11. Du, Z., Cocks, A.C.F.: Acta Metall. Mater. **40**, 1969–1979 (1992)
12. Cocks, A.C.F., Pan, J.: Mech. Mater. **18**, 269–287 (1994)
13. Cocks, A.C.F.: Mech. Mater. **13**, 165–174 (1992)
14. Bernard-Granger, G., Addad, A., Fantozzi, G., Bonnefont, G., Guizard, C., Vernat, D.: Acta Mater. **58**, 3390–3399 (2010)
15. Ding, L., Davidchack, R.L., Pan, J.: Comput. Mater. Sci. **45**, 247–256 (2009)
16. Rankin, J., Sheldon, B.W.: Mater. Sci. Eng. A **A204**, 48–53 (1995)
17. Pan, J., Le, H., Kucherenko, S., Yeomans, J.A.: Acta Metall. **46**, 4671–4690 (1998)
18. Parhami, F., McMeeking, R.M., Cocks, A.C.F., Suo, Z.: Mech. Mater. **31**, 43–61 (1999)
19. Saitou, M.: Philos. Mag. Lett. **79**, 257–263 (1999)
20. Ch'ng, H.N., Pan, J.: Acta Mater. **55**, 813–824 (2007)
21. Suryanarayana, C.: Inter. Mater. Rev. **40**, 41–64 (1995)
22. Mayo, M.J.: Inter. Mater. Rev. **41**, 85–115 (1996)
23. Johnson, K.L., Kendall, K., Roberts, A.D.: Surface energy and the contact of elastic solids. Proc. R. Soc. Lond. Ser. A Math. Phys. Sci. **324**, 301–313 (1971)
24. Derjaguin, B.V., Muller, V.M., Toporov, Y.P.: J. Colloid Interface Sci. **53**, 314–326 (1975)
25. Tabor, D.: J. Colloid Interface Sci. **58**, 2–13 (1977)
26. Maugis, D.J.: J. Colloid Interface Sci. **150**, 243–269 (1992)
27. Li, F., Pan, J., Sinka, C.: J. Mech. Phys. Solids **57**, 81194–81208 (2009)
28. Li, F., Pan, J., Sinka, C.: Mech. Mater. **43**, 157–167 (2011)
29. Slamovich, E.B., Lange, F.F.: J. Am. Ceram. Soc. **75**, 2498–2508 (1992)
30. Kingery, W.D., Francois, B.: The sintering of crystalline oxides. I. Interaction between grain boundaries and pores. In: Kuczynski, G.C., et al. (eds.) Sintering Related Phenomena, pp. 471–496. Gordon and Breach, New York (1967)
31. Kingery, W.D.: J. Appl. Phys. **30**, 301–306 (1959)
32. Flinn, B.D., Bordia, R.K., Zimmermann, A., Rodel, J.: J. Eur. Ceram. Soc. **20**, 2561–2568 (2000)
33. Pan, J., Ch'ng, H.N., Cocks, A.C.F.: Mech. Mater. **37**, 705–721 (2005)
34. Pan, J., Cocks, A.C.F., Rodel, J., Huang, R., and Ch'ng, H.N.: J. Am. Ceram. Soc. 92, 1414–1418 (2009)

Nano-Scaled Grain Growth

Feng Liu and Mingming Gong

Abstract One of the main goals in sintering is to obtain dense compacts with retained grain sizes. Therefore, a detailed understanding of the phenomenon of grain growth and the parameters affecting it is of prime importance for a successful processing. In this chapter, two kinds of models (thermodynamic and kinetic ones) are constructed to explain the role of segregation playing in controlling the thermal stability and the grain growth of nanocrystalline materials. Thermodynamically, analogous to the Gibbs adsorption theorem, a concept that solute atoms segregating in GBs could decrease the GB energy is proposed, i.e. once the GB energy reduces to almost zero with solute segregation, the system approaches metastable equilibrium state. Kinetically, the difference of solute concentrations between the GBs and the bulk produces a drag force on the GB migration. Incorporating a constant drag term into the parabolic equation, a model describing the nanocrystalline growth kinetics subjected to the GB segregation is presented. Considering that the thermodynamic method cannot describe the process of grain growth and that the kinetic one could do nothing for predicting the metastable stability, a coupling of thermodynamic and kinetic ways seems particularly important to provide an insight for understanding the thermal stability and grain growth of nanocrystalline materials. On this basis, from Borisov's empirical relationship, the rationality of coupling thermodynamic and kinetic ways has been demonstrated. Assuming a linear relationship between the GB energy and the average grain size, an analytical thermo-kinetic model with incorporating the reduced GB energy into the drag equation of grain growth is proposed.

F. Liu (✉) · M. Gong
State Key Laboratory of Solidification Processing, Northwestern Polytechnical University,
Xi'an, 710072, Shaanxi, People's Republic of China
e-mail: liufeng@nwpu.edu.cn

R. H. R. Castro and K. van Benthem (eds.), *Sintering*, Engineering Materials 35,
DOI: 10.1007/978-3-642-31009-6_3, © Springer-Verlag Berlin Heidelberg 2013

1 Introduction

Generally, sintering is accompanied by grain growth. Particularly in industrial applications, how to suppress the grain growth of nanocrystalline materials and to hold their excellent properties appear to be extremely important. As a promising method to improve the stability (or to inhibit the grain growth), solute addition has been adopted in various nanocrystalline materials. This is ascribed to the effect due to solute segregation at the grain boundaries (GBs) [1–7].

Considering a different solute concentration in the GBs and in the bulk, a drag force was proposed to retard the grain growth [1]. Originally, this drag term was assumed to be solely dependent on the final grain size. Nevertheless, this assumption is only correct when a steady-state solute distribution has been established [2]. Actually, a non-steady solute distribution prevails upon grain growth. Assuming that the drag force exerted by the solute segregation is proportional to the difference between the solute concentration in the bulk and the GBs, a grain size dependent drag force results [2]. This is compatible with Cahn [3], where the drag force acts as a function of both the grain size and the GB velocity. From this, we can deduce that the drag force can only retard but not stop the GB migration [4].

As the driving force for grain growth, the GB energy is regarded generally as constant. However, according to the Gibbs adsorption theorem (described in more details later in this chapter), the GB energy is expect to decrease with the segregation of solutes [5, 6]; see the classical experiment performed for Fe–P alloys [8]. Then, a thermodynamically metastable equilibrium state, where the GB energy reduces to almost zero, was proposed [7]. That is to say, the GB segregation reduces the driving force of grain growth; once the GB energy is negligible, the grain growth virtually stops.

Hence, the reduction of GB energy and the generation of drag force affect thermodynamically and kinetically the grain growth of nanocrystalline materials, respectively. Individually addressing each of these factors using the classical parabolic equation can indeed provide insights for the “nano-scale effects” on grain growth, but not lead to a physically sounded description. For example, the thermodynamic approach cannot describe by itself the evolution of the grain size; whereas, the kinetic approach cannot determine the grain size at the metastable equilibrium. Thus, a combined model for the nano-scale growth incorporating the above two factors into the parabolic equation is required.

In the following sections, grain growth formulas subjected to the thermodynamic factor, the kinetic factor and the coupling of these two factors will be described and applied to a related experimental data. One will see that the reduction of the GB energy, i.e. the thermodynamic factor, plays a predominated role in inhibiting the nano-scale grain growth, whereas, the solute drag, i.e. the kinetic factor, only retards this process.

2 Classical Equation for Grain Growth

As described in previous chapters, grain growth in nanocrystalline materials is primarily driven by the excess energy stored in the grain. Analogous to the growth of cells in soap froths, the kinetics of normal grain growth can be described using the following equation [1, 9],

$$v = M_{gb} \cdot \frac{\gamma_{gb}}{r} \tag{1}$$

where v (=dr/dt) is the velocity of GB migration, M_{gb} is the GB mobility, γ_{gb} the GB energy, and r the grain size. Then integration of Eq (1) gives,

$$r^2 - r_0^2 = kt \tag{2}$$

with r_0 as the initial grain size and t the annealing time. As described in Eq. (16) of the introductory chapter, the constant k contains the diffusion parameter, and hence can be re-written as $k = k_0 \exp(-Q/RT)$, representing the reaction rate constant with Q as the activation energy for GB migration, R as the molar gas constant, and k_0 a constant independent on the absolute temperature T. Frequently, Q is found to be close to the activation energy for GB diffusion or lattice diffusion [10–12].

Upon sintering ceramics, such as ZrO_2-3 mol % Y_2O_3 [13], SnO_2 [14] and Al_2O_3 [15], the mechanism of grain growth often deviates from Eq. (2), the classic parabolic equation. Aiming to describe precisely the grain growth phenomenon, a more widely used equation incorporating an empirical exponent n has been proposed as:

$$r^n - r_0^n = kt \tag{3}$$

Generally, the value of n is equal to or larger than 2. For grain growth in the nanocrystalline Fe-10Cr samples annealed at 500, 600 and 700 °C, n was determined as 1/0.083, 1/0.088 and 1/0.091, respectively [16]. Ganapathi and his coworkers [17] fitted Eq. (3) to the data from grain growth in nanocrystalline Cu and obtained n values as 2, 3 and 4. Malow and Koch [10] summarized the n values for some nanocrystalline materials and pointed out that the increased n and the decreased V at low temperatures can be ascribed to the restricted GB mobility most commonly due to the pore or the solute effect. Actually, the value of n can not physically reflect the mechanism of nano-scale grain growth taking place. For example, basing on the same experimental data, Malow and Koch [10] yielded $n = 1/0.32$ by fit of Eq. (3) to the experimental result, while $n = 2$ was obtained using the solute drag model [2].

Regarding that Eq. (2) is rarely observed except for high purity materials at high homologous temperature, the effect of solute (impurity) atoms, especially the GB segregation, on the grain growth of real materials must be discussed.

3 GB Segregation and Grain Growth

Due to high excess volume and small atom density, the GBs in the nanocrystalline materials enriched by the solute (impurity) atoms could reduce drastically the system free energy. Therefore, the energetically favorable GB segregation often happens in nanocrystalline solutions; that is, one component is preferentially located in a segregation layer at the GBs between crystals of other component [5]. This phenomenon has been observed in several systems, as pointed out in the literature [18, 19]. For instance, the GB segregation in nanocrystalline TiO_2 doped with Ca has been studied using a STEM microanalysis technique; the GBs became saturated with calcium when the coverage reaches approximately one half of an equivalent monolayer [20]. Another example, due to the segregation of copper, an enhanced apparent solubility (about 10 mol %) of copper in nanocrystalline CeO_2–Cu_2O was obtained [21].

GB segregation in the nanocrystalline materials can have a pronounced effect on both kinetics and thermodynamics of grain growth. The kinetic effect aims to retard the GB migration. Upon annealing a nanocrystalline $Pd_{81}Zr_{19}$ at 600 °C, the GB segregation increases continuously with grain growth; this gives rise to an increased effect of solute drag, thus decreasing the velocity of GB migration [22]. For the double zone-fined lead annealed at 210 °C, the addition of Sn substantially retards the grain growth [23]. The thermodynamic effect aims to increase the thermal stability, i.e. to reduce the grain size at the thermodynamically metastable equilibrium. Addition of Zr atoms in Pd-Zr alloy decreases sharply the final grain size; particularly with 19 and 20 at. % additions, the samples can hold nano-scale even at approximately 0.95 T/T_M (where T_M represents the melting point of pure solvent) [24]. Compared to pure nanocrystalline Fe, the segregation of Zr in the GBs sharply reduced the grain size of nanocrystalline Fe-1 at. % Zr [25]. In electrolytically and electroless plated Ni–P alloys, the grain size decreases with increasing P content and hold smaller than 5 nm once P content exceeds 10 at. % [7].

In the following two sections, the mechanism of nano-scale grain growth subjected to the GB segregation will be analyzed, kinetically and thermodynamically, respectively.

4 Kinetics of Grain Growth for Nanomaterials

4.1 GB Segregation and Solute Drag

Upon grain growth, the GB migration will be affected by interactions occurring between GBs and other imperfections in the crystal (e.g. vacancies, dislocations, solutes (impurities), etc.) [26]. In this section, the interactions between GBs and solutes are discussed. As the GB migrates, the solute atoms not only tend to segregate to the GBs, but also attempt to remain at the GBs, i.e. the GBs have to drag their solute load and only migrate as fast as the slower moving solutes do [26].

Dopants have been widely used to suppress the grain growth by providing a drag force on the moving boundaries during sintering of ceramics. For instances, 6 % Y leads to retardation on grain coarsening in TiO_2 [27]; Ca and Sn are inhibitors for grain growth in nano-TiO_2 [28]. With Fe as the solute, Ni–Fe alloys show drastically reduction of grain growth [29]. Besides, an addition of B atoms produces a drag force on the grain growth of nanocrystalline Fe–B [30]. Now, a question arises that, how does the drag force decrease the velocity of grain growth? From Eq. (1), it is proposed that, by reducing the GB mobility, the solute drag retards the velocity of grain growth. One example for the retardation of grain growth by reducing the GB mobility is given as follows [26]: In Al containing impurity, the <111> tilt GB presents a reduction of GB mobility. Furthermore, the reduction of GB mobility upon grain growth has been modeled [1–4], where the nature of retardation lies in the decrease of GB mobility ascribed to the drag of enriched solute.

4.2 Drag Forces Arising From GB Segregation

Various ways of distribution of solute atoms in the bulk and the GBs may occur during grain growth. This leads to several forms for the drag forces, and in turn, a number of kinetic models for the nano-scale grain growth. Suppose that the interaction between the enriched solute atoms and the moving GB can be described by a drag force represented by the function $f(\mathrm{r})$. Different analytical expressions have been used to derive $f(\mathrm{r})$ for distinct grain growth conditions (as detailed in Refs. [1–4]).

A drag force independent on the mean grain size was first considered by Burke [1], where a maximum grain size r_{max} is introduced to account for the effect of the second-phase, the impurities, and/or the sample thickness on the GB mobility. Once the growth velocity vanishes, the mean grain size reaches its maximum value. So, f can be expressed as [1],

$$f = \frac{M_{gb}\gamma_{gb}}{r_{\max}} \tag{4}$$

In the case of second-phase inclusions or pores affecting grain growth, if the volume fraction and the size distribution of inclusions (or pores) are fixed, the assumption that f is independent on the grain size is reasonable. Besides, in the case of GB pinning by the segregation of solute (impurity), once the concentration of solute segregating to the GBs holds a constant value, i.e. a steady-state solute distribution in the GBs, the drag force f can also be expected to be independent on the grain size.

However, when the solute excess varies with the GB migration, the drag force should be dependent on the grain size. Assuming that the drag force exerted by the segregated solute atoms is proportional to the difference of solute concentrations between the GBs and the bulk, and using a linear relationship between the difference of the solute concentrations and the average grain size, as described by Michels et al. [2], one can write the drag force as:

$$f = \frac{r M_{gb} \gamma_{gb}}{r_{\max}^2} \tag{5}$$

It should be noted that, in deriving Eq. (5), the dependence of the drag force on the GB migration is ignored. Indeed, from Cahn [3], the drag force acts as function of both the GB concentration and the GB velocity. For low GB velocities, the drag force is proportional not only to the solute excess depending on the grain size, but also to the GB velocity. On that basis, Rabkin pointed out that the drag force should be expressed as proportional to the product of the grain size and the GB velocity [4],

$$f = \beta M_{gb} r \frac{dr}{dt} \tag{6}$$

with β as a constant dependent on the interface energy and initial radius.

In general, the classical parabolic equation subjected to the drag component can be given as,

$$\frac{dr}{dt} = \frac{M_{gb} \gamma_{gb}}{r} - f(r) \tag{7}$$

Meaning that the grain size will be directly proportional to both interface energy and mobility, but slowed down by the drag force. Substituting the above expressions for the drag forces, i.e. Eqs. (4–6) into Eq. (7), we can derive three models for grain growth according to Burke, Michels, and Rabkin [1, 2, 4]:

$$\frac{\alpha}{r_{\max}^2} t = \frac{r_0 - r}{r_{\max}} + \ln\left(\frac{r_{\max} - r_0}{r_{\max} - r}\right) \tag{8}$$

$$r = \left[r_{\max}^2 - \left(r_{\max}^2 - r_0^2\right) \exp\left(-2\alpha t / r_{\max}^2\right) \right]^{1/2} \tag{9}$$

and

$$\alpha t = \frac{1}{2}\left(r^2 - r_0^2\right) + \frac{1}{3} \beta M_{gb} \left(r^3 - r_0^3\right) \tag{10}$$

with α as the product of M_{gb} and γ_{gb}.

A comparison for the three models subjected to the drag force is illustrated in Fig. 1, where the evolution of r/r_{max} with time was calculated using Eqs. (8) (solid line), (9) (dashed line) and (10) (dotted line), respectively.

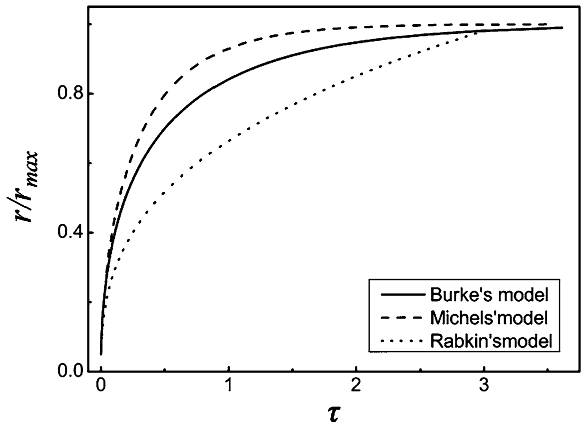

Fig. 1 Comparison of Burke' model (Eq. 8), Michels' model (Eq. 9), and Rabkin's model (Eq. 10). Assuming an initial grain size r_0 equaling to $0.05r_{max}$, the scaled grain size r/r_{max} is plotted as function of the scaled annealing time $\tau = (\alpha/r_{max}^2)t$

The solid and the dashed lines due to Burke and Michels predict a stable grain size, whereas, the dotted line due to Rabkin indicates a continuous process of growth. This can be ascribed to the fact that, in the kinetic description from Burke and Michels, the contribution from the driving force can be alleviated by that from the drag force, but in the kinetic description of Rabkin, the above balance does not exist, because the drag force depends on both the grain size and the GB velocity. Also from Fig. 1, it can be seen that the grain growth following Burke's model is always slower than that following Michels' model, which is mainly ascribed to the fact that the drag force in Burke's model is larger than that in Michels' model. This phenomenon is actually consistent with the essence of kinetic mechanism, i.e. the drag force reflects only the interaction of the moving GBs and the segregated solute atoms. That is to say, the kinetic effect cannot inhibit but retard the GB migration.

It is important to note, though, that all these models assume constant grain boundary energy. However, if there is a significant change in the composition of the boundary (enough to disturb the drag force), it is likely that the grain boundary energy will also be affected, and a manner to predict the effect of segregation in the driving force of grain growth has to be addressed.

5 Thermodynamics of Grain Growth for Nanomaterials

5.1 GB Segregation and Reduced GB Energy

Analogous to the Gibbs adsorption theorem, a concept that solute atoms segregating at the GBs could decrease the GB energy was proposed in 1993 [5]. This is consistent with Hondros et al. [8], where the reduction of GB energy of Fe due to P segregation was observed in the famous zero creep experiment. The evolution of the GB energy with solute segregation was calculated in Ref. [31], and is

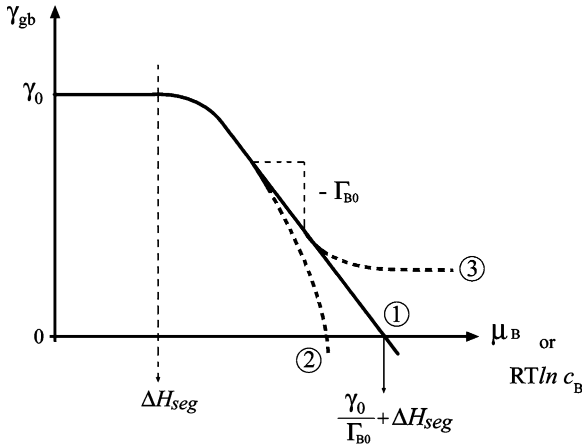

Fig. 2 Schematic illustration of the GB energy, γ_{gb} with increasing chemical potential, μ_B according to the Gibbs adsorption isotherm. At low chemical potentials, the solute can be negligible and the slope of the curve equals approximately to zero. When the chemical potential reaches the segregation enthalpy, ΔH_{seg}, the GB energy will decrease. If the GBs are saturated by solute atoms, the slope will be constant and the GB energy decreases linearly with the chemical potential, see *line 1*. However, if the solute excess does not reach its saturated value, *line 2* describes the expected tendency. In *line 3*, the evolution of the GB energy with the logarithm of solute content (instead of the chemical potential) corresponds to the case where a precipitation of a solute-rich phase happens. Reprinted from [31], p. 5133 with permission from Elsevier

illustrated in Fig. 2 as the GB energy as function of the chemical potential μ_B. Note that as soon as the enthalpy of segregation is trespassed, the increase in the chemical potential decreases the GB energy. For sufficiently low values of μ_B, the solute excess is so small that the GB energy will not change. For high values of μ_B, the GB gradually becomes saturated with solute atoms due to a limited number of segregation sites in one or two monolayers. In this case, the GB energy decreases linearly with increasing μ_B (see line 1 in Fig. 2). However, if the solute excess does not reach its saturated value, the reduction in the GB energy is even more pronounced, see line 2. Besides, line 3 describes the case where, if a new solute-rich phase forms, the solute excess and the GB energy will remain constant during phase-separation despite increasing the logarithm of solute content.

Accordingly, once the GB energy approaches zero with segregating solute, the system should approach the thermodynamically metastable equilibrium state (though it is naturally impossible, a zero grain boundary energy serves here as a reference). Then following an empirical relation between the terminal solubility of solute and its GB segregation, the metastable equilibrium with a certain GB area can be described [6]. In combination with McLean's equilibrium segregation model, an analytical relation was further derived to predict that the metastable equilibrium can be reached with saturated GBs; the metastable equilibrium grain size is determined by the GB energy of solvent, the enthalpy change of GB segregation and the solute excess amount of an equivalent GB monolayer at saturation [7]. Given the effect of solute segregation on the GB energy, it can be deduced that the solute addition will play an important role in improving the system's thermal stability. The stabilized role of solute segregation has been highlighted using experimental results from Ni-W [32], Ni-P [32], and Pd-Zr [33] et al.

5.2 Models of GB Energy Reduced by Solute Segregation

Gibbs first proposed that the atom segregation in phase boundary could decrease the phase boundary energy, i.e. the classical Gibbs adsorption theorem,

$$d\gamma_{gb} = -\Gamma_B d\mu_B \tag{11}$$

where Γ_B is the solute excess in the phase boundary, and μ_B the solute chemical potential. Although the idea of reduced boundary energy due to solute segregation was first proposed for the phase boundary, its extension to the GBs is also physically allowable.

5.2.1 Weissmuller's Work

Analogous to the Gibbs adsorption theorem, Weissmüller pointed out that the GB energy can be decreased by the solute segregation [5]. Assuming the matrix (bulk) as a dilute solid solution, the reduced GB energy can be expressed as,

$$\gamma_{gb} = \gamma_0 - \Gamma_B\left(\frac{\Delta H_{mix}^{bulk}}{N_B^{bulk}} - \frac{[\Delta H_{mix}]}{\Gamma_B}\right) - T\left([\Delta S_{mix}] + \Gamma_B R \ln X_B^{bulk}\right) \tag{12}$$

where γ_0 represents the GB energy of solvent, $\Delta H_{mix}^{bulk}$is the enthalpy change in the bulk upon alloying, N_B^{bulk} the amount of solute atoms in the bulk, $[\Delta H_{mix}]$ is the excess of enthalpy change in the GBs, $[\Delta \mathrm{S}_{mix}]$ the excess of entropy change in the GBs, and X_B^{bulk} the solute content in the bulk. The specific GB energy in the case of low temperature and upper limit of solute excess then takes a simple form [5],

$$\gamma_{gb} = \gamma_0 - \Gamma_{B0}\left(RT \ln X_B^{bulk} - \Delta H_{seg}\right) \tag{13}$$

with the enthalpy of segregation as,

$$\Delta H_{seg} = \frac{[\Delta H_{mix}]}{\Gamma_B} - \frac{\Delta H_{mix}^{bulk}}{N_B^{bulk}} \tag{14}$$

In the case of solute segregating at the GBs, the value of ΔH_{seg} holds negative. The total Gibbs free energy of the polycrystal is then presented as [5],

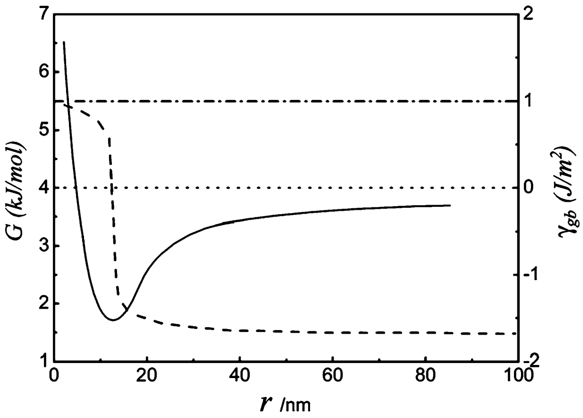

Fig. 3 Evolutions of the systemic Gibbs free energy and the GB energy with grain size for a global solute content of $X_B = 0.05$ at fixed P and T. The solid line means the systemic Gibbs free energy; the dash line stands for the GB energy; the dotted line represents the Gibbs free energy of the solid solution single crystal with the same X_B and zero GB energy; the dash dotted line describes the specific GB energy in the pure solvent polycrystal

$$\begin{aligned} G =& N_A\mu_A^0 + N_B\mu_B^0 + \gamma_0 S + \Delta H_{mix}^{bulk} + \Delta H_{mix}^{GB} \\ &+ RT\left(N_A^{bulk}\ln X_A^{bulk} + N_B^{bulk}\ln X_B^{bulk} + N_A^{GB}A^{GB} + N_B^{GB}\ln X_B^{GB}\right) \end{aligned} \tag{15}$$

where N_A and N_B represent the amounts of solvent and solute atoms, μ_A^0 and μ_B^0 the chemical potentials of pure solvent and pure solute, S the GB area, ΔH_{mix}^{GB} the enthalpy change in the GBs, respectively. The superscripts "*bulk*" and "*GB*" represent the intracrystalline and the GBs, meanwhile the subscripts "*A*" and "*B*" stand for the solvent and solute, respectively.

In combination with the Langmuir-Mclean adsorption isotherm [34], the system free energy of a polycrystal only depends on the grain size at fixed temperature, pressure and global solute content. Figure 3 shows the evolution of G with r and the relationship between GB energy and r, respectively. Note that a thermodynamically metastable equilibrium state is reached at the size corresponding to the minimum of G at fixed solute content, temperature and pressure (Fig. 3). With the increment of grain size, the GB energy decreases, and once the grain size approaches its critical value where the system Gibbs free energy holds the minimum, the GB energy is close to zero. This strongly declares that the metastable equilibrium state can be achieved only in the case of zero GB energy. After that, a negative grain boundary is predicted, what is obviously an impossible situation.

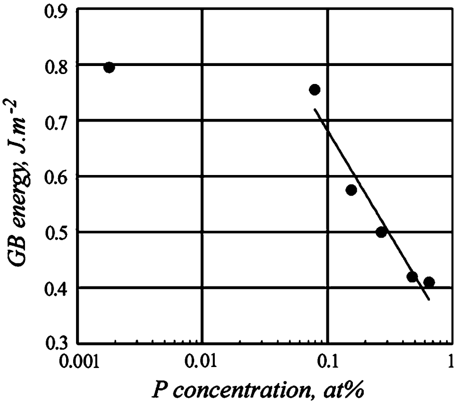

Fig. 4 Grain boundary energies in Fe–P alloys at 1723 K as measured in a zero creep experiment [8] and plotted versus total phosphorous content. The straight line is calculated from Eq. (16) with $\Gamma_B = 1.1 \times 10^{-5}$ mol/m^2. At low P contents, the GB energy nearly holds constant and the solute excess approaches to zero. Reprinted from [6], p. 416 with permission from Elsevier

5.2.2 Kirchheim's Work

From the contribution of segregated atom to entropy and enthalpy, Kirchheim [6] proposed an analytical expression for the reduced GB energy analogous to Eq. (13), and further, deduced,

$$\frac{d\gamma_{gb}}{d\ln X_B^{bulk}} = -\Gamma_B RT \tag{16}$$

In the zero creep experiment of Fe–P alloys, a linear decrease of the GB energy at high P-contents with the logarithm of P-concentration has been observed by Hondros [8], see Fig. 4. Note that the picture is similar to Fig. 2, and the linear behavior is observed after a critical concentration of P is achieved. With $X_B^{bulk} \approx X_B$ ascribed to the large grain size (μm range), a fit of Eq. (16) to the experimental data of Fe–P was performed and the parameter Γ_B was fitted as 1.1×10^{-5} mol/m^2, which is analogous to the value 1.5×10^{-5} mol/m^2 determined directly for the chemically similar Ni–P system using the three-dimensional atom probe [6].

5.2.3 Liu and Kirchheim's Work

Combining McLean's equilibrium segregation equation described in a previous section and the Gibbs adsorption theorem, an expression of GB energy analogous to Eq. (13) has also been derived by Liu and Kirchheim. With an assumption of a spherical grain, Eq. (13) can be rewritten as [7],

$$\gamma_{gb} = \gamma_0 - \Gamma_{B0}\left[RT\ln\left(X_B - \frac{3\Gamma_B V_M}{r}\right) - \Delta H_{seg}\right] \tag{17}$$

with V_M as the molar volume of alloys. As the GB energy reduces to zero, the grain growth stops. Then, the metastable equilibrium size is obtained as [7],

$$r_{\max} = \frac{3\Gamma_B V_M}{X_B - \exp\left(\frac{\gamma_0 + \Gamma_{B0}\Delta H_{seg}}{\Gamma_{B0} RT}\right)} \tag{18}$$

If the solute excess approaches its saturated vale as grain growth stops, Eq. (18) can be further given as [7],

$$r_{\max} = \frac{3\Gamma_{B0} V_M}{X_B - \exp\left(\frac{\gamma_0 + \Gamma_{B0}\Delta H_{seg}}{\Gamma_{B0} RT}\right)} \tag{19}$$

Considering the temperature dependence of the metastable grain size, the following expression can be obtained [7],

$$\frac{d\left(1/r_{\max}\right)}{d\ln T} = \frac{X_B^{bulk}\ln X_B^{bulk}}{3\Gamma_{B0} V_M} \tag{20}$$

For the grain growth of Ni–P nanocrystalline alloy, application of Eq. (18) leads to a small error of fitting [7]. Furthermore, Eq. (19) was applied to successfully describe the experimental data from nanocrystalline Pd-Zr alloy [7]. Besides, good linear relationships between the reciprocal of grain size and the logarithm of solute concentration in $Pd_{80}Zr_{20}$ and $Pd_{90}Zr_{10}$ nanocrystalline solid solution demonstrated the dependence of grain size on temperature from the theoretical prediction of Eq. (20) [7]. Upon fitting Eq. (18) to nanocrystalline Ni–P alloy, the fitted Γ_{B0} is found to be almost equal to Γ_B, implying that the GBs have been saturated with P-atom in the heat-treated Ni–P layer [7].

5.2.4 Krill's Work

Different from Weissmüller [5], Kirchheim [6] and Liu [7], Krill ignored the entropic contribution from solute segregation and proposed a relationship between the GB energy and the solute excess at the GBs [22]. Ascribed to the enrichment of solute atoms in the GBs, the reduction of GB energy is in proportion to the product of the segregation enthalpy and the difference of solute concentration between the GBs and the bulk, i.e. [22].

$$\gamma_{gb} = \gamma_0 + \Delta H_{seg}\frac{N^{GB}\left(X_B^{GB} - X_B^{bulk}\right)}{S} = \gamma_0 + \Delta H_{seg}\Gamma_B \tag{21}$$

With $Pd_{1\text{-}x}Zr_x$ nanocrystalline as examples, Krill (2005) calculated the reduction of GB energy with the increment of temperature. In terms of Eq. (21), the GB energy of $Pd_{1\text{-}x}Zr_x$ subjected to solute segregation can be estimated as [22],

$$\gamma_{gb} = \gamma_0 + \frac{4}{3}\Delta H_{seg}\frac{\Delta X_{Zr}^{bulk}}{N_A a^3}\langle L\rangle_{vol} \tag{22}$$

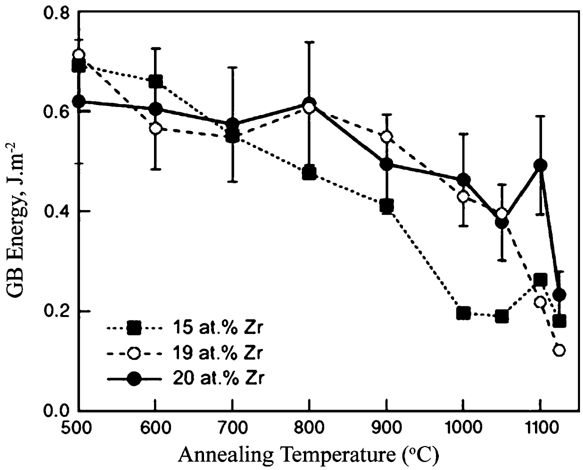

Fig. 5 Evolution of the GB energy calculated by Eq. (22) with temperature in nanocrystalline $Pd_{85}Zr_{15}$, $Pd_{81}Zr_{19}$ and $Pd_{80}Zr_{20}$. Reprinted from [22], p. 1139 with permission from c Carl Hanser Verlag, Muenchen

where ΔX_{Zr}^{bulk} represents the change of Zr concentration in the bulk, N_A the Avogadro constant, a the lattice constant, and $\langle L \rangle_{vol}$ the volume-weighted average grain intercept length. Applying the values of the related parameters, calculation of Eq. (22) shows that, the GB energy decreases continuously as the annealing temperature increases; see Fig. 5. Note that the data is not perfectly linear as predicted by Eq. (22) since the concentration of segregated amounts is experimentally determined, leading to the error bars and deviations from linearity.

As mentioned above, the effect of solute segregation on grain growth can be reflected from two aspects: the reduced GB mobility due to solute drag and the reduced GB energy. The kinetic model subjected to solute drag can describe the evolution of grain size but not determine the metastable grain size. Meanwhile, the thermodynamic model considering the reduced GB energy can predict the stop of grain growth but not describe the process of grain growth. Given that the real grain growth is probably accompanied with by these two factors (solute drag and reduced GB energy), it is necessary to consider the mixed effect of kinetics and thermodynamics.

6 Thermo-Kinetic Analysis for Grain Growth

6.1 Reduced GB Energy and GB Mobility upon Grain Growth

With Ref. to Eq. (2), the grain growth corresponds to defined values for GB mobility and GB energy, both of which, however, decrease as a result of the solute segregation at the GBs. Accordingly, it is necessary to incorporate the reduced GB energy and the reduced GB mobility into the grain growth equation, to more accurately describe the process.

In nanocrystalline materials, the reduced GB mobility due to solute drag may be reflected by the reduced diffusion coefficient in the GBs, i.e. an increment of activation energy for GB diffusion [35]. That is to say, the decreased GB energy contrasts with the increased activation energy for GB diffusion, and approximately, a single grain growth process can be separated as several domains, where Q and γ_{gb} hold constant within each domain [36]. Following the classical equation of grain growth, the grain growth subjected to increased activation energy and decreased GB energy can be described as [36],

$$r^2 - r_0^2 = \left\{ \begin{array}{ll} k_1 t & t_1 \geq t \geq 0 \\ k_1 t + k_2(t - t_1) & t_2 \geq t > t_1 \\ \ldots & \ldots \\ k_1 t + k_2(t - t_1) + \ldots + k_{n-1}(t - t_{n-2}) & t_{n-1} \geq t > t_{n-2} \\ k_1 t + k_2(t - t_1) + \ldots + k_{n-1}(t - t_{n-2}) + k_n(t - t_{n-1}) & t_n \geq t > t_{n-1} \end{array} \right\} \quad (23)$$

where, the subscript n represents the number of domains and the terms k_1, k_2 untill k_n holds constant. Since $k \sim \exp(-Q/RT)\gamma_{gb}$ holds, the rate constant k is smaller in the later domain, i.e. $k_1 > k_2 > \ldots > k_n$. The applicability of Eq. (23) has been shown by fitting Eq. (23) to the related experiments [2, 37]. Applying the continuously increased activation energy for GB diffusion and the continuously decreased GB energy, the process of grain growth in nanocrystalline materials can be described qualitatively.

6.2 Thermo-Kinetic Treatment

From the previous sections, it is known that the reduced GB mobility or the increased activation energy for GB diffusion results originally from the kinetic effect, i.e. solute drag; whereas, the reduced GB energy is due to the thermodynamic effect. Actually the grain growth subjected to solute segregation can be defined as a GB migration process which is accompanied with by reduced GB energy and solute drag. As mentioned above, we cannot obtain the stabilized grain size only by a kinetic model considering solute drag, whereas the evolution of grain size cannot be described using a thermodynamic approach relating to reduced GB energy. Until now, for nanocrystalline materials, the thermodynamics and kinetics of grain growth have been studied only independently. Thus a question needs to be solved: is it physically practicable to incorporate the thermodynamic factor, i.e. reduced GB energy into a kinetic process subjected to solute drag? That is to say, how to derive a model for grain growth that considers the mixed effect of kinetics and thermodynamics?

Grain growth relies upon GB diffusion while diffusion is concerned with the GB structure. On this basis, an expression for GB energy was derived by Borisov et al. [38] as,

$$\gamma_{gb} = \left(\frac{kT}{\alpha a_0^2}\right) m_a \left[\ln\left(\frac{\delta \frac{D_{gb}}{D_l}}{a_0 \lambda^{\alpha}}\right) - \ln m_a\right] \tag{24}$$

where $\alpha = 1$ for the interstitial mechanism and $\alpha = 2$ for the vacancy mechanism, a_0 represents the average inter-atomic distance, m_a the number of atomic layer forming the GB, δ the GB width, D_{gb}, D_l the diffusion coefficients due to GB and due to lattice (bulk), and $\lambda \approx 1$. The diffusion coefficients in the GBs and the lattice are presented as [39, 40],

$$\begin{aligned} D_i &= K \exp\left(\frac{\Delta S^i}{R}\right) \exp\left(\frac{-\Delta H^i}{RT}\right) \\ &= \frac{1}{2}\, x f a_0^2 v \exp\left(\frac{\Delta S_v^i + \Delta S_m^i + \Delta S_b^i}{R}\right) \exp\left(\frac{-\left(\Delta H_v^i + \Delta H_m^i + \Delta H_b^i\right)}{RT}\right) \end{aligned} \tag{25}$$

Here, the vacancy mechanism and mono-atomic layer GB segregation are assumed. Besides, x is the geometrical factor, f the correlation factor, v the jump frequency; superscript i equals to gb or l, meanwhile subscripts v, m, and b respectively represent the vacancy formation, migration, and the binding between vacancy and diffusion atom. By incorporating the expressions of D_b and D_l into Eq. (24), a formula of the reduced GB energy analogous to Eq. (13) is obtained; see the detailed derivation in Ref. [41].

Accordingly, a thermodynamic (decreasing) tendency of GB energy must be incorporated into a kinetic change of GB diffusion, i.e. a kinetic process for grain growth. With grain growth, the solute distribution must change due to GB area decreasing. Upon GB segregation, the activation energy for GB diffusion increases meanwhile the GB diffusion coefficient decreases as their Arrhenius relation. Furthermore, from Eq. (24), it can be inferred that, once D_b equals to D_l, the GB energy reduces to zero and grain growth is stopped. Considering the above quantitative derivation, it still provides some evidence about the relevance between reduced GB energy and kinetic process. Therefore, we may conclude that the incorporation of decreasing GB energy into kinetic process subjected to solute drag is physically practicable.

Aiming to predict a stabilized grain size and to describe the process of nano-scale grain growth, a combination of effects due to kinetics and thermodynamics is derived as follows. From Ref. [41], for strongly segregating systems, the expression of solute excess can be presented as,

$$\Gamma_B \approx X_B \rho \left(\frac{r}{6} + \delta\right) \tag{26}$$

Here, for a specific grain growth process, the values of X_B, ρ and δ (the GB thickness assumed to be 0.8 nm [42]) are all available. Thus, Eq. (26) describes a linear relation between the solute excess and the average grain size, which corresponds to the experimental evidence in nanocrystalline Pd-Zr alloys [22].

With grain growth progressing, the solute excess increases and approaches to its saturated value.

Combing Eq. (26) and the GB energy model from Krill, i.e. Eq. (21), leads to [41],

$$\gamma_{gb} = \gamma_0 + \frac{\Delta H_{seg} X_B \rho (r + 6\delta)}{6} \tag{27}$$

From Eq. (27), the GB energy reduces linearly with decreasing the global solute concentration, which is consistent with the conclusion from phase field approach [43]. Furthermore, if $\gamma_{gb} = 0$, grain growth is stopped and the metastable grain size can be reached.

As discussed before, grain growth due to solute segregation should be a process subjected to the reduced GB energy and the drag force. Therefore, substituting Eq. (6) and Eq. (27) into Eq. (7) leads to [41],

$$\int_{r_0}^{r} \frac{r\left(1/M_{gb} + \beta r\right)}{\gamma_1 - \gamma_2 r} dr = \int_{0}^{t} dt \tag{28}$$

with $\gamma_1 = \gamma_0 + \Delta H_{seg} X_B \delta \rho$ and $\gamma_2 = -\Delta H_{seg} X_B \rho/6$. On the basis of the boundary conditions $t = 0$, $r = r_0$ and $t = t$, $r = r(\mathrm{t})$, integrating Eq. (28) then leads to the evolution of grain size with time [41],

$$\begin{aligned} &\frac{\beta}{2\gamma_2^3}\left[(\gamma_1 - \gamma_2 r)^2 - (\gamma_1 - \gamma_2 r_0)^2\right] + \left(\frac{1}{M_{gb}\gamma_2} + \frac{2\beta\gamma_1}{\gamma_2^2}\right)(r - r_0) \\ &\qquad + \left(\frac{\gamma_1}{M_{gb}\gamma_2^2} + \frac{\beta\gamma_1^2}{\gamma_2^3}\right)\ln\left(\frac{\gamma_1 - \gamma_2 r}{\gamma_1 - \gamma_2 r_0}\right) = -t \end{aligned} \tag{29}$$

Compared to the kinetic model from Rabkin [4] and the thermodynamic models [5–7, 22], the present model couples the effects due to the reduced GB energy and the drag force. Subjected to specific limitations, Eq. (29) will reduce to some models as follows:

I By neglecting the thermodynamic effect due to grain-size-dependent GB energy (i.e. γ_{gb} holds constant during grain growth), Eq. (29) will reduce to Rabkin's model [4], i.e. Eq. (10);

II Without considering both the thermodynamic effect due to grain-size-dependent GB energy and the kinetic effect due to Rabkin's treatment for solute drag (i.e. solute drag is only dependent on grain size), Eq. (29) will reduce to Michels'model [2];

III By only considering the thermodynamic effect due to grain-size-dependent GB energy, Eq. (29) is consistent with the incorporation of grain-size-dependent GB energy into parabolic equation.

A pulse reverse technique was used to deposit nanocrystalline nickel doped with nickel oxide [44]. A study of the thermal stability of nanocrystalline nickel at

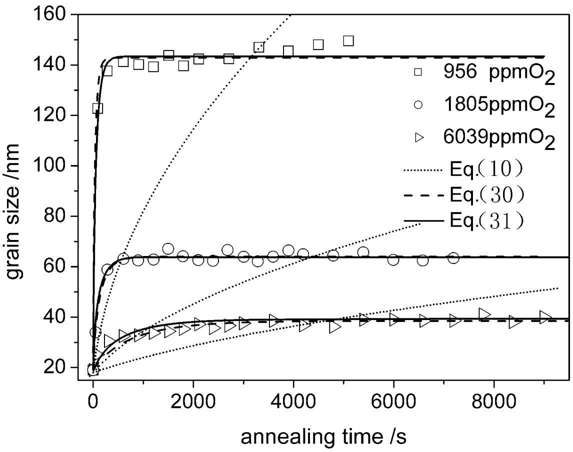

Fig. 6 Evolutions of average grain size of the oxygen-doped nickel samples with different oxygen contents at 673 K [44] with annealing time. Meanwhile, the dotted, dashed and solid lines are calculated using Eqs. (10, 30, 31), respectively (Reprinted from Ref. [41], p. 1471 with permission from Elsevier). Note that the dashed and solid lines for Eqs. (30, 31) almost overlap, and are hard to see in the figure

an annealing temperature of 673 K showed that a stabilized grain size after a rapid increase in grain size over a short period was reached (see Fig. 6).On this basis of the experimental data from nanocrystalline nickel, the kinetic effect, the thermodynamic effect and the mixed effect of thermodynamics and kinetics (i.e. thermo-kinetic effect) are all studied in detail individually.

By only considering the kinetic effect, fits of Eq. (10) (corresponding to case I) to the grain sizes of the nanocrystalline nickel [44] have been done; see Fig. 6. The result indicates that the model subjected to solute drag dependent on growth velocity cannot be brought into agreement with the experimental data.

Setting β as zero, the effect of solute drag is ignored. Then, Eq. (29) reduces to a model solely considering the thermodynamic effect; see case III [41],

$$\left(\frac{\gamma_1}{\gamma_2^2}\right)\ln\left(\frac{\gamma_1-\gamma_2 r}{\gamma_1-\gamma_2 r_0}\right)+\frac{(r-r_0)}{\gamma_2}=-M_{gb}t \tag{30}$$

From Ref. [45], the GB energy of nickel, γ_0, is given as 0.87 J m^{-2}. With ΔH_{seg} and M_{gb} as fitting parameters, fits of Eq. (30) to the grain sizes of nanocrystalline nickel [44] have been performed. Obviously, the Eq. (30) can describe the experimental data well; see Fig. 6.

In order to derive an analytical model with considering both effects due to thermodynamics and kinetics, a case of $\beta = \gamma_2/M_{gb}$ is assumed [41]. Then Eq. (29) can changed as,

$$\begin{aligned}\frac{1}{2\gamma_2^2}\left[(\gamma_1-\gamma_2 r)^2-(\gamma_1-\gamma_2 r_0)^2\right]+\left(\frac{1}{\gamma_2}+\frac{2\gamma_1}{\gamma_2}\right)(r-r_0)\\+\left(\frac{\gamma_1}{\gamma_2^2}+\frac{\gamma_1^2}{\gamma_2^2}\right)\ln\left(\frac{\gamma_1-\gamma_2 r}{\gamma_1-\gamma_2 r_0}\right)=-M_{gb}t\end{aligned} \tag{31}$$

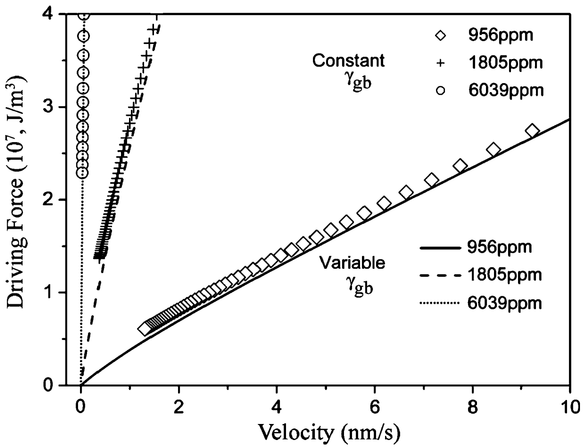

Fig. 7 Evolution of driving force, *P*(V), with growth velocity *V*. With constant gb the discrete symbols are calculated using Eq. (10); meanwhile with variable γgb the continuous lines are calculated using Eq. (31). Reprinted from Ref. [41], p.1473 with permission from Elsevier

Fits of Eq. (31) (corresponding to case III) to the experimental data of nanocrystalline nickel [44] have been also performed. From Fig. 6, one can know that Eq. (31) also describes the experimental data well.

According to Ref. [34], ΔH_{seg} is defined as the energy difference between a molar of solute atoms in the grain interior and that at the GBs. For the samples containing 956, 1805 and 6039 ppm oxygen, ΔH_{seg} is fitted as −66, −76 and −37 kJ mol^{-1}. Using the relation $\Delta H_{seg} \approx RT\ln X_B-(10 \pm 6)$ with $X_B = 0.87$ at. % O in Ni at 1440 °C [46], the value of ΔH_{seg} is estimated as $\sim(-68$ kJ mol$^{-1})$, which is compatible with the values (−66 and −76 kJ mol^{-1}) but far away from the value −37 kJ mol^{-1}. Actually, from Ref. [46], the content of 6039 ppm is well above the solubility limit of oxygen in Ni at 673 K, i.e. 0.87 at. %. According to the classical Fowler–Guggenheim segregation isotherm [45], [47], the driving force for segregation, i.e. the absolute value of ΔH*seg*, will decrease when the solute content beyond the dilute limit.

6.3 Thermodynamic and Kinetic Nano-scale Analysis

From the above model description, it can thus be concluded that two cases, i.e. the reduced GB energy alone (Eq. (30) and the reduced GB energy mixed with the solute drag (Eq. 31), are physically practicable to describe the nano-scale grain growth.

Corresponding to the GB mobility, M_{gb} in Eq. (1), the term γ_{gb}/r can be defined as the driving force, *P*. Subjected to the solute drag effect (i.e. Eqs. 4–6), the driving force, *P*, as function of the GB velocity *V*, can be calculated by the equation $P = \gamma_{gb}/r + \beta \mathrm{d}r/\mathrm{d}t$. In combination with Eqs. (10, 31) and the fitted values of ΔH_{seg} and M_{gb} (see Table 3 in Ref. [41]), the evolution of *P* with *V* can be obtained; see Fig. 7. With the increment of the oxygen content from 956 to

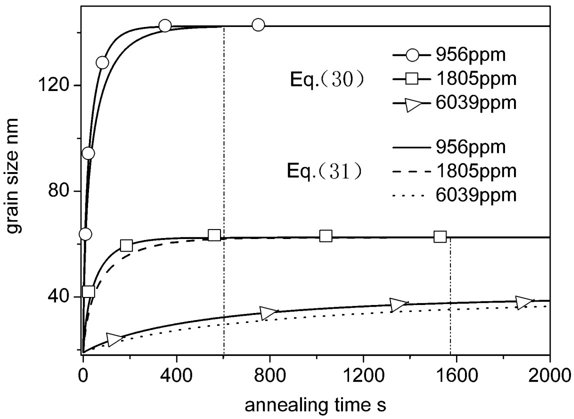

Fig. 8 Evolution of average grain size with annealing time by numerically calculating Eq. (30) (the pure thermodynamic model) and Eq. (31) (the mixed model considering thermodynamics and kinetics). Obviously, the solute drag reduces the growth velocity at the beginning of grain growth but gradually vanishes with time increasing (Reprinted from Ref. [41], p. 1473 with permission from Elsevier)

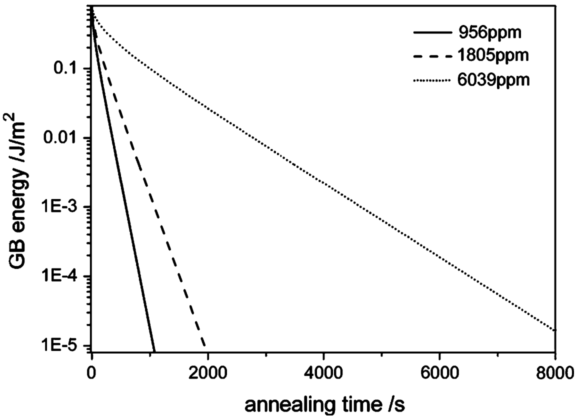

Fig. 9 Evolution of GB energy with annealing time by calculating Eq. (33). The GB energy only infinitely approaches to zero with time increasing (Reprinted from Ref. [41], p. 1474 with permission from Elsevier)

6039 ppm, P(V) is increased; meanwhile at a given solute content, P(V) decreases with V decreasing. Different from the case corresponding to Eq. (10) (i.e. the discrete symbols representing pure kinetic effect), the case corresponding to Eq. (31) (i.e. the continuous lines representing the mixed effect) could predict a zero driving force corresponding to zero velocity. This shows that for a constant γ_{gb}, neither $P(V)$ nor V could tend to zero.

From Fig. 7, it can be inferred that solute drag alone is not able to inhibit the grain growth. Employing the values of parameters (see Table 2 and Table 3 in Ref. [41]), numerical calculations using Eqs. (30) and (31) can be performed to give the evolution of grain size with time; see Fig. 8. At the initial stage of grain growth, the effect of solute drag decreases the growth rate; however, with time increasing, the two cases coincide exactly (Fig. 8). For these two cases, a stabilized grain size can be obtained, indicating that the effect of GB energy plays a dominant role on nano-scale grain growth, and moreover, the solute drag effect vanishes with growth proceeding.

By differentiation of Eq. (27) over t, an analysis for the effect of GB energy on the grain growth is obtained as [41],

$$\frac{d\gamma_{gb}}{dt} = -\gamma_2 \frac{dr}{dt} \tag{32}$$

In combination with Eq. (31), integrating Eq. (32) leads to an evolution of GB energy with annealing time [41],

$$-\gamma_1(\gamma_2 + 1)\ln\frac{\gamma_{gb}}{\gamma_0} - (1 + 2\gamma_1)\left(\gamma_{gb} - \gamma_0\right) + \frac{1}{2}\left(\gamma_{gb}^2 - \gamma_0^2\right) = -\gamma_2^2 M_{gb} t \tag{33}$$

with the boundary conditions of $t = 0$, $\gamma = \gamma_0$ and $t = t$, $\gamma = \gamma_{gb}$. Using the related parameters (see Table 3 in Ref. [41]), the calculated result of Eq. (33) is presented in Fig. 9. One can see that, γ_{gb} decreases with grain growth and infinitely approaches zero. Here, thermodynamically, zero GB energy could be considered as an ideal limitation. The evolution of GB energy indicates that only the incorporation of GB energy effect could achieve the ideal zero driving force. Then, it can be concluded that the stabilized mechanism for the nanocrystalline is not the solute drag but the reduction of GB energy.

7 Summary

Segregation of dopants during grain growth shows an interesting and useful way to improve controlling over grain size. The effect of the dopants is typically twofold, as it can influence the kinetics of the boundary, as well as the thermodynamics. We have described the accepted models describing the effect of the dopants in both kinetics and thermodynamics, and then combined both analyses in a unified model. The model predicts well the growth behavior in micro-sized systems, and gives insights on the nano-scaled grain growth. The effect of GB energy plays a dominant role on nano-scale grain growth, and moreover, the solute drag effect vanishes as growth proceeds.

References

1. Burke, J.E.: Trans. Am. Inst. Min. Metall. Eng. **180**, 73–91 (1949)
2. Michels, A., Krill, C.E., Ehrhardt, H., Birringer, R., Wu, D.T.: Acta Mater. **47**(7), 2143–2152 (1999)
3. Cahn, J. W.: Acta Metall. **10**(9), 789–798 (1962)
4. Rabkin, E.: Scripta Mater. **42**(12), 1199–1206 (2000)
5. Weissmuller, J.: Nanostruct. Mater. **3**(1–6), 261–272 (1993)
6. Kirchheim, R.: Acta Mater. **50**(2), 413–419 (2002)
7. Liu, F., Kirchheim, R.: J. Cryst. Growth **264**(1–3), 385–391
8. Hondros, E.D.: Proc. R. Soc. London Ser. A **286**(1407), 479–498 (1965)

9. Beck, P.A., Kremer, J.C., Demer, L.J., Holzworth, M.L.: Trans. Am. Inst. Min. Metall. Eng. **175**, 372–400 (1948)
10. Malow, T.R., Koch, C.C.: Thermal stability of nanocrystalline materials. In: Schulz, R., (ed.) Metastable, Mechanically Alloyed and Nanocrystalline Materials, Pts 1 and 2, vol. 225, pp. 595–604. (1996)
11. Malow, T.R., Koch, C.C.: Acta Mater. **45**(5), 2177–2186 (1997)
12. Eckert, J., Holzer, J.C., Krill, C.E., Johnson, W.L.: J. Mater. Res. **7**(7), 1751–1761 (1992)
13. Mayo, M.J.: Inter. Mater. Rev. **41**(3), 85–115 (1996)
14. Lai, J.K.L., Shek, C.H., Lin, G.M.: Scripta Mater. **49**(5), 441–446 (2003)
15. Zhao, J.H., Harmer, M.P.: Philos. Mag. Lett. **63**(1), 7–14 (1991)
16. Gupta, R., Raman, R.K.S., Koch, C.C.: Mater. Sci. Eng. A **494**(1–2), 253–256 (2008)
17. Ganapathi, S.K., Owen, D.M., Chokshi, A.H.: Scripta Metall. Mater. **25**(12), 2699–2704 (1991)
18. Bouchet, R., Weibel, A., Knauth, P., Mountjoy, G., Chadwick, A.V.: Chem. Mater. **15**(26), 4996–5002 (2003)
19. Dong, Z.F., Lu, K., Hu, Z.Q.: Nanostruct. Mater. **11**(3), 351–360 (1999)
20. Terwilliger, C.D., Chiang, Y.M.: Acta Metall. Mater. **43**(1), 319–328 (1995)
21. Knauth, P., Tuller, H.L.: Solid State Ionics **136–137**, 1215–1224 (2000)
22. Krill, C.E., Ehrhardt, H., Birringer, R.: Z. Metallkd. **96**(10), 1134–1141 (2005)
23. Drolet, J.P., Galibois, A.: Metall. Trans. **2**(1), 53–64 (1971)
24. Okamoto, H.: Phase diagrams for binary alloys. Metal Park, ASM International (2000)
25. Darling, K.A., Chan, R.N., Wong, P.Z., Semones, J.E., Scattergood, R.O., Koch, C.C.: Scripta Mater. **59**(5), 530–533 (2008)
26. Gottstein, G., Shvindlerman, L.S.: Grain Boundary Migration in Metals: Thermodynamics, Kinetics, Applications. CRC Press, Boca Raton (1999)
27. Averback, R.S., Hofler, H.J., Hahn, H., Logas, J.C.: Nanostruct. Mater. **1**(2), 173–178 (1992)
28. Terwilliger, C.D., Chiang, Y.M.: Nanostruct. Mater. **4**(6), 651–661 (1994)
29. Ebrahimi, F., Li, H.Q.: Scripta Mater. **55**(3), 263–266 (2006)
30. Chen, Z., Liu, F., Zhang, K., Ma, Y.Z., Yang, G.C., Zhou, Y.H.: J. Cryst. Growth **313** (1), 81–93 (1994)
31. Kirchheim, R.: Acta Mater. **55**(15), 5129–5138 (2007)
32. Trelewicz, J.R., Schuh, C.A.: Phys. Rev. B **79**(9), 094112 (2009)
33. Singh, M., Shpargel, T.P., Asthana, R.: J. Mater. Sci. **43**(1), 23–32 (2008)
34. McLean, D.: Grain Boundaries in Metals. Oxford University Press, Oxford (1957)
35. Höfler, H.J., Tao, R., Kim, L., Averback, R.S., Altstetter, C.J.: Nanostruct. Mater. **6**(5–8), 901–904 (1995)
36. Liu, F., Yang, G.C., Wang, H.F., Chen, Z., Zhou, Y.H.: Thermochim. Acta **443**(2), 212–216 (2006)
37. Liu, K.W., Mucklich, F.: Acta Mater. **49**(3), 395–403 (2001)
38. Borisov, V.T., Golikov, V.M., Shcherbedinskii, G.V.: Fiz. Met. Metalloved. **17**(6), (1964)
39. Kaur, I., Mishin, Y., Gust, W.: Fundamentals of Grain and Interphase Boundary Diffusion. John Wiley, Chichester and New York (1995)
40. Christian, J.W.: Theory of transformations in metals and alloys. I. Equilibrium and general kinetic theory, 2nd edn. (1975)
41. Chen, Z., Liu, F., Wang, H.F., Yang, W., Yang, G.C., Zhou, Y.H.: Acta Mater. **57**(5), 1466–1475 (2009)
42. Färber, B., Cadel, E., Menand, A., Schmitz, G., Kirchheim, R.: Acta Mater. **48**(3), 789–796 (2000)
43. Cha, P.R., Kim, S.G., Yeon, D.H., Yoon, J.K.: Acta Mater. **50**(15), 3817–3829 (2002)
44. Natter, H., Löffler, M.S., Krill, C.E., Hempelmann, R.: Scripta Mater. **44**(8–9), 2321–2325 (2001)
45. Detor, A.J., Schuh, C.A.: Acta Mater. **55**(12), 4221–4232 (2007)
46. Merica, P.D., Waltenberg, R.G.: Trans. Am. Inst. Min. Metall. Eng. **71**, 709–716 (1925)
47. Seah, M.P.: J. Phys. F **10**(6), 1043–1064 (1980)

Effect of Powder Characteristics on Nanosintering

J. P. Kelly and O. A. Graeve

Abstract If all other things are equal, nanopowders will sinter faster and at lower temperatures than larger powders. However, the increased surface area to volume ratio of these materials presents additional processing challenges that correspond to greater difficulty in achieving the goal of sintering for finer powders. This is not related to the "nano" effects as described in previous chapters, but to powder characteristics that can strongly influence the sintering behavior. These characteristics can be seen as the "real life" parameters, such as agglomeration state and contaminations that if not addressed properly can confuse sintering tendencies and complicate sintering effects at the nanoscale. This chapter presents the effects that may contribute to nanosintering and the importance of adequate processing of nanopowders for achieving optimum sintering behavior.

1 Introduction

When sintering nanopowders into a dense specimen, the sintering behavior is certainly related to the inherent sinterability (i.e., physical properties) of the material(s), but also to the morphological characteristics of the powders and how the powders are arranged in the green compact (green forming is intimately related to the powder characteristics). There is an extensive amount of information on these topics that would be difficult to fully summarize in an entire book, let alone one chapter. Therefore, this chapter is meant to introduce the reader to the topic

---

J. P. Kelly · O. A. Graeve (✉)
Alfred University, Kazuo Inamori School of Engineering,
2 Pine St, Alfred, NY 14802, USA
e-mail: graeve@alfred.edu

R. H. R. Castro and K. van Benthem (eds.), *Sintering*, Engineering Materials 35,
DOI: 10.1007/978-3-642-31009-6_4,

and provide insight into the considerations that should be made prior to sintering of nanopowder compacts.

One could argue that the synthesis process for obtaining nanopowders is the most important decision one is to make in order to obtain fully dense nanostructured specimens effectively, since the characteristics of the powders are directly related to how the powders are prepared. The synthesis method will also dictate the post-synthesis processing that is necessary and the state that this post-synthesis processing has on the morphological characteristics of the powders. The powder characteristics, the forming technique used to prepare the green compact, and the conditions/additives necessary for forming will dictate the final state of the compact. This represents the entire preparation methodology of nanopowders before sintering. Without proper understanding of the synthesis of the nanopowders and how that affects the powder characteristics, each step thereafter may be poorly controlled for achieving properly dense nanostructured specimens.

This chapter addresses the processing of nanopowders and its consequences on the morphological characteristics of the powders. First, a variety of synthesis methodologies will be discussed. After, the effects of the characteristics of the synthesized nanopowders on sintering will be discussed, and finally, a brief review of forming techniques and considerations that must be made for generating suitable nanopowder green compacts will be provided.

2 Controlled Synthesis of Nanopowders

The synthesis of nanoparticles can be separated into three categories: *top-down*, *bottom-up*, and *intermediate approaches*. In the top-down approach, a large structure (larger than 100 nm) is broken into smaller components using physical or chemical methods. In the bottom-up approach, atomic or molecular species are assembled into nanostructures such as particles, wires, or rods. Intermediate approaches may involve a combination of top-down and bottom-up syntheses or the development of one nanostructure from another nanostructure. The entire breadth of nanopowder synthesis cannot be covered easily and therefore only an introduction will be provided here, with a focus on the important considerations that should be made during synthesis. To obtain further details on the various nanopowder synthesis methods, there are many resources available to the interested reader [1–10].

2.1 Top-Down Methods

Top-down syntheses involve the reduction in size of a material by providing sufficient energy for breakage or atomization. The most common technique is providing mechanical energy. However, it is also possible to use thermal energy, chemical energy, electromagnetic energy, sonic energy, electrical energy, or a

Table 1 Examples of top-down methods

Technique	Specific examples
Mechanical energy methods	Ball milling; rolling and beating; extrusion and drawing; mechanical machining/polishing/grinding; mechanical cutting; compaction and consolidation; atomization
Thermal fabrication methods	Annealing; chill-block melt spinning; electrohydrodynamic atomization; electrospinning; liquid dynamic compaction; gas atomization; evaporation; template extrusion; sublimation; polymer carbonization
High-energy and particle methods	Arc-discharge; laser ablation; solar energy vaporization; RF sputtering; ion milling; electron-beam evaporation; reactive ion etching (RIE); pyrolysis; combustion; high-energy sonication
Lithographic methods	LIGA techniques; photolitography; immersion lithography; deep ultraviolet lithography; extreme ultraviolet lithography; electron-beam lithography; electron beam projection lithography; focused ion beam lithography; microcontact printing methods; nanoimprint lithography; nanosphere lithography; scanning AFM nano-stencil; scanning probe nano-lithographies
Chemical methods	Chemical etching; chemical–mechanical polishing; electropolishing; anodizing

Fig. 1 Schematic representation of a conventional ball-mill

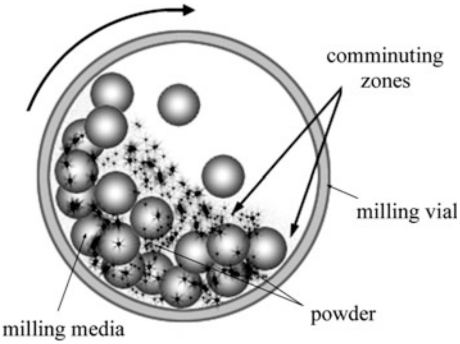

mixture of energy forms. A listing of specific top-down methods is provided in Table 1.

For the case of mechanical milling, nanoparticle formation is achieved by high-energy collisions and abrasion. Grinding media is typically included in the mill to help achieve comminuting. Impact and shear at the particle surfaces as the media/particles collide and slide past each other are achieved by agitating (stirring, vibration, spinning, etc.) and can result in particle fracture. Typically, high-energy mills, such as planetary mills, rapid mills, or attrition mills, are employed for obtaining nanopowders [11]. Important variables include the *type of material* being milled, the *type of media* that is used (material, shape, size, size distribution, and size relative to the material), the media and material *loading levels*, the *agitation amplitudes or speeds*, type of milling (*wet or dry*), characteristics of *fluid* (liquid or gas), *solids loading* if wet milling, and milling *time* [12, 13]. A schematic representation of a conventional ball mill is shown in Fig. 1.

The fracture characteristics of the material should be understood when milling a sample, as these may affect the morphology of the final powders. For most materials, the morphology after milling is typically irregular rather than the ideal spherical morphology that is favorable for sintering. For example, a ductile metal has a tendency to deform rather than fracture. Initially, metal particles will deform, flatten, and smear. Eventually, the cold working of the metal induces strain hardening and may result in embrittlement of the metal and allow for fracture to occur. Ceramics are naturally elastic and therefore brittle and prone to fracture without deformation. The ductile/brittle nature of the material will also dictate how much stored energy (residual stress) due to inelastic deformation might be present in the resulting powders after comminuting.

The hardness of the material with respect to the milling media is also important. The media should be harder than the material being milled and should be of similar material as the mill liner. As the material being milled approaches the hardness of the media and liner, wear of the media becomes more pronounced. Media and liner wear are inevitable and can lead to contamination of the resulting powders. High energies and long milling times are often required to generate nanopowders and, therefore, nanopowders are very susceptible to contamination. Media and liner having high toughness, in addition to hardness, is desirable for minimizing wear.

In addition to the mechanical characteristics of the media, the media size is also important. There are more contact points and media collisions for smaller media. For a given volume and mill conditions, the rate of grinding will increase inversely as the radius of the balls. However, the balls should not be too small because they must impart sufficient mechanical energy to the particles in order to cause fracture. A media size distribution or two-step milling procedure can provide more optimum grinding conditions, as can the shape of the media. Spherical media action relies mostly on point contact collisions whereas cylindrical media will also contain shear action.

From the perspective of morphological characteristics of the powders, fine particles have a reduced comminuting rate and it becomes more difficult to achieve finer sizes. This results in a grinding limit for a set of milling conditions at which milling effectively ceases with increased milling time. The limit will depend on the tendency for particles to agglomerate. As particles agglomerate in the mill, energy is expended breaking up the agglomerates, which leads to an equilibrium particle size that does not change with milling time. To expand on this issue of agglomeration, the reader is directed to a discussion on the interaction forces in interfacial systems [14]. The reduced tendency for agglomeration in a fluid allows for a finer particle size for a given set of milling conditions, as compared to dry milling. Furthermore, optimization of the milling fluid (by minimizing the difference between the solid and fluid Hamaker constants[1]) will minimize the tendency for

---

[1] Hamaker constant provides the means to determine an interaction parameter from the Van der Waals pair potential.

agglomeration and further reduce the particle size that is obtainable. Even with matched Hamaker constants, resulting in no attraction for agglomeration, there are other factors that limit the minimum particle sizes that can be obtained.

For efficient comminuting, proper loading of the mill is required. This includes both the media and material amounts as well as the relative amounts of the two. With excessive media, proper agitation might not be achievable, depending on the mill design. With too much solids, not enough media-particle-media impacts occur. With too little solids, unnecessary contamination is introduced into the powders. Finally, the gas or fluid in a mill might also have consequences that affect the powder characteristics. As new particle surfaces are being generated, they may absorb or react with the chemical species present in the milling vial, particularly oxygen.

So far, only the use of mechanical energy for comminuting has been discussed, but other energy forms can be utilized for top-down syntheses of nanopowders, if not directly, then as supplemental energy. Laser ablation is an example of using electromagnetic energy (laser pulses) for top-down synthesis of nanopowders [15, 16]. Cryomilling (usually at liquid nitrogen temperature) is an example of using temperature control during milling. High-energy impacts during milling can increase the temperature of the mill and its load. This increase in temperature can have negative effects on powder characteristics such as agglomeration, crystallinity, and elasticity/ductility [17–20], justifying the use of lower temperature in order to control these effects.

Agglomeration and the energy associated with breaking agglomerates results in the loss of energy for comminuting. Therefore, reduction of agglomeration during comminuting is favorable for decreasing crystallite size of the powders. For this purpose, agglomeration has been reduced with sonic energy and re-agglomeration prevented with electrostatic stabilization, where the surface charges are significant in magnitude, allowing electrostatic repulsion between particles [21–23].

2.2 Bottom-Up Methods

Bottom-up methods involve the assemblage of atomic or molecular materials to form nanopowders, either directly or through further manipulations such as a calcining treatment. This is the preferred method for making nanopowders because it offers the highest level of control over the powder morphology. Again, there are many methods available (a few examples are shown in Table 2) and not all techniques will be mentioned or elaborated on. The focus of this section is to provide some considerations and examples when performing bottom-up syntheses, such as the form of the precursors that are used (including additives), the conditions under which the precursors are assembled into shapes, and any processing aspects that require post-synthesis treatments. Some important material properties that can affect powder synthesis are listed in Table 3.

Table 2 Examples of bottom-up methods

Techniques	Specific examples
Gas-phase bottom-up methods	Atomic layer deposition; thermolysis-pyrolysis; organometallic vapor phase epitaxy, etc.
Liquid-phase methods	Molecular self-assembly; nucleation and sol–gel processes; reduction of metal salts; combustion, etc.
Physical vapor deposition	Vacuum evaporation; sputtering; molecular beam epitaxy (MBE), etc.
Chemical vapor deposition	Atmospheric pressure chemical vapor deposition (APCVD); low pressure chemical vapor deposition (LPCVD), etc.

Table 3 Material properties that can affect powder synthesis (adapted from [24])

Properties	Specifics
Physical	Crystal structure, bonding type, bond strength, dielectric constant, dielectric dispersion, ferroelectricity, ferromagnetism
Chemical	Solid and liquid phase equilibria, solubility products, solubility limits, complex species in solution
Colloidal	Surface species, hydrophilicity, isoelectric point, Hamaker constant

Bottom-up methods can use either solid, liquid, or vapor precursors. The solid precursors for the final nanopowders are generally made into a liquid, gaseous species, or highly reactive solid. This can be accomplished, for example, by dissolving the compound in a solvent or by decomposing the compound. Regardless of the state of the precursors, the specifics of the precursors used in a process should be considered. The consequences between using a nitrate, chloride, sulfate, carbonate, hydroxide, organometallic, complexes, organics etc., should be established. Furthermore, precursors have different types of impurities associated with how they are prepared. The precursor characteristics may result in impurities in the final powders, which may have consequences on the powder sintering behavior even at trace levels.

Impurities may result independently of the purity of the precursor material. For instance, combustion synthesis is typically performed using at least one precursor that is an oxidizer and at least one precursor that is a fuel [25–30]. The composition of the mixture (i.e., controlling the fuel-to-oxidizer ratio) is an important synthesis variable that controls the reaction temperature for a given system by changing the proportion of exhaust gases as well as the composition of unburned organic species. The specific chemistry of the exhaust gases and unburned organic material will be determined by the reaction sequence involving the evolution of the solid products, carbon monoxide, water, carbon dioxide, nitrogen, oxygen, hydrogen, and carbon for metal/carbon/hydrogen/oxygen/nitrogen mixtures. The reaction products are complex and therefore the exact consequences on synthesis are sometimes difficult to predict. Nevertheless, one should be aware of the potential for residual *organic impurities* and proper characterization should be performed to understand the resulting powder characteristics.

After determining what impurities might be present and at what levels, knowing where they go and what consequences they have on processing and properties is the next important step. For instance, it may be favorable for impurities to accumulate at defect-rich regions like surfaces or grain boundaries when sintered. Accumulation of impurities at the grain boundary can change the kinetics of grain-boundary related phenomena that can relate to the final stages of sintering and/or change the properties of a material. Most of the impurity segregation research is based on cation impurities. It is much more difficult to track and model anion impurities in solids, but this does not mean it is not an important consideration.

If precursors in the form of vapor are used, such as in chemical vapor synthesis techniques [31–43], then gas partial pressures, gas flow rates, temperature, and time are important. Secondary treatments, such as the flow of a secondary gas during cooling, can change the characteristics of the surface. For instance, sometimes it is necessary to introduce controlled access to oxygen to non-oxide ceramics or metals to create a passivation layer for preventing complete oxidation upon full exposure to oxygen.

If solution based synthesis is used, then reactant concentration, solvent, pH, temperature, pressure, time, etc., can affect the powder characteristics [4, 44–50]. Additives are often included to modify crystal nucleation and growth and/or dispersion of nanopowders when they are being synthesized in solution. This can affect the particle surfaces. Washing procedures can be used to remove the majority of these additives after synthesis, but it may be difficult to remove impurities incorporated into the particle bulk (chemisorbed impurities) or the first few monolayers of adsorbed surface species (which may chemisorb or physisorb to the particle surface). Even if the surface adsorbed species can be removed, the washing procedures can result in the adsorption of other compounds present in the washing solvents.

3 Phase Effects

3.1 Amorphous Phases

Many synthesis techniques result in amorphous or metastable crystalline phases instead of the desired fully crystalline structure. This depends on the specific synthesis conditions and the material that is being synthesized. For instance, during top-down methods, it is possible for order–disorder transformations to occur. This is better known as amorphization and has been observed during milling [51, 52]. High-energy impacts can cause local deformation and the short time scales of the impacts do not allow the structure to relax back to the original state. Ductile materials are more prone to order–disorder transformations and such transformations apply mostly to metals and their alloys. However, order–disorder

Fig. 2 X-ray diffraction pattern of yttria-stabilized zirconia prepared by an emulsion/sol–gel process and calcined at different temperatures [59]. Note that the sample is not crystalline after synthesis, and requires thermal treatment to allow crystallization

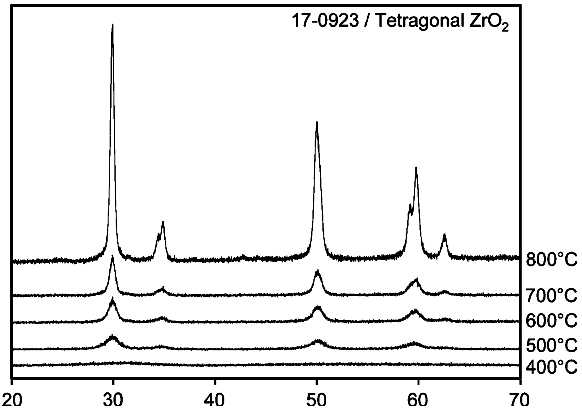

transformations have been observed for ceramics having weak-bonded layers as well, such as graphite and boron nitride [53, 54].

Bottom-up methods are by definition disorder–order transformations. Disordered molecular species in the vapor or liquid state are ordered into a solid state. The degree of ordering depends on the synthesis conditions. Kinetically limited conditions may not allow the lowest energy equilibrium crystalline state to be formed. Whether an amorphous or metastable crystalline phase can form depends on whether or not the material can accommodate a metastable crystalline phase, the available energy during synthesis, and the time for which this energy is available. Therefore, low temperature (i.e., low thermal energy input) and fast reactions are favorable synthesis conditions for forming amorphous and metastable crystalline phases.

For example, powders obtained by precipitation or sol–gel synthesis are likely to be amorphous and calcination is necessary to decompose/crystallize the phase that is formed [55–58]. As an example, Fig. 2 illustrates the X-ray diffraction patterns of yttria-stabilized zirconia nanopowders as they are progressively treated at higher temperatures after preparation by an emulsion/sol–gel process. The as-synthesized powders consist of an amorphous zirconium hydroxide. As the temperature of calcination is increased beyond 400 °C, the crystallinity of the powder increases, eventually forming the desired tetragonal zirconia.

To avoid this crystallization ‘delay’, liquid-phase methods that utilize self-assembly or templating can be used to assist in the direct arrangement of molecules into a crystalline state even at low temperatures. This can be as simple as using crystalline seeds or more complex approaches, like using polymer engineering to build specific templates which may even alter the crystal structure. Another strategy is to use more energetic methods, such as hydrothermal and solvothermal synthesis. These are liquid-phase precipitation methods that use a combination of pressure and temperature above the vaporization temperature of the liquid. This is typically accomplished by heating the solution in an autoclave.

The additional thermal energy and pressure may allow the direct precipitation of equilibrium crystalline phases that might not be achieved by precipitation below the vaporization temperature of the liquid. Dissolution/re-precipitation during a long soaking time during these synthesis methods may also favor crystallization.

Gas-phase synthesis methods are performed at higher temperatures compared to liquid-phase methods and therefore have more energy for a disorder–order transformation. Thus, crystalline phases are more readily obtained. However, the ordering may be kinetically limited by the time scale for which higher temperature is available. For instance, in gas-phase condensation the particle may form in a hot-zone, but the particle can be rapidly removed from the hot-zone and collected in a cold-zone, preventing crystallization. Flame pyrolysis is another example where precursors are introduced into a hot-zone (flame) only to be quickly removed. The fast removal from the hot-zone helps obtain nanopowders, but may also prevent full crystallization of some materials due to quenching effect as a result of removal from the hot-zone. The synthesis parameters may be varied to achieve different levels of crystallinity.

As it is with liquid-phase synthesis, crystallinity during gas-phase synthesis can also be assisted by templating. A substrate (clean or modified surface) can serve as a template during atomic layer deposition or chemical vapor deposition, for example. The template may provide preferred deposition sites for automatic ordering into a crystalline phase. Already deposited material may act as its own template, such as is the case for epitaxial growth. Thermal barrier coatings, which protect and extend the life of internal jet and rocket engine components, are an example for which columnar grains, acting as their own templates, are grown onto the surface of superalloy components.

3.1.1 Effects on Sintering

If amorphous or metastable-phase powders are to be used directly in a sintering process, then the effect of phase transformations during densification should be understood. Typically, phase changes during sintering should be avoided, if possible, because of the volume changes resulting from them. The volume changes can make achieving full densification more difficult. However, pressure-assisted sintering techniques can at least partially alleviate issues associated with volume changes of phase transformations.

On the other hand, the transition from amorphous to crystalline phase through nucleation and growth requires energy that a sintering schedule can provide, which ultimately leads to a lower free energy state. The net energy released has the potential to contribute to sintering and needs to be accounted for when trying to develop a fundamental understanding of sintering processes and models in which these transitions are found. For example, enhanced sintering in alumina utilizing a combination of amorphous powders and a non-traditional sintering technique has been observed [60]. Well-defined studies, in which crystallinity is varied while being certain to maintain other powder characteristics constant, would greatly improve our understanding of this type of effect.

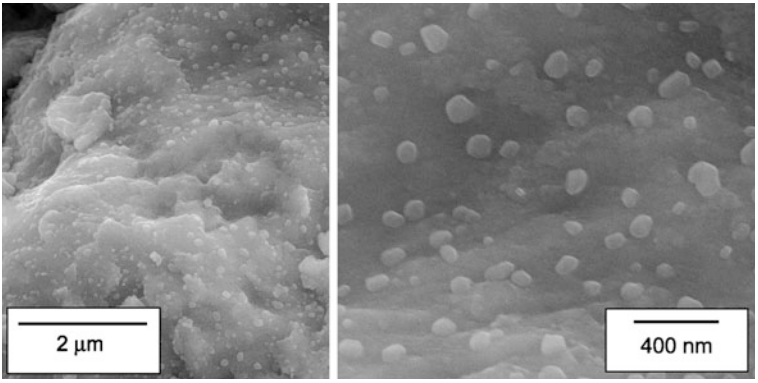

Fig. 3 Sintered composite of an iron-based amorphous metal as the matrix and crystalline yttria nanoparticles as the reinforcing phase [61]. Short sintering times avoid recrystalization

An interesting area of research that highlights the potential for the use of amorphous powders in a sintering process is the sintering of amorphous metals. Bulk amorphous metal specimens have successfully been prepared by various researchers using the spark plasma sintering technique (SPS) [58, 61, 62], as illustrated in Fig. 3.

Perhaps more pertinent to this discussion are instances in which crystallization of the amorphous powders is not prevented [63–66]. This highlights the possibility to utilize the amorphous to crystalline transition through use of homogeneous nucleation and growth of the crystalline phase. Controlled heterogeneous nucleation through additives should also be a possibility.

Some researchers have had success with purposely incorporating nanocrystalline phases into amorphous metals [58, 61, 67–70]. Similar to the well-developed ideology of glass–ceramics, in which glasses are brought to a temperature beneficial for nucleation and then the temperature is lowered to grow crystals from the nuclei in a controlled manner, it seems that nanocrystalline composite compacts can be made through in situ sintering. Like glass ceramics, this may lead to intermediate properties between the amorphous and crystalline phases.

3.2 Metastable Phase Transformations

Synthesis of nanopowders can lead to the formation of metastable crystalline phases as well, thus, it may be necessary to calcine nanopowders immediately after synthesis. This is because nanopowders with metastable crystalline phases may go through phase transformations during sintering. Therefore, the consequences of a transformation from an amorphous or metastable crystalline phase to a stable crystalline phase, and the indirect consequences of the transformation, can be utilized as a design tool if it is properly understood. Likewise, a phase transformation from one stable crystalline phase to another stable crystalline phase can produce similar effects.

Calcium pyrophosphate is an example of a material that exhibits a low- and high-temperature form and the sintering characteristics of the two phases, as well as mixtures of the two phases, have been previously evaluated [71]. The high-temperature form can exist metastably at low temperature and can be used to generate metastable powders, stable powders, and mixtures of metastable and stable powders for sintering. Unfortunately, the particle sizes of the powders in Ref [71] were not the same, making a direct correlation of the effect of metastability difficult, and also highlighting one of the key difficulties in evaluating the effects of processing on nanosintering. Regardless, the authors highlight a few important features of the presence of a metastable phase. The metastable phase was reported to have an effect on densification (detrimental in this case). Another important feature was that the transformation from the metastable phase to the stable phase, which has a $\sim 7\ \%$ volume expansion, generated enough stress to cause cracking of the sample and is an important possibility to be aware of when sintering a material that may go through a phase transformation.

It may be possible to induce beneficial thermomechanical stresses by utilizing phase transformations to reduce the grain size of sintered specimens. Reduced grain size has been observed in systems exhibiting a phase transformation under high pressures. In the TiO_2 system, the transformation of metastable anatase to rutile at pressures of 1.5 GPa and sintering temperatures $\sim 1/3T_m$ resulted in a finer rutile grain size than the parent anatase phase prior to sintering and the effect was enhanced by increasing the sintering temperature [72]. The effect is described as being controlled by an increased nucleation rate and lower crystal growth rate and the shift of rates is due to a combination of both pressure and temperature. It is unclear what role thermomechanical properties might have on the grain size reduction. There is an approximately 5–13 % volume reduction by transforming from anatase to rutile assuming an anatase density of 3.8–4.0 g/cm^3 and a rutile density of 4.2–4.3 g/cm^3.

No matter what the underlying contributions, thermomechanical stresses, nucleation and growth, both, or even other factors, it is clear that phase transformations can have a significant impact on sintering. The effects can be negative or positive depending on the system and what one is trying to achieve. It is important to realize that phase transformations can have an effect and that they can be prevented, suppressed, or accelerated to fit the sintering need. Phase transformations are one of several ways for manipulating a sintering process.

3.3 Multi-Phase Considerations

Multi-phase compositions should be understood when sintering a material with more than one component. Relevant factors might include whether or not the phases will react, solubility of the phases in each other, interphase versus intraphase bonding and at what temperatures the bonding will occur at, the distribution of the phases, and variation in thermomechanical properties, for instance. Reaction between phases can provide a driving force for sintering. Solubility of phases within each other can determine how well grain growth is prevented. Interphase versus intraphase bonding will have important consequences on the sintering schedule that must be applied to the system. Some of these considerations can be directly related to synthesis conditions.

Some synthesis techniques might not provide full conversion to a product phase of interest, creating a multi-phase situation where one was not intended, and causing full product conversion to occur during sintering. Both endothermic and exothermic reactions have the potential to contribute to sintering. Besides having unreacted components left from the synthesis process, the sintering process may be intentionally designed using individual components that are expected to react. In an extreme case the smallest contribution to reactive sintering is the result of a chemical potential only, with little-to-no heat liberation or even requiring heat for the reaction to occur. The opposite extreme is a result of chemical potential as well, but with large heat liberation, such as is used in self-propagating high-temperature synthesis, or SHS, in which the reaction, once initiated, is self-sustaining and can even provide the energy for simultaneous densification without any other energy besides that used to initiate the reaction [73, 74].

Prevention of grain growth is often necessary to maintain a nanostructured specimen after sintering. Grain growth was covered in another chapter in more detail. However, a brief mention of using multiple phases to achieve grain-boundary pinning is appropriate. Two phases, preferably with low solubility in each other, can create a bottleneck for diffusion to slow down grain growth kinetics. If this effect is desired, then design of a synthesis process incorporating a multi-phase system is a potential method to achieve this goal [75].

3.4 Sub-Stoichiometry

Synthesis and post-processing conditions can also result in sub-stoichiometric compounds if the material structure allows for it. Sub-stoichiometry can be varied during gas-phase synthesis methods by controlling the partial pressures of the reactants. Heat treatments of nanopowers in different atmospheric conditions (i.e., gas mixtures, different types of gases, vacuum, etc.) can also affect sub-stoichometry due to various gas partial pressures that the nanopowder must come into equilibrium with. For example, during combustion synthesis methodologies or pyrolysis techniques, the oxygen balance affects the stoichiometry.

Point defects, such as vacancies, can enhance diffusion. As we have discussed, diffusive processes, facilitating mass transport, are important to sintering. An enhancement in transport by diffusion results in an enhancement in sintering rates. Conversely, vacancies in certain proportions can lead to vacancy ordering. Once they become ordered, their mobility is reduced and diffusion by vacancy controlled transport is no longer significant, therefore, sintering processes can be hindered. The effects of the vacancy diffusion mechanism on sintering behavior have been a

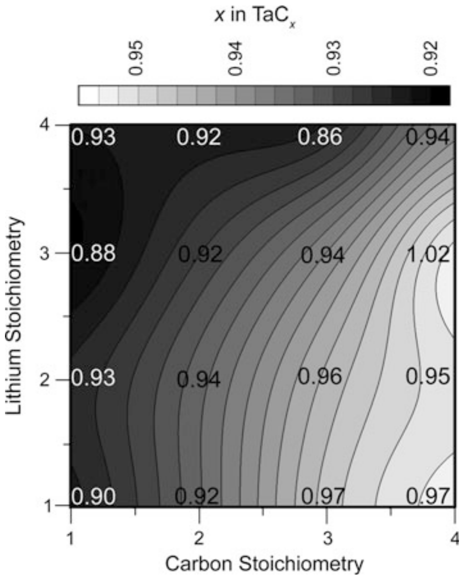

Fig. 4 Compound stoichiometry, C/Ta, with respect to lithium and carbon stoichiometries during solvothermal synthesis of TaC after a data-smoothing algorithm was applied (actual data are superimposed over the contoured surface) [78]

topic of interest in sintering models [76]. Vacancy diffusion at the surface is generally faster than vacancy diffusion in the bulk so this mechanism is expected to be very important for nanopowders.

Synthesis conditions can be altered or used intentionally to achieve sub-stoichiometric conditions as well. For example, TaC_x is a compound capable of incorporating significant amounts of carbon vacancies into its structure [77]. For example, varying either carbon stoichiometry or the reductant type can be used to vary x from approximately 0.90–0.97 when using a solvothermal method for synthesizing TaC_x [78]. In this case, the compound stoichiometry is controlled by carbon diffusion into the compound. Carbon stoichiometry increases the carbon chemical gradient and the reductant type controls the reaction temperature.

Figure 4 illustrates this variation for the case of lithium as the reductant during the following specific solvothermal reaction:

$$TaCl_5 + C + 5Li \rightarrow TaC + 5\,LiCl \tag{1}$$

The carbon stoichiometry is important because the grain size of sintered tantalum carbide ceramics is a strong function of carbon stoichiometry [79]. The grain size increases with increasing sub-stoichiometry due to enhanced mass transport.

In addition to synthesis conditions, post-processing treatments can sometimes be used to generate sub-stoichiometry if the compound structure permits sub-stoichiometry. One method for producing sub-stoichiometry in oxides is to expose the compound to heat in a reducing atmosphere. Another method is to blend compounds, such as a monoxide and dioxide, to achieve some intermediate stoichiometry.

Although sub-stoichiometry can be designed in some compounds, producing too many vacancies can be detrimental. The vacancies may order into clusters or aggregates [80]. In this case, the vacancies are in a lower energy configuration because of the ordering, but the mobility of the vacancy is reduced and it is now considered a more permanent structural feature. There is still much work to be done to understand the vacancy ordering in different structures and systems and what effects they may have on sintering.

4 Chemical Purity

Chemical purity of the powders is of fundamental importance to nanosintering. The chemical purity of the powders will depend on the precursors and processing that were used to synthesize and/or treat the powders prior to sintering. Sintering characteristics of a material may be sensitive to relatively small quantities of impurities. Impurities may be present as a result of the type of precursors that are used, the processing conditions and atmosphere, cleaning procedures, and adsorption characteristics of the nanopowder surface.

The metallic/inorganic impurities of a nanopowder are typically dependent on the purity of the precursor. When purchasing chemical reactants for any synthesis technique, the purity that a manufacturer defines is most often on a *metals basis*. The non-metallic impurities will also depend on precursor selection, but also on their incorporation due to the synthesis technique itself. For example, reverse micelle synthesis makes use of a significant amount of organics that will be difficult to remove after powder synthesis [58].

High-temperature synthesis is favored for eliminating non-metallic impurities because organic impurities are burned off in situ. Lower temperature techniques can also be utilized to obtain low non-metallic impurities if the use of organics can be avoided and/or the reaction waste products are highly soluble and therefore readily removed through washing procedures. However, non-metallic impurities are not necessarily all organics, the impurities can consist of oxygen in non-oxides, for example.

From the discussion so far, it should be no surprise that gas-phase synthesis methods with their associated higher temperatures and using high-purity precursors, result in the best purity. This is demonstrated by Toya Soda Manufacturing Co.'s TSK TS-7 grade silicon nitride, which has very low metallic and non-metallic impurities compared to other vendors. UBE Industries' SN-E 10 grade silicon nitride is produced by liquid-phase synthesis and uses high-purity precursors, but has nearly twice as much non-metallic impurities as the TSK TS-7 grade silicon nitride. H.C. Stark's and Toshiba's silicon nitride powders have higher metallic impurities and non-metallic impurities [13].

Some synthesis techniques can generate a very wide range of impurities. Combustion synthesis is a good example. Combustion synthesis utilizes a mixture of an oxidizer and a fuel. When the oxygen balance for the mixture is close to zero, the reaction temperature is the highest and the lowest impurity levels are obtained. However, as the oxygen balance deviates further from zero, incomplete burning results in either excess fuel or oxidizer. Very high impurity content can result in this case and chemical or thermal treatments will be necessary to remove them.

4.1 Precursors and Processing

For top-down synthesis methods, the precursor selection can be as simple as buying the same composition of the powder that one wants to obtain. The precursor for gas-phase synthesis is either going to be a gas at room temperature and pressure or a compound that will volatilize by introducing it to higher temperature in the reaction chamber. For liquid phase synthesis, soluble compounds are desired and may include organometallics, complexes, nitrates, chlorides, etc. Of course, solubility will depend on both the precursor and the solvent. Modifications to synthesis processes often involve selection of atypical precursors, which further complicates specific synthesis techniques.

When performing powder synthesis, there are often several precursor options. Even for the same compound, manufacturers may offer several purity grades. It is important to be aware of the fact that these impurities may remain throughout and after a synthesis process. Processing, such as chemical or thermal treatments, after synthesis might be able to remove these impurities, but if not, then one must rely on careful precursor and precursor grade selection if an impurity may be a problem for sintering or the final application.

As an example, it has been shown that the sintering behavior of aluminosilicates is influenced by trace mineral impurities that were inherently present in the kaolin-based zeolite starting material [81, 82]. The sintering behavior of zeolites synthesized from the kaolin precursor was studied and a comparison to a zeolite starting from other precursors was included for comparison. In particular, the amounts of titanium and iron in the zeolites were believed to affect the sintering. These impurities were thought to contribute to the phase development for differing heating rates such that lower crystallinity was observed for a 1 °C/min heating rate compared to using a 3 °C/min heating rate. Additionally these impurities were thought to retard sintering at lower temperatures (750 °C) while promoting sintering at higher temperatures (>900 °C) as a consequence of the phase development.

Besides metallic impurities, non-metals can also have an impact on sintering. As an example, the sintering behavior of zirconia in the presence of chlorine has been demonstrated [83, 84]. Readey and Readey's results [83] are an extreme case in which a hydrochloric acid atmosphere was used to induce vapor phase transport due to the formation of volatile chloride compounds. Densification was hindered and attributed to neck growth that was due to vapor phase mass transport.

Karapetrova et al.'s work [84] evaluated the effects of chlorine in zirconia by investigating different precursors and processing. They showed that even small quantities of chlorine present in zirconia powders have significant consequences. Although the chlorine is ultimately removed via vapor-phase transport at higher temperature (as was observed by condensation in cooler sections of the furnace), the presence of the chlorine during the sintering process still hindered densification. Furthermore, in addition to increasing vapor-phase transport, the oxygen vacancy concentration was suppressed by the presence of chlorine.

The examples provided are just a few in which impurities have had an impact on sintering. In the first case, impurity levels were a result of precursor selection. In the second case, the impurity level was varied by precursor selection and the processing method. It is important to be aware of the potential impurities that may be present in a powder and the potential those impurities have to change the sintering process. Chemical or thermal treatments can sometimes be used to remove impurities, but one must be aware that those treatments can also affect other powder characteristics that may be important for sintering, such as the formation of hydroxide surface layers on oxides or oxygen surface layers on metal, which are generally detrimental. A particularly interesting example of the opposite is the surface cleaning of magnesium nanopowders, which in the absence of their oxide layer are highly pyrophoric and practically impossible to handle.

4.2 Surface Impurities

The surface of a particle is energetically different than the bulk due to differences in atomic or molecular bonding. The excess free energy of a surface can be estimated as the difference between the atomic contributions of the atoms that are fully coordinated in the bulk and the missing contributions due to missing or dangling bonds at the surface, although it is actually more complicated than this due to anisotropy, relaxations, and restructuring. The higher surface energy of the surface of a particle is reduced by chemisorption or physisorption, which changes the chemical composition of the surface.

Surface adsorption is therefore very important to nanopowders, which have high surface areas. Whatever processing technique is followed, in a liquid phase or vapor phase, there will be a tendency to adsorb molecular species from the environment (whether it be oxygen, nitrogen, hydrocarbon molecules, water, solvents, etc.) at low temperatures and these can even persist in the best vacuum systems. Physisorbed molecules may react to become chemisorbed over time. At higher temperatures, physisorbed and chemisorbed molecules are desorbed from the surface by providing enough thermal energy to overcome their adsorption energies. However, removing them may not be enough because other particles may readsorb immediately or over time during storage. Also, mass transport is active at significantly high temperatures and rapid diffusion of impurities within the bulk can migrate to the particle surfaces to minimize the excess free energy of a surface (which may or may not be beneficial).

A few practical examples of surface impurities as a result of liquid and vapor phase processing follow. During the solvothermal synthesis and processing of yttria-stabilized zirconia nanopowder, organic molecules on the surface of the nanopowders are likely responsible for the agglomeration of the powders [85]. Sol–gel-synthesis of layered oxides such as $LiNi_xCo_{1-x}O_2$, a material relevant to Li-ion battery cathodes, results in carbonate formation on the surface [86, 87]. These carbonate layers could not removed using thermal treatments, but could be removed by replacing the carbonate layer with an apparent nitrate layer through washing. Whereas the carbonate layer remained after thermal treatment, the nitrate layer could be removed by a similar heat treatment. It appears that water was persistent on the surface with the absence of the carbonate or nitrate phase.

Calcining precursor nanopowders can also have significant effects. For instance, it has been shown that molecular reactivity of tin oxide, iron oxide, molybdenum oxide, or composites of these oxides is significantly influenced by the ratio of acid-center types on the surfaces due to a change in the reaction mechanism [88]. Heat treatments result in the reduction of hydroxyl groups and an increase in unsaturated cations at the surface. By doping the tin oxide, which has unsaturated Sn^{4+} cations, with either iron oxide or molybdenum oxide (which has Fe^{3+} or Mo^{6+} cations to contribute to the surface), the reactivity of the surfaces is significantly altered. This could be due to unsatisfied charge as a result of the Fe^{3+} and Mo^{6+} aliovalent ions present at the surface. Molybdenum is not so effective at low concentrations and may be a result of Mo^{6+} ions avoiding the surface due to the high valence.

Segregation of processing impurities and doping ions in rutile and anatase pigments after high-temperature heat treatments has been studied by X-ray photoelectron spectroscopy [89]. In this case, sulfur segregates to the boundaries and is then removed via volatilization of sulfur oxides. Bulky ions like potassium and phosphate ions have a high tendency to segregate to the surface. Smaller ions such as zinc and aluminum are only partially segregated to the surface, if at all, while the rest are likely occupying interstitial sites. This could be a result of a charge argument just as well as a size argument. The segregation in the anatase phase is always lower than in the rutile phase and can be attributed to the presence of accessible interstitial sites in the anatase phase versus the rutile phase. However, segregation in rutile may be a result of the fact that rutile is the higher temperature phase and requires higher temperatures to stabilize it. Under this higher temperature conditions, segregation is more likely due to removal of adsorbed species and higher atomic diffusion, which influences the driving force for segregation.

The configuration of adsorbing molecules may also be affected by calcining treatments. For example, the configuration of carbonyl groups as a result of carbon monoxide adsorbed at room temperature onto cobalt aluminate calcined at different temperatures, results in differing amounts of carbon monoxide and oxidized carbon monoxide (dioxide and carbonate) due to redox reactions [90]. Despite the heat treatment temperature, tricarbonyls were present over reduced cobalt centers, but were in lower concentrations relative to carbon monoxide for higher heat treatment temperatures. A higher heat treatment temperature resulted in a surface containing monocarbonylic species that were not present in the sample heat treated at lower temperature. These results suggest that a higher calcining treatment resulted in a decrease in the ability for carbon monoxide to reduce cobalt at the surface. This may be due to more octahedrally coordinated aluminum ions being present at the surface at higher temperatures, relative to cobalt ions, as evidenced by the high carbon monoxide adsorption over these sites. At the lower temperatures, carbon monoxide adsorption is also observed over tetrahedrally-coordinated aluminum ions and some of the cobalt ions.

4.3 Grain Boundary Impurities

Whether or not impurities segregate to a powder surface prior to sintering, there is the opportunity for them to segregate during a sintering process and accumulate at the grain boundaries. Segregation to a grain boundary is more likely than segregation to a surface because there is no competition from vapor adsorption and there are two additional driving forces, mechanical strain energy and electrical energy due to charge development at the boundary. This enhances segregation to the grain boundaries at relatively low temperatures. If the segregation occurs prior to or during sintering, then the impurities can have a significant effect on sintering.

Impurities on the particle surface, or at the grain boundary as the grains begin to sinter, can influence several aspects of sintering, as described in a previous chapter. In addition to the kinetics and thermodynamic roles of these impurities, more critical effects can be observed if second phases are present. For instance, the difference in chemistry can cause a new phase to precipitate out. In this way, grain boundaries act as nucleation sites. The consequences of multi-phase and reactive sintering have been discussed in a previous section. It is unclear what kind of local effects might arise from reactive or multi-phase sintering.

The difference in chemistry at the grain boundary can assist in localized eutectic melting at lower temperatures than might otherwise be expected and result in a localized dissolution/precipitation sintering mechanism where transport is accelerated if there is sufficient solubility in the liquid phase. A localized melting can also lead to vaporization/condensation mechanisms. Both of these sintering mechanisms are undesired for densification in the solid state, but could be beneficial for developing intentionally porous materials. Regardless, these mechanisms can be present in the initial stages of sintering.

In solid state sintering, impurity atoms at the grain boundary can have several effects. Solid-state sintering mechanisms require mass transport that is highly dependent on defects. Grain-boundary diffusion and lattice diffusion from the grain boundary influence sintering and depend on the grain boundary chemistry. These mechanisms are particularly important in the final stages of sintering. Impurity atoms at a grain boundary can both enhance or deter densification depending on the nature of the defects present at the grain boundary and how they affect mass transport.

Densification of tin oxide with additions of iron or magnesium dopant is an example of utilizing grain boundary segregation to enhance densification [91].

When sintering the tin oxide without dopants, the compact could only be sintered to 55 % density when sintering at 1200 °C for 300 s. The low density was attributed to a non-densifying evaporation–condensation mechanism. In comparison, densities as high as 95 % could be achieved within 25 s at 1200 °C when doping the compacts and segregating the dopants to the surface prior to sintering. Improvements in densification were observed almost immediately. The enhanced densification was explained as a result of higher concentrations of dopants at the surfaces and then ultimately the grain boundary. The high dopant concentrations result in high oxygen vacancies at the grain boundary and a reduction in the surface energy and both of these factors enhance grain boundary diffusion. The enhanced diffusion was apparently great enough to promote grain boundary diffusion dominated sintering rather than an evaporation/condensation mechanism.

In addition to transport, impurities can also affect the volume of the grain boundary phase. For example, the grain boundary thickness was reduced from 8 to 4 nm by sintering a zirconia material doped with 4 mol % yttria [92]. Another example is the initial decrease in the equilibrium grain boundary thickness, followed by an increase, when sintering silicon nitride having ppm concentrations of Ca doping [93]. The grain boundary thickness depends on how many neighboring atoms are perturbed by the defective grain boundary region. Ions that segregate to the grain boundary can create stresses that either add or subtract to the atomic perturbation according to their ionic size and therefore the type of impurity is expected to be a contributing factor to the grain boundary thickness.

Activated sintering is a phenomenon in which densification rates are significantly improved upon addition of a sintering aid. In this case, the boundaries are of markedly different chemistry and structure than the bulk, but appear to be in equilibrium with each other. Liquid-like interface complexion below eutectic temperatures, or an extension of Gibbs definition of bulk phases to equilibrium grain boundary features, has been described to explain this [94]. Such features can have independent equilibrium phases, transformations, and reactions. As such, a long-term goal in the materials science community is to develop grain boundary phase diagrams for material systems for utilization as a design tool. These complexions will help control microstructure evolution during sintering as well as material properties, since impurity-based interfacial films are often retained after cooling. Six distinct grain boundary complexions have been observed in alumina, being the most systematic characterization of grain boundary complexions to date. Grain boundary complexion interactions have been used to explain abnormal grain growth in alumina and computations quantitatively supports this explanation of abnormal grain growth. Intricate study of many systems is still in its infancy.

5 Size Effects

The physical characteristics of a nanopowder can provide very valuable information about how well a nanopowder will sinter. However, the accurate characterization of crystallite size (sometimes referred to as primary particle size) and particle size is often an issue in nanomaterials research due to agglomeration and aggregation. The confusion in defining the effects of the physical characteristics of nanopowders arises from the *misinterpretation of terminology*, *insufficient characterization*, and/or the *improper understanding and treatment of agglomeration*.

Terminology A particle is a collection of crystals that acts as an independent unit amongst other particles. The particle can be a primary particle, in which case the crystallite size and particle size are equivalent, or it can be a collection of crystallites, schematically illustrated on the left side of Fig. 5. If a particle is a collection of crystallites, then it is considered an agglomerate or aggregate. An agglomerate is a particle consisting of crystallites that are held together by weak Van der Waals forces. An aggregate is similar to an agglomerate, but is distinguished by the fact that strong forces (i.e., primary bonding) hold the crystallites together. As such, the agglomerates are sometimes referred to as soft agglomerates because of the ability to overcome the weak bonding forces to separate the primary particles whereas aggregates are sometimes referred to as hard agglomerates because of the greater difficulty in separating them. The right side of Fig. 5 presents an SEM image of a zirconia particle prepared by an emulsion/sol–gel process, showing that while the crystallite size is in the nanometer range, the particle size is not. This is quite common in nanoparticle synthesis.

There is significant difficulty in evaluating the synthesis processes that are more suitable for obtaining small particle sizes because of the difficulties in defining particle size and accurately measuring it. Much of the literature does not contain enough information to properly evaluate the accuracy of their determinations or whether or not their synthesis conditions have been optimized towards this goal.

5.1 Crystallite Size Effects

The crystallite size, also referred to as the primary particle size or grain size, refers to a single crystalline domain. This is an important feature of nanosintering. Herring's scaling laws, developed in the 1950s, describe the effect of changing scale on sintering [95]. Of particular importance is the effect of crystallite size on the rate of sintering.

According to Herring's scaling laws, decreasing the primary particle size from the micrometer scale to the nanoscale has the potential to increase the sintering rate by up to twelve orders of magnitude, depending on the sintering mechanism. The significant consequence of this is that nanopowders can be sintered at either lower temperatures, where sintering rates are too low for larger powders, or that sintering time can be reduced for similar temperatures.

The experimental observation of Herring's scaling laws is not always apparent from crystallite size data. If significant agglomeration or aggregation is present, a non-uniform green density of a specimen may result. The relatively high packing density within the agglomerate or aggregate results in faster local sintering. Shrinking is not observed without significant sintering amongst the agglomerates or

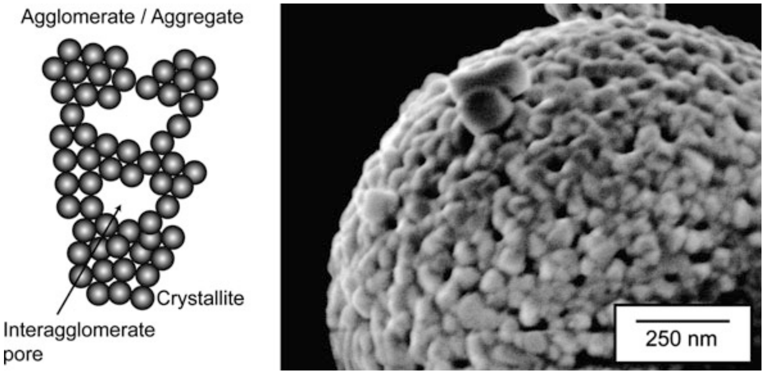

Fig. 5 (*Left-side*) schematic of an agglomerate or aggregate illustrating the difference between particle size and crystallite size. (*Right-side*) scanning electron microscope image of a zirconia particle prepared using an emulsion/sol–gel process

aggregates and the primary particles within can ripen into a large primary particle of similar size to the original agglomerate or aggregate. In this case, one is sintering larger particles and the benefit of having small-scale features is lost. Shrinkage will not occur until the agglomerates or aggregates (now a large primary particle) begin to sinter amongst themselves. Indeed, experimentally, Herring's scaling laws seem to apply more to the agglomerate or aggregate size than to the crystallite size. Therefore, it is critical to minimize the agglomerate or aggregate size. In fact, sometimes it is beneficial to increase the crystallite size to minimize agglomeration as smaller crystallites have a higher tendency to agglomerate or aggregate.

5.2 Aggregation and Agglomeration Effects

The fact that the Herring's scaling laws relate more to the agglomerate or aggregate size than the crystallite size can be exemplified by comparing the sintering characteristics of nanocrystalline titania (anatase) from different sources [96]. Powders having a crystallite size of 8–10 nm had a corresponding particle size of 340 nm. Temperatures in excess of 1,100 °C were necessary to achieve densities greater than 90 % of theoretical and full density was not readily obtained. A powder with a slightly larger crystallite size (16 nm) and smaller particle size (80 nm) was sintered to above 90 % of theoretical density at temperatures above 800 °C and to full density between 900 and 950 °C. A further increase in crystallite size (near 40 nm) with an unspecified (but apparently smaller) particle size obtained densities greater than 90 % of theoretical at temperatures as low as 650 °C and approached a maximum density at temperatures as low as 800 °C. Other demonstrations of the effect of scale on sintering are available for other systems [97, 98].

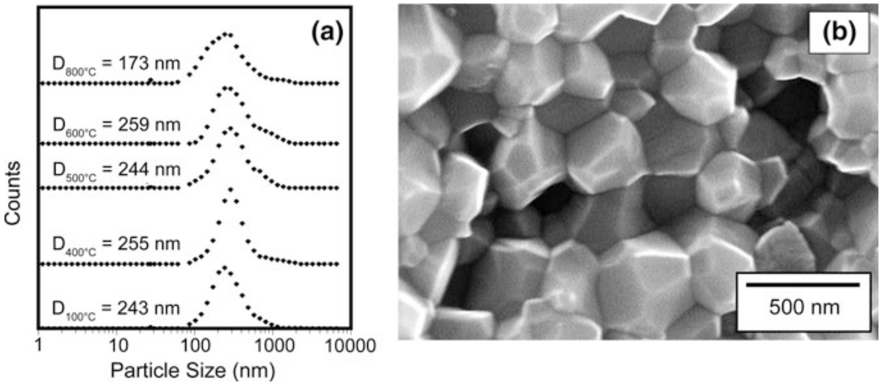

Fig. 6 **a** Particle size of yttria-stabilized zirconia (3YSZ) powders after several post-synthesis calcination treatments. The powders were synthesized by an emulsion/sol–gel process. **b** Scanning electron microscope image of the powders after spark plasma sintering

In addition to the effect of particle size on density, there is also the effect of particle size on the grain size of sintered compacts. For the case of zirconia powders with particle sizes around 250 nm (Fig. 6a), the grain sizes after sintering are also around 250 nm (Fig. 6b). The X-ray diffraction patterns for these powders (Fig. 6a) show that the crystallite size is increasing with heat treatment temperature, evident from the gradual narrowing of the diffraction peaks, but the particle size (Fig. 6b) is not changing. Thus, the particle size defines the grain size of the sintered compacts, at least under standard sintering conditions. Another example is $BaAl_2Si_2O_8$, where again the particle size (Fig. 7a) defines the grain size of the sintered compact (Fig. 7b), both around 500 nm. Thus, to adequately make use of the benefits of sintering nanomaterials according to the scaling laws, it is imperative to understand and control the agglomeration and aggregation in the nanopowders.

5.3 Agglomerates Form from “Soft Agglomeration”

The title of this section is meant to demonstrate the diverse terminology that is used in describing particle sizes that often results in confusion during use. To further demonstrate this, we will introduce a few new terms: *flocculation* and *coagulation*. Sometimes these terms are used interchangeably although there is a technical difference. *Floccs* are another version of *soft agglomeration* that is a result of overdispersion and form due to a destabilization process called *coagulation*. *Flocculation* is the process by which the *floccs* conglomerate into larger particles after the destabilization process. More depth on the topics discussed herein is provided in an appropriate text [14].

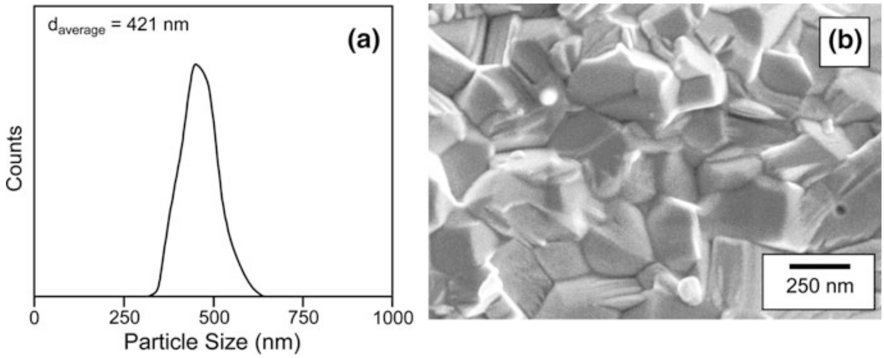

Fig. 7 **a** Particle size of $BaAl_2Si_2O_8$ powders. The powders were synthesized by a combustion synthesis process. **b** Scanning electron microscope image of the powders after spark plasma sintering modified from [46]

As previously mentioned, agglomerates are particles consisting of multiple primary particles or crystallites which are held together by weak Van der Waals forces. Three forces contribute to the Van der Waals attractive force between atoms or molecules: Keesom orientation forces, Debye induction forces, and London dispersion forces. These three forces are a result of dipole–dipole, dipole-induced dipole, and induced dipole-induced dipole molecular interactions. Spherical inert atoms or molecules are held together solely by dispersion forces.

The arguments that can be made for two interacting spherical inert atoms or molecules can be extended to particles by summing the London dispersion forces over all molecules in a two-body system. Mathematical manipulations lead to the development of the Hamaker constant (H_{11}). The Hamaker constant is a material constant that measures the attraction between two particles of that material in a vacuum. This is a reasonable approximation for gas-phase interactions. Dry nanopowders (or dry powders in general) have a very high tendency for agglomeration and no barrier to prevent agglomeration.

In a liquid medium, the Hamaker constant is reduced. For two particles (subscript of 1) separated by a liquid medium (subscript of 2), the Hamaker constant becomes $H_{121} = (H_{11}^{1/2}–H_{22}^{1/2})^2$. If H_{11} (particle–particle interactions in vacuum) does not equal H_{22} (molecule–molecule interactions of the liquid), then there is always an attractive potential for the particles to agglomerate in the liquid, but the attractive potential is reduced in comparison to the attractive potential in a gas phase because $H_{121} < H_{11}$.

There are three significant consequences of a reduction in the attractive potentials in the condensed phase versus a gas phase. The first is that even if particles do not agglomerate in a liquid phase, they may still agglomerate after the removal of the liquid phase and exposure to the vapor phase. The second consequence is that it is easier to break up agglomerates in a liquid phase if trying to disperse or control agglomeration. The third consequence is that the solvent in which particles are dispersed is important. The closer H_{11} and H_{22} are, the lower the tendency for agglomeration as a result of dispersion forces, which can be eliminated altogether if the two Hamaker constants are matched.

To characterize aggregation, agglomeration must be eliminated through dispersion. Dispersion of agglomerates is usually achieved by introducing the powders into a liquid phase, separating the particles, and using a stabilization method to keep them separated. The use of ultrasound can sometimes be used to break up the agglomerates suspended in the liquid, but if significant tendency for particle agglomeration exists in the liquid, then the powders will agglomerate again given some time. Once the agglomerates are broken up, there are several common dispersion techniques for keeping the particles dispersed. The most common dispersion techniques are electrostatic stabilization, steric stabilization, and electrosteric stabilization. The last technique is a combination of the two former dispersion techniques.

Electrostatic stabilization is probably the easiest and most practical dispersion technique for nanopowders and the most common solvent is water. When dispersed in aqueous media, powders will have a hydroxylated surface. Most metals or non-oxide ceramics will have at least a thin oxide layer at the surface, which will become hydroxylated when dispersed in water.

At a certain pH, known as the isoelectric point (IEP), there will be a zero net charge at the shear plane of a hydroxylated particle as a result of the interaction between the hydroxylated surface and contact solution. The shear plane is the boundary between immobilized contact solution molecules around a particle and those that are part of the solvent bulk and free to move about. Instead of acidic and basic being defined as less than or greater than seven, respectively, they will be defined as being less than or greater than the IEP, respectively, according to the preferential absorption or desorption of H^+ ions. Acidic conditions cause preferential absorption of H^+ and the surface to become OH^- terminated. Conversely, basic conditions causes preferential desorption of H^+ and the surface becomes O^- terminated. By controlling the pH, the surface charge and potential can be varied.

The Guoy–Chapman theory describes how a charged surface of a particle interacts with potential determining ions in solution. We can use this theory to calculate how ionic concentrations vary with distance in solution to create a decaying potential. As two particles with decaying surface potentials come in close proximity to each other, the overlapping potentials can generate repulsion between the particles.

The combination of attractive and repulsive energies for a given geometry and dispersion system leads to the DLVO equation. For two identically sized interacting spheres for which electrostatic stabilization is applicable, the DLVO equation is:

$$V_T(h) = V_{att}(h) + V_{rep}(h) = \pi R\left(\frac{H_{121}}{12\pi}\frac{1}{h} + \frac{64c_{Io}^{*}kT\Gamma_o^2\exp(-\kappa h)}{\kappa^2}\right) \tag{2}$$

where $V_T(h)$ is the total interaction energy, $V_{att}(h)$ is the energy of attraction, $V_{rep}(h)$ is the energy of repulsion, h is the sphere separation distance (for spherical particles), R is the radius of the spheres, H_{121} is the Hamaker constant, $c_{Io}{*}$ is the ion concentration with no surface potential, T is the temperature, Γ_o is the Guoy–Chapman coefficient, and κ is the inverse Debye length.

The DLVO equation can be used to determine the conditions for which particles can be dispersed by creating a secondary energy minimum for which there is a barrier for coagulation. Under proper conditions, the agglomerates can be prevented from flocculating, but improper conditions lead to slow flocculation or rapid flocculation when the barrier to coagulation is eliminated completely, by reducing V_{rep}. In practice, the ability for a system to do this is measured by performing a dispersion study. The dispersion can be evaluated using zeta potential measurements and viscosity measurements. A dispersed system can be expected to have a high zeta potential and low viscosity compared to a similar system that is not dispersed or for which flocculation occurs.

There are circumstances in which the energy barrier to coagulation can be overcome, causing flocs to form via flocculation. Increased temperature (thermal energy greater than the barrier for coagulation) can induce coagulation and flocculation. Compression of the electrical double layer around a particle due to significantly high counterion concentrations can also be the cause of coagulation and flocculation.

An example of using viscosity measurements to evaluate dispersion is provided for the slip casting and pressureless sintering of yttria-stabilized zirconia [99]. In this work, a reduction in viscosity was observed with increasing dispersant, associated with dispersion of agglomerates, followed by a minimum in viscosity and an increase in viscosity with further additions as a result of coagulation and flocculation. The researchers used this information to effectively slip cast components and sinter to 99 % density with an average grain size of approximately 120 nm despite the long 60 h dwell time. From the transmission electron micrograph provided in their work, the crystallite sizes of the powders prior to sintering were less than 10 nm and the agglomerate shown in the micrograph was approximately 50 nm in size. The reported surface area was 37 m^2/g. Their dispersion information is given in weight percentage, although it might be more useful to normalize the dispersant amount to the surface area of the powder so that it can be applied to similar powders with a different surface area.

Steric stabilization is another method for preventing particles from forming agglomerates. In this method, a polymer is absorbed on the surface of a particle. Ionic polymers can be chemisorbed to oppositely charged surfaces via ionic bonding or non-ionic polymers can be physisorbed via Van der Waals forces. The polymers on the surface act as physical barriers that prevent the particles from getting close enough to agglomerate. However, entanglement of polymer chains can also lead to agglomeration. One method that can be used to prevent entanglement and further enhance dispersion is known as electrosteric stabilization in which the polymer has multiple dissociation sites along the polymer chain adding an additional electrostatic effect.

Steric and electrosteric stabilization techniques are not preferred for nanopowders. Due to the high surface area of nanopowders, relatively large quantities of polymer are necessary to cover the surfaces of the particles. These polymers must be removed before sintering occurs, which presents some difficulties.

Even electrosteric stabilization has its difficulties. For instance, it was found that the electrokinetic behavior of barium titanate nanopowders was extremely variable [65]. It was very difficult to develop a significant zeta potential at any pH for commercial nanopowders and left in the as-received condition. However, a significant positive zeta potential could be obtained by treating with hydrogen peroxide and a significant negative zeta potential could be obtained by treating with hydrochloric acid. The differences were related to the surface state of the particles. This research highlights two important features. First, that the surface state of a nanopowder can have a significant impact on agglomeration/dispersion characteristics that the DLVO model does not account for and second that zeta potential measurements are useful, if not a necessary tool, for evaluating nanopowder dispersion so that agglomeration can be eliminated or controlled.

5.4 Aggregates Form from "Hard Agglomeration"

Agglomeration is required for aggregation so the two are intimately linked. Aggregates are distinguished by the strong chemical bonds that hold the primary particles together, which make them very difficult to disperse. Therefore, aggregation should be avoided, if at all possible. To avoid aggregation, it is important to understand the mechanisms by which aggregation occurs and this section will cover a few of these mechanisms. If aggregation cannot be avoided, then comminuting or chemical etching are possible techniques for breaking the aggregates to improve the sintering behavior of nanopowders.

Agglomeration can lead to aggregation in several instances. For synthesis in the vapor phase, where the tendency for agglomeration is high (especially at elevated temperatures), the probability of the gas phase reactants condensing at particle contacts or in neck regions is more favorable than elsewhere on the particle surfaces due to the high curvature at the contact points. Similarly, for synthesis in a liquid phase, precipitation of reactants from the liquid phase is more likely to condense at particle contacts. Evaporation/condensation or dissolution/precipitation can also result in aggregation of particles if they are already agglomerated. To minimize aggregation, evaporation/condensation or dissolution/precipitation reactions must be carefully controlled.

When working with aqueous solutions, nanopowders can become hydroxylated. Particle aggregation can occur from agglomerates having hydroxylated surfaces by a dehydration reaction during calcining [100]. Specifically, a dehydration reaction of two hydroxyl groups from different particles can free a water molecule and create a strong bridging oxygen bond between the two particles, as illustrated in Fig. 8 for the formation of zirconia. Most precipitation processes for the formation of oxides result in hydroxide powders and must be calcined. Thus, in most cases the powders are aggregated via this mechanism.

Other surface functional groups can react to form free molecules of hydrochloric acid, alcohols, acetic acid, etc. Reactions releasing other molecules besides water are

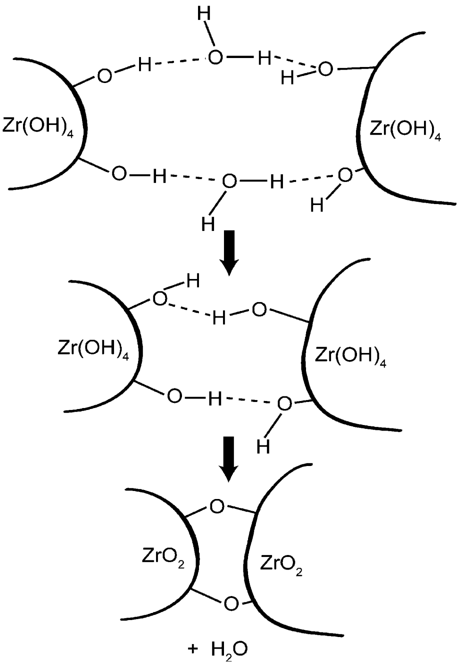

Fig. 8 Aggregation mechanism during calcination of zirconium hydroxide to form zirconium oxide

known as condensation reactions. Acids and bases are capable of catalyzing condensation reactions, so pH of a solution can be an important variable for aggregation. Ions in electrolyte solution can also act to catalyze condensation reactions.

Another mechanism for aggregation arises during the drying process. At particle–particle contacts, there is a capillary force that can retain water at temperatures that are greater than the vaporization temperature of the solvent. The persistence of the solvent in capillaries can retain and concentrate small amounts of salts that were present in the solvent before evaporation. Even small amounts of dissolved salts can have significantly high concentrations when water is eliminated in all but the capillaries of a nanopowder. As liquid is removed and the solubility limit of the salt is exceeded, salt bridges can form in the capillaries of particle contacts to form solid-mass bridges between the particles.

It may be impossible to avoid aggregation in some synthesis or post-synthesis processes. Comminuting is a common physical method for breaking aggregates. However, recall that a large portion of energy is expended deforming or dispersing agglomerates, which is then unavailable for breaking aggregates. Therefore, care should be taken to disperse agglomerates for efficient reduction of aggregation. Also comminuting is susceptible to contamination from the media, particularly if high-energy milling is used. One example of improved sintering due to high-energy planetary milling has been shown for the sintering of alumina nanopowders [101]. The researchers observed a 15 % improvement in the green density for the milled powders compared to untreated powders. Corresponding sintered density was also improved and fully dense specimens were obtained.

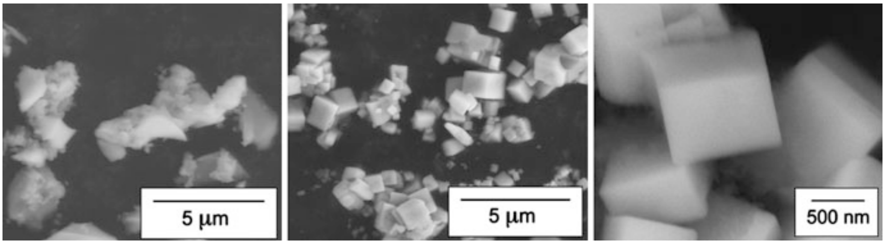

Fig. 9 Scanning electron micrograph of LaB_6 powders prepared by a solution combustion process

Chemical methods can be used to break up aggregates as well. It is necessary to etch the neck regions of a nanoparticle to use this method effectively. This is best demonstrated by considering a salt-bridge between nanopowders. Redispersing nanopowders with salt-bridge aggregates can dilute and eliminate salts by repetitive rinsing. If the salt is eliminated, it cannot redeposit into the neck regions of agglomerated powders during drying. This argument can be extended to nanoparticles having a different surface phase, like a non-oxide with oxide surfaces that become aggregated. Chemical dissolution of the oxide, without dissolving the non-oxide, can eliminate the aggregation of the non-oxide powders. An example of this can be seen for the case of the dissolution of $LaBO_3$ from the surfaces of LaB_6, leading to square like morphologies after surface cleaning with HCl and H_2SO_4 (Fig. 9). Previous to the surface-etching step, the powders had about 3 mol % $LaBO_3$ and the morphology was as illustrated on the left-hand side of Fig. 9. As can be seen, the powders were significantly aggregated, as expected for powders prepared using a combustion process. The acid cleaning step is effective in removing oxide impurities from the surfaces of the powders and for elimination of the aggregates (Fig. 9, middle and right-hand side images).

For single-phase primary particles in an aggregate, chemical etching can still be used to eliminate aggregates in an appropriate solvent. A solvent will attack areas of highest curvature first, such as a particle neck. Slow crack-growth of ceramics or glasses in water is a well-studied example demonstrating this potential and may serve as inspiration for developing such techniques. However, this method does not come without difficulties. Re-precipitation can have an opposite effect, causing aggregation, if the etching process is not carefully controlled. Again here, we can show as an example (Fig. 10) that if the LaB_6 powders from Fig. 9 are etched for an extended period of time, the powders suffer from a re-precipitation process that eliminates all signs of the cubic morphology and aggregates the particles into larger sizes.

5.5 *Particle-Size Distribution*

The particle size distribution is also of importance during sintering. Having a particle size distribution instead of a monodisperse powder can typically help achieve better

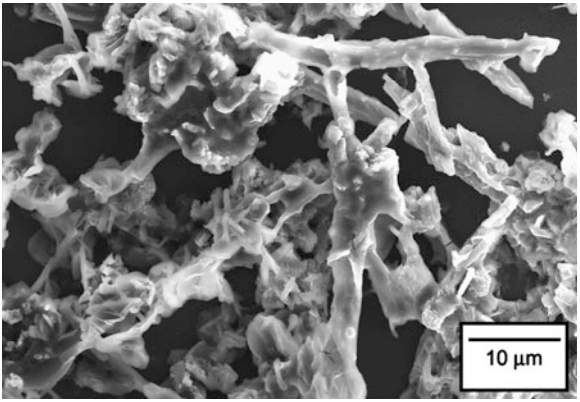

Fig. 10 Scanning electron micrograph of LaB_6 powders etched in acid for a very extended period of time, resulting in a reprecipitation process that completely eliminates the original morphology [27]

green densities and uniform shrinking during sintering. On the other hand, too large of a distribution, particularly if there is a long upper-tail in the particle size distribution or a secondary mode at larger particle sizes can have significant consequences for grain growth. This section will highlight some literature demonstrating a few effects that particle size distribution can have on sintering.

The particle size distribution on the microstructural evolution during the intermediate stage of sintering has been evaluated for alumina powders [102]. It was found that the evolution of pore-channels was influenced by the particle-size distribution due to the effects of pore-channel pinch off. More specifically, it was determined that a compact with finer size and uniform particle size distribution prolonged the intermediate stage of sintering and helped inhibit grain growth due to the pinch-off of pore channels occurring at a higher critical density.

The sintering of alumina was also evaluated to test a model for the effect of particle size distribution and its effect on grain growth [103, 104]. The model predicts that the densification rate depends on the width of the particle size distribution, but the dependency on the width also depends on grain growth. Without grain growth, there is an increase in the densification rate as the particle size distribution is widened. However, this only occurs up to a finite width, after which further increase in the particle size distribution results in decreased densification rate, suggesting an optimum width to the particle size distribution. While grain growth is occurring, the densification rate is decreased with increasing width in the particle size distribution. The densification rate during grain growth is important and modeling and experimental evidence indicates that powders with a narrow size distribution are preferable for minimizing grain growth of the final sintered specimen. These results agree well with more recent modeling and experimental work that showed polydispersity enhances particle rearrangement, but the densification rate declines significantly with the width of the distribution [105]. The overall behavior was independent of whether the distribution was bimodal or lognormal.

From the discussion so far, the ideal powders for achieving improved sintering behavior have a fine particle size with a narrow particle size distribution. Although in some cases, it may be beneficial to have a wide particle size distribution. For a wide particle size distribution was useful for creating a functionally graded porous ceramic without warping or cracking during sintering due to differential shrinkage [106]. The wide particle size distribution of a given layer provided overlap of distribution with adjacent layers, homogenizing local sintering characteristics and facilitating non-warped specimens.

6 Morphology

It may be possible to alter particle morphology by varying synthesis conditions. Various terms can be used to describe particle morphology and they are typically of a qualitative nature: spherical, faceted, cubic, equiaxed, platelets, elongated, needles, fibers, etc. From a sintering standpoint, spherical particles are ideal for achieving highly dense specimens. High green densities can be achieved for particles having a spherical morphology. Furthermore, most models and characterization techniques work under the assumption that the particles are of spherical morphology. The morphology of the particles will also dictate the pore-channel morphology, which can be important in the early stages of sintering.

It may be useful to use a non-spherical morphology for sintering a porous material. The lower green density, limitation of particle–particle contacts, and pore-channel morphology can significantly hinder densification to assist in achieving high levels of porosity. Flat surfaces from various types of morphologies, such as platelets or cubes, will have a lower driving force for sintering due to the lack of curvature. Although one may not be intentionally trying to alter morphology, it is an important variable with respect to sintering behavior and one should at least be aware of what the powder morphology is for a given set of sintering experiments.

7 Forming Techniques and Drying Processes

One of the biggest issues with processing of nanopowders is associated with forming them into a useful shape. It is at this stage that problems may first become apparent on a macroscale. Parts may begin to warp or crack, for instance. This may lead one to think that it is the forming and drying processes or the sintering processes that are causing problems, but in many cases the problems are a result of the powder characteristics. To understand how to approach the problem of forming nanopowders, it may be useful to understand the optimization of forming techniques in general. The rest of this section will be focused on desirable powder characteristics for a particular forming process.

It does not make sense to discuss one or another synthesis process that is more suitable for obtaining the powder characteristics necessary for excellent forming and drying characteristics. This is because the powder characteristics for forming are typically achieved by post-synthesis processing, such as breaking of aggregates, adequately redispersing the powders, and controlling the agglomerate size for the forming process. However, the powder characteristics at the end of the synthesis process will dictate the post-synthesis processing that will be necessary to obtain the powder characteristics that will be necessary for sintering.

Common forming methods include pressing (uniaxial, isostatic, etc.), plastic forming (extrusion, injecting molding, etc.), and casting (slip casting, gel casting, pressure casting, tape casting, etc.). Each forming technique requires stringent control of the feed material and often requires additives to get suitable forming characteristics. Such additives include solvents, binder, plasticizer, dispersant, coagulants, lubricants, defoamers, and bactericides, for example. Such additives must be removed prior to sintering with drying and thermal or chemical treatment. Obtaining the correct forming characteristics, as well as removing additives from a system when using nanopowders, proves to be a difficult challenge.

A general review of pressing techniques, such as dry pressing and cold isostatic pressing, can be found in the Engineered Materials Handbooks that are published by ASM International [107, 108]. Critical steps include die filling, compaction, and removal of a pressed piece. From the very beginning of the process, the powder characteristics are critical. The powder must flow readily for achieving uniform die fill and optimal performance in later stages of pressing. Spherical agglomerates having high interagglomerate density and in the size range of 40–200 μm are desirable. The presence of excessive amounts of fine powders inhibits flow and gives poor filling characteristics. Under ideal conditions, the die fill will result in a fill density of at least 20–35 %. The flow characteristics can be evaluated by tap density measurements. Vibration may also be used to improve fill characteristics, but vibration can also lead to particle size segregation (larger particles will segregate upwards while fines will segregate downward).

Once a die is properly filled and the pressing begins, the green density is improved by the application of pressure. In the initial stage of pressing, the density is improved by particle sliding and rearranging of the agglomerates. This is known as transitional restacking and occurs for pressures up to about 10 MPa. As higher pressure is applied, the compact generates considerable resistance. Deformation, compaction, crushing, and fragmentation of the agglomerates occur to further improve the green density. Void spaces persist, but begin to be filled during this process. The primary particles play an important role at this point. They should not be aggregated so that they can slide relative to each other. The smaller the primary particle size is, the more resistance to deformation due to high Van der Waals attractive forces between the particles. Proper additives can help achieve lower friction between the particles to assist deformation and rearrangement of the agglomerates to fill the vacant spaces in the compact. After most of the spaces between the agglomerates become filled, the remaining compaction process is by bulk compression. Depending on the nature of the material being pressed, fragmentation of the primary particles may also improve the green density. It is at pressures of 50–200 MPa, depending on the material, that the green density will begin to approach theoretical values and the green density uniformity is either at its best or worst depending on how well the powders were prepared beforehand. Spray drying is the usual method for properly engineering agglomerates for a pressing process [109].

Casting methods require a slip of specific characteristics and control of the colloidal powders in the slip is an important aspect to successful casting [110, 111]. The dispersion of the slip is a critical step for achieving the highest green bulk density with good uniformity. The uniformity is important for preventing warping and distortion during drying or sintering. Full dispersion can result in excessively long casting times due to a low transfer of liquid through the cast layer. A small amount of controlled flocculation due to under-dispersion, can assist in achieving an optimum balance between a uniform microstructure and reasonable casting times. However, excessive agglomeration can produce spatial variations in the green density that will lead to warping or cracking. In slip casting, the control over the rheology of the slip is a critical indicator of both dispersion and casting performance. Control of particle–particle interactions in a fluid responsible for agglomeration and dispersion are critical for obtaining high solids content with appropriate rheology. With improper dispersion (leading to large agglomerates) or if large aggregates are present, settling may occur and result in localized thickness and density variations that can lead to cracking or warping.

Besides the solid-forming and liquid-forming techniques discussed, extrusion and injection molding are useful for ceramic systems that can be made to behave plastically during extrusion or injection [112, 113]. These systems represent some of the most challenging processes to optimize. They require high contents of binder(s) and plasticizer(s) to make them plastic and to perform adequately. The powders must be highly dispersed in the plastic body, which requires high shear mixing with sufficient shear stress and continual change in flow pattern to eliminate the agglomerates and achieve homogenous particle packing. Cracks, which can be observed in green compacts using non-destructive evaluation techniques, are the most difficult problem for these processes. The cracks are believed to form due to localized stress concentrations as a result of uneven packing. The non-uniform packing results in density variations due to non-uniform shrinking during further processing. Removal of the additives, which are in large quantities for these processes, is also a difficult challenge. Thermal or chemical methods can be used to remove the additives, but surface tension and capillary forces can generate warpage or cracking. Supercritical extraction is an attractive method for removing additives without disrupting the structure. Supercritical fluids have diffusion coefficients similar to gas with solubility similar to the liquid state. This helps avoid capillary attraction and irregular rearrangement of packed particles that may lead to problems. This can be extended to drying processes in general, rather than slow and lengthy drying for parts that are susceptible to such kind of damage.

A common attribute of each forming technique is that the control of agglomeration and aggregation is necessary for all of them. The difficulty of using nanopowders is the increasing difficulty to control aggregation and agglomeration due to the higher surface area-to-volume ratio of the primary particles as the primary particle size decreases, which causes them to have a higher tendency for agglomeration and more difficulties avoiding aggregation or eliminating aggregation when it cannot be initially avoided. Most additives are surface active and therefore higher amounts are necessary, representing additional challenges when it is time to remove these additives. It also becomes increasingly difficult to obtain high solids loadings and maintain the necessary rheology for nanopowders in suspension. This can lead to less-than-ideal green densities. Traditionally, high green densities are sought because this means the particle packing in the green body is uniform and minimal shrinkage will occur during sintering.

While high green density helps with sintering, it is not absolutely necessary. Slip casting, which benefits from powders being slightly flocculated, is a testament to this. More important than a high green density is a uniform microstructure such that uniform shrinkage occurs. Differential shrinkage as a result of non-uniformity can cause stress development that may lead to warpage or cracking. The problem is that the more a part has to shrink to become fully dense (i.e., the lower the green density), the less tolerance there is for non-uniformity. Once a portion of the green compact shrinking away from adjacent material introduces a flaw, it will continue to grow upon further shrinkage. If it does not grow to the point of failure in the green compact, it can still grow to failure in the sintering process. Or worse, the sintered specimen could fail prematurely during application.

Although forming, drying, and sintering of nanopowders presents a difficult challenge due to the increased difficulty in obtaining suitably controlled powders, it is comforting to know that it is not impossible. Many years of research have gone into understanding how to properly form and sinter nanopowders, so we should not expect to solve all of the nanosintering problems overnight. There is still much work to be done. Several companies have spent years to develop innovative solutions to overcome such difficulties. For example, Evonik Degussa GmbH has more than 30 patents to protect their SiVARATM sol–gel technology. Their sol–gel technology utilizes dispersed nanopowders of silica to make an aerogel. A solvent exchange process replaces water with ethanol, which is then removed under supercritical conditions. Calcination, purification, and sintering are done at various temperatures under three different atmospheric conditions. Despite the low green density and high shrinkage ($\sim$50 %), the uniformity of the green specimens result in isotropic densification that allows a precise and predictable final shape with unprecedented tolerance that conventional techniques obtain only after expensive treatments or polishing. The key to the success of this process is materials processing that results in uniformity of the green structure to produce uniform shrinkage during the sintering process.

Unfortunately, laboratory-scale activities do not always allow the necessary efforts to work out all of the specifics for a given synthesis method and subsequent processing to obtain fully dense specimens from nanopowder compacts. In situ pressure-assisted techniques such as hot isostatic pressing (HIP), hot pressing (HP), and spark plasma sintering (SPS) are more forgiving sintering processes with respect to the state of the green compact because the heat allows for the redistribution of stresses through deformation. These techniques can help eliminate otherwise persistent porosity. However, HIP and HP processes are still slow high-temperature processes that allow grain growth. Electric current/pressure assisted sintering, such as SPS, is a very attractive technique for sintering of nanopowders while maintaining a nanostructure because of the fast sintering times and relatively low level of powder preparation for successful sintering [114].

7.1 Green-Body Microstructure

The prior section has discussed the importance of the forming processes and drying of a nanopowder compact. The conditions of the powder being formed and the forming parameters will dictate both the green density and the nature of the porosity. Density and porosity are intimately related. Even if theoretical green densities are achieved, based on packing efficiencies, there will still be a significant amount of porosity in the green compact. Achieving high uniformity in the green-body microstructure is more important than the ultimate green-body density. This section will focus further on the importance of the uniformity of the green-body by describing some of the causes and consequences of pore size distributions in the green body.

7.1.1 Inter Versus Intra Particle Porosity

One of the major causes of a non-uniform microstructure in a compact is the result of inter- versus intra-particle porosity. An agglomerate or aggregate will have a certain level of porosity between the primary particles that will depend on the conditions under which the agglomerate or aggregate formed. If they form from a dispersed state, then the agglomerates or aggregates should have relatively large packing density with low and uniform porosity. If the agglomerates or aggregates form under non-dispersed conditions, then they may or may not have uniform porosity within them and the overall packing density will be lower. Therefore, it is important to limit aggregation and control agglomeration to obtain a uniform agglomerate structure. Uniform porosity and lower density particles can be favorable for sintering depending on intra-particle porosity resulting from the forming process. The key to efficient processing and forming of a nanopowder compact is to obtain microstructural uniformity. This correlates to conditions in which inter- and intra-particle porosities are similar.

7.1.2 Pore Size and Pore-Size Distribution

Just as particle size and particle size distribution have an impact on the sintering behavior, it should be expected that the pore size and pore size distribution comprising the voids between the particles should also be an important feature. Porosity can be used to complete the picture that has been described for explaining faster inter-particle densification versus intra-particle densification. Like large grains growing at the expense of finer grains, large pores can grow or be sustained during densification by the elimination of small pores. Large pores are more persistent in the microstructure, making them difficult to remove.

7.2 Tying It Together

Although the last two sections separate pore size and particle size effects, it is interesting to note that the size distribution of particles or the pores alone do not correlate so well with the casting conditions (flocculated or dispersed) on densification during sintering [115]. Rather, the effects seem to be related to the localized spatial arrangement of both grains and pores, or homogeneity/heterogeneity in the microstructure as densification occurs, as has been stressed conceptually throughout earlier sections of this chapter. McAfee and Nettleship [115] found that although the end result of sintering two green bodies was somewhat similar, the path by which the two systems arrived there was quite different and accounts for the differences in densification rate that was observed in their study and subtle microstructural differences. Densification in the intermediate stage of sintering for the dispersed sample progressed by pore shrinkage as a result of isotropic densification whereas the flocculated sample progressed by both pore shrinkage and pore breakup (due to anisotropic shrinkage). After this stage, final-stage sintering occurred via similar mechanisms for the two different systems. The primary difference then is the homogeneity or heterogeneity of the green-body microstructure.

A similar approach in showing the effects of microstructural heterogeneity may help establish the conditions for which flaw development, stress development, and failures during sintering occur as a result of accommodating the break-up of the inter-agglomerate pore channel during sintering of heterogeneous microstructures. In McAfee and Nettleship's work, densities greater than 96 % were not achieved. The large inter-particle porosity was persistent and supports the notion that ideal conditions result from uniform intra- and inter-particle porosity such that isotropic elimination of the pores can lead to full density.

A method for quantifying heterogeneities during the intermediate stages of sintering has been presented recently [116]. A key feature of the results is that the area fraction of dense heterogeneities and the largest heterogeneity in the size distribution were appreciably higher for pressed material (not granulated) in comparison with slip cast materials (flocculated and dispersed) made from the same batch of powder. This suggests that agglomeration is an important feature in controlling the microstructural heterogeneities as the tendency for agglomeration is expected to be worse for the powders in the dry state versus the wet state (i.e., pressed versus slip cast) and worse for flocculated versus a dispersed state when slip casting.

8 Summary

Obtaining a fully dense sintered compact relies on the formation of a uniform green body using appropriate forming conditions. To achieve this, aggregation should be eliminated and agglomeration of the powders should be controlled. The tendency for agglomeration is going to be dictated by the crystallite size and the surface state of the crystallites. The surface state will lead to the incorporation of surface impurities during the synthesis method and subsequent post-synthesis processing steps, of which non-detrimental impurities are desired. The impurities that are present in a powder can result from decisions as early as precursor selection for the synthesis process.

Not until more systematic research is performed will the exact contributions of each effect be decoupled because all of the features are often intimately intertwined. Attempting to change one aspect of powder synthesis might have a profound effect on several aspects of the powder characteristics. Then, the sintering behavior cannot be attributed to any one of these characteristics alone. Once this is possible, then we may be able to reconcile two synthesis methods to show that it is not the synthesis method that affects nanosintering, but that it is the powder characteristics. This notion suggests that better post-synthesis processing to achieve optimal powder characteristics is necessary and that the synthesis method should only dictate what post-synthesis processing is necessary to achieve adequate powder characteristics.

Acknowledgments This chapter was written with support from the National Science Foundation under grant DMR 0503017.

References

1. Edelstein, A.S., Cammarata, R.C.: Nanomaterials: Synthesis, Properties and Applications. Taylor and Francis Group, New York (1996)
2. Pokropivny, V.V.: Powder Metall. Met. Ceram. **40**, 485–496 (2001)
3. Cao, G.: Nanostructures and Nanomaterials: Synthesis, Properties and Applications. Imperial College Press, London (2004)
4. Shankar, K.S., Raychaudhuri, A.K.: Mater. Sci. Eng. **C 25**, 738–751 (2005)
5. Sergeev, G.B.: Nanochemistry. Elsevier, Amsterdam (2006)
6. Yoshimura, H.: Colloids Surf. A **282**, 464–470 (2006)
7. Vollath, D.: Nanomaterials: An Introduction to Synthesis, Properties and Applications. Wiley-VCH, Weinheim (2008)
8. Ashby, M.F., Ferreira, P.J., Schodek, D.L.: Nanomaterials, Nanotechnologies and Design: An Introduction for Engineers and Architects. Butterworth-Heinemann, Burlington (2009)
9. Wu, B., Kuang, Y., Zhang, X., Chen, J.: Nano Today **6**, 75–90 (2011)
10. Kannan, N., Subbalaxmi, S.: Rev. Adv. Mater. Sci. **27**, 99–114 (2011)
11. Chawla, V., Prakash, S., Sidhu, B.S.: Mater. Manuf. Process. **22**, 469–473 (2007)
12. Reed, J.S.: Principles of Ceramic Processing. Wiley, New York (1995)
13. Rahaman, M.N.: Ceramic Processing. CRC Press, Boca Raton (2007)
14. Stokes, R.J., Evans, D.F.: Fundamentals of Interfacial Engineering. Wiley-VCH, New York (1997)

15. Yang, X.C., Riehemann, W., Dubiel, M., Hofmeister, H.: Mater. Sci. Eng. **B 95**, 299–307 (2002)
16. Semaltianos, N.G.: Crit. Rev. Solid State Mater. Sci. **35**, 105–124 (2010)
17. Huang, J.Y., Liao, X.Z., Zhu, Y.T., Zhou, F., Lavernia, E.J.: Philos. Mag. **83**, 1407–1419 (2003)
18. Stranz, M., Koster, U.: J. Mater. Sci. **39**, 5275–5277 (2004)
19. Lavernia, E.J., Han, B.Q., Schoenung, J.M.: Mater. Sci. Eng. A **493**, 207–214 (2008)
20. Vogt, R.G., Zhang, Z., Topping, T.D., Lavernia, E.J., Schoenung, J.M.: J. Mater. Process. Technol. **209**, 5046–5053 (2009)
21. Mandzy, N., Grulke, E., Druffel, T.: Powder Technol. **160**, 121–126 (2005)
22. Fazio, S., Guzman, J., Colomer, M., Salomoni, A., Moreno, R.: J. Eur. Ceram. Soc. **28**, 2171–2176 (2008)
23. Chung, S.J., Leonard, J.P., Nettleship, I., Lee, J.K., Soong, Y., Martello, D.V., Chyu, M.K.: Powder Technol. **194**, 75–80 (2009)
24. Adair, J.H., Kerchner, J.A., Bell, N.S., Carasso, M.L.: Application of chemical principles in the solution synthesis and processing of ceramic and metal particles. In ACS Symposium Series, Washington, DC (1997)
25. Aruna, S.T., Mukasyan, A.S.: Curr. Opin. Solid State Mater. Sci. **12**, 44–50 (2008)
26. Patil, K.C., Aruna, S.T., Mimani, T.: Curr. Opin. Solid State Mater. Sci. **6**, 507–512 (2002)
27. Kanakala, R., Escudero, R., Rojas-George, G., Ramisetty, M., Graeve, O.A.: ACS Appl. Mater. Interf. **3**, 1093–1100 (2011)
28. Kanakala, R., Rojas-George, G., Graeve, O.A.: J. Am. Ceram. Soc. **93**, 3136–3141 (2010)
29. Lopez, O.A., McKittrick, J., Shea, L.E.: J. Lumin. **71**, 1–11 (1997)
30. Shea, L.E., McKittrick, J., Lopez, O.A., Sluzky, E.: J. Am. Ceram. Soc. **79**, 3257–3265 (1996)
31. Kumar, M., Ando, Y.: J. Nanosci. Nanotechn. **10**, 3739–3758 (2010)
32. Campbell, S.A.: Mater. Sci. Eng. **R 20**, 1–36 (1997)
33. Lee, D.-W., Tolochko, O.V., Turaev, F.R., Kim, D., Kim, B.-K.: J. Nanosci. Nanotechn. **10**, 349–354 (2010)
34. Choi, Y.J., Choi, J.W., Sohn, H.Y., Ryu, T., Hwang, K.S., Fang, Z.Z.: Int. J. Hydrogen Energy **34**, 7700–7706 (2009)
35. Reuge, N., Bacsa, R., Serp, P., Caussat, B.: J. Phys. Chem. **C 113**, 19845–19852 (2009)
36. Ahmad, M.I., Bhattacharya, S.S., Fasel, C., Hahn, H.: J. Nanosci. Nanotechnol. **9**, 5572–5577 (2009)
37. Bacsa, R.R., Dexpert-Ghys, J., Verelst, M., Falqui, A., Machado, B., Bacsa, W.S., Chen, P., Zakeeruddin, S.M., Graetzel, M., Serp, P.: Adv. Funct. Mater. **19**, 875–886 (2009)
38. Choi, J.W., Sohn, H.Y., Choi, Y.J., Fang, Z.Z.: J. Power Sources **195**, 1463–1471 (2010)
39. Komoda, H., Mori, T., Kominami, H., Nakanishi, Y., Hara, K.: J. Cryst. Growth **311**, 2966–2969 (2009)
40. Ryu, T., Sohn, H.Y., Hwang, K.S., Fang, Z.Z.: Int. J. Refract. Met. Hard Mater. **27**, 149–154 (2009)
41. Jin, W., Lee, I.-K., Kompch, A., Doefler, U., Winterer, M.: J. Eur. Ceram. Soc. **27**, 4333–4337 (2007)
42. Schmitt, A.L., Higgins, J.M., Jin, S.: Nano Lett. **8**, 810–815 (2008)
43. Park, H., Jie, H., Chae, K.-H., Park, J.-K., Anpo, M., Lee, D.-Y.: Curr. Appl. Phys. **8**, 778–783 (2008)
44. Saterlie, M.S., Sahin, H., Kavlicoglu, B., Liu, Y., Graeve, O.A.: Nanosc. Res. Lett. **6**, 217 (2011)
45. Graeve, O.A., Madadi, A., Kanakala, R., Sinha, K.: Metall. Mater. Trans. A. **41A**, 2691–2697 (2010)
46. Sinha, K., Pearson, B., Casolco, S.R., Garay, J.E., Graeve, O.A.: J. Am. Ceram. Soc. **92**, 2504–2511 (2009)
47. Xia, Y., Xiong, Y., Lim, B., Skrabalak, S.E.: Angew. Chem. Int. Ed. **48**, 60–103 (2009)
48. Lu, X., Rycenga, M., Skrabalak, S.E., Wiley, B., Xia, Y.: Chemical synthesis of novel plasmonic nanoparticles. Annu. Rev. Phys. Chem. **60**, 167–192 (2009)

49. Bittner, A.M.: Surf. Sci. Rep. **61**, 383–428 (2006)
50. Chenjie, X., Shouheng, S.: Polym. Int. **56**, 821–826 (2007)
51. Weeber, A.W., Bakker, H.: Phys. B **153**, 93–135 (1988)
52. Koch, C.C.: Scripta Mater. **34**, 21–27 (1996)
53. Tang, J., Zhao, W., Li, L., Falster, A.U., Simmons, W.B., Zhou, W.L., Ikuhara, Y., Zhang, J.H.: J. Mater. Res. **11**, 733–738 (1996)
54. Huang, J.Y., Yasuda, H., Mori, H.: J. Am. Ceram. Soc. **83**, 403–409 (2000)
55. Macwan, D.P., Dave, P.N., Chaturvedi, S.: J. Mater. Sci. **46**, 3669–3686 (2011)
56. Chander, H.: Mater. Sci. Eng. R **49**, 113–155 (2005)
57. Sternitzke, M.: J. Eur. Ceram. Soc. **17**, 1061–1082 (1997)
58. Singh, A., Harimkar, S.P.: J. Alloys Compd. **497**, 121–126 (2010)
59. Singh, H., Graeve, O.A.: Reverse micelle synthesis of zirconia powders: the use of hydrogen peroxide as washing solvent, In: Materials research society, pp. Z10.28.11–Z10.28.16 (2005)
60. Fang, Y., Cheng, J.P., Agrawal, D.K.: Mater. Lett. **58**, 498–501 (2004)
61. Graeve, O.A., Kanakala, R., Kaufman, L., Sinha, K., Wang, E., Pearson, B., Rojas-George, G., Farmer, J.C.: Mater. Lett. **62**, 2988–2991 (2008)
62. Kim, C.K., Lee, S., Shin, S.Y., Kim, D.H.: J. Alloys Compd. **453**, 108–114 (2008)
63. Roy, D., Mitra, R., Chudoba, T., Witczak, Z., Lojkowski, W., Fecht, H.J., Manna, I.: Mater. Sci. Eng. **A 497**, 93–100 (2008)
64. Li, Q., Wang, G., Song, X., Fan, L., Hu, W., Xiao, F., Yang, Q., Ma, M., Zhang, J., Liu, R.: J. Mater. Process. Technol. **209**, 3285–3288 (2009)
65. Varela, J.A., Perazolli, L.A., Longo, E., Leite, E.R., Cerri, J.A.: Radiat. Eff. Defects Solids **146**, 131–143 (1998)
66. Mula, S., Mondal, K., Ghosh, S., Pabi, S.K.: Mater. Sci. Eng. A **527**, 3757–3763 (2010)
67. Kim, C.K., Lee, H.S., Shin, S.Y., Lee, J.C., Kim, D.H., Lee, S.: Mater. Sci. Eng. **A 406**, 293–299 (2005)
68. Roy, D., Kumari, S., Mitra, R., Manna, I.: Intermetallics **15**, 1595–1605 (2007)
69. Roy, D., Chakravarty, D., Mitra, R., Manna, I.: J. Alloys Compd. **460**, 320–325 (2008)
70. Sasaki, T.T., Hono, K., Vierke, J., Wollgarten, M., Banhart, J.: Mater. Sci. Eng. **A 490**, 343–350 (2008)
71. Bian, H.H., Kim, D.W., Hong, K.S.: Mater. Lett. **58**, 347–351 (2004)
72. Liao, S.C., Pae, K.D., Mayo, W.E.: Nanostruct. Mater. **8**, 645–656 (1997)
73. Munir, Z.A., Anselmi-Tamburini, U.: Mater. Sci. Rep. **3**, 277 (1989)
74. Merzhanov, A.G.: Ceram. Int. **21**, 371–379 (1995)
75. Liu, J., Yao, W., Kear, B., Mukherjee, A.K.: Mater. Sci. Eng. B **171**, 149–154 (2010)
76. Asp, M., Agren, J.: Acta Mater. **54**, 1241–1248 (2006)
77. Bowman, A.L.: J. Phys. Chem. **65**, 1596 (1961)
78. Kelly, J.P., Graeve, O.A.: J. Am. Ceram. Soc. **94**, 1706–1715 (2011)
79. Talmy, I.G., Zaykoski, J.A., Opeka, M.M.: J. Eur. Ceram. Soc. **30**, 2253–2263 (2010)
80. West, A.R.: Basic Solid State Chemistry. Wiley, New York (1999)
81. Chandrasekhar, S., Pramada, P.N.: Ceram. Int. **27**, 105–114 (2001)
82. Chandrasekhar, S., Pramada, P.N.: Ceram. Int. **27**, 351–361 (2001)
83. Readey, M.J., Readey, D.W.: J. Am. Ceram. Soc. **69**, 580–582 (1986)
84. Karapetrova, E., Platzer, R., Gardner, J.A., Torne, E., Sommers, J.A., Evenson, W.E.: J. Am. Ceram. Soc. **84**, 65–70 (2001)
85. Wang, X.M., Lorimer, G., Xiao, P.: J. Am. Ceram. Soc. **88**, 809–816 (2005)
86. Deptula, A., Lada, W., Olczak, T., Wawszczak, D., Sartowska, B., Goretta, K.C.: Ceram. Int. **33**, 1617–1621 (2007)
87. Bacha, E., Deniard, P., Richard-Plouet, M., Brohan, L., Gundel, H.W.: Thin Solid Films **519**, 5816–5819 (2011)
88. Kovalenko, V.V., Zhukova, A.A., Rumyantseva, M.N., Gaskov, A.M., Yushchenko, V.V., Ivanova, I.I., Pagnier, T.: Sens. Actuators B **126**, 52–55 (2007)
89. Garbassi, F., Melloceresa, E., Occhiello, E., Pozzi, L., Visca, M., Lenti, D.M.: Langmuir **3**, 173–179 (1987)

90. Busca, G., Lorenzelli, V., Bolis, V.: Mater. Chem. Phys. **31**, 221–228 (1992)
91. Castro, R.H.R., Pereira, G.J., Gouvea, D.: Appl. Surf. Sci. **253**, 4581–4585 (2007)
92. Maeland, D., Suciu, C., Waernhus, I., Hoffmann, A.C.: J. Eur. Ceram. Soc. **29**, 2537–2547 (2009)
93. Tanaka, I., Kleebe, H.J., Cinibulk, M.K., Bruley, J., Clarke, D.R., Ruhle, M.: J. Am. Ceram. Soc. **77**, 911–914 (1994)
94. Luo, J.: Curr. Opin. Solid State Mater. Sci. **12**, 81–88 (2008)
95. Herring, C.: J. Appl. Phys. **21**, 301–303 (1950)
96. Mayo, M.J., Hague, D.C.: Nanostruct. Mater. **3**, 43–52 (1993)
97. Yan, M.F., Rhodes, W.W.: Mater. Sci. Eng. **61**, 59–66 (1983)
98. Groza, J.R., Dowding, R.J.: Nanostruct. Mater. **7**, 749–768 (1996)
99. Vasylkiv, O., Sakka, Y.: Scripta Mater. **44**, 2219–2223 (2001)
100. Kaliszewski, M.S., Heuer, A.H.: J. Am. Ceram. Soc. **73**, 1504–1509 (1990)
101. Ferkel, H., Hellmig, R.J.: Nanostruct. Mater. **11**, 617–622 (1999)
102. Shiau, F.S., Fang, T.T., Leu, T.H.: J. Am. Ceram. Soc. **80**, 286–290 (1997)
103. Ting, J.M., Lin, R.Y.: J. Mater. Sci. **30**, 2382–2389 (1995)
104. Ting, J.M., Lin, R.Y.: J. Mater. Sci. **29**, 1867–1872 (1994)
105. Wonisch, A., Kraft, T., Moseler, M., Riedel, H.: J. Am. Ceram. Soc. **92**, 1428–1434 (2009)
106. Darcovich, K., Toll, F., Hontanx, P., Roux, V., Shinagawa, K.: Mater. Sci. Eng. **A 348**, 76–83 (2003)
107. McEntire, B.J.: Dry pressing. In: Engineered Materials Handbook, vol. 4, pp. 141–146. ASM International, Materials Park (1991)
108. Kennard, F.: Cold isostatic pressing. In: Engineered Materials Handbook, vol. 4, pp. 147–152. ASM International, Materials Park (1991)
109. Lukasiewicz, S.J.: Granulation and spray drying. In: Engineered Materials Handbook, vol. 4, pp. 100–108. ASM International, Materials Park (1991)
110. Schilling, C.H, Aksay, I.A.: Slip casting. In: Engineered Materials Handbook, vol. 4, pp. 153–160. ASM International, Materials Park (1991)
111. Mistler, R.E.: Tape casting. In: Engineering Materials Handbook, vol. 4, pp. 161–165. ASM International, Materials Park (1991)
112. Ruppel, I.: Extrusion. In: Engineered Materials Handbook, vol. 4, pp. 166–172. ASM International, Materials Park (1991)
113. Mutsuddy, B.C.: Injection molding. In: Engineered Materials Handbook, vol. 4, pp. 173–180. ASM International, Materials Park (1991)
114. Munir, Z.A., Quach, D.V., Ohyanagi, M.: J. Am. Ceram. Soc. **94**, 1–19 (2011)
115. McAfee, R.J., Nettleship, I.: J. Am. Ceram. Soc. **89**, 1273–1279 (2006)
116. Dengiz, O., McAfee, R., Nettleship, I., Smith, A.E.: J. Eur. Ceram. Soc. **27**, 1927–1933 (2007)

Discrete Element Method Sintering Simulation: A Grain-Scale Simulation Approach

Andreas Wonisch, Tobias Rasp, Torsten Kraft and Hermann Riedel

Abstract The sintering models described in previous chapters consider only a limited number of particles or analytical analyses of sintering, without a close connection to the sintering of large parts. While the previous chapter addressed the serious issues that have to be considered in the "real world" of sintering, great advances have been made on the simulations of sintering of real complex shapes. This chapter addresses simulations based on the Discrete Element Method (DEM), a promising new technique to model sintering by directly taking the microstructure into account. Each grain is modeled as an individual particle which interacts with its neighbors by given force laws that depend on the diffusion mechanisms. In this chapter the grain-scale simulation model is explained in detail and it is shown how it can be used to model sintering of both standard and nanoparticle powders. By directly considering effects like rearrangement, crack formation and anisotropy development new insights into many sintering processes are gained. Especially the influence of grain rearrangement, which cannot directly be considered with traditional continuum mechanical approaches, is studied in detail. As a demonstration example constrained sintering of inkjet printed silver powders is given. Since the method is still relatively new, not all sintering mechanisms are fully considered yet. It is shown how grain coarsening models could be improved by considering the growth process on the grain scale as well.

1 Introduction

An important motivation for developing better sintering models arises from the possibility to simulate industrial sintering processes. Simulation of sintering of real,

---

A. Wonisch (✉) · T. Rasp · T. Kraft · H. Riedel
Fraunhofer Institute for Mechanics of Materials IWM, Freiburg, Germany
e-mail: andreas.wonisch@iwm.fraunhofer.de

R. H. R. Castro and K. van Benthem (eds.), *Sintering*, Engineering Materials 35,
DOI: 10.1007/978-3-642-31009-6_5, © Springer-Verlag Berlin Heidelberg 2013

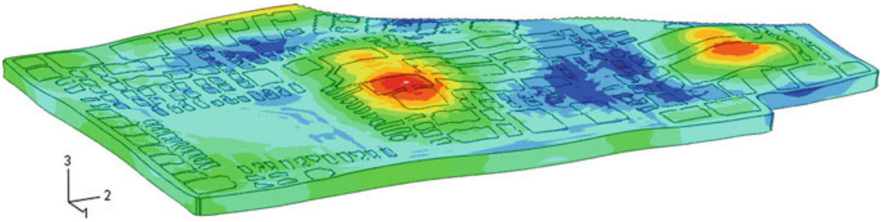

Fig. 1 Deviation of the desired part shape after sintering (plot enhanced)

complex shaped 3-D parts by the finite element method (FEM) has developed to a stage where practical applications can be performed on a daily basis in product development. Typical applications of sinter simulations are, for example, the prediction of warpage due to density inhomogeneity in the hard metal industry [1]. Many other applications have been reported in recent years (e.g. [2, 3]), dealing mainly with predicting the distortion of a single material part. In these applications often quite simple material laws are used, which is justified in many cases e.g. when density gradients are predominant in determining the degree of distortion.

Handling composite materials—either co-fired or post-fired—is much more demanding due to the internal stresses that develop during sintering, which cannot be neglected any more. Here more sophisticated sintering laws must be used in order to model the changing viscosities over time and temperature with sufficient accuracy. If such a model is used together with appropriate model parameters distortion and warpage even in very complex multi-layered structures can be simulated.

A typical example is a ceramic based circuit produced by low temperature co-fired ceramics (LTCC) technology. In this technology, multi-layered thick-film sheets (50–250 μm) or so-called green tapes, which are screen-printed with thick-film pastes such as conductors, resistors, etc. are sintered together. As a demonstration for the present state-of-the-art in sinter modeling, Fig. 1 shows the calculated warpage after firing of a layered LTCC structure. Each of the four ceramic tape layers is individually screen-printed with metallic pastes and subsequently laminated together.

In order to further improve the continuum sinter models used in these finite element calculations and get a deeper understanding of the process, discrete element simulations of sintering are a promising new tool. Going back to the pioneering work of Cundall and Strack who developed the DEM for the study of rock mechanics [4], this simulation technique allows to study sintering on the grain-scale. It takes the granular nature of the material into account by treating every grain as a distinct element (particle). For example, during the initial stages of sintering rearrangement processes take place, which cannot be described adequately by continuum mechanics. Also crack formation or anisotropy development can occur and they also have their origins in microstructural changes that cannot be described with purely continuum mechanical approaches.

In powder technology, the DEM has been adapted only recently, with applications ranging from die filling [5] and power transfer [6] to powder compaction

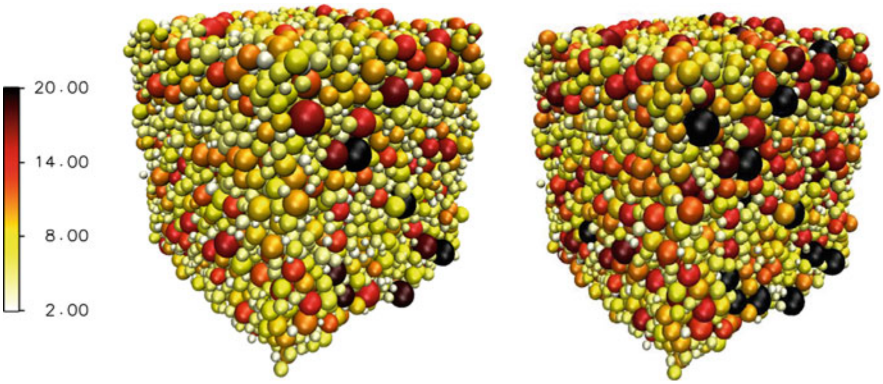

Fig. 2 Representative DEM simulation cell consisting of several thousand particles with different sizes (*left* initial state, *right* at the end of sintering). The colors represent the number of neighbors for each particle

[7]. So far work on sintering has been limited, even though the method shows good promise [8–12]. In this chapter an application of the Discrete Element Method for solid-state sintering is described in detail. It is shown how it can be used to study effects like rearrangement and crack formation. Also applications for sintering processes involving nanoparticles are given.

2 DEM Simulation Method

The DEM simulation method treats individual grains as discrete elements (particles), which interact through mechanical forces with each other. This provides a very realistic microscopic approach. A simulation consists of N randomly distributed particles with a given relative initial density of the powder compact. It is possible to either simulate a complete powder part, consisting of *millions* of individual particles or to use representative periodic cell with several thousand to 10,000 particles (Fig. 2). Using representative cells keeps computational time down, while allowing making predictions about macroscopic properties like densification rate, which depend on microscopic properties.

2.1 Equations of Motion

The particles are described by their number i ($i = 1, N$), their position $\mathbf{r}_i$, velocity $\mathbf{v}_i$, angular velocity $\boldsymbol{\omega}_i$, radius R_i, mass m_i and moment of inertia I_i. For simplicity, spherical particles are assumed (which means that $I_i = 2/5\ m_i R_i^2$), even though non-spherical particles could be simulated as well by combining several particles through rigid body constraints.

In each simulation time step, Δt, first the neighbors of each particle are determined—these are the interacting particles, defined by a previously specified interaction radius r_c (for contact forces $r_c = R_i + R_j$). Then forces between neighboring particles are calculated depending on the sintering force laws, as described later on. The total force acting on a particle is calculated as the sum of the forces $\mathbf{F}_{ij}$ between particle pairs. Likewise, the total torque acting on a particle is calculated from the sum of the particle–particle torques $\mathbf{T}_{ij}$. The temporal evolution of the particle system is governed by Newton's equations of motion:

$$\frac{d}{dt}\mathbf{r}_i = \mathbf{v}_i, m\frac{d}{dt}\mathbf{v}_i = \mathbf{F}_i^{tot} = \sum_{j\neq i} \mathrm{F}_{ij}, I\frac{d}{dt}\boldsymbol{\omega}_i = \mathbf{T}_i^{tot} = \sum_{j\neq i}\mathbf{T}_{ij} \tag{1}$$

Here $\mathbf{F}_i^{tot}$ denotes the total force acting on the i^{th} particle and $\mathbf{T}_i^{tot}$ the total torque acting on the i^{th} particle, calculated from the particle–particle torques $\mathbf{T}_{ij} = -1/2\,\mathbf{r}_{ij} \times \mathbf{F}_{ij}$ with $\mathbf{r}_{ij} = \mathbf{r}_i - \mathbf{r}_j$.

The equations of motion can be integrated by a suitable method, e.g. by the Velocity-Verlet propagation scheme:

$$\mathbf{r}_i(t+\Delta t) = \mathbf{r}_i(t) + \Delta t\mathbf{v}_i(t) + \frac{1}{2m}(\Delta t)^2\mathbf{F}_i^{tot} \tag{2a}$$

$$\mathbf{v}_i(t+\Delta t) = \mathbf{v}_i(t) + \frac{1}{2m}\Delta t\left(\mathbf{F}_i^{tot}(t) + \mathbf{F}_i^{tot}(t+\Delta t)\right) \tag{2b}$$

$$\boldsymbol{\omega}_i(t+\Delta t) = \boldsymbol{\omega}_i(t) + \frac{1}{2I}\Delta t\left(\mathbf{T}_i^{tot}(t) + \mathbf{T}_i^{tot}(t+\Delta t)\right) \tag{2c}$$

2.2 Sintering Force Laws

The force law used to simulate solid-state sintering is based on the assumption that grain boundary diffusion is the dominant transport mechanism, a mechanism that leads to densification (as discusses in previous chapters) and which is usually valid over a wide range of densities. Then the normal force acting between two spherical grains is obtained by integrating the stress over the contact area and by adding the surface tension along the circumference [12]:

$$F^n = \gamma_s(2\kappa A + L\sin\psi) + \frac{\pi c^4 k_B T}{8\Omega\delta D_{GB}}v_{ij}^n = F_s + F_v \tag{3}$$

(note this equation comes from the chemical potential differences in a similar manner to the description in previous chapters, representing curvature forces and diffusion limitations). In Eq. (3), k_B is the Boltzmann constant, T the temperature, Ω the atomic volume, δD_b the grain boundary thickness times the grain boundary diffusion coefficient, which has an Arrhenius type temperature dependence,

$D_{GB} = D_{GB,0}\exp(-Q_{gb}/R_gT)$, where Q_{gb} is the activation energy and R_g the universal gas constant, $A = \pi c^2$ is the grain contact area with radius c, L the length of its perimeter, κ the curvature of the surface, γ_s the specific surface energy, ψ the dihedral angle, and $\mathbf{v}_{ij}{}^{n}$ the component of the relative grain–grain velocity in the direction perpendicular to the contact area. The surface curvature and the radius, area and perimeter of the particle contacts are taken from [13].

The sintering stress and the radius of the contact area, c, are given by polynomial approximations to numerical solutions (also taken from [13]), resulting in the following sintering force:

$$F_s = \frac{\pi^{2/3} R\gamma_s}{3^{1/6}(1-f)^{2/3}} Y(f,\psi) \qquad f = 1 - \pi\sqrt{3}\left(R/d_{ij}\right)^3 \tag{4}$$

$$\frac{c}{R} = 0.5998 + 0.0533\psi + (-1.271 + 0.4144\psi)f \tag{5}$$

where $Y(f,\psi)$ is a polynomial function of the porosity f and the dihedral angle ψ given in [13], the numerical values are those calculated in [13] for body-centered cubic grain arrangements with coordination number $Z = 8$, and $d_{ij} = |\mathbf{r}_{ij}|$ is the mid-point distance between two particles.

Additionally, if the contacts exhibit a viscous resistance against sliding, a tangential force is required [12]:

$$\mathbf{F}^t = \eta A\left(\left(\mathbf{v}_{ij} - v_{ij}^n \hat{\mathbf{r}}_{ij}\right) + \frac{\mathbf{r}_{ij}}{2} \times \left(\boldsymbol{\omega}_i + \boldsymbol{\omega}_j\right)\right) \tag{6}$$

where η is a phenomenological viscosity parameter, $\mathbf{v}_{ij} = \mathbf{v}_i - \mathbf{v}_j$ is the relative grain–grain velocity and $\hat{\mathbf{r}}_{ij} = \mathbf{r}_{ij}/\left|\mathbf{r}_{ij}\right|$ is the unit vector in the direction perpendicular to the contact area.

To account for particles of different sizes, the particle radius R in Eqs. (4), (5) and (6) is replaced by the equivalent radius $R^* = 2\,R_i\,R_j/(R_i + R_j)$.

Grain coarsening is assumed to take place in a self-similar manner, thus preserving the initial size distribution. This is achieved by introducing a rate equation for the increase of the average particle radius R, as proposed by Hillert [14]:

$$\dot{R} = \frac{\gamma_{gb} M_{gb}}{4R}, \qquad M_{gc} = M_{gc0}\exp\left(-\frac{Q_{gc}}{R_g T}\right) \tag{7}$$

Here γ_{gb} is the specific grain boundary energy, M_{gb} is the grain boundary mobility, which exhibits an Arrhenius type temperature dependence with the coefficient $M_{gb,0}$ and the activation energy Q_{gc}. R_g is the universal gas constant and T the temperature.

In this scheme individual particles *do not grow or shrink*, instead the sintering force laws change because of the change in the average particle radius. For a more realistic simulation of grain growth, the size change of individual particles should be considered, which will be discussed later.

2.3 Boundary Conditions

Either open boundary conditions or periodic boundary conditions for simulations in representative volume cells can be specified. In periodic boundary conditions, the simulation cell is replicated throughout space to form an infinite lattice. This means that particles that leave the simulation box on a given face are translated to the opposite face. Similarly, particles within a distance of r_c to a face of the periodic simulation cell interact with particles at the opposite face.

Strain rate boundary conditions can be prescribed for such a periodic cell. At the beginning of each time step, every particle center and the faces of the simulation box are displaced by

$$\Delta x_i = \dot{\varepsilon}_{ij} x_j \Delta t \tag{8}$$

where $\dot{\varepsilon}_{ij}$ is the macroscopic strain rate. For sintering simulations of periodic cells, stress boundary conditions are usually prescribed because the strain rate is unknown and the stress tensor, σ, is zero for free sintering. The 'zero' condition is achieved by calculating the difference $\Delta\boldsymbol{\sigma} = \boldsymbol{\sigma} - \boldsymbol{\sigma}_{\mathrm{des}}$ between the desired value $\boldsymbol{\sigma}_{\mathrm{des}}$ of the stress tensor, and the actual value $\boldsymbol{\sigma}$ in each time step. Then the strain rate is modified in the next step according to $\dot{\varepsilon}_{t+\Delta t} = \dot{\varepsilon}_t + \Delta\boldsymbol{\sigma}\Delta t/(2\mu)$. The constant of proportionality μ is chosen appropriately so that equilibrium is reached after a few hundred time steps. This stress tensor can be calculated from the particle interaction forces through:

$$\boldsymbol{\sigma} = \frac{1}{2V} \sum_i \sum_{j \neq i} \boldsymbol{F}_{ij} \otimes \boldsymbol{r}_{ij} \tag{9}$$

where V is the volume of the simulation cell.

2.4 Initial Configurations Generation Scheme

The initial configurations of randomly distributed particles are generated by a dynamic generation scheme which works in three steps: First the particles are filled into the simulation box one by one. The particle size is chosen randomly according to a prescribed size distribution function (usually a log-normal size distribution with distribution width λ, corresponding to a monodisperse packing for $\lambda = 0$), but to facilitate the filling process, the size is reduced of 50 % of its intended value during filling. Then the particle center is placed randomly in the simulation box and the cell expanded. If the program detects an overlap between the currently deposited particle and a previously deposited particle, the deposition is repeated until the particle can be accommodated without overlap. In the second step, a DEM simulation is used to expand all particles to their predefined value, with strong repulsive forces acting between particles. The final step creates particle contacts by using a force which is attractive for long-range interactions but repulsive for distances below $R_i + R_j$. For numerical reasons a contact is considered closed if the distance between neighboring particle centers is less than $1.005\ (R_i + R_j)$.

3 Effects of Rearrangement

One still poorly understood effect during sintering is rearrangement of the grains, especially during the initial stages. Only recent advances in X-ray synchrotron microtomography have allowed observing rearrangement effects directly on a grain scale. The DEM simulation method used here provides another possibility to study them in detail since they are already included by design.

3.1 Densification Rate

The densification rate is one of the most important quantities for characterizing the sintering process and is directly affected by grain rearrangement. When performing DEM simulation in representative volume cells stress boundary conditions allow switching between a collective translation of all particles according to the external strain field and an individual movement of particles. If the propagation scheme [Eq. (2a, b, c)] is deactivated for the particles, only affine movement is left, which makes it possible to investigate the influence of particle rearrangement.

Here, simulations in periodic volume cells consisting of several thousand particles have been performed with initial densities of 60 % and different particle size distributions. The densification rate can then be directly taken from Eq. (8).

If grain rearrangement is deactivated (so called Taylor-Bishop-Hill approximation), the numerical results show a nearly perfect agreement with the analytical prediction by Riedel et al. [12], on which the DEM model is based. This can be seen in Fig. 3 when plotting the densification rate as a function of density. For higher densities, the results differ slightly because in the DEM simulations new contacts, which are formed during the sintering process, are taken into account, causing a higher densification rate than the model which is based on a BCC structure with a constant coordination number. If grain rearrangement is allowed (full DEM simulation) the results are surprisingly similar, showing only a small increase for higher densities, even though there should be enough space right from the beginning of the simulation. This behavior can be explained by the fact that when using contact forces between pairs of equally sized particles all particles feel the same forces and thus are not attracted to open gaps.

This behavior changes if a grain size distribution is introduced though. While simulations with a log-normal distribution show an overall decrease in

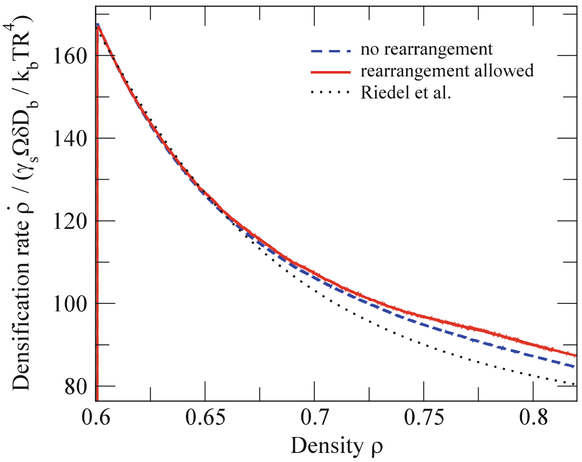

Fig. 3 Densification rate as a function of relative density for a monodisperse particle packing (with and without rearrangement allowed)

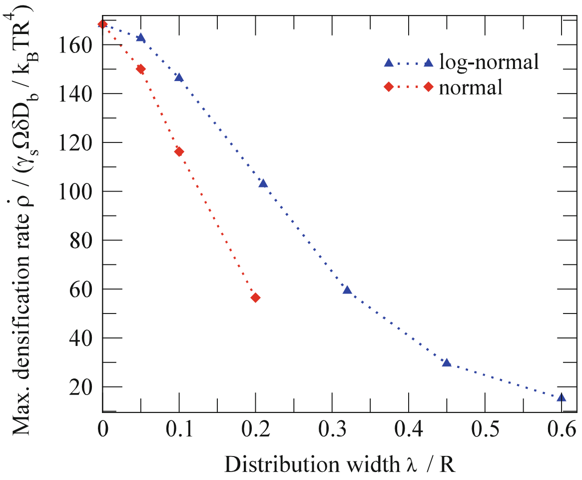

Fig. 4 Maximum densification rate as a function of distribution width (with rearrangement allowed)

densification as a function of the distribution width (see Fig. 4), they also show a higher degree of difference between simulation with and without rearrangement.

This can be seen in Fig. 5 for a log-normal distribution: The larger the distribution width λ, the higher is the increase in densification rate with relation to the normal. For $\lambda = 0.6$ the densification rate with rearrangements is more than twice as higher than without them. However, this significant increase cannot overcome the general trend of a decreasing rate with distribution width (at least not for the widths studied here). Looking at the ratio between densification rates with and without rearrangement it is observed that initially this ratio is highest and then slowly declines. This can be explained because initially, when the density is still below that of a random close packing, there is still a lot of space to fill up which then gradually decreases.

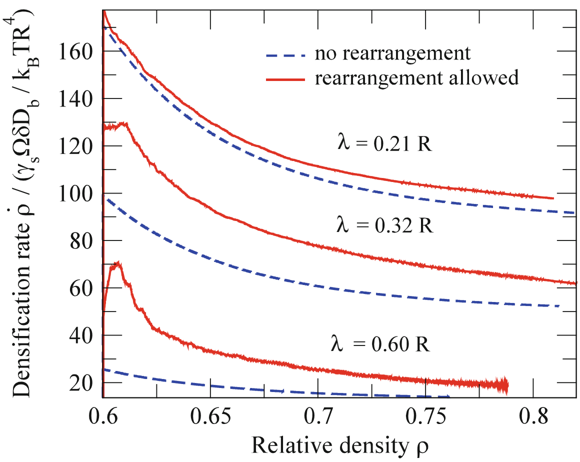

Fig. 5 Densification rate as a function of relative density for a polydisperse particle packing (with and without rearrangement allowed)

Introducing polydispersity thus offers a natural mechanism for enhancing rearrangements between particles. Particles are able to fill small gaps in the packing because of the differences in size. This is especially true for particles which are smaller in size than average.

3.2 Bulk and Shear Viscosities

In all simulations the tangential viscosity parameter η was set to zero, meaning that there is no resistance against particle sliding and rotation. This corresponds to an idealized case which allows maximum rearrangement. If η is increased grain sliding becomes more difficult and, accordingly, rearrangement has a smaller effect on the densification rate. For a sufficiently high η particle rearrangement can be suppressed completely, corresponding to the Taylor-Bishop-Hill approximation case. For real powders the value of η depends on the specific powder properties.

The bulk and shear viscosities during sintering are important quantities for continuum mechanical simulations. This actually represents the phenomenon of movement of particles during real sintering that is strongly affected by external pressure. Continuum simulations are usually based on the following isotropic, viscous constitutive equation:

$$\dot{\varepsilon}_{ij} = \frac{\sigma'_{ij}}{2G} + \delta_{ij}\frac{\sigma_m - \sigma_s}{3K} \tag{10}$$

with σ_m being the hydrostatic and σ_s the sintering stress, δ_{ij} the Kronecker symbol and K and G the bulk and shear viscosity, respectively. The prime denotes the derivative.

Fig. 6 Bulk viscosity as a function of relative density and applied pressure for a monodisperse particle packing

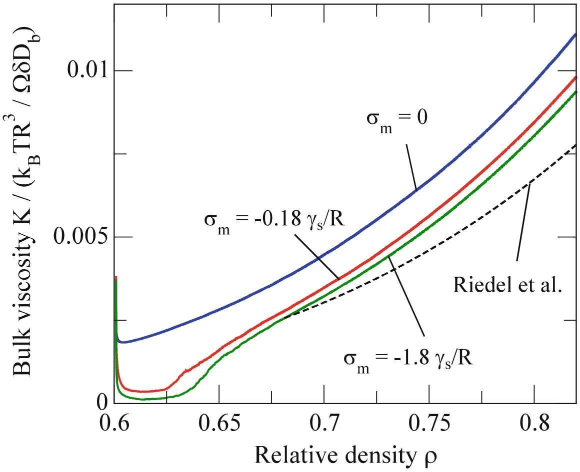

Fig. 7 Shear viscosity as a function of relative density and applied pressure for a monodisperse particle packing

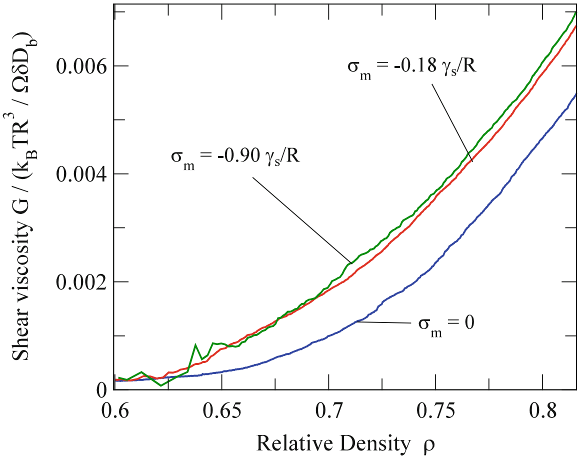

The viscosities can be determined numerically by performing short "mechanical" tests during a simulation run. Figure 6 shows the bulk viscosity calculated for various external pressures for periodic simulations cells with an initial relative density of 60 %. For a monomodal packing and $\sigma_m = 0$, when virtually no rearrangement takes place, the bulk viscosity gradually increases with density, similar to the analytical solution [12]. However, when rearrangement is activated by a small pressure, the bulk viscosity drops drastically at relative densities below about 64 %, and it remains smaller than in the case $\sigma_m = 0$ for all densities.

In Fig. 7 the shear viscosity is shown for different macroscopic isostatic pressures. Compared to the case without rearrangement, the viscosity is moderately smaller, meaning rearrangement leads to a decrease of viscosity. The shear viscosity is pressure-dependent and increases with increasing pressure in the

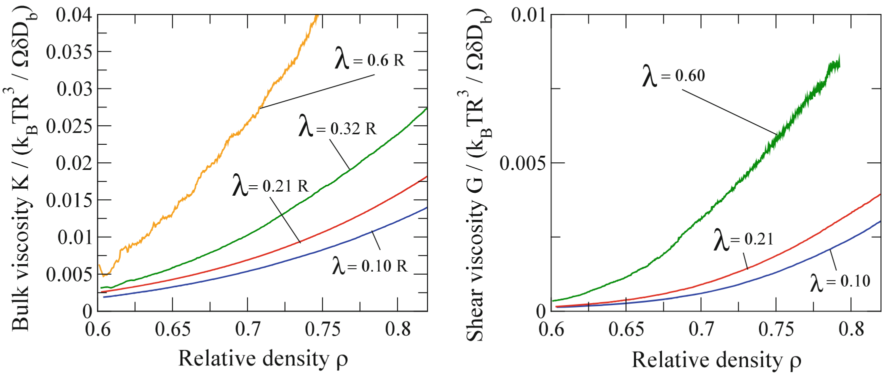

Fig. 8 Bulk viscosity (*left*) and shear viscosity (*right*) as a function of relative density and applied pressure for a polydisperse particle packing

higher density region. Again the results converge above a certain pressure. This is already the case for $\sigma_m = -0.18\ \gamma_s/R$.

It is observed that the introduction of a particle size distribution increases viscosity as can be seen in Fig. 8. Both the bulk viscosity (Fig. 8, left image) and the shear viscosity (right image) grow significantly when the width of the distribution is increased. As it was observed for monomodal structures, particle rearrangement consistently leads to lower viscosity. This decrease, however, is more uniform over the whole density range and not limited to densities below those of a random close packing. In agreement with the results on the densification rate, this effect increases with the distribution width and is another indicator that rearrangement becomes more pronounced for wide particle size distributions. Also, the difference between simulations based on the Taylor-Bishop-Hill approximation and those with rearrangement is significantly larger for the shear than for the bulk viscosity.

It should be noted that within the DEM simulations Eq. (9) is no longer an exact representation of the macroscopic behavior of the particle aggregates because K is no longer a unique function of density. Furthermore, under non-isostatic loading the particle aggregate develops anisotropic properties, which cannot be described by the isotropic equation. However, appropriate anisotropic, constitutive equations can be employed as well, as has been demonstrated elsewhere [15].

3.3 Crack Formation

The formation and propagation of cracks during sintering is essential for the quality of sintered parts, but can be hardly described by current continuum models. DEM simulations with their grain-scale approach, however, offer a natural description of it. As a demonstration example a cubic green body with an initial

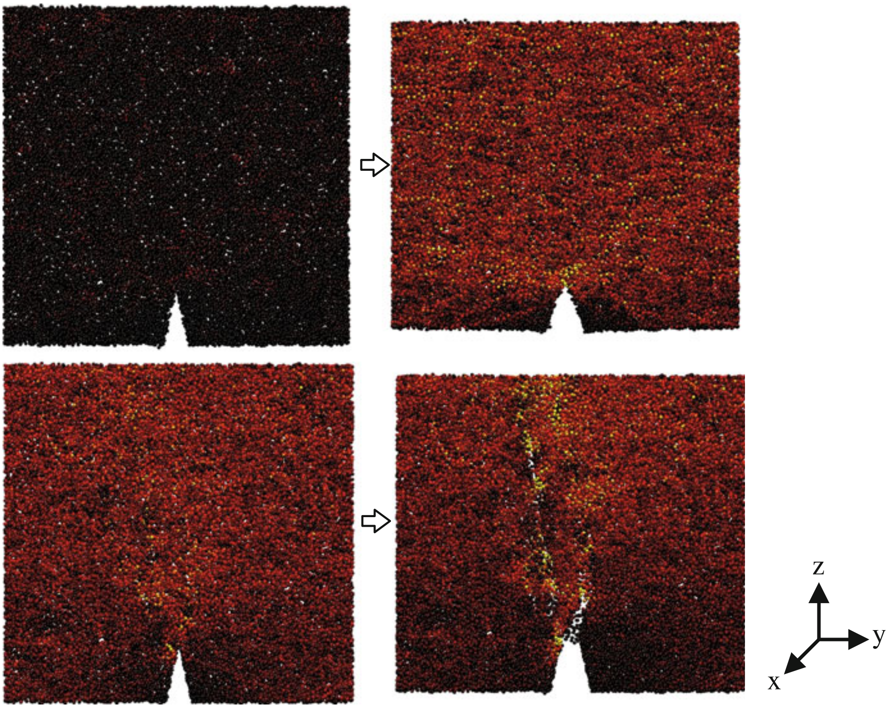

Fig. 9 Crack propagation through a constrained film (in y- and z-direction) for particles without (*top images*) and with tangential friction (*bottom images*). The *left images* show the initial state, the *right images* the final state after sintering. Colors denote the local stress fore each particle

density of 48 % consisting of about 40,000 equally sized particles was simulated with a crack notch cut into it (see Fig. 9).

The notch acts as a seed for crack propagation in the simulation. The green body is constrained in horizontal direction with standard periodic boundary conditions and free to shrink in the two other directions. In Fig. 9 the temporal evolution of the crack is shown with the colors denoting the local stress. In the case of high tangential sliding resistance particle rearrangements are suppressed. Figure 9 (bottom left) shows larger stresses near the tip of the crack at the beginning of the simulation. At the end of the sintering process the specimen has shrunk in vertical direction, and the crack has propagated through the specimen due to the constraint in horizontal direction. Without tangential viscosity ($\eta = 0$) particle rearrangements are much easier and so local stresses can be avoided as seen in Fig. 9 (top). It should be noted that compared to the free sintering case here the stresses facilitate rearrangement. At higher densities the particles become more jammed, i.e. rearrangements become more and more difficult, which leads to an increase of the average stress. Especially near the tip of the crack the local stress

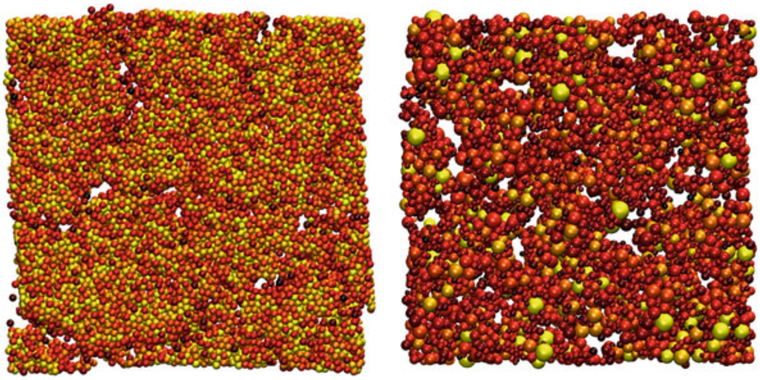

Fig. 10 Spontaneous crack formation during constrained sintering of a thin film (*top view*) for two different packings after sintering: monosized particles (*left image*) and polydisperse particles (*right image*)

increases although it is smaller than in the previous case (Fig. 9, top right). However, no crack propagation can be observed in this case.

Also, the spontaneous formation of cracks can studied using DEM. Two initial configurations (monodisperse vs. polydisperse) of thin films constrained on a substrate with a relative density of $\sim 50~\%$ were generated. The constraint leads to randomly oriented cracks forming during sintering in the plane perpendicular to the shrinkage direction, as depicted in Fig. 10. For both the monodisperse and polydisperse packings several cracks appear spontaneously which differ in their magnitude. For the polydisperse packing higher local stresses are observed, indicating that it is more difficult for particles to relax. Again, a strong dependence on grain rearrangement is observed: Without tangential viscosity no visible cracks develop.

4 Grain Growth Models

In the analytical grain growth model described above [Hillert method, see Eq. (7)] all grains in a sample grow with the same coarsening rate, which only works in periodic boundary conditions and does not consider the changing microstructure. Therefore, an improved grain growth model is described here that shrinks and grows individual particles, providing a more realistic grain-scale approach.

As we have discussed in the initial chapters of this book, if two particles with unequal sizes are in contact, matter from the smaller particle is transferred to the larger particles. From a geometrical perspective, the amount of transported matter depends on the intersection volume of the particle pair. Assuming two particles with different particle radii r_i and r_j and a distance d between the particle centers, the intersection volume can be computed by

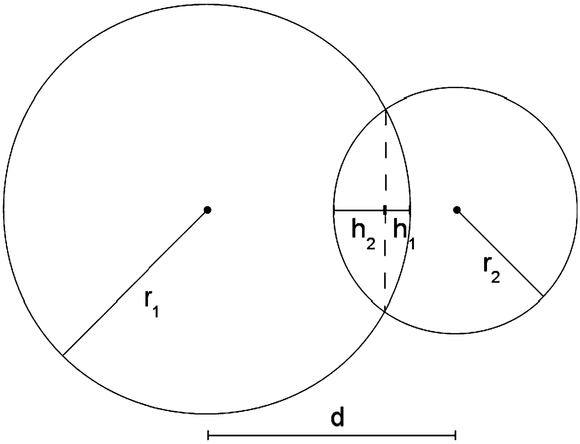

Fig. 11 Contact geometry of two particles

$$V_I^{ij} = \frac{\pi}{3} \left[h_i^2(3r_i - h_i) + h_j^2\left(3r_j - h_j\right) \right] \tag{11}$$

with $h_i = r_i - \left(d^2 + r_i^2 - r_j^2\right)/2d$ being the height of the spherical cap defined by particle i and the intersection plane between the two particles (see Fig. 11). In the coarsening procedure, the volume V_i^k of particle i at time step k is then updated by

$$V_i^{k+1} = V_i^k + c_i V_I^{ij} \Delta t \tag{12}$$

where c_i is a number between -1 and $+1$, and Δt the time step. To account for the fact that small particles shrink for the benefit of larger partners and to ensure global mass conservation, the condition $c_i = -c_j$ must hold. The new particle radius can subsequently be computed from the new particle volume.

The coefficients should depend on the mean radius of the powder grains R, the temperature T, the specific grain boundary energy γ_{GB} and the grain boundary mobility $M_{gc} = M_{gc,0}\ \exp\left(-Q_{gc}/R_g T\right)$, which exhibits an Arrhenius-type temperature dependence, as described previously. Though a good analytical description of the functional relationship for c is feasible, it is still an object of research and will not be considered here.

When applying the discussed method, the size of small particles decreases for the benefit of a larger particle, ultimately leading to very small particles. Thus, a lower threshold of particle size r_{min} is introduced. Particles with radii below this value are taken out of the simulation. For reasons of mass conservation, their volume is distributed equally to remaining particles.

In addition, for particle pairs with large size ratios the parameter $\mu_{ij} = (r_{ij} - r_i)/r_j$ provides a measurement of the absorption of small particle with radius r_j into a large particle with radius r_i. In the case of passing over a limit μ_{min}, the volume of the small particle is handed over entirely to the partner. This procedure offers an elegant way to mimic coalescence of particles during sintering.

In order to demonstrate the general practicability of the introduced model, the development of a sintered sample (initially consisting of ca. 1800 particles) is

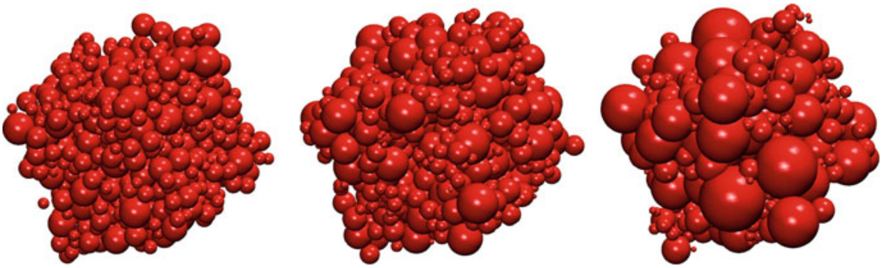

Fig. 12 Particle packing at three different sintering stages with the grain coarsening model

shown in Fig. 12. It should be noted that the model is still under development and should be as a first test-case compared with predictions from the simple Hillert model.

5 Nanoparticle Sintering of Printed Circuits

Ink-jet printing is a promising technique which allows low cost mass production of circuits used for new technologies like RFIDs, OLEDs or thin film solar cells. In this process a conductive ink, consisting of metallic nanoparticles suspended in a solvent, is printed on a substrate (e.g. polyimide foil), dried and subsequently sintered. The conductivity of the printed circuits is decisive for the performance of the resulting part.

With DEM simulations it is possible to investigate the sintering step of circuits containing hundred of thousands nanoparticles at the grain scale. The initial configuration matches the green sample properties of the real dried track. The simulated track consists of randomly distributed particles that are assumed to be spherical. Both particle size and particle size distribution of the nanoparticles are adapted to measured data on the applied powder. Cross-sectional shape and dimensions, which are in the range of micrometers, can be reproduced in the simulation, whereas in the length direction of the track, which is much longer, periodic boundary conditions are applied. For the lateral and the top surface, free boundary conditions are used while at the bottom, a constraining boundary is imposed by a rigid substrate. The substrate is represented explicitly by particles which have the same properties as the particles used for the track but are fixed during the simulation.

Because of the constraining condition caused by the substrate, in-plane shrinkage is inhibited in its vicinity. The densification during the sintering process is therefore not uniform, which leads to a deformation of the track with respect to the cross-section profile. As there is a preferred densification direction perpendicular to the substrate, emerging pores become anisometric resulting in a

Fig. 13 Initial and final state of the cross-sectional area of a constrained sintered thin track with initial dimensions 24 × 6 µm (scale in x-direction 2.4:1)

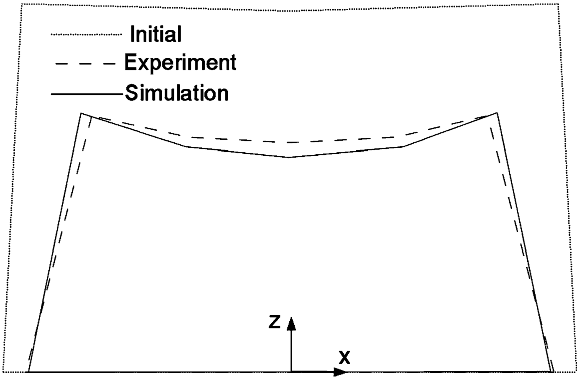

microstructural anisotropy. Moreover, an in-plane biaxial tensile stress develops that can cause defects such as cracks or debonding.

For the case of a nanoparticle Al_2O_3 ceramic powder (TM-DAR), it can be shown that the cross-sectional shape of an experimentally sintered thin line closely fits those of DEM simulations (see Fig. 13). In addition, debonding effects could be reproduced as well as a preferential appearance of pores in vicinity of the substrate (see Fig. 14). Detailed analysis of the pores revealed a preferential orientation perpendicular to the substrate, which was also observed in experimental studies [16].

The relevant parameters on the particle scale concerning the conductivity of a printed track are the mean number of neighbouring particles and the mean contact area between the particles in contact. Both values are not easily accessible by experiments but can be calculated in a DEM simulation. By combining these parameters with the cross-section area and the length of the track, a model for the electrical conductance can be developed.

After a successful verification of the simulation results by experiments, it is possible to vary certain simulation parameters like particle size or the dimensions of the cross section in order to analyze their influence and to investigate if any improvements regarding the conductivity of the inkjet-printed line can be achieved.

6 Summary

Sintering simulations by the Discrete Element Method are still a relatively new, yet very promising tool for a better understanding of sintering on the grain scale. It has been show that the method is particularly suited to investigate rearrangement effects in detail and also make predictions about crack formation and anisotropy development. By allowing to easily change properties of the grains (e.g. size distributions, friction parameters and other material properties) their effects can directly studied, without having to resort to expensive experiments. While it is not

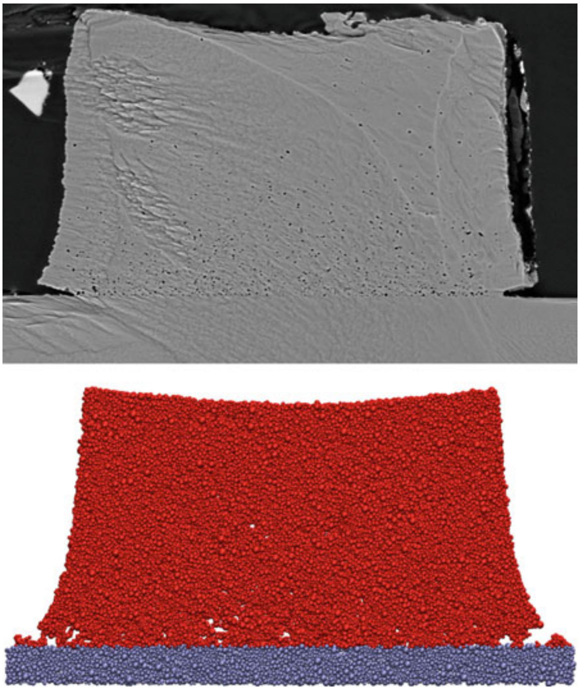

Fig. 14 Thin ceramic film after sintering on a rigid substrate; comparison between experiment (*top*, courtesy of TU Darmstadt) and simulation (*bottom*)

yet possible to simulate complex shaped 3-D parts consisting of billions of individual particles, it is possible to study smaller parts like printed circuits in the micrometer range. It is also possible to use the simulation results to improve current continuum mechanical simulation models that allow the simulation of real parts.

However, there are still several open questions that need to be addressed in the future to make DEM simulations even more realistic. As an example it has been shown how the currently implemented grain growth model could be replaced by a new model that explicitly grows or shrinks individual particles but which still needs further work. Also, the sintering force laws used right now only consider grain-boundary diffusion but could be easily extended to include surface and volume diffusion as well. Work to simulate other sintering mechanisms like liquid-phase sintering are already underway [17].

References

1. Coube, O., Huber, R., Kösters, R., Plankensteiner, A., Magin, M.: In: Kneringer, G., Rödhammer, P., Wildner, H. (eds.) Proceedings of 16th International Plansee Seminar. PLANSEE AG, Reutte, Austria, vol. 2, p. 234 (2005)
2. Song, J., Gelin, J., Barriere, T., Liu, B.: J. Mater. Process. Technol. **177**, 352–355 (2006)

3. Huang, R., Pan, J.: J. Eur. Ceram. Soc. **28**, 1931–1939 (2008)
4. Cundall, P.A., Strack, O.D.L.: Geotechnique **29**, 47 (1979)
5. Bierwisch, C., Kraft, T., Riedel, H., Moseler, M.: J. Mech. Phys. Solids **57**, 10–31 (2009)
6. Coube, O., Cocks, A.C.F., Wu, C.Y.: Powder Metall. **48**, 68–76 (2005)
7. Martin, C.L., Bouvard, D., Delette, G.: J. Am. Ceram. Soc. **89**, 3379–3387 (2006)
8. Martin, C.L., Schneider, L.C.R., Olmos, L., Bouvard, D.: Scripta Mater. **55**, 425–428 (2006)
9. Luding, S., Manetsberger, K., Mullers, J.: J. Mech. Phys. Solids **53**, 455–491 (2002)
10. Henrich, B., Wonisch, A., Kraft, T., Moseler, M., Riedel, H.: Acta Mater. **55**, 753–762 (2007)
11. Wonisch, A., Guillon, O., Kraft, T., Moseler, M., Riedel, H., Rödel, J.: Acta Mater. **55**, 5187–5199 (2007)
12. Riedel, H., Zipse, H., Svoboda, J.: Acta Metall. Mater. **42**, 445–452 (1994)
13. Svoboda, J., Riedel, H., Zipse, H.: Acta Metall. Mater. **42**, 435–443 (1994)
14. Hillert, M.: Acta Metall. **13**, 227–237 (1965)
15. Bordia, R.K., Zuo, R.Z., Guillon, O., Salamone, S.M., Rödel, J.: Acta Mater. **54**, 111–118 (2006)
16. Guillon, O., Weiler, L., Rödel, J.: J. Am. Ceram. Soc. **90**, 1394–1400 (2007)
17. Wonisch, A., Korn, K., Kraft, T., Riedel, H.: Anisotropic liquid-phase sintering investigated by means of micromechanical and discrete element modeling. In: Gumbsch, P. (ed.) Proceedings of the Third International Conference On Multiscale Materials Modeling, Fraunhofer IRB, Stuttgart, Germany, p. 578 (2006)

Sintering of Porous Materials

Kathy Lu, Wenle Li and Bo Chen

Abstract This chapter focuses on the sintering of nanoparticle-based porous materials. First, nanoparticle-based porous materials are defined. Then, the fundamentals of sintering are briefly revisited but from a porous point of view, describing effects of parameters on porous structure and shrinkage, and the unique characteristics and challenges for the sintering of nanoparticle-based porous materials are addressed. The discussion on the sintering is divided into single composition systems and composites. For single composition systems, porous materials can be obtained by partial sintering, template-based sintering, or reaction sintering. For porous composite materials, the microstructures can be realized by direct sintering of composite systems, using nanoparticles as a second phase in the sintering of larger-sized particle matrix, or unique reaction processes. Finally, the current state of nanoparticle-based porous material sintering is summarized and future directions are analyzed.

1 Introduction

Porous materials are a subset of materials that possess unique surface, structural, and bulk properties with a solid phase and a pore phase co-existing [1–5]. While the solid phase needs to be continuous, the pore phase may be continuous or discrete. If the pore phase is continuous, the pores are often open pores. If the pore phase is discrete, the pores are often closed pores. Nanoparticle-based porous

---

K. Lu (✉) · W. Li · B. Chen
Department of Materials Science and Engineering, Virginia Polytechnic
Institute and State University, Blacksburg, VA 24061, USA
e-mail: klu@vt.edu

R. H. R. Castro and K. van Benthem (eds.), *Sintering*, Engineering Materials 35,
DOI: 10.1007/978-3-642-31009-6_6, © Springer-Verlag Berlin Heidelberg 2013

materials are the porous materials that are created from nanoparticles. There is no strict definition on the amount of porosity in nanoparticle-based porous materials. However, the consideration generally excludes the particulate materials with only a couple of percent residual porosity that cannot be removed by sintering. The highest amount of porosity can be as high as 95 %. The final products should have grain sizes less than 100 nm but this aspect is often relaxed to include materials with grains as large as 200 nm. In addition, there has been no strict limits on pore sizes, which can range from nanometers to microns. While porous green samples can be created through many different ways, sintering is a necessary step to produce stable and strong nanoparticle-based porous materials for actual applications and is the focus of this chapter. Because of the fast grain growth of nanoparticle-based materials during sintering, the pores in the sintered materials are often open pores.

Porous nanoparticle-based materials have high surface area, high permeability, and low density. They are of scientific and technological importance because of their vast ability to adsorb and interact with atoms, ions, and molecules on their large surfaces (interior and exterior) and in the nanometer- to micron-sized pore space. Nanoparticle-based porous materials have important uses in various fields such as ion exchange, separation, catalysis, filters for metal smelting or hot gases, porous burners, bone implants, sensors, and biological molecular isolation and purifications [6–8]. They also offer new opportunities in guest–host synthesis and molecular manipulation and reaction at the nanoscale for making nanoparticles, nanowires, and other quantum nanostructures.

2 Fundamentals of Sintering and Porosity Control

As we have seen, traditionally sintering is defined as the bonding of a particle packing into a coherent, predominantly solid structure by the application of heat to enable one or more mechanisms of atomic movement to the particle contact interface to occur [9, 10]. For *porous* nanoparticle-based materials, grain growth is typically rapid, sintering strength is generally limited, and the structures have grain-pore bi-continuous phases (alternating pore and grains). In light of these, it may be more suited to define nanoparticle-based porous material sintering as the process of atomic diffusion and bi-continuous microstructure formation between nanoparticles with the application of heat. On the macroscopic scale, the process is accompanied by strengthening and dimensional decrease (shrinkage) but to a less extent than that for the fully dense counterparts. Also, the strength increase and the shrinkage are strongly dependent on the final density. On the microstructural scale, bonding occurs as cohesive necks grow at the points of contact between particles. As the bonds between contacting particles enlarge and merge, grain growth proceeds. However, the grain size and porosity can vary widely.

Classical sintering studies focus on rigorously defined geometric models such as simplified two sphere model or tetrakaidecahedron model [11–14]. From mechanistic point of view, sintering proceeds by evaporation–condensation, surface diffusion, grain boundary diffusion, volume diffusion, plastic deformation or creep (if a pressure is applied). Only grain boundary diffusion, volume diffusion densification, and plastic deformation/creep lead to shrinkage/densification. The other diffusion processes lead to microstructural coarsening. For porous nanoparticle-based materials, surface diffusion may be substantial. Lowering the surface energy by the elimination of particle (grain)-pore interface is the driving force for sintering. Particles/grains change their shapes by rounding off sharp corners or developing facets at low surface energy orientations. Classical sintering theories almost always divide the process into three stages (initial, intermediate, and final). With the designation that the particle (grain) size is D and the particle–particle neck size is X, initial stage of sintering refers to the state when the neck size ratio X/D is less than 0.3; during this sintering stage the pore structure is open and fully interconnected. Intermediate stage of sintering refers to the state when X/D is greater than 0.3 but the porosity is 10 % or more; during this sintering stage pores are much smoother and have an interconnected, cylindrical structure; grain growth and pore isolation occur in the latter portion of the intermediate stage of sintering. At 8–10 % porosity, sintering proceeds into final stage; cylindrical pores collapse into spherical pores; densification substantially slows down and extensive grain growth is most likely to occur. Based on this understanding, porous nanoparticle material sintering can also be viewed as the sintering process that only involves initial and/or intermediate stage of sintering. From this point of view, porous nanoparticle material sintering can be viewed as a shortened version of the entire sintering process.

At free sintering conditions, diffusion occurs locally based on curvature difference. Nanoparticles need to “smooth” out their surfaces and transition into a stable shape before grain boundary diffusion and volume diffusion set in. The morphological change to lower the system energy is the dominant event during sintering. Taking grain boundary diffusion as an example, we have discussed in the previous chapters the parameters affecting the sintering behavior. Overall, for very small shrinkage, the densification can be expressed as for the initial stages of sintering [15–17]:

$$\frac{d\rho}{\rho \cdot dt} = C \cdot A \cdot \Sigma \mathbf{H} \tag{1}$$

where C represents the system and temperature related constants, A is the volumetric grain boundary area, and $\Sigma \mathbf{H}$ is the vector sum of the mean curvature $\mathbf{H}$ with the consideration of the relative orientation of the grain boundaries in the compact. Note that this equation could be re-written replacing the density term by porosity, as they are closely related to each other. This simple conversion is not shown here as the overall goal of each parameter used to control microstructure is still the same. That is, for a given material under a specific temperature (given C), Eq. (1) shows that A and $\Sigma \mathbf{H}$ comprehensively represent the densification/shrinkage rate (pore elimination). A represents grain packing density, contact, and the available grain boundary area for densification. $\Sigma\mathbf{H}$ represents grain size, shape, and inter-grain neck geometry. $\Sigma\mathbf{H}$ also represents pore size and shape. C, A, and $\Sigma\mathbf{H}$ collectively represent the spontaneous densification tendency of a sintering system. With temperature change, C varies based on intrinsic material properties such as diffusion coefficients and interfacial energies.

Clearly, the intrinsic properties of the material play essential roles in sintering shrinkage, reflected by C in Eq. (1). Composition and sintering temperature can be modified to adjust these values. However, porous microstructure morphology changes cannot be easily predicted by dimensional changes. From the above discussion, it can also be realized that sintering has been mainly addressed by considering solid phases. Pore size and porosity evolution with sintering is generally derived based on the sintering density and grain size data but direct evaluation of these factors has been scarce. Even though porosity mostly decreases with sintering, pore size can decrease or increase. Pore shape change is even more convoluted with initial particle packing and sintering diffusion mechanisms. However, no correlation between grain size and pore size has been established. Pore shape evolution before final stage sintering is an area that needs to be more rigorously described and studied. Since porosity is generally more straightforward to obtain (it can be derived easily from sintered density), many studies skip over pore description and use porosity to describe material microstructure changes in a very simplified way. Lastly, nanoparticle-based materials generally have a substantial amount of surface area, which is directly related to many applications and should be analyzed.

3 Nanoparticle-Based Sintering

There are many unique phenomena related to nanoparticle-based porous material sintering. Examples are: higher percent of more amorphous-like particle surface species; pore size and shape change and different classes of pores; more adsorbed foreign species on particle surfaces.

Sintering of nanoparticle-based materials also shares many of the common principles as that of micron- and submicron-based particulate systems. This includes the fundamental diffusion mechanisms, grain growth rules, and intrinsic material property effects such as dihedral angle and interfacial energy. However, nanoparticle sintering has its unique issues and needs to be carefully considered in order to achieve the desired microstructures and macroscopic properties.

Compared to conventional micrometer sized or submicrometer sized particles, the densification behavior of nanoparticles during sintering is notably different with respect to the rate of densification and the temperature range at which densification occurs. Because of the excessive surface area of nanoparticles, agglomeration has been a ubiquitous issue. The densification of nanoparticle-based materials is strongly affected by agglomeration of particles, pores, and other processing variables. Although many of these factors also impact the sintering of conventional micrometer sized particles, the effects are more dramatic and magnified during the sintering of nanosized particles.

Particle surfaces are known to have higher concentration of defects and dangling bonds than the interior of particles. As a result, the atomic mobility on the particle surface is higher. For nanoparticles, particle surfaces take up a much larger volume fraction of the total sintering system than in the micron-sized systems. Collectively, nanoparticles demonstrate more activated behavior and have a much early onset of sintering temperatures. For many nanoparticles, sintering onset temperature is in the range of 0.2–0.3 T_m (where T_m is the melting point of the sintering species in Kelvin), as compared with the much delayed onset of sintering temperature in micron-sized particulate systems, normally 0.5–0.8 T_m [18–20]. Several studies on the sintering of Y_2O_3 stabilized ZrO_2 nanoparticles (YSZ) have shown that the sintering temperature of nanocrystalline ZrO_2 initiates at a temperature 200 °C lower than that of the micron-sized powders [21–23]. An even greater difference in sintering temperature, 400 °C, is reported for nanosized TiO_2 compared to commercial TiO_2 powders [24]. Similar results are observed when sintering CeO_2 [25] and TiN nanoparticles and other materials [26–31].

Nanoparticle-based sintering systems also have much lower sintering activation energies. This is often reflected by the low sintering temperatures required. The densification activation energy for nano-ZrO_2 is less than 50 % of that for submicron ZrO_2 [32]. ZnO nanoparticle grain growth activation energy is less than 10 % of that for the micron-sized ZnO particles [33]. In fact, these energies can only be labeled as apparent activation energy. Multiple mechanisms may be operating simultaneously. This is especially true during the early stage of sintering, when no one clearly dominant mechanism can be identified, the results calculated using the kinetic data give apparent activation energy values that are the combined contribution of multiple mechanisms. Majority of studies point toward lower activation energies for early stage of sintering. This is reasonable for the obvious reason of the huge surface areas and the expected high activity of nanoparticles.

Surface diffusion is one of the most cited mechanisms that contribute to the sintering of nanosized particles [34]. Surface diffusion induces coarsening, which perturbs the equilibrium configuration to reinitiate neck growth (sintering) and densification. When the coordination number reaches a critical value, the pore is at equilibrium. The shrinkage of the pore (i.e. sintering) cannot progress until the equilibrium condition is tipped in favor of sintering by grain growth. With respect to the densification mechanisms of nanoparticles, surface diffusion can cause coarsening of nanoparticles which, in turn, contributes to densification. Therefore, it can be stated that by inducing coarsening, surface diffusion will contribute indirectly to densification. However, excessive surface diffusion means excessive coarsening and loss of desired fine microstructures, which should be avoided.

From a different perspective, low sintering temperature and activation energy of nanoparticles imply the added ability to manipulate and tailor sintering that has not been possible before. For example, non-equilibrium and high concentration of vacancies at the grain boundaries are beneficial for grain boundary diffusion and pore removal.

Considering that the initial grain growth during sintering is a result of the coarsening of nanoparticles due to interparticle diffusion, there are other interparticle diffusion mechanisms, other than surface diffusion, that could also contribute to the coarsening of particles. In particular, there is a relaxation period for migration, redistribution, and annihilation of defects due to the fact that nanoparticles are usually not at equilibrium states and likely to contain excess amounts of defects that are created during the synthesis of nanoparticles. Owing to the non-equilibrium structure of nanoparticles, diffusivity is dramatically enhanced during the relaxation process, which may contribute to dynamic grain growth at the beginning of sintering. Dynamic grain growth usually dominates during the heat-up stage and for the first few minutes after reaching a preset isothermal holding temperature. Therefore, rapid dynamic grain growth accounts for the experimental observation that the first grain size data point during isothermal holding is several times of that of the initial grain size. The relaxation time depends on material, nanoparticle synthesis method, and temperature.

From a kinetic perspective of grain growth as a function of time, the experimental observations as described above suggest that the grain growth of nanosized particles during sintering can be treated as consisting of two steps: a dynamic grain growth process that occurs during heating-up up to the beginning of isothermal holding; and the static grain growth during isothermal holding. The grain growth during sintering consists of two stages: first, when the relative density is lower; and second, when the relative density is greater. Early stage grain growth that occurs during heating can be significant and sufficient to exceed nanoscale. Thus, if grain size is to be maintained at nanoscale, this part of grain growth must be controlled.

4 Nanoparticle-Based Porous Materials

Many techniques have been developed to synthesize porous materials by using nanoparticles as initial materials, and they can be classified into three main methods: (a) partial sintering of initially porous nanoparticle compacts, (b) template method using monosized polymer particles as sacrificial templates and nanoparticle-based material as a matrix to fill the voids among the polymer particles; (c) reaction of the initial nanoparticles during the sintering to create porosity in the sample.

4.1 Partial Sintering

Porous materials can be obtained by maintaining the residual porosity of nanoparticle-based green samples through partial sintering. In the classical sintering approach, a two-step sintering method (a short, high temperature sintering step followed by a prolonged isothermal holding at low temperatures) is often used in

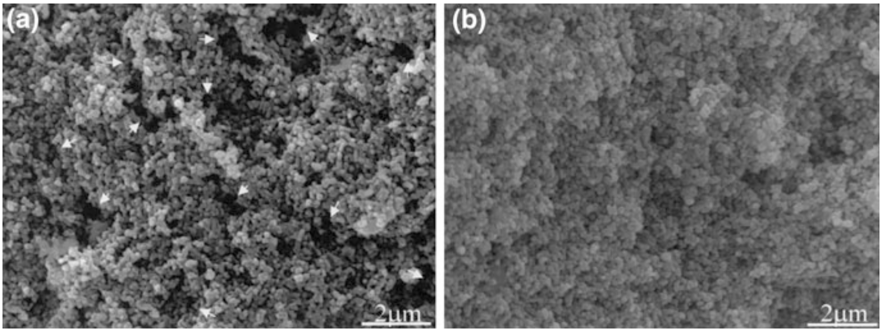

Fig. 1 SEM images of the surface structure of porous ZrO_2 materials after being sintered at 1200 °C for 30 min from **a** green body compacted at 30 MPa pressure, **b** green body compacted at 75 MPa pressure. The porosity of **a** is 47.4 %, and the porosity of **b** is 44.5 % [39]. Reprinted from Deng et al. [75] copyright (2011), with permission from Elsevier

the attempt to obtain dense nanoparticle-based materials [35–37] while one-step partial sintering can fabricate porous materials with small grain sizes and low densities.

Porous nanocrystalline Gd-doped CeO_2 is prepared by a one-step sintering process from commercial 10 mol % Gd-doped CeO_2 nanoparticles of ~5 nm size and 176.5 m^2/g specific surface area [38]. After being mixed through ball-milling and compacted through cold isostatic pressing, the green body is sintered to 800 °C for 30 min with a heating rate of 5 °C/min, which suppresses the grain growth and results in porous nanostructured Gd-doped CeO_2. After the one-step sintering process, the grain size is limited to 30 nm and the porosity is 26 %.

Porous ZrO_2 is fabricated by compacting ZrO_2 nanoparticles and partial pressureless sintering in air atmosphere at 1100–1450 °C for 30 min with a heating and cooling rate of 10 °C/min [39, 40]. The average size of initial ZrO_2 nanoparticles is 28 nm. Porosity ranges between 12–60 % based on different compaction and sintering conditions. Since ZrO_2 nanoparticles have the inherent tendency for agglomeration (as discussed in the previous chapter), which cannot be eliminated by ball-milling, the green body of compacted ZrO_2 nanoparticles is composed of numerous ZrO_2 agglomerates. During the sintering process, the densely packed regions sinter faster than the loosely packed regions. Therefore, non-uniform shrinkage occurs, which causes strains, voids, and crack-like flaws, and results in degraded mechanical properties. Increase in compaction pressure of the green body can efficiently reduce these voids and flaws because of the collapse and break-up of the ZrO_2 agglomerates (Fig. 1). Addition of $Zr(OH)_4$ is another way to obtain uniform microstructures in the green compacts, due to the space constraint of $Zr(OH)_4$ large particles and an internal friction between $Zr(OH)_4$ hard agglomerates [40]. As a result, there is no significant difference in pore coordination number throughout the specimen and the shrinkage is homogeneous. $Zr(OH)_4$ decomposes into ZrO_2 during sintering and porous ZrO_2 with 400–800 MPa fracture strength is formed.

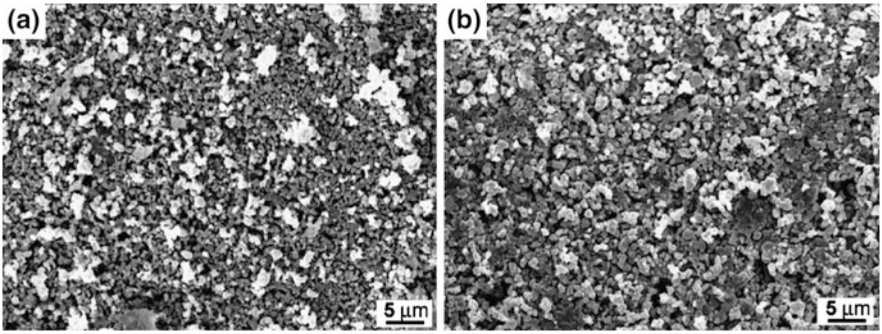

Fig. 2 SEM images of sintered $ZrTiO_4$ from equimolar mixture of TiO_2 and ZrO_2 nanoparticles at different sintering temperatures: **a** 1100 °C, **b** 1200 °C [42]. Reprinted from Gajović et al. [76] copyright (2011), with permission from Elsevier

High energy ball milling of powder precursors has been employed for the fabrication of porous materials [41, 42]. Equimolar mixture of TiO_2 (crystallite sizes 76 nm) and ZrO_2 (crystallite sizes 63 nm) by high energy ball milling decreases the sintering temperature of $ZrTiO_4$ ceramics. The crystallite sizes from the oxides ball milled for 7 h are between 5 and 7 nm. Before sintering, the ball milled powder is compacted at 180 MPa. Sintering is carried out in air for 8 h at 1100–1400 °C with a heating rate of 23 °C/min. Sintered morphology and porosity are dependent on the sintering temperature (Fig. 2). The nanosized precursors allow the solid-state reaction of the oxides to form $ZrTiO_4$ at a temperature 200 °C lower than that of the conventional solid-state synthesis. This facilitates the formation of small grain sizes and small pores. Long time high energy ball milling can also synthesize well dispersed nano-sized particles from bulk materials [43]. A crystalline Si wafer with (111) orientation is extensively ball milled for up to 72 h, leading to a decrease in the average crystallite size to 15 nm. After pressing at 400 MPa and sintering at 900 °C for 60 min in high purity argon atmosphere, porous silicon structure with uniform porosity is obtained.

4.2 Template Method

Nanocrystalline ceramics with well-controlled macropores are fabricated via colloidal processing using mono-sized polymer particles as sacrificial templates [44–46]. Obtaining oppositely charged particle suspensions is the key for the fabrication of such macroporous materials. Polymer particles are removed after sintering, and the porosity can be controlled by modifying the volume ratio of the nanoparticles to the polymer particles.

The preparation of well-dispersed polymer and nanoparticle suspensions is essential for the fabrication of uniform porous materials for the template method.

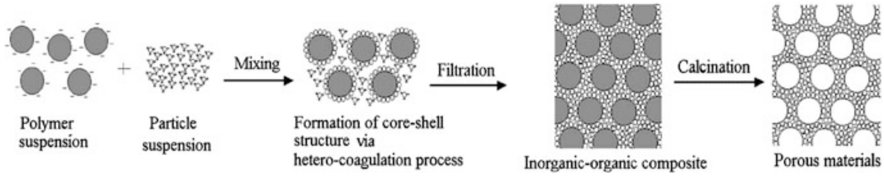

Fig. 3 Schematic procedure for the fabrication of porous materials via spherical polymer particle template and nanoparticles [44]. Reprinted from Tang et al. [77] copyright (2011), with permission from Elsevier

The nanoparticles should be surface modified to adjust the zeta potential suspension [1] to higher than 40 mV, such as using short chain organic compound 3,6,9-trioxadecanoic acid for ZrO_2 nanoparticles and polyethylenimine for Al_2O_3 and TiO_2 nanoparticles. The sacrificial organic species need to have opposite surface charges and large zeta potential vs. the nanoparticles under the same pH condition. γ-Al_2O_3 and poly(methyl methacrylate) (PMMA) particle mixtures have been studied with this principle (Fig. 3).

The electrostatic attraction of nanoparticles and PMMA enables the formation of stable core–shell composites of polymer/ceramics. The green body is then formed by vacuum filtration of the suspensions and humidity-controlled drying. The first step of the sintering process is to burn-out the PMMA template. A too high volume fraction of the decomposed organic gas might produce macro-cracks because of the lower diffusion rate of the generated gas molecules towards the sample surface compared to their formation rate. Therefore, the burn-out process should be chosen in air at very low heating rates (<0.2 °C/min). After the PMMA removal, the Al_2O_3 (34 nm) green body is sintered at 1100 °C for 2 h with a heating rate of 1 °C/min (the PMMA size used is 800 nm); the sintered pore size is 280 nm and the porosity is 75.5 %, which is very close to the theoretical porosity of close packed spheres (Fig. 4) [44]. The total and closed porosities slightly decrease with higher sintering temperatures. For ZrO_2 nanoparticle suspension (with 12 nm mean particle size) and 2 µm size PMMA sacrificial template, the synthesized porous ceramic has around 20 % porosity after being sintered at 1200 °C for 4 h [45]. The self-assembly of the polymer spheres enables the creation of ordered and uniform 3D porous materials [47, 48]. For example, ordered TiO_2 porous structure with $\sim$70 % porosity is fabricated by sintering polystyrene (160 nm – 1 µm) template with TiO_2 nanoparticles (50 nm). The pore size, wall thickness, and porosity of the materials can be controlled by adjusting the size of the polymer and the ratio of the nanoparticles to the polymer.

---

[1] Zeta potential is a measure of the surface charge of a particle in a liquid suspension. More precisely, it is the potential at the sliding plane when a particle is in movement under an electric field.

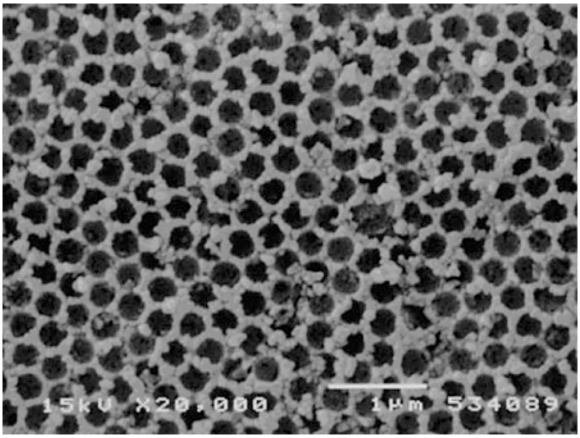

Fig. 4 Macroporous materials prepared with 34 nm γ-Al_2O_3 and 350 nm PMMA after sintering at 1100 °C for 2 h [44]. Reprinted from Tang et al. [77] copyright (2011), with permission from Elsevier

4.3 Reaction Sintering

During the sintering process, reaction(s) might occur and can be used to tailor the porosity of porous materials [49–55]. The large shrinkage of the nanoparticles due to the reaction within the green body leads to pores in the sample. The distribution and size of the pores can be controlled by the amount of the initial nanoparticles and the sintering conditions.

High strength porous Al_2O_3 is fabricated by spark plasma sintering using nanocrystalline $Al(OH)_3$ ($\sim$20 nm) as the starting powder (Fig. 5) [50]. After the spark plasma sintering between 1000 and 1200 °C with a uniaxial pressure of 10 MPa and a heating rate of 175 °C/min, the volumetric decrease due to the decomposition of $Al(OH)_3$ and the further shrinkage due to the θ-Al_2O_3 to α-Al_2O_3 phase transformation lead to vacant space near the decomposed particles. Thus porous Al_2O_3 with porosity ranging between 20 and 60 % is fabricated after sintering. The low sintering temperature and short holding time during the spark plasma sintering help to retain the fine pores and narrow pore size distribution in the Al_2O_3 matrix [51, 52]. At 1000 and 1050 °C the pore size distribution is extremely narrow and varies between 3 and 50 nm at 10 MPa pressure. Beyond 1100 °C the pore size distribution becomes wider and is around 100 nm. Increase in the pore size distribution has also been observed with increasing pressure at a constant temperature of 1050 °C. Therefore, the pore size distribution becomes wider and the pore size grows larger with the increases in sintering temperature and pressure. This is contrary to the normally observed phenomena that pores shrink and the pore distribution becomes smaller with increasing sintering temperature. Due to the relatively low spark plasma sintering temperature, the average grain size is retained around 50–150 nm. The dominance of the neck growth of grains during spark plasma sintering also leads to high fracture strength (150–300 MPa).

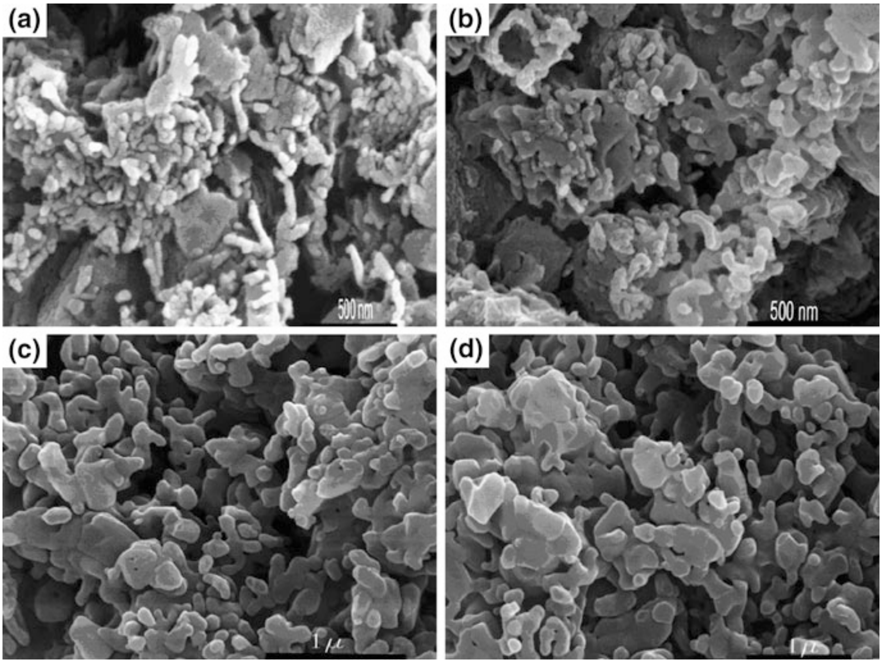

Fig. 5 SEM images of porous Al_2O_3 after sintering under 10 MPa pressure and at different sintering temperatures: **a** 1000 °C, **b** 1050 °C, **c** 1100 °C, and **d** 1150 °C, respectively [50]. Reprinted from Chakravarty et al. [78] copyright (2011), with permission from Elsevier

Similarly, Al_2O_3-based porous ceramics with high surface areas are fabricated through the mixture of Al_2O_3 and $Al(OH)_3$ powders by pressureless sintering at $>$1100 °C (Fig. 6) [53–55]. The green body is obtained by cold isostatic pressing under a pressure of ~30 MPa. Sintering is conducted in an air atmosphere with a heating rate of 1 °C/min at $<$1000 °C and a heating rate of 10 °C/min at $>$1000 °C. The sample is held at the sintering temperature for 30 min and then cooled down to room temperature at a rate of 10 °C/min. The pore size distribution of the porous Al_2O_3 is bimodal, with one peak at ~100 nm and the other at ~10 nm. The porosity is 40–60 %. The Al_2O_3 grains produced by the decomposition of $Al(OH)_3$ are several tens of nanometers in size. The fine pores (~10 nm) are located between these fine particles, and the large pores (~100 nm) are the channels between the large particles. The fine pores are formed due to the incomplete phase transformation of θ-Al_2O_3 (produced by decomposition of $Al(OH)_3$) to α-Al_2O_3. When the sintering temperature increases to $>$1200 °C, the fine pores disappear because of the complete phase transformation of θ-Al_2O_3. Due to the 60 % volume decrease during the decomposition of $Al(OH)_3$, the large pores in the specimen prepared from the powder with $Al(OH)_3$ are stable and can grow when the sintering temperature increases.

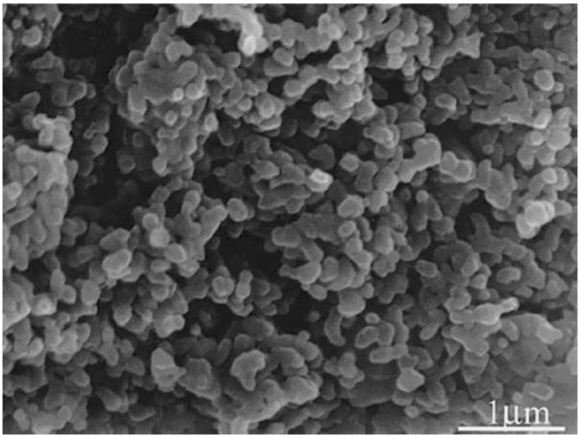

Fig. 6 SEM image of the fracture surface of the porous Al_2O_3 specimen prepared from Al_2O_3 powder with 60 vol % $Al(OH)_3$ in the mixture and sintered at 1200 °C (porosity 43.07 %) [53]. Reprinted from Deng et al. [79] copyright (2011), with permission from Elsevier

5 Nanoparticle-Based Porous Composites

As discussed, one challenge for nanoparticle-based material sintering is maintaining nanosized grains since nanoparticles experience extremely rapid grain growth during the sintering process due to their high surface energy and larger sintering driving force [56, 57]. Sintering of nanoparticle-based composites possesses the advantage of efficiently controlling the grain size either by prohibiting nanoparticle agglomeration and grain growth or by inducing chemical reactions between different species. The porosity of the sintered nanocomposites can be tailored by introducing foaming agents, controlling green density, conducting partial sintering, or using volume expansion from the reactions during the sintering process [58]. From nanoparticle function point of view, sintering of nanoparticle-based composites can be divided into two groups: nanoparticles act as initial materials or as a second phase. This section focuses on the sintering of porous composites, which can be made by either of the above strategies. The porosity and microstructure of the resulting nanocomposites and the role of different nanoparticles are discussed. Unique nanocomposite systems such as sintering of special starting powders are also included.

5.1 Nanoparticles as Initial Materials

For nanocomposite sintering, there can be one species [59] or multiple species [58, 60] with nanosized initial particles. A typical example for one species with nanosized initial particles is the sintering of SiO_2-kaolinite nanocomposite. In this system, SiO_2 particles are 22 nm in size, while kaolinite particles are micron-sized with disk-like shapes. In the composite preparation, the SiO_2 nanoparticles and kaolinite particles are first mixed in water. With the introduction of NaCl, the

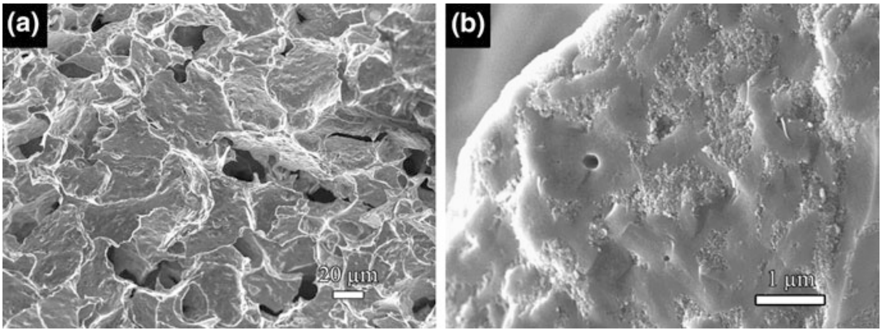

Fig. 7 Microstructures of SiO_2-kaolinite composite sintered at 1100 °C: **a** low maginifaction, **b** high magnification

suspension experiences a gel formation process. The prepared gel can be then freeze cast and sintered at 1100 °C. The microstructures of sintered SiO_2-kaolinite nanocomposite are shown in Fig. 7. The porous microstructures are fabricated by the sublimation of ice crystals during freeze drying and then partial sintering. The sintering process leads to the densification of the pore walls while maintaining the nanosized SiO_2 grains. Diffusion between SiO_2 nanoparticles and kaolinite particles occurs. Compared to the freeze cast green sample, the strength of the sintered SiO_2-kaolinite nanocomposite is greatly improved without significant loss of porosity.

The fabrication of Al_2O_3/Al_2TiO_5 porous composites is an example of nanoparticle sintering with multiple species of nanosized particles. The composites are produced by spark plasma sintering using 20–45 nm Al_2O_3 and 20–50 nm TiO_2 as raw materials [58].

Above 1280 °C, excess TiO_2 reacts with Al_2O_3 with an 11 vol% expansion per mole:

$$\alpha - Al_2O_3 + TiO_2(\text{rutile}) \rightarrow Al_2TiO_5 \tag{2}$$

The microstructures of the sintered Al_2O_3/Al_2TiO_5 composites are shown in Fig. 8. Pores with an average size of 15 µm (ranging from 1 to 35 µm) are homogeneously dispersed in the composite matrix. Due to the use of nanosized initial powders and spark plasma sintering technique, the composite possesses both porous structure and strong dense walls since necking between particles occurs at relatively low temperatures under the electric current and pressure. The resulting porous composites possess good mechanical properties, such as high flexural strength, fracture toughness, Vickers hardness, and elastic modulus [58]. These improvements are attributed to the combination of homogeneous Al_2O_3 and TiO_2 grains, the uniformly distributed pores, the strong ceramic walls, the necks between grains, and strengthened grain boundaries.

Another example is Al_2O_3/ZrO_2 nanocomposite fabricated by microwave sintering process [60]. The initial mean particle sizes of Al_2O_3 and ZrO_2 are 150 nm

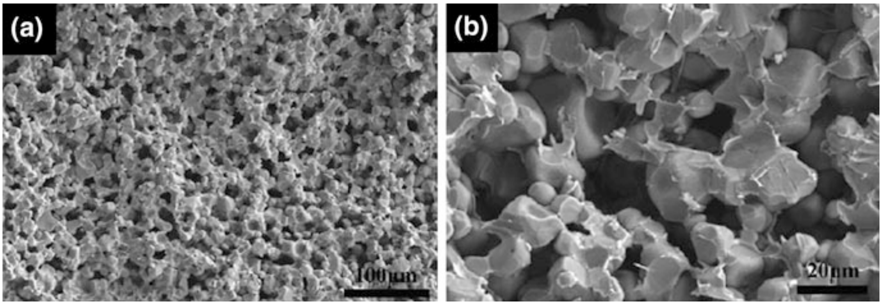

Fig. 8 Microstructures of the fracture surface of porous Al_2O_3/Al_2TiO_5 nanocomposites fabricated by spark plasma sintering: **a** low magnification, **b** high magnification [58]. Reprinted from Yang et al. [80] copyright (2011), with permission from Elsevier

and 50 nm, respectively. Since the microwave absorbency is sensitively dependent on the change of dielectric loss factors of materials with heat, ZrO_2 absorbs significant microwave energy due to its great increase of dielectric loss factor from 25 to 1000 °C [60]. Therefore, localized heating at Al_2O_3 boundaries (where ZrO_2 is situated) can be realized by microwave sintering. The preferential neck growth between grains is promoted by this selective heating; and the sintering temperature is lower than that of conventional sintering for the same sintered density. Porous nanocomposite of 55 % dense can be obtained by microwave sintering at 1000 °C for 15 min, whereas 1100 °C is required for the same sintered density for conventional sintering. In addition, the microwave sintered nanocomposites possess higher elastic modulus and fracture strength due to the growth of grain necks through surface diffusion.

5.2 Nanoparticles as Second Phases

Nanoparticles can act as a second phase in nanocomposite sintering [61–63]. Nanosized particles can disperse in the matrix, inhibit the grain growth, and adjust the grain size and mechanical properties [64–69]. For example, 5 vol % β-SiC nanoparticles with size less than 300 nm are added into 200 nm alumina (α-Al_2O_3) powders and sintered with a pulse electric current under an applied pressure of 5.5 MPa and a vacuum of 6 Pa to obtain a porous nanocomposite [64]. The starting powder mixture is ball-milled and sintered at 1000 °C for 15 min. In comparison, pure α-Al_2O_3 powder is sintered at 950 °C for 15 min. The fracture surface microstructures of the sintered samples are shown in Fig. 9. The nanosized SiC particles indicated by the arrows in Fig. 9a disperse at the boundaries of Al_2O_3 grains. Both samples possess around 20% porosity. However, obvious neck growth appears only in pure Al_2O_3 samples and the grain size of Al_2O_3 in the composites is smaller than that of the pure Al_2O_3 sample. This phenomenon indicates that the

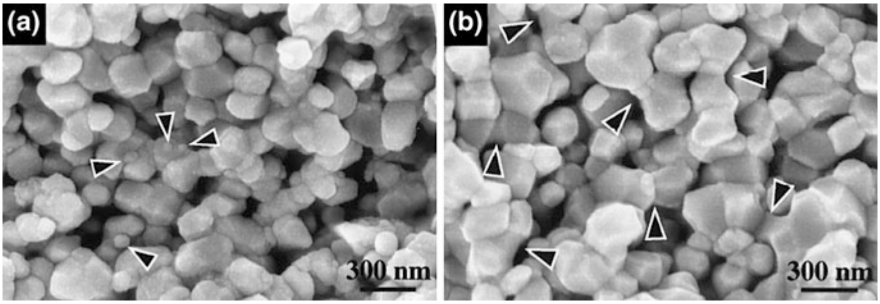

Fig. 9 Microstructures of the fracture surface of **a** sintered Al_2O_3/5 vol %-SiC nanocomposite at 1000 °C for 15 min, **b** sintered Al_2O_3 nanomaterial at 950 °C for 15 min, via pulse electric current sintering process. The *arrows* in **a** indicate the SiC nanoparticles, while the *arrows* in **b** show the neck growth [64] reprinted from Oh et al. [81] copyright (2011), with permission from Elsevier

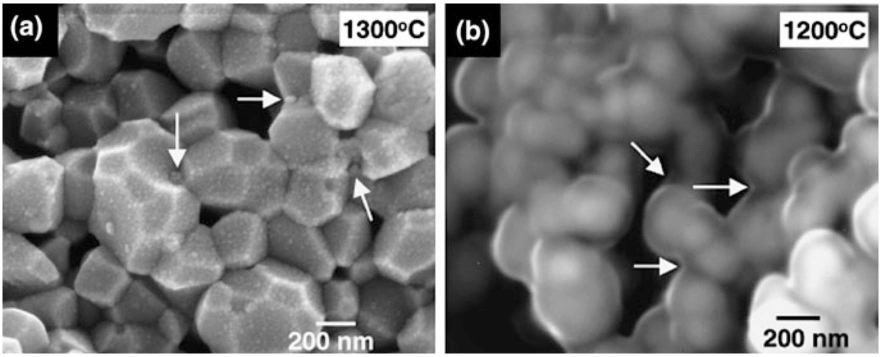

Fig. 10 Microstructure evolution of Al_2O_3 (200 ppm MgO)/3 vol % ZrO_2 composites sintered at: **a** 1300 °C and **b** 1200 °C [65] reprinted from Doni Jayaseelan et al. [82] copyright (2011), with permission from Elsevier

SiC nanoparticles located at the grain boundaries of the Al_2O_3 restrict the growth of the Al_2O_3 grains. With SiC nanoparticle addition, the mass transport by evaporation–condensation and surface diffusion is inhibited by the second phase, which creates an extra diffusion barrier. The refined microstructure reinforces the strength of the sintered nanocomposites.

The sintering behaviors of Al_2O_3 nanoparticles can also be modified by other secondary phases [65]. Figure 10 shows the microstructure evolution of Al_2O_3 (200 ppm MgO)/3 vol % ZrO_2 composites sintered at 1200 and 1300 °C by pulse electric current sintering. As indicated by the arrows, the ZrO_2 grains locate at the Al_2O_3 grain boundaries and restrict the grain growth. Similarly, MgO and TiO_2 dopants are able to inhibit the grain growth and affect the grain boundary mobility of Al_2O_3 according to the solute drag mechanism [66]. The strength of the resulting sintered nanocomposites is greatly improved without significant porosity

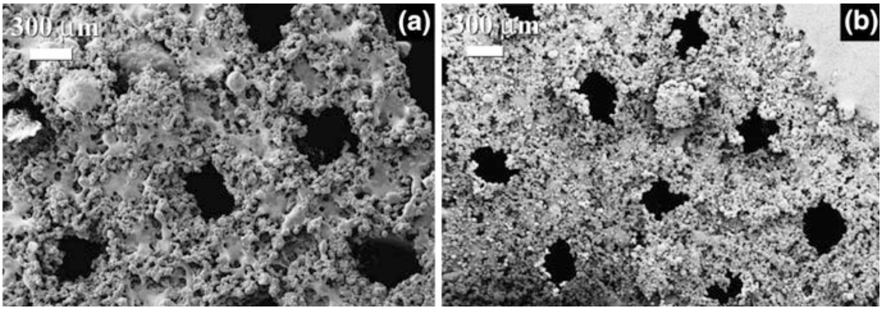

Fig. 11 SEM images of microstructures of sintered **a** PLLA scaffold, **b** PLLA/CHAp nanocomposite scaffold [67] Zhou [83]. With kind permission from Springer Science+Business Media

loss, due to the neck formation and the enhanced contacts between grains during the sintering process.

Porous scaffolds are made using nanoparticles as secondary phases during the sintering process. An example is selective laser sintering process, which is effective in producing porous nanocomposite scaffolds since it can control the microstructure and properties by adjusting sintering conditions such as laser power, scan spacing, and part bed temperature [67, 68]. Carbonated hydroxyapatite (CHAp) of 20 nm size is added into poly(L-lactide) (PLLA) at 10 wt % to fabricate nanocomposite microspheres, and sintered by a Sinerstation 2000 SLS machine [67]. The layer structures of the PLLA and PLLA/CHAp nanocomposite scaffolds are shown in Fig. 11 [67]. Both samples show a porous microstructure with a combination of macro-pores that are purposely designed and micro-pores that are formed by partial sintering. In comparison, the PLLA/CHAp nanocomposite scaffold has much smaller grain sizes while PLLA scaffold displays a higher degree of fusion within the particles. This is because the added CHAp nanoparticles locate on the boundaries of the PLLA and produce an extra barrier against fusion and diffusion during the sintering process. Calcium phosphate/poly(hydroxybutyrate-co-hydroxyvalerate) nanocomposite scaffolds (with calcium phosphate particle size in the range of 10–30 nm) fabricated by the selective laser sintering process have similar results on microstructure evolution [68].

Nanoparticles can also act as a second phase to inhibit the grain growth by chemical reaction. Porous Si_3N_4/SiC nanocomposites are fabricated by reactions between carbon and SiO_2 on the Si_3N_4 particle surfaces or carbon and Si_3N_4 particles, with porosity ranging from 50 to 70 % [69, 70]:

$$2C(s) + SiO_2(s) \rightarrow SiC(s) + 2CO(g) \tag{3}$$

$$3C(s) + Si_3N_4(s) \rightarrow 3SiC(s) + 2N_2(g) \tag{4}$$

At green state, Si_3N_4 particles are 0.5 μm and C particles are 13 nm. At high temperatures (above 1850 °C), α-Si_3N_4 transforms to β-Si_3N_4 which can be

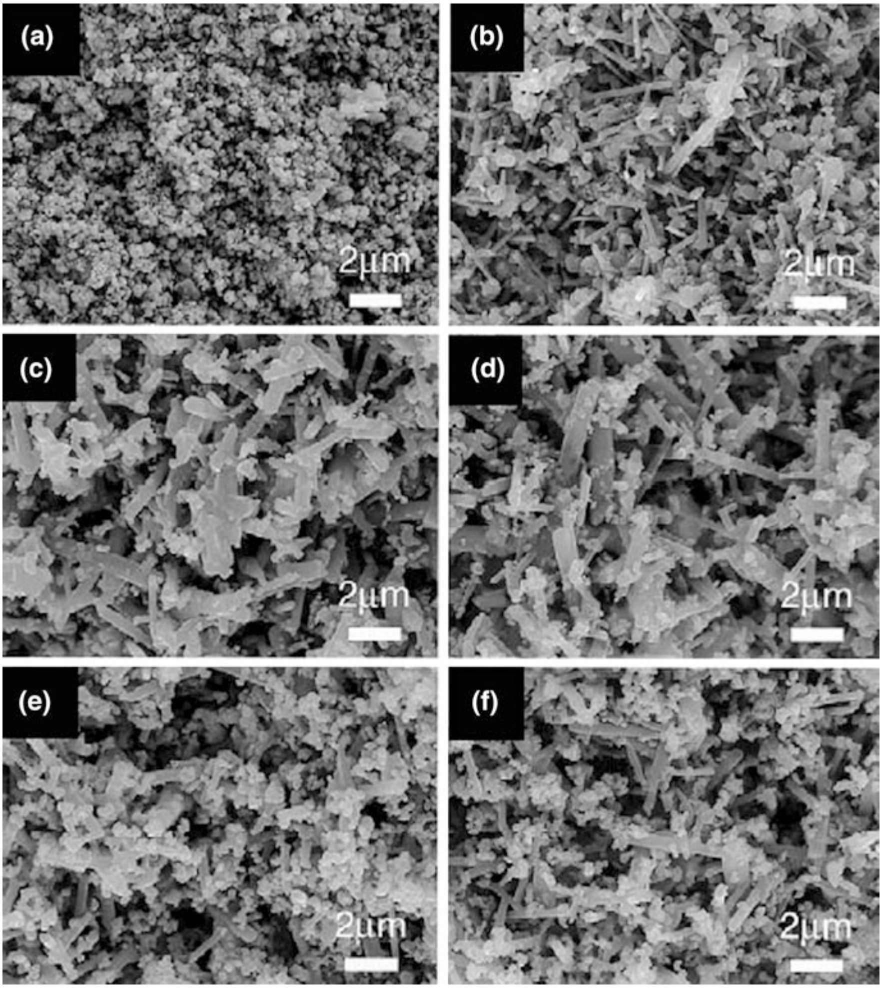

Fig. 12 SEM images of Si_3N_4/SiC nanocomposites: **a** 20 vol % SiC green body, **b** 20 vol % SiC sintered at 1750 °C, **c** 20 vol % SiC sintered at 1850 °C, **d** 20 vol % SiC sintered at 1900 °C, **e** 50 vol % SiC sintered at 1850 °C, and **f** 50 vol % SiC sintered at 1900 °C [69]. Reprinted from Yang et al. [84] copyright (2011), with permission from Elsevier

identified by its elongated morphology. SiC grains form according to the above chemical reactions. With the temperature increase, more elongated β-Si_3N_4 grains and SiC nano-grains appear, indicating the completion of the chemical reactions. The microstructure difference with various SiC contents can be seen by comparing Fig. 12c, e, d, and f. The high SiC solid loading corresponds to fine size grains. SiC nano-grains locate at the boundaries of β-Si_3N_4 grains, restrain the diffusion between the β-Si_3N_4 grains, and consequently prohibit the densification of the composite matrix. Thus, the porosity and microstructure of Si_3N_4/SiC

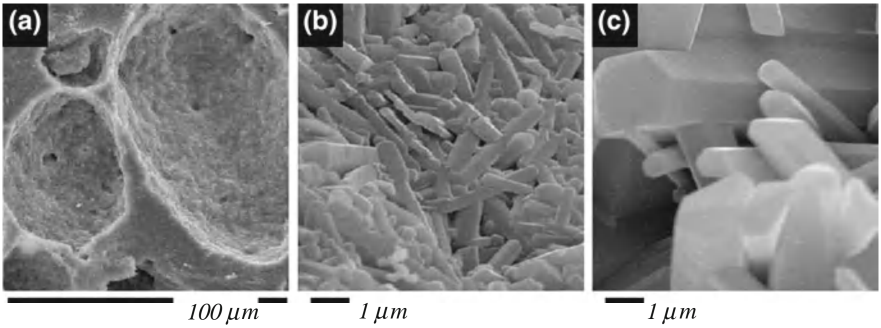

Fig. 13 Microstructures of sintered Si_3N_4-based porous composite: **a** low magnification showing large and small pores, **b** characteristic microstructure with β-Si_3N_4 grains, **c** well developed β-Si_3N_4 grains [71]. Reprinted from Doni Balázsi et al. [85] copyright (2011), with permission from Elsevier

nanocomposites can be controlled by adjusting the initial carbon content. In addition, varying the green density by applying pressure on the sample is also effective in modifying the resulting porosity.

The second phase nanoparticles can also act as a pore-forming agent. Si_3N_4-based composites are fabricated by hot isostatic pressing of starting powders consisting of Si_3N_4, Al_2O_3, Y_2O_3, and ~50–100 nm carbon black particles [71]. The powder is oxidized at 1000 °C for 150 h and then milled in ethanol. Sintering is applied to the prepared powder at 1700 °C with 2 MPa pressure for 1 h. With the continuous temperature increase, carbon nanoparticles are oxidized and removed as CO or CO_2, resulting in the formation of pores in the samples. The existence of pores provides space and promotes the phase transformation from α-Si_3N_4 to β-Si_3N_4. The microstructure of fabricated Si_3N_4-based composites is shown in Fig. 13. The porous composite possesses 20–100 µm large pores and 1–2 µm small pores.

5.3 Unique Nanocomposite Systems

Porous nanocomposites can also be obtained by taking advantage of unique starting powders. Copper coated SiC nanoparticles (average diameter 120 nm) are sintered in ammonia or nitrogen atmosphere, and porous or dense nanocomposites are obtained respectively [72]. In the ammonia atmosphere, ammonia decomposes at high temperature and the resulting H_2 reduces Cu_2O:

$$2NH_3 \rightarrow N_2 + 3H_2 \tag{5}$$

$$Cu_2O + H_2 \rightarrow 2Cu + H_2O \tag{6}$$

Copper melts at 1050 °C in this system and coagulates to form large blocks. Since the copper/SiC interface is non-wetting, segregation between SiC clusters and copper blocks occurs and results in porous microstructures. In contrast, when sintering is applied in the nitrogen atmosphere, Cu_2O remains in the system, promotes the wetting behaviors between copper and SiC, and leads to the formation of dense nanocomposites. The porosity of the resulting porous nanocomposites can be effectively controlled by modifying the sintering atmosphere.

Porous TiO_2/SiO_2 and TiO_2/ZrO_2 nanocomposites are fabricated by surfactant-template method [73]. After hydrolysis of titanium isopropoxide ($Ti(OPri)_4$) and zirconium propoxide (or tetraethyl orthosilicate [$Si(OC_2H_5)_4$]) with a surfactant (decaoxyethylene cetyl ether, $C_{16}(EO)_{10}$), the precursor is sintered at different temperatures from 350 to 800 °C. The well dispersed Si or Zr in the Ti matrix enhances the mechanical properties and thermal stabilities of the porous nanocomposites by inhibiting grain growth and maintaining surface areas (SiO_2 or ZrO_2 prohibits the phase transformation of TiO_2 from anatase to rutile). The second phases are also able to inhibit the grain growth and allow TiO_2 to maintain <10 nm size until 800 °C. As a result, the surface area of the nanocomposite is much higher than that of pure TiO_2 sample.

Porous nanocomposite can also be made by reduction reaction during sintering [74]. Tetragonal spinel $CuFe_2O_4$, formed by calcining CuO and α-Fe_2O_3 at 1000 °C in air, is sintered at 360 °C in H_2 atmosphere. Cu nanoparticles are synthesized by the reduction of $CuFe_2O_4$ and are well dispersed in the fine Fe_2O_3 matrix.

$$3CuFe_2O_4 + 4H_2 \rightarrow 3Cu + 2Fe_3O_4 + 4H_2O \tag{7}$$

Because of the immiscibility between copper and Fe_3O_4, the sintering of Cu nanoparticles is inhibited and the Cu nanoparticles are conserved. One possible explanation for the formation of porous structure is the removal of oxygen. Pores form in the Fe_3O_4 matrix as a result of loss of oxygen [74].

6 Summary

Sintering of nanoparticle-based porous materials has been driven by the need for manufacturing large surface area materials such as sensors, catalysts, and solar cell components. Different sintering techniques discussed in this chapter are a natural outgrowth of this development. The challenges in forming porous materials with desired microstructures while controlling grain growth have pushed the efforts to closely examine the critical sintering factors and design effective sintering processes. Each sintering technique has its own strength as well as limitation in meeting the specific needs.

At the fundamental level, there is a need to decouple densification and coarsening diffusion mechanisms so that porous materials can be obtained without incurring too much grain growth. The relative contribution of each diffusion mechanism should be assessed. The activation energy change of each diffusion mechanism with temperature should be quantified. Efforts are desired to understand and control the evolution of nanosized grains.

Three main methods are developed to fabricate porous, single composition materials by using nanoparticles. The partial sintering method maintains the porosity of nanoparticle-based samples by leaving a certain amount of porosity in the sample before terminating the sintering. The template method controls the pore size and porosity of the sintered materials by adjusting the size of the polymer template and the ratio of the polymer to the nanoparticles. The reaction sintering method relies on the volume shrinkage from the reactions during the sintering to obtain porous microstructures.

As for the sintering of porous nano-composite, nanoparticles can be used as either initial materials or a second phase. In the first situation, the nanoparticles are conserved by partial sintering and diffusion/reaction between species. When used as a second phase, the nanoparticles can inhibit the grain growth by either dispersing in the matrix or chemical reaction(s). The grain size and the corresponding mechanical properties are adjusted by the added nanoparticles. In addition, the second phase nanoparticles can act as a pore-forming agent, which introduces pores into the resulting composite. With modified starting powders, coated- and surfactant-adsorbed-particles are also used to fabricate nano-composites.

There is much work ahead in the field of nanoparticle-based porous material sintering. The prospects for further growth are evident with the expanding base of nanomaterials and sintering techniques. Advance in the scientific base by quantifying the microstructure-property-processing links for increasingly complex porous materials will remain to be a research focus. The beneficial impact from the new processing options includes shorter processing times, unique nanostructures, and in the long run, improved properties. Porous nanomaterial sintering also needs to improve the processing efficiency with low complexity and cost.

Acknowledgments The authors acknowledge the financial support from National Science Foundation under grant Nos. CMMI-0824741, CMMI-0969888, and CBET-0827246.

References

1. Kumar, B.V.M., Kim, Y.W., Adv. Mater. **11**(4), 044303-1-16 (2010)
2. Lefebvre, L.P., Banhart, J., Dunand, D.C.: Adv. Eng. Mater. **10**(9), 775–787 (2008)
3. Polarz, S., Smarsly, B.J.: Nanosci. Nanotechnol. **2**(6), 581–612 (2002)
4. Frenzer, G., Maier, W.F.: Annu. Rev. Mater. Res. **36**, 281–331 (2006)
5. Rowsell, J.L.C., Yaghi, O.M.: Microporous Mesoporous Mater. **73**(1–2), 3–14 (2004)
6. Schuth, F.: Annu. Rev. Mater. Res. **35**, 209–238 (2005)
7. Levine, B.: Adv. Eng. Mater. **10**(9), 788–792 (2008)
8. Simske, S.J., Ayers, R.A., Bateman, T.A.: Mater. Sci. Forum **250**, 151–182 (1997)
9. McColm, I.J.: Dictionary of Ceramic Science and Engineering. Plenum Press, New York (1994)
10. German, R.M.: Sintering Theory and Practice. Wiley, New York (1996)
11. Kuczynski, G.C.: Met. Trans. **185**, 896–897 (1949)

12. Kingery, W.D., Berg, M.: J. Appl. Phys. **26**, 1205–1212 (1955)
13. Coble, R.L.: J. Am. Ceram. Soc. **41**, 55–62 (1958)
14. Johnson, D.L.: J. Appl. Phys. **40**, 192–200 (1969)
15. Nishikawa, Y., et al.: Langmuir **14**(5), 1242–1249 (1998)
16. German, R.M.: Sintering Theory and Practice. Wiley, New York (1996)
17. Barsoum, M.W.: Fundamentals of Ceramics. The McGraw-Hill Companies Inc., New York (1997)
18. Mayo, M.J., Hague, D.C., Chen, D.J.: Mater. Sci. Eng. A **166**(1–2), 145–159 (1993)
19. Skandan, G., et al.: Mater. Lett. **20**(5–6), 305–309 (1994)
20. Risbud, S.H., et al.: J. Mater. Res. **10**(2), 237–239 (1995)
21. Lee, H.Y., Riehemann, W., Mordike, B.L.: J. Eur. Ceram. Soc. **10**, 245–253 (1992)
22. Hahn, H.: Nanostruct. Mater. **2**, 251–265 (1993)
23. Skandan, G.: Nanostruct. Mater. **5**(2), 111–126 (1995)
24. Mayo, M.J.: Mater. Des. **14**, 323–329 (1993)
25. Zhou, Y.C., Rahaman, M.N.: J. Mater. Res. **8**(7), 1680–1686 (1993)
26. Rabe, T., Waesche, R.: Nanostruct. Mater. **6**, 357–360 (1995)
27. Maheshwari, P., Fang, Z.G.Z., Sohn, H.Y.: Int. J. Powder. Metall. **43**(2), 41–47 (2007)
28. Dominguez, O., Champion, Y., Bigot, J.: Metall. Mater. Trans. A **29A**, 2941–2949 (1998)
29. Malewar, R., et al.: J. Mater. Res. **22**(5), 1200–1206 (2007)
30. Oda, E., Ameyama, K., Yamaguchi, S.: Mater. Sci. Forum **503–504**, 573–578 (2006)
31. Wang, H.; Fang, Z.Z.: Study of size-dependant sintering behavior of tungsten powders. In: Proceedings 2008 International Conference on 'Tungsten, refractory and hardmaterials VII', Washington, DC, USA, June 2008, Metal Powder Industries Federation, 2008, 05.72–05.77
32. Maca, K., Trunec, M., Dobsak, P.: Rev. Adv. Mater. Sci. **10**(1), 84–88 (2005)
33. Hynes, A.P., Doremus, R.H., Siegel, R.W.: J. Am. Ceram. Soc. **85**(8), 1979–1987 (2002)
34. Fang, Z.Z., Wang, H.: Int. Mater. Rev. **53**(6), 326–352 (2008)
35. Chen, I.W., Wang, X.H.: Nature **404**(6774), 168–171 (2000)
36. Wang, X.H., Chen, P.L., Chen, I.W.: J. Am. Ceram. Soc. **89**(2), 431–437 (2006)
37. Wang, X.H., et al.: J. Am. Ceram. Soc. **89**(2), 438–443 (2006)
38. Jo, S.H., Muralidharan, P., Kim, D.K.: Solid State Ion. **178**(39–40), 1990–1997 (2008)
39. Deng, Z.Y., et al.: J. Am. Ceram. Soc. **85**(8), 1961–1965 (2002)
40. Deng, Z.Y., et al.: Acta Mater. **51**(3), 731–739 (2003)
41. Gajovic, A., et al.: J. Am. Ceram. Soc. **89**(7), 2196–2205 (2006)
42. Gajovic, A., et al.: J. Alloy Compd. **479**(1–2), 525–531 (2009)
43. Jakubowicz, J., Smardz, K., Smardz, L.: Physica E **38**(1–2), 139–143 (2007)
44. Tang, F.Q., et al.: J. Eur. Ceram. Soc. **24**(2), 341–344 (2004)
45. Cruz, H.S., Spino, J., Grathwohl, G.: J. Eur. Ceram. Soc. **28**(9), 1783–1791 (2008)
46. Tang, F., et al.: Chem. Lett. **32**(3), 276–277 (2003)
47. Qi, L., Sorge, J.D., Birnie, D.P.: J. Am. Ceram. Soc. **92**(9), 1921–1925 (2009)
48. Wang, D.Y., et al.: Adv. Mater. **14**(12), 908–912 (2002)
49. Yang, Y., et al.: Scripta Mater. **60**(7), 578–581 (2009)
50. Chakravarty, D., Ramesh, H., Rao, T.N.: J. Eur. Ceram. Soc. **29**(8), 1361–1369 (2009)
51. Jayaseelan, D.D., et al.: J. Am. Ceram. Soc. **85**(1), 267–269 (2002)
52. Oh, S.T., Tajima, K., Ando, M., Ohji, T.: J. Am. Ceram. Soc. **83**(5), 1314–1316 (2000)
53. Deng, Z.Y., et al.: J. Am. Ceram. Soc. **84**(11), 2638–2644 (2001)
54. Deng, Z.Y., et al.: J. Am. Ceram. Soc. **84**(3), 485–491 (2001)
55. Deng, Z.Y., et al.: Acta Mater. **49**(11), 1939–1946 (2001)
56. Fang, Z.Z., Wang, H.: Int. Mater. Rev. **53**(6), 326–352 (2008)
57. Lu, K.: Int. Mater. Rev. **53**(1), 21–38 (2008)
58. Yang, Y., et al.: Scripta Mater. **60**(7), 578–581 (2009)
59. Fujita, H., et al.: J. Am. Ceram. Soc. **87**(2), 261–267 (2004)
60. Oh, S.T., et al.: Mater. Lett. **48**(3–4), 215–218 (2001)
61. Tuan, W.H., Huang, Y.C.: Mater. Chem. Phys. **118**(1), 187–190 (2009)
62. Cao, M.R., Wang, S.B., Han, W.B.: Mater. Sci. Eng. A **527**(12), 2925–2928 (2010)

63. Pee, J.H., et al.: Res. Chem. Intermed. **36**(6–7), 801–809 (2010)
64. Oh, S.T., et al.: J. Am. Ceram. Soc. **83**(5), 1314–1316 (2000)
65. Jayaseelan, D.D., et al.: J. Am. Ceram. Soc. **85**(1), 267–269 (2002)
66. Bennison, S.J., Harmer, M.P.: J. Am. Ceram. Soc. **68**(1), C22–C24 (1985)
67. Zhou, W.Y., et al.: J. Mater. Sci. Mater. Med. **19**(7), 2535–2540 (2008)
68. Duan, B., Wang, M.: Polym. Degrad. Stab. **95**(9), 1655–1664 (2010)
69. Yang, J.F., et al.: Acta Mater. **50**(19), 4831–4840 (2002)
70. Yang, J.F., Zhang, G.J., Ohji, T.: J. Am. Ceram. Soc. **84**(7), 1639–1641 (2001)
71. Balazsi, C., et al.: J. Eur. Ceram. Soc. **24**(12), 3287–3294 (2004)
72. Zhang, R., Gao, L., Guo, J.K.: Compos. Part A-Appl. Sci. Manuf. **35**(11), 1301–1305 (2004)
73. Chen, X.F., Wang, X.C., Fu, X.Z.: Energy Environ. Sci. **2**(8), 872–877 (2009)
74. Kameoka, S., Tanabe, T., Tsai, A.P.: Appl. Catal. A **375**(1), 163–171 (2010)
75. Deng, Z.-Y., Zhou, Y., Inagaki, Y., Ando, M., Ohji, T.: Role of Zr(OH)4 hard agglomerates in fabricating porous ZrO2 ceramics and the reinforcing mechanisms, Acta Mater. **51**(3) (2011)
76. Šantić, A., Djerdj, I., Tomašić, N., Moguš-Milanković, A., Sheng Su, D.: Structure and electrical conductivity of porous zirconium titanate ceramics produced by mechanochemical treatment and sintering, J. Alloy. Compd. **479**(1−2) (2011)
77. Tang, F., Fudouzi, H., Uchikoshi, T., Sakka, Y.: Preparation of porous materials with controlled pore size and porosity , J. Eur. Ceram. Soc. **24**(2) (2011)
78. Chakravarty, D., Ramesh. H., Rao, T.N.: High strengh porous alumina by spark plasma sintering, J. Eur. Ceram. Soc. **29**(8) (2011)
79. Deng, Z.-Y., Fukasawa, T., Ando, M.: Microstructure and Mechanical Properties of Porous Alumina Ceramics Fabricated by the Decomposition of Aluminum Hydroxide , J. Amer.Ceram. Soc. **84**(11) (2011)
80. Yang, Y., Wang, Y., Tian, W., Wang, Z., Li, C.-G., Zhao, Y ., Blan, H.-M.: In situ porous alumina/aluminum titanate ceramic composite prepared by spark plasma sintering from nanostructured powders, Scripta Mater. **60**(7) (2011)
81. Oh, S.-T., Tajima, K.-I., Ando, M., Ohji, T.: Strengthening of porous alumina by pulse electric current sintering and nanocomposite processing, J. Amer. Ceram. Soc. **83**(5) (2011)
82. Doni Jayaseelan, D., Kondo, N., Brito, M.E.,Ohji.T.: High strength porous alumina ceramics by the pulse electric current sintering technique, J. Amer. Ceram. Soc. **85**(1) (2011)
83. Zhou, W.Y.: j mater sci mater med. **19** (2007)
84. Yang, J.-F., Zhan, G.-J., Kondo, N., Ohji, T.: Synthesis and properties of porous Si3N4/SiC nanocomposites by carbothernal reaction between Si3N4 and carbon, Acta Meter. **50**(19) (2011)
85. Balázsi, Cs.,Clinar, F.S., Addemir, O., Wéber, F., Arató, P.: Manufacture and examination of C/Si3N4 nanocomposites, J. Eur. Ceram. Soc. **24** (12) (2011)

Electric Field and Current Effects on Sintering

Zuhair A. Munir, Dat V. Quach and Manshi Ohyanagi

Abstract The goal of consolidating powders to achieve high densities at lower temperatures and with a small grain size has motivated considerable efforts in the search for methods to activate the sintering process. Enhancement of the consolidation process has been attempted through various approaches including mechanical activation of the powders, the addition of sintering aids, and the use of electromagnetic fields. The latter approach has received considerable attention in recent years, largely due to the widespread use of devices utilizing current and pressure to consolidate powders. The Spark Plasma Sintering method (also known by other names) has seen a remarkable increase in its utilization over the past two decades. This was largely due to the many significant, and in some cases, unique accomplishments. In this chapter we will focus then on the role of the electric field in sintering with emphasis on recent observations, particularly those pertaining to the consolidation of nanostructured materials.

Z. A. Munir (✉) · D. V. Quach
Department of Chemical Engineering and Materials Science,
University of California, Davis, CA 95616, USA
e-mail: zamunir@ucdavis.edu

M. Ohyanagi
Department of Materials Chemistry, Ryukoku University, Ohtsu, Japan

R. H. R. Castro and K. van Benthem (eds.), *Sintering*, Engineering Materials 35,
DOI: 10.1007/978-3-642-31009-6_7, © Springer-Verlag Berlin Heidelberg 2013

1 Introduction

Spark plasma sintering (SPS)[1] is a process that involves the consolidation of powders under the action of a current and a uniaxial pressure. The current provides Joule heating to achieve the sintering conditions, thus making the process fundamentally different from hot pressing. Figure 1 shows a schematic representation of an SPS machine. In a typical sintering experiment, the sample (powder) is loaded into a graphite die, and placed inside the SPS chamber, where electrodes force a current through the graphite die (and through the sample if it is conducting) to promote high heating rates and with combined pressure application.

The nature of SPS method along with its accomplishments has been discussed in recent reviews [1, 2]. Among the benefits of this process, the shorter times of consolidation when compared to other methods and the capability to diminish grain growth are the most attractive features, especially when in the preparation of nanostructured dense materials. The question then arises as to the role of the applied field (or current) in influencing the sintering behavior and making possible the reported accomplishments.

As was stated in the cited review articles, the use of an electric field (or current) is not new and its beginning is more than a century old [2]. However, only relatively recently has there been a significant effort devoted to the understanding of the role of the field in sintering. The observed enhancement of sintering in the presence of an applied field has been attributed in different materials systems to different roles, including Joule heating [3], the alteration of the grain boundary characteristics [4], electromigration [5], the electrostatic interaction with grain boundary charge [6], and the cleansing of surface impurities [7]. The latter relates to the SPS process, which uses a pulsed DC current. The concept originates from a proposal that plasma is generated during the pulsing of the current and that its existence leads to the destruction of surface films. However, conflicting observations have been reported and the more convincing of these suggest the absence of plasma [8–11].

In what follows we will focus on the effect of the field on mass transport, on the sintering process, both in general and under SPS conditions, and on selected remarkable achievements made with the influence of the field. It should be pointed out at the outset that the observed phenomena are due to both field and current contributions.

---

[1] Several names have been proposed for SPS. The diversity of names comes from the limit understanding of the process mechanisms. Among the names one will find Current Activated and Pressed Assisted Densification (CAPAD), Electric Field Assisted Sintering (EFAS), Pulsed Electric Current Sintering (PECS), and others. We will use SPS in this chapter as is the most accepted for historical reasons.

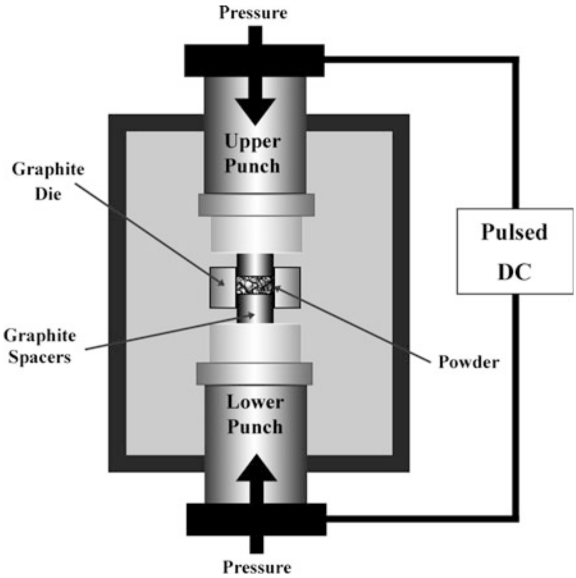

Fig. 1 Schematic representation of a generic SPS machine, using a pulsed electric current to heat up the sample and graphite dies to press the powder simultaneously

2 Effect of Electric Field on Mass Transport

The effect of an electric field or current on mass transport has been demonstrated in numerous studies, including reactivity between metals, oxides, and metals and ceramics. Studies have also demonstrated the effect of the field on grain boundary mobility in oxide systems.

2.1 Field Effects on Reactivity and Diffusion

More than three decades ago, Mackenzie and co-workers investigated the effect of an electric field on solid-state reactions between oxides and demonstrated an enhancement of product formation in the presence of the DC field [12–15]. They investigated phase formation and species diffusion in the systems Al_2O_3-CaO, Al_2O_3-MgO, and CaO-SiO_2. The field was shown to shift the concentration profiles of diffusing species downfield. The displacement of the profile, Δ, is dependent on the effective electrical mobility of the migrating species,[2] μ_{eff}, and the field such that,

$$\Delta = \mu_{eff} Et \tag{1}$$

---

[2] Effective electrical mobility is defined by the net movement in the direction of the field, disregarding the random movement of the charged specie.

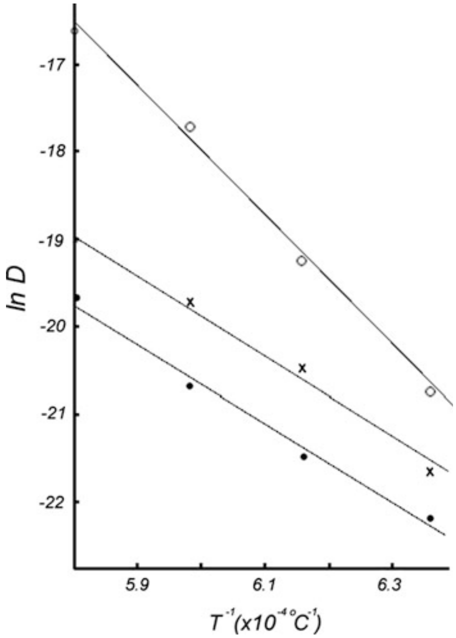

Fig. 2 Diffusion coefficient (D) of Mg in MgO/Al_2O_3 diffusion couple: annealing time = 48 h; • no field, x electrolyzed with alumina pellet positive, and ○ electrolyzed with alumina pellet negative; mean field strength = 5×10^4 V m^{-1}. Adapted from Ref. [14]

where E is the field strength and t is time. In these experiments, Mackenzie and co-workers employed high fields, with values in the proximity of 10^5 V.cm^{-1}. The effect of the field and its polarity on reactivity in the system MgO-Al_2O_3 is demonstrated by Fig. 2 in which the temperature dependence of the diffusion coefficient of Mg is depicted for the cases where no field was applied and where an applied field with negative and positive polarity was imposed on the alumina side [14]. The figure shows a substantial increase in the diffusion coefficient in the temperature range 1300–1450 °C when a field was applied relative to the case of no electric field, with the alumina side being the negative pole. A lesser increase was observed when the field was imposed such that alumina is the positive electrode. These results were interpreted in terms of field-enhanced diffusion of Mg into Al_2O_3 when alumina is negatively biased.

Similar conclusions were reached in more recent investigations on the role of an electric field with regards to field-enhanced reactions. Korte et al. [16, 17] investigated the formation of the spinel $MgIn_2O_4$ from a reaction between MgO and In_2O_3 with and without the application of a field of 20 V.cm^{-1}. The field was found to significantly enhance the formation of the spinel [17]. The grain boundaries of the starting materials were found to play an important role in the enhancement of the reaction, acting as fast diffusion paths.

Studies on the influence of an electric field (and induced current) on reactions in multi-layer metallic systems have demonstrated significant effects on the kinetics of product phase formation [18–21]. In these experiments a three-layer geometry (e.g. Al–Au-Al) was utilized so that the effect of the polarity of the DC current can

Fig. 3 Effect of electrical current on the growth rate of intermetallic layer forming between Al and Au layers. Adapted from Ref. [20]

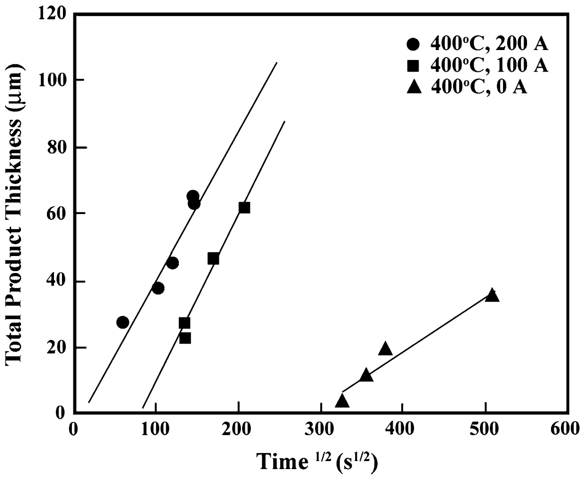

be determined. The results, exemplified by Fig. 3 for the Au–Al system [20, 21], showed a significant influence of the current on the formation of intermetallic phases between Al and Au. The samples were annealed at 400 °C under different currents, as indicated in the figure. The growth rate (from the slope of the lines) and the incubation time for the nucleation of the product phase (from the extrapolation to zero thickness) are highly dependent on the value of the imposed current.

When annealing is carried out in the absence of a current (Fig. 3), the product layer is not noticeable until after more than 20 h of annealing. But when a current density of 10^3 A.cm^{-2} was imposed during annealing, the incubation time is about zero. Observations of a similar nature were made in a study on the Ni–Ti system [19]. In this case, it was shown that the intrinsic growth rate constant could be as much as a factor of 40 higher with the application of the current.

In the above investigations it was observed that the direction of the DC current had no effect on the growth of the product layer. Similar observations were made in studies of the field effect on the reactivity in an SPS apparatus (where the electric field is small but currents are high). In studies on the reactivity between Mo and Si [22] and between carbon and refractory metals [23–25], no dependence on the direction of the current was observed.

On the assumption that the observed effect is driven by electromigration, the lack of dependence on the polarity of the field (direction) is attributed to the need to maintain stoichiometry and structure of the newly formed phase, and hence the diffusion of both species. That is, the process rate is limited by the kinetics of phase formation, and not the diffusion of components to the interface. In cases where no compound results from the interaction (e.g., in the case of the Ni–Cu system), the direction of the field (or current) was shown to be important. Using a three-layer setup with a nickel foil sandwiched between two copper foils, the direction of the current had a pronounced effect. Figure 4 shows the concentration

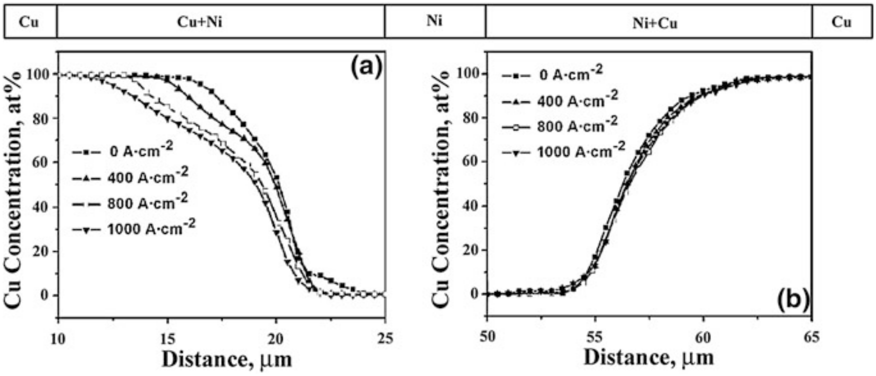

Fig. 4 Concentration profile of Cu in **a** concurrent region and in **b** countercurrent region. Adapted from [26]

Fig. 5 Effect of current density on the interdiffusion coefficient at 40 at % Cu. Adapted from [26]

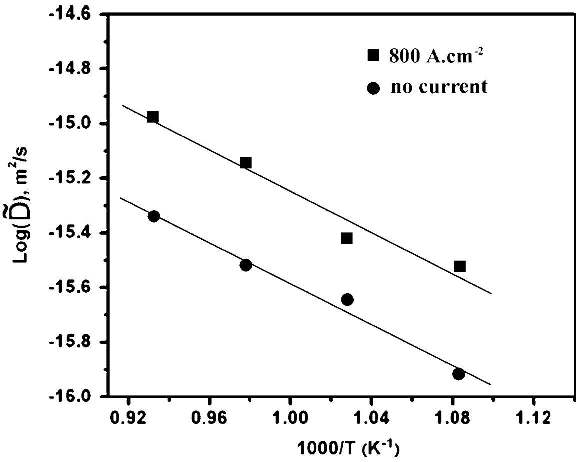

profiles of copper at the two interfaces in the layer system Cu–Ni–Cu as a function of the applied current density [26]. The interface one on the left (Fig. 4 a) is for the case where the electrons flow is from the nickel to copper (from right to left) and the interface on the right (Fig. 4b) is for electron flow from copper to nickel.

These results show a significant dependence on current direction, as anticipated from the electromigration enhanced diffusion flux. The effect of the field (current) can be clearly seen by examining its influence on the interdiffusion coefficient, $\check{D}$,

$$\check{D} = D_{Ni}X_{Cu} + D_{Cu}X_{Ni} \tag{2}$$

where X_{Cu} and X_{Ni} are the atomic fractions of copper and nickel, respectively. And D_{Cu} and D_{Ni} are the intrinsic diffusivities of copper and nickel, respectively. The effect of the current on $\check{D}$ is shown in Fig. 5. $\check{D}$ was calculated from concentration profiles, and plotted as a function of the inverse of temperature in an Arrhenius plot. Note that the activation energy (from the slope), for this composition is unchanged, but the absolute numbers for inter diffusion is significantly shifted up when applying 800 A.cm^{-2}.

2.2 Field Effect on Grain Boundary Mobility

Grain boundaries play an important role in mass transport in such solid-state processes as sintering, reactivity, and phase transformation. Thus any alteration of the character of the boundaries, whether structurally, compositionally, or electrostatically is expected to have an influence on these processes. The influence of field application on grain boundary mobility has been demonstrated in recent experiments [6, 27, 28], as will be discussed below. In the absence of other effects including an interfacial charge, the rate of grain boundary mobility is governed by the rate at which atoms cross it, a process that is dictated by capillary driving force related to curvature of the boundary and hence size of the grain (see Chaps. 1 and 3). However, in ionic solids the difference in the energy of formation of anion and cation defects results in the creation of a charge and an electrostatic potential at the grain boundary and a compensating layer, the space charge layer, adjacent to the boundary [29, 30]. The influence of electric fields on interface-related (surface and grain boundary) processes has been investigated before in several studies. These include the influence of the field on the mobility of low-angle grain boundaries [31] and on the sublimation of single crystals of alkali halides [32–34]. In addition to point defect considerations, as above, interfacial charge can result from the presence of impurities (aliovalent dopants).

In the presence of a grain boundary charge, the activation energy for an ion crossing the grain boundary is [6],

$$\Delta G_i = \Delta G_i^0 - z_i \cdot e \cdot s \left[\frac{\partial \phi}{\partial x} \right]_{x=0} \tag{3}$$

Where ΔG_i^0 is the activation energy for an ion crossing a boundary that has no charge, z_i is the charge of the ion, e is the elementary charge, s is the distance of the jump of the ion, ϕ is the electrostatic potential at the boundary (resulting from the charge at the boundary), and x is the direction along which the ion is moving. The potential gradient is evaluated at the grain boundary ($x = 0$). When an electric field is also imposed, the migration energy (driving force, ΔG_m) for the ion to jump across the interface can be approximated as [6],

$$\Delta G_m \cong \Delta G_c + z_i \cdot e \cdot s \left[\frac{U_B}{2 l_D} \right] \tag{4}$$

where ΔG_c is the driving force due to the difference in curvature (related to grain size), U_B is the applied (biased) voltage for one grain boundary, and l_D is the

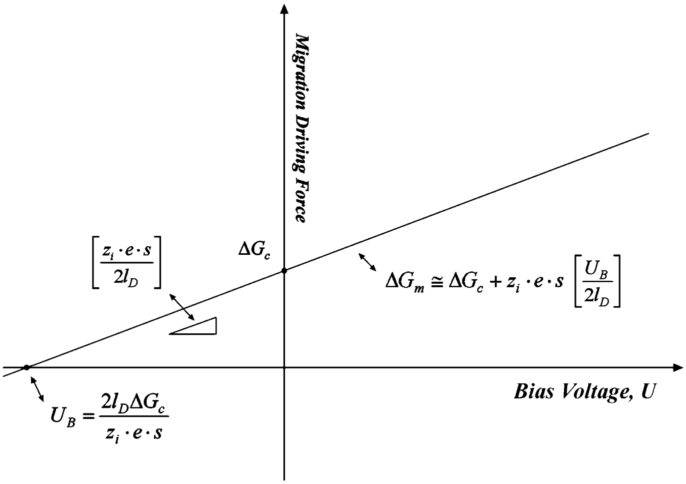

Fig. 6 A schematic on the effect of bias voltage on the activation energy for grain boundary migration [6]

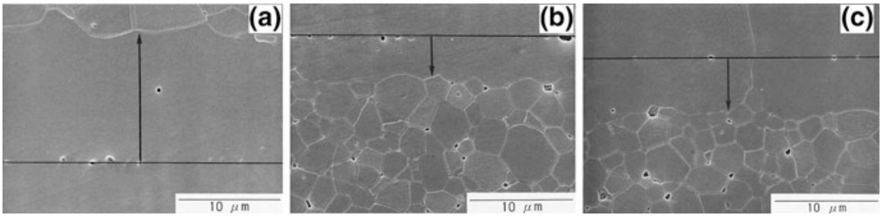

Fig. 7 Effect of polarity of a bias of 2 × 10 4 V.m^{-1} on grain boundary migration of alumina during heat treatment at 1600 °C for 2 h: **a** small-grained region is positively biased **b** small-grained region is negatively biased, and **c** no bias [6]

Debye length (width of space charge region). A schematic plot of the changes of ΔG_m with the bias for a grain boundary, U_B, is shown in Fig. 6.

When the grain boundary bias is zero, the driving force is due to curvature, ΔG_c. And in order to overcome this driving force, a bias in the opposite direction is needed of magnitude, $U_B = \frac{2l_D \Delta G_c}{z_i \cdot e \cdot s}$.

To assess these predictions, Jeong et al. [6] investigated the effect of an electric field on the mobility of grain boundary in alumina. They formed a bilayer of alumina in which the grain size in one layer was significantly larger than in the other (~170 and ~4 μm) and annealed these at 1600 °C for 2 h under a field of 200 V.cm^{-1}. Since the grain boundaries of Al_2O_3 have a positive charge [35], the polarity of the applied field had a significant effect on the grain boundary displacement. They observed a significantly higher mobility (displacement) when the small grain side was positively biased relative to the case when it was negatively biased, as seen in Fig. 7. In the figure, the horizontal line represents the position of

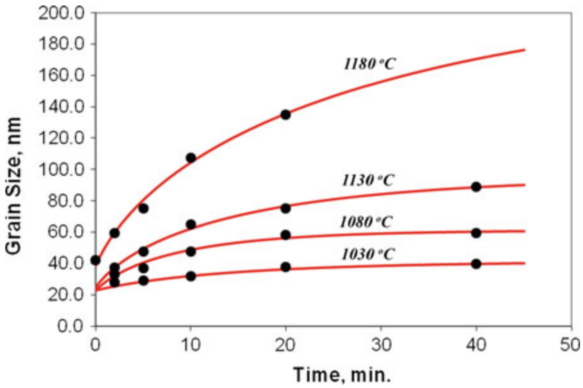

Fig. 8 Grain growth under pulsed electric current treatment of 8 mol % YSZ for different sintering temperatures as indicated in the figure [39]

the grain boundaries at time zero, and size of the vertical line with an arrow shows the distance of movement (scale bars are the same for consistency).

3 Observations on the Effect of an Electric Field on Sintering

In addition to the studies cited above in which the application of a field was shown to have an influence on mass transport and grain boundary mobility, other recent investigations have shown an effect on grain growth. Field-induced grain growth retardation was observed in YSZ (3 mol % Yttria) [36–38] and in the sintering of YSZ (8 mol % yttria) [39]. In the former, the retardation was explained in terms of changes to the grain boundary properties (e.g. the grain boundary energy). In the latter study [39], grain growth retardation kinetics were investigated for the case of 8Y-YSZ under SPS conditions. The results, depicted in Fig. 8, show the grain size evolution for 8Y-YSZ at different temperatures with the best-fit curves based on grain boundary retardation with grain size dependence according to the relationship [40],

$$\frac{dr(t)}{dt} = \frac{a}{r(t)} - br(t) \tag{5}$$

where r is grain size, t is time, a is a temperature dependent constant, and b is a constant (refer to the third chapter of this book, by Liu and Gong, for details on the constants).

In the referenced study, the activation energy for grain growth was determined to be 252 ± 34 kJ mol^{-1}. This value is at the low end of the range of values reported in the literature (226–340 kJ mol^{-1}) for grain growth of 8Y-YSZ [41–43], and is close to the value reported for nanocrystalline cubic-YSZ consolidated in a hot press. Thus, these results indicate that the application of a field during sintering had no apparent influence on the activation energy. Similar conclusions were arrived at in a different study by Yang and Conrad on 3Y-YSZ [36].

A related investigation by Ghosh et al. [35] on tetragonal YSZ showed that the application of a modest field (<4 V.cm^{-1}) resulted in a smaller grain size. They proposed that the application of the field altered the interfacial energy and thus reduced the driving force for grain growth. Conrad and Yang [36, 37] investigated the effect of AC and DC fields on the plastic deformation of tetragonal-YSZ and again demonstrated that the imposition of the field retarded grain growth in this oxide. Grain growth retardation was attributed to possible field effects, such as an increase in the segregation of Y ions at grain boundaries, a decrease in grain boundary energy, or a decrease in Y ion mobility. The implications of these proposed effects are significant, especially in light of the recent success in obtaining, for the first time, dense cubic-YSZ with very small grain size (as low as 13 nm) and the discovery that in this microstructural form, the oxide conducts by protons, as will be discussed in a later section of this chapter.

Although as indicated above, field effects on various materials processing and transformation have been investigated for many decades, the renewed focus on this topic has been largely the consequence of the widespread use of the SPS method [1, 2]. In addition to the success of sintering to higher density in shorter time, the use of this method has been shown to produce sintered materials with better properties relative to the same materials consolidated by other means. Many examples have been given and discussed in the literature, as indicated in the cited review articles [1, 2]. That the field (and/or current) plays a role in sintering in the SPS has been indirectly demonstrated, for example by the increased reactivity due to the application of a current [22–25]. However, direct demonstration of the role of the current is not possible in the SPS without experimental modifications since the current and temperature are dependent variables. The nature of these modifications and the results of the study made will be discussed subsequently in this section.

However, the most recent investigations on the effect of a field on sintering were not made under SPS condition, thus providing evidence of field effects independent of pressure. Conrad and co-workers [4, 44] and Raj and co-workers [3, 45–47] have investigated the sintering of YSZ under the influence of electric fields. Yang and Conrad [44, 45] reported an enhancement of the sintering rate of 3Y-YSZ under the influence of a DC field of about 14 $\mathrm{V.cm^{-1}}$ and attributed that to the effect of the field on its interaction with the space charge in this oxide, decreasing the grain boundary energy. Figure 9 shows the microstructure of samples consolidated at 1500 °C under no field, a DC field, and an AC field (both fields = 19 $\mathrm{V.cm^{-1}}$). A significant reduction in grain size is clearly shown in samples sintered under the influence of a field. A possible factor for the greater effect of the AC field is suggested to be related to the RMS value in the AC case being $(2)^{1/2}$ that with the DC case.

The nature of the proposed effect of the field on the space charge is not well understood and no direct observations have been made on changes in the grain boundary that relates to that. However, evidence has been provided linking the valence of the dopants in 3Y-YSZ on grain growth. Hwang and Chen [48] reported that solutes with valence less than the host retarded grain growth and those with higher valence enhanced growth. When the solute ions had the same valence as the host, no effect was observed. The authors concluded that these observations suggest a role of the space charge in grain growth. In the sintering study of 3Y-YSZ,

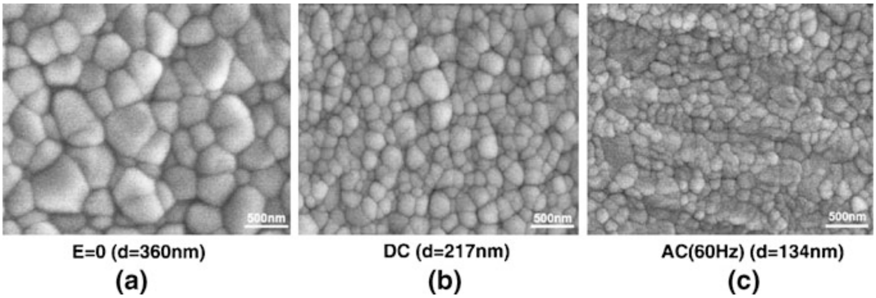

Fig. 9 SEM micrographs and average grain size d of 3Y-TZP annealed under **a** no field **b** DC field of 19 V.cm^{-1} and **c** AC field of 19 V.cm^{-1}. After [45]

which showed an effect for the field [4], the activation energy was found not to be affected, implying an alteration of the pre-exponential only. Similar observations were made in the study cited above on 8Y-YSZ [39].

The effect of the field on surface diffusion during the early stages of sintering of 3Y-YSZ was investigated by Cologna and Raj [47]. The application of a DC field of about 10 V.cm^{-1} was found to have no effect on surface diffusivity and neck growth rate, in contrast to its effect on grain growth. These observations were taken by the authors as indication that the current rather than the field is the operative parameter in such studies. The fact that a contacting field of 10 V.cm^{-1} used by Cologna and Raj [47] did not have any effect on neck growth rate cannot be taken to mean that current is playing a role in densification in their “flash” sintering studies. This is because the field could not be high enough to give any significant effect. This is supported by their observations in a study on 3Y-YSZ [3]. It was shown that there was no significant difference in sintering behavior up to 1000 °C when no field and an electric field of 40 V.cm^{-1} were applied. However, when a field strength of 60 V.cm^{-1} was applied, it induced an abrupt densification around the same temperature.

In the more recent investigations by Cologna et al. [3, 46]. it was shown that the application of higher strength fields resulted in very rapid sintering of tetragonal and cubic zirconia. Referred to as “flash sintering”, the consolidation process under these conditions was attributed to Joule heating at grain boundaries. Figure 10 shows the influence of the applied field on the linear shrinkage of cubic YSZ sintered at different temperatures.

An abrupt increase in the shrinkage rate (as indicated from the slopes of the data points) takes place at progressively lower temperature as the applied field is increased. “Flash sintering” took place when the applied field was above a critical value which was different for the two modifications of the YSZ samples used, 30 and 60 V.cm^{-1} for 8Y-YSZ and 3Y-YSZ, respectively. This difference is expected to be related to the electronic conductivity of the two oxides and on its dependence on temperature. Aside from the proposed Joule heating effect, an interesting aspect in such studies is the possible nature of the changes at the grain boundaries and the effect of the magnitude of the applied field on these changes.

Fig. 10 Effect of electric field on linear shrinkage of 8 mol % YSZ with a heating rate of 10 °C min^{-1}. From [46]

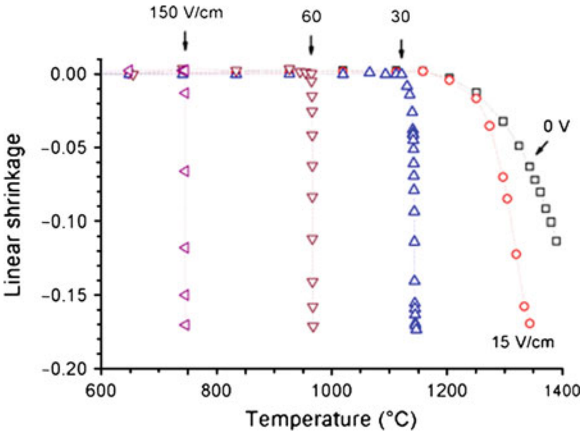

Fig. 11 Dependence of relative neck size of Cu on time and current at 900 °C. After [5]

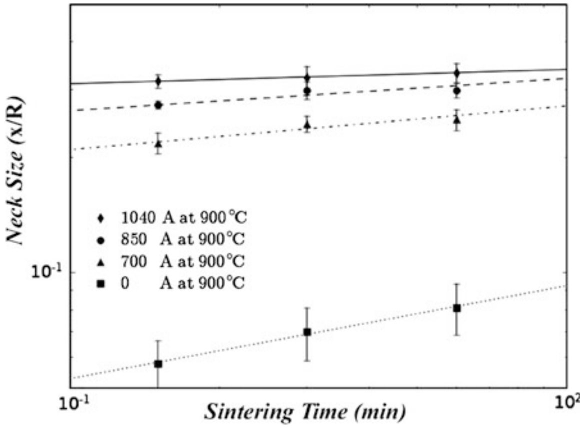

Investigations have also been made on the effect of a field on the sintering of metals [5, 49]. Here the consideration of a space charge is not applicable and contributions from electromigration and Joule heating would be the likely causes of any effect. Frei et al. studied the effect of a current on the sintering of copper spheres to copper plates under SPS conditions [5]. With a modification of the SPS experimental setup, it was possible to vary the current while keeping the temperature constant. Measurements of diameters of necks formed were made at different times under the influence of varying current levels.

Figure 11 shows a plot of the x/R (where x the neck radius and R is the sphere radius) vs time for sintering at 900 °C under total currents ranging from zero to 1040 A. The results show a clear enhancement of the neck growth as a result of the application of a current. For example, after 30 min of sintering x/R is about 0.07 when there is no current but it becomes about 0.32 when a current of 1040 A was applied during sintering, an increase by more than a factor of 4.5 in the neck radius.

Electromigration contributes significantly to the observed enhanced neck growth when sintering was carried out under the influence of a current. The density of the current is highest in the neck area, especially near the perimeter of the neck, as can be seen from a simulation made of this experiment with an imposed current of 30 A, Fig. 12. The simulation depicts one sphere and two contacting plates, Fig. 12a. Figure 12b shows the current density profile along a line from the center of the 300 μm radius neck to the plate. The corresponding temperature profile is shown in Fig. 12c.

These results show that the temperature inside the neck (central area) is constant but decreases very slightly beyond the perimeter of the neck. However, the current density distribution is uneven, with a peak value at the edge of the neck and decreasing to zero beyond the perimeter. The high current density outside the perimeter of the neck appears to have an effect on evaporation, as was deduced from the development of surface morphology, as was discussed in the cited paper [5].

In a study by Fu et al. [49] the sintering of spheres of Cu–Ni and Fe–Cu was carried out by the SPS and the hot-pressing methods. The results showed a considerable increase in neck formation when sintering was done under the influence of a current (in the SPS) [2]. From concentration profiles, the diffusion coefficients of Ni, calculated from concentration across necks formed between spheres of nickel and copper for samples sintered in the SPS and in a hot-press are shown in Fig. 13. The coefficients obtained with SPS sintering are greater by factors in the range of 2–3 than those obtained with hot pressing. Sintering enhancement by a current was also observed by Ohyanagi et al. [50] in a study on the sintering of W wires to W plates. Over the span of sintering time, the neck radius for sintering with a field was about 1.5 times that when no field was applied. Also, evidence of a possible effect of the current on evaporation was seen in this study, as was the case in the sintering of copper spheres to plates [5]. However, in the case of W, it is more likely that the effect is due to the reduction of surface oxide, as has been observed in prior work on the sintering of tungsten [51, 52].

4 Observations on the Effect of a Field on Consolidation and Mass Transport

4.1 Defect Formation, Mass Transport, and Phase Transformation

An area of field effect that has an important practical consideration deals with void formation in, and failure of integrated circuits due to electromigration. This has been related to the effect of a current on defect formation and the coalescence of these defects into voids. The imposition of a current has been shown to result in an increase in the concentration of point defects (mainly vacancies) in metallic systems. Using in situ positron annihilation spectroscopy (PAS), Asoka-Kumar et al. [53] demonstrated a marked increase in vacancy concentration when a current density of

Fig. 12 Simulation results for a copper sphere between two copper plates: **a** current density distribution **b** current density profile and **c** temperature profile. After [5]

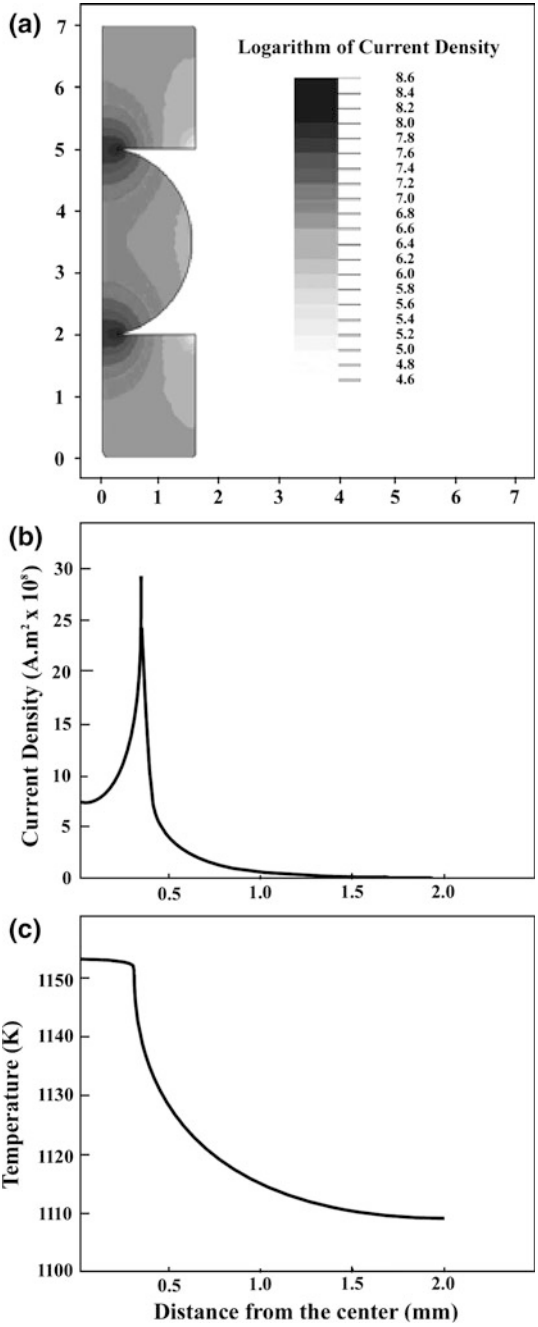

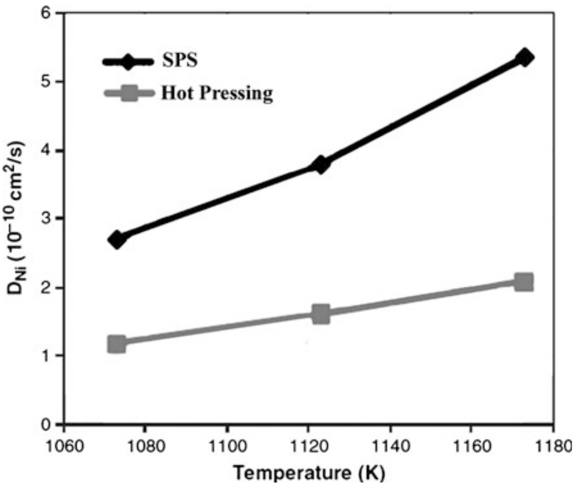

Fig. 13 Temperature dependence of diffusion coefficient of Ni for SPS and hot pressing [49]

8×10^4 A.cm^{-2} was passed through Al-5 wt % Cu lines at 275 °C. The current-induced vacancy concentration was one order of magnitude larger than the normal vacancy concentration generated by thermal activation. Although the current density applied in the cited study is higher than the macroscopic current density in a typical SPS experiment (~ several hundreds A.cm^{-2}), the local current density is expected to be high at particle contacts in the SPS especially during the initial stages of sintering. Even a current density in a moderate range (100–200 A.cm^{-2}) can have a pronounced effect on electronic defect structures and materials properties. Bi_xSb_2-xTe_3 specimens prepared under the passage of electrical current had a slightly lower concentration of carriers (holes) but had a higher mobility [54]. The results were attributed to the current-enhanced diffusion of Sb and precipitation of this element at grain boundaries. In addition, the fast atomic migration might also reduce the number of Frenkel-type defects existing in this material.

The effect of current is not limited to thermodynamic considerations. While the enhanced kinetics in metallic systems under application of electrical current is often attributed to the electron wind effect, the role of the current can be more complex. Garay et al. [55] also utilized positron annihilation spectroscopy (PAS) and demonstrated that non-equilibrium defects in Ni_3Ti disappeared faster upon annealing under application of high current density. Interestingly, the authors found a reduction in the activation energy for defect migration for samples annealed under the influence of electrical current. It is possible that additional diffusion mechanisms become activated with the passage of a current.

The effect of electric field on phase transformation in dielectrics was reviewed by Munir and Schmalzried [56]. Depending on the dielectric constant of the product(s) relative to that of the reactant(s), an electric field can increase or decrease the Gibbs free energy of the system. Therefore, nucleation of a new phase under a field application can be suppressed or enhanced. In metallic systems where the passage of electrical current is more relevant, studies on reaction kinetics in

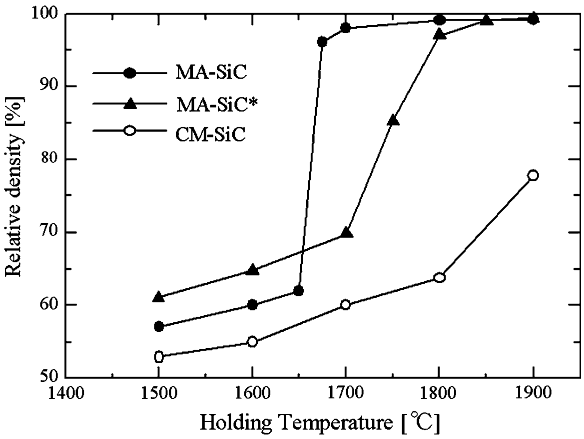

Fig. 14 Relative density of MA-SiC, MA-SiC* and CM-SiC sintered by SPS at different temperatures for 10 min [66]

many diffusion couples have shown enhanced reactivity with increasing current density [18–20]. Although these studies were for crystalline phases, similar effects have also been found in metallic glasses. Holland et al. [57] investigated the influence of electrical current on the crystallization of metallic glasses. They found that high current density promoted crystallization and increased both the crystallite size and fraction of the crystalline phases. This phenomenon was explained by both thermodynamics and kinetics. While diffusion of different species in the metallic glass was believed to be enhanced, the authors showed that the thermal stability of bulk metallic glass was also reduced under application of current.

4.2 Effect of Disorder-Order Transformations

The concept of mass transport enhancement by the ordering of the structure has been observed previously. Seo et al. [58] investigated the annealing of stacking faults in *β*-SiC and reported a significant grain growth occurring during this process. In a study on the conventional liquid phase sintering of WC, Sommer et al. [59] also reported a correlation between grain growth and twin boundaries. In addition, the latest results from Ohyanagi and co-workers demonstrated a connection between disorder-order transformation and enhanced densification in spark plasma sintering [60–66]. Identical SPS conditions were applied to three different types of SiC powders: mechanically alloyed SiC using zirconia balls and vial (designated as MA-SiC), mechanically alloyed SiC using boron nitride balls and vial (MA-SiC*) and commercial nanostructured SiC formed by plasma CVD (CM-SiC) [66]. XRD patterns of the two mechanically alloyed powders showed a totally disordered cubic structure. Figure 14 shows the effects of sintering temperature and the type of powder on densification.

For MA-SiC powder, the relative density changed by a small amount (from about 57 to 60 %) as temperature was increased from 1500 to 1650 °C.

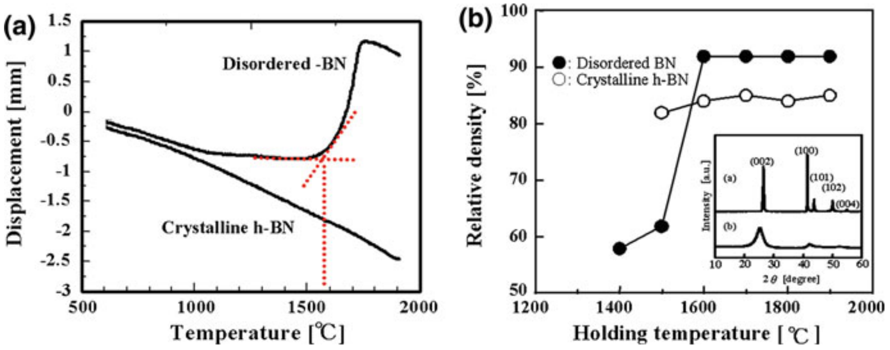

Fig. 15 **a** Displacement profiles of crystalline h-BN and disordered BN during SPS at 60 °C min^{-1} under 40 MPa of applied pressure, and **b** dependence of relative density on sintering temperature and the type of powder. (Inset shows XRD patterns of disorder BN sintered at **a** 1600 °C and **b** 1500 °C)

Its density, however, increased abruptly to 95 % when sintering was carried out at 1675 °C and to 98 % when sintering was done at 1700 °C. This remarkable change coincided with a transformation from disordered to ordered cubic structure as confirmed by XRD. The densification of the MA-SiC* powder showed similar behavior although the abrupt increase in relative density occurred at a higher temperature (1700 °C). The commercial SiC powder (CM-SiC) did not show such behavior. These observations imply that disorder-order transformation plays a major role in enhanced sintering and that the nature of impurities (from the milling process) may influence this type of transformation in SiC.

In addition, spark plasma sintering of disordered and crystalline BN also supported the above conclusion [61, 62]. Densification curve for disordered BN started to show a contraction at temperature above 1550 °C while that for crystalline h-BN had only expansion up to 1900 °C (Fig. 15a). The dissimilarity translated into a difference in final density for these two different types of boron nitride (Fig. 15b). Although disordered BN started out at lower density (about 62 % at 1550 °C) as compared to crystalline BN (about 82 %), specimens sintered from disordered BN ended up with higher density (about 92 %) at 1600 °C and above as compared to those obtained from crystalline BN (about 85 %). The enhanced densification also coincided with a transformation from disordered to an ordered structure as shown by XRD patterns at 1500 and 1600 °C (inset in Fig. 16b).

5 Consolidation of Nanostructured Functional Oxides Using SPS

Oxides such as doped zirconia and ceria have been extensively investigated as electroceramics for such applications as fuel cells, batteries, sensors, and ionic membranes. Considerable attention was paid to the goal of increasing their ionic

Fig. 16 Grain size dependence of percentage of atoms in grain boundaries assuming boundary widths of 0.5 and 1 nm. From [71]

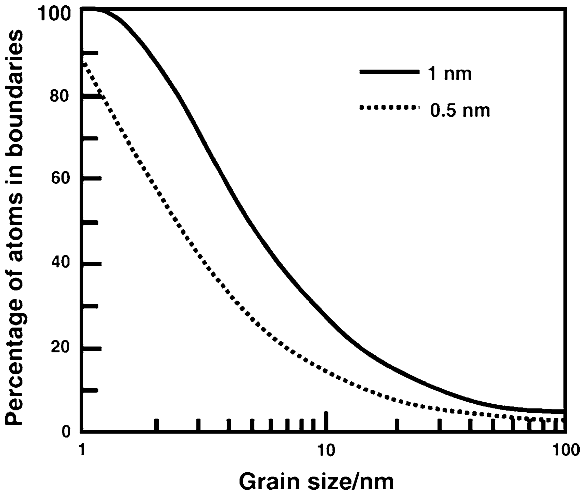

conductivity at, ideally, lower relative temperatures. An increase in conductivity can be achieved by the addition of acceptor dopants, e.g. yttria in the case of zirconia and samaria in the case of ceria. However, such an approach has a limitation due the association of oxygen vacancies and Y ions (on Zr sublattice). In the face of such a limitation subsequent research focused on increasing the mobility of these species through modifications of microstructure, e.g., through grain size modification. The effect of grain size on ionic conductivity has been investigated in thin films [67, 68]. The conductivity was reported to be as much as two orders of magnitude higher in nanometric thin films as compared to that in micrometric or single crystal samples [68, 69]. This was attributed to the increased contribution of interfaces (surfaces and grain boundaries), relative to bulk in the enhanced conductivity.

These observations bring to focus the relationship between structure and properties of solid oxide electrolytes, particularly when the grain size is in the nanometric scale. The focus is driven by theoretical and experimental evidence that with grain sizes in this range (nominally <100 nm), materials possess unusual, and sometime unique properties [70] The rationale for these observations focuses on the two considerations: the relationship between grain size and a critical dimension for certain properties (e.g., the width of the space charge layer in ionic conductors), and dominance of surfaces in the effective thermodynamic properties of the material. The latter has examples that include crystal structure, surface topography, and reactivity.

The effect of grain size refinement can be seen by the relative contribution of atoms residing in the grain boundary region, Fig. 16. The figure depicts the percentage of atoms in the grain boundaries as a function of grain size for two assumed values for the width of the grain boundary, 0.5 and 1 nm [71] When the grain size is 5 nm, for example, the percentage of atoms in the boundary is about 30 % if the width of the boundary is 0.5 nm and about 50 % if the width is 1 nm. As the grain size decreases the contribution of bulk atoms decreases, as shown

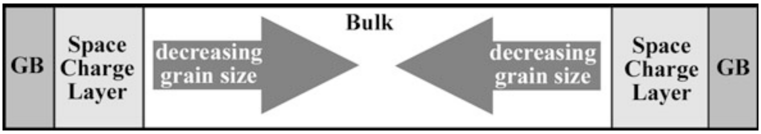

Fig. 17 Reduction in the bulk relative to space charge layer and grain boundary as grain size decreases. Schematics show a representation of a grain within two grain boundaries (GB). The thickness of the Space Charge Layer becomes comparable to the grain size for small nanosizes

schematically in Fig. 17. With continued decrease in grain size, the contribution of bulk atoms approaches zero with concomitant overlap of the space charge layers and expected changes in the properties of such electroceramics [72].

In view of the importance of functional oxides in fuel cell and sensor applications, investigations on the grain size dependence of their properties were initiated. The focus was on the preparation of dense nanostructured oxides. Prior attempts aimed at obtaining dense nanostructured cubic yttria-stabilized zirconia with a grain size of less than about 50 nm by pressureless sintering [73], microwave sintering [74, 75], and by SPS [76, 77] have not been successful. The difficulty in obtaining the nanostructure for cubic zirconia is in part related to its relatively low grain growth activation energy [74]. More recent investigations using a modified SPS experimental arrangement have succeeded in obtaining dense (98 % +) cubic zirconia (8 mol % yttria, YSZ) with a grain size as small as 13 nm [78]. Details of the experimental modification have been provided elsewhere [2]. The success in this first time accomplishment is attributed to the role of pressure (destruction of agglomerates) and the current (grain growth retardation) [39].

While the preparation of nanostructured YSZ with a grain size less than 20 nm is a significant first time accomplishment, subsequently measured electrical properties provided an unprecedented observation. Yttria-stabilized zirconia (YSZ) and samaria and gadolinia-doped ceria, when prepared in dense, bulk form with a grain size in lower end of the nano-scale (<20 nm), were found to exhibit protonic conductivity [78]. It should be emphasized that such a behavior was not observed in samples with a grain size in the micrometric range (1–2 μm). The occurrence of protonic conductivity was substantiated by electrical measurements under moisture and additional investigations showing an effect of water partial pressure [78] and secondary ion mass spectroscopy (SIMS), as reported in the literature [79].

The discovery of the unexpected protonic conduction in nanostructured oxides was made possible by the utilization of the SPS process. The success in obtaining highly dense oxides with a grain size in the low nanometric range is believed to be the result of current effects (retardation of grain growth) and pressure contribution (the destruction of agglomerates). While a total understanding of the fundamentals of the SPS process is still not at hand, such unique accomplishments will undoubtedly lead to increased effort to provide the needed understanding.

6 Summary

In this chapter, the basics of the role of an electric field or current in sintering were discussed. The field was shown to have a marked effect on mass transport: it enhanced diffusivity and interdiffusion, increased rates of phase formation, shortened the nucleation time of product phases, and enhanced defect mobility. Direct evidence of enhanced sintering in the SPS has been provided for metallic systems. The field (current) has also been shown to retard grain growth in oxide electroceramics in the many observations which were attributed to changes in grain boundary energy or composition.

However, while these studies have provided significant insight on the effect of the field on materials processing, a complete understanding of all the fundamental aspects of field-activation is not at hand at present. It is hoped that the recent resurgence of investigations on this topic will provide additional insights, leading to the desired understanding.

References

1. Munir, Z.A., Anselmi-Tamburini, U., Ohyanagi, M.: J. Mater. Sci. **41**(3), 763–777 (2006)
2. Munir, Z.A., Quach, D.V., Ohyanagi, M.: J. Am. Ceram. Soc. **94**(1), 1–19 (2011)
3. Cologna, M., Rashkova, B., Raj, R.: J. Am. Ceram. Soc. **93**(11), 3556–3559 (2010)
4. Yang, D., Conrad, H.: Mat. Sci. Eng. A-Struct. **528**(3), 1221–1225 (2011)
5. Frei, J.M., Anselmi-Tamburini, U., Munir, Z.A.: J. Appl. Phys. **101**(11), 114914/114911–114918 (2007)
6. Jeong, J.W., Han, J.H., Kim, D.Y.: J. Am. Ceram. Soc. **83**(4), 915–918 (2000)
7. Tokita, M.: Ceram. Trans. **194**, 51–59 (2006)
8. Misawa, T., Shikani, N., Kawakami, Y., Enjoji, T., Ohtsu, Y.: Mater. Sci. Forum **638–642**, 2109–2114 (2010)
9. Hulbert, D.M., Anders, A., Dudina, D.V., Andersson, J., Jiang, D., Unuvar, C., Anselmi-Tamburini, U., Lavernia, E.J., Mukherjee, A.K.: J. Appl. Phys. **104**(3), 033305/033301–033307 (2008)
10. Misawa, T., Shikatani, N., Kawakami, Y., Enjoji, T., Ohtsu, Y., Fujita, H.: J. Mater. Sci. **44**(6), 1641–1651 (2009)
11. Nanko, M., Maruyama, T., Tomino, H.: J. Jpn. Inst. Met. **63**(7), 917–923 (1999)
12. Mackenzie, K.J.D., Banerjee, R.K., Kasaai, M.R.: J. Mater. Sci. **14**(2), 333–338 (1979)
13. Mackenzie, K.J.D., Banerjee, R.K.: J. Mater. Sci. **14**(2), 339–344 (1979)
14. Mackenzie, K.J.D., Ryan, M.J.: J. Mater. Sci. **16**(3), 579–588 (1981)
15. Brown, I.W.M., Mackenzie, K.J.D.: J. Mater. Sci. **17**(12), 3663–3671 (1982)
16. Korte, C., Ravishankar, N., Carter, C.B., Schmalzried, H.: Solid State Ion. **148**(1–2), 111–121 (2002)
17. Korte, C., Franz, B., Hesse, D.: Phys. Chem. Chem. Phys. **7**(2), 413–420 (2005)
18. Friedman, J.R., Garay, J.E., Anselmi-Tamburini, U., Munir, Z.A.: Intermetallics **12**(6), 589–597 (2004)
19. Garay, J.E., Anselmi-Tamburini, U., Munir, Z.A.: Acta Mater. **51**(15), 4487–4495 (2003)
20. Bertolino, N., Garay, J., Anselmi-Tamburini, U., Munir, Z.A.: Philos. Mag. B **82**(8), 969–985 (2002)

21. Bertolino, N., Garay, J., Anselmi-Tamburini, U., Munir, Z.A.: Scripta Mater. **44**(5), 737–742 (2001)
22. Chen, W., Anselmi-Tamburini, U., Garay, J.E., Groza, J.R., Munir, Z.A.: Mater. Sci. Eng. A-Struct. **394**(1–2), 132–138 (2005)
23. Kondo, T., Yasuhara, M., Kuramoto, T., Kodera, Y., Munir, Z.A., Ohyanagi, M.: J. Mater. Sci. **43**(19), 6400–6405 (2008)
24. Kondo, T., Kuramoto, T., Kodera, Y., Ohyanagi, M., Munir, Z.A.: J. Jpn. Soc. Powder Metall. **55**, 643–650 (2008)
25. Kondo, T., Kuramoto, T., Kodera, Y., Ohyanagi, M., Munir, Z.A.: J. Ceram. Soc. Jpn. **116**(1359), 1187–1192 (2008)
26. Zhao, J., Garay, J.E., Anselmi-Tamburini, U., Munir, Z.A.: J. Appl. Phys. **102**(11), 114902/114901–114907 (2007)
27. Choi, J.I., Han, J.H., Kim, D.Y.: J. Am. Ceram. Soc. **86**(2), 347–350 (2003)
28. Jin, H.R., Yoon, S.H., Lee, J.H., Lee, J.H., Hwang, N.M., Kim, D.Y., Han, J.H.: J. Am. Ceram. Soc. **87**(9), 1747–1752 (2004)
29. Kliewer, K.L., Koehler, J.S.: Phys. Rev. **140**(4A), 1226–1240 (1965)
30. Kliewer, K.L.: Phys. Rev. **140**(4A), 1241–1246 (1965)
31. Schwensfeir, R.J., Elbaum, C.: J. Phys. Chem. Solids. **26**(4), 781–782 (1965)
32. Munir, Z.A., Nguyen, T.T.: Philos. Mag. A **47**(1), 105–117 (1983)
33. Munir, Z.A., Yeh, A.A.: Philos. Mag. A **56**(1), 63–71 (1987)
34. Machida, C.A., Munir, Z.A.: J. Cryst. Growth **68**(3), 665–670 (1984)
35. Kingery, W.D.: J. Am. Ceram. Soc. **57**(1), 1–8 (1974)
36. Yang, D., Conrad, H.: J. Mater. Sci. **43**(13), 4475–4482 (2008)
37. Yang, D., Conrad, H.: Scripta Mater. **36**(12), 1431–1435 (1997)
38. Ghosh, S., Chokshi, A.H., Lee, P., Raj, R.: J. Am. Ceram. Soc. **92**(8), 1856–1859 (2009)
39. Quach, D.V., Avila-Paredes, H., Kim, S., Martin, M., Munir, Z.A.: Acta Mater. **58**(15), 5022–5030 (2010)
40. Michels, A., Krill, C.E., Ehrhardt, H., Birringer, R., Wu, D.T.: Acta Mater. **47**(7), 2143–2152 (1999)
41. Kanters, J., Eisele, U., Boder, H., Rodel, J.: Adv. Eng. Mater. **3**(3), 158–162 (2001)
42. Tekeli, S., Erdogan, M., Aktas, B.: Ceram. Int. **30**(8), 2203–2209 (2004)
43. Dahl, P., Kaus, I., Zhao, Z., Johnsson, M., Nygren, M., Wiik, K., Grande, T., Einarsrud, M.A.: Ceram. Int. **33**(8), 1603–1610 (2007)
44. Yang, D., Conrad, H.: Scripta Mater. **63**(3), 328–331 (2010)
45. Yang, D., Raj, R., Conrad, H.: J. Am. Ceram. Soc. **93**(10), 2935–2937 (2010)
46. Cologna, M., Prette, A.L.G., Raj, R.: J. Am. Ceram. Soc. **94**(2), 316–319 (2011)
47. Cologna, M., Raj, R.: J. Am. Ceram. Soc. **94**(2), 391–395 (2011)
48. Hwang, S.-L., Chen, I.-W.: J. Am. Ceram. Soc. **73**(11), 3269–3277 (1990)
49. Fu, Z., Wang, K., Tan, T., Xiong, Y., He, D., Wang, Y., Munir, Z.A.: Ceram. Trans. **194**, 3–21 (2006)
50. Togofuku, N., Kuramoto, T., Imai, T., Ohyanagi, M., Munir, Z.A.: J. Mater. Sci. **47**, 2201–2205 (2012)
51. Shearwood, C., Ng, H.B.: Spark plasma sintering of wire exploded tungsten nano-powder. In: Hariz, A.J., Varadan, V.K. (eds.) pp. 67981B-67981–67910, Canberra, Australia (2007)
52. Kim, D.Y., Gladel, G., Accary, A.: Morphological study of tungsten powder obtained by hydrogen reduction of tungsten trioxide powder at 700–900 C. In: European Symposium on Powder Metallurgy, vol. 2, pp. 185–193 (1978)
53. Asoka-Kumar, P., O'Brien, K., Lynn, K.G.: Appl. Phys. Lett. **68**(3), 406–408 (1996)
54. Liao, C.-N., Wu, L.-C.: Appl. Phys. Lett. **95** 052112/052111–052113 (2009)
55. Garay, J.E., Glade, S.C., Anselmi-Tamburini, U., Asoka-Kumar, P., Munir, Z.A.: Appl. Phys. Lett. **85**(4), 573–575 (2004)
56. Munir, Z.A., Schmalzried, H.: J. Mater. Synth. Process. **1**(1), 3–16 (1993)
57. Holland, T.B., Loffler, J.F., Munir, Z.A.: J. Appl. Phys. **95**(5), 2896–2899 (2004)
58. Seo, W.S., Pai, C.H., Koumoto, K., Yanagida, H.: Nippon Seram Kyo. Gak. **99**(6), 443–447 (1991)

59. Sommer, M., Schubert, W.D., Zobetz, E., Warbichler, P.: Int. J. Refract. Met. Hard Mater **20**(1), 41–50 (2002)
60. Toyofuku, N., Nishimoto, M., Arayama, K., Kodera, Y., Ohyanagi, M., Munir, Z.A.: Ceram. Trans. (ACS) **212**, 31–40 (2010)
61. Toyofuku, N., Yamasaki, N., Kodera, Y., Ohyanagi, M., Munir, Z.A.: J. Ceram. Soc. Jpn. **117**(2), 189–193 (2009)
62. Yamamoto, T., Ishibashi, N., Toyofuku, N., Kodera, Y., Ohyanagi, M., Munir, Z.A.: Consolidation of h-BN with disorder-order transformation. Innovative Processing and Synthesis of Ceramics, Glasses and Composites, Materials Science and Technology (MS&T) 2006: Processing, pp. 531–538 (2006)
63. Kodera, Y., Yamamoto, T., Toyofuku, N., Ohyanagi, M., Munir, Z.A.: J. Mater. Sci. **41**(3), 727–732 (2006)
64. Kodera, Y., Kotera, H., Yamamoto, T., Ohyanagi, M., Munir, Z.A.: Phys. Stat. Solid C **3**, 2876–2879 (2006)
65. Yamamoto, T., Kitaura, H., Kodera, Y., Ishii, T., Ohyanagi, M., Munir, Z.A.: J. Am. Ceram. Soc. **87**, 1436–1441 (2004)
66. Ohyanagi, M., Yamamoto, T., Kitaura, H., Kodera, Y., Ishii, T., Munir, Z.A.: Scripta Mater. **50**(1), 111–114 (2004)
67. Puin, W., Rodewald, S., Ramlau, R., Heitjans, P., Maier, J.: Solid State Ion. **131**(1–2), 159–164 (2000)
68. Joo, J.H., Choi, G.M.: Solid State Ion. **177**(11–12), 1053–1057 (2006)
69. Zhang, Y.W., Jin, S., Yang, Y., Li, G.B., Tian, S.J., Jia, J.T., Liao, C.S., Yan, C.H.: Appl. Phys. Lett. **77**(21), 3409–3411 (2000)
70. Gleiter, H.: Acta Mater. **48**(1), 1–29 (2000)
71. Chadwick, A.V., Savin, S.L.P.: Solid State Ion. **177**(35–36), 3001–3008 (2006)
72. Maier, J.: Solid State Ion. **131**(1–2), 13–22 (2000)
73. Martin, M.C., Mecartney, M.L.: Solid State Ion. **161**(1–2), 67–79 (2003)
74. Upadhyaya, D.D., Ghosh, A., Gurumurthy, K.R., Prasad, R.: Ceram. Int. **27**(4), 415–418 (2001)
75. Zhang, C., Zhang, G., Leparoux, S., Liao, H., Li, C.X., Li, C.J., Coddet, C.J.: Eur. Ceram. Soc. **28**(13), 2529–2538 (2008)
76. Chen, X.J., Khor, K.A., Chan, S.H., Yu, L.G.: Mater. Sci. Eng. A-Struct. **341**(1–2), 43–48 (2003)
77. Trunec, M., Maca, K., Shen, Z.: Scripta Mater. **59**(1), 23–26 (2008)
78. Kim, S., Anselmi-Tambtirini, U., Park, H.J., Martin, M., Munir, Z.A.: Adv. Mater. **20**(3), 556–559 (2008)
79. Quach, D.V., Kim, S., De Souza, R.A., Martin, M., Munir, Z.A.: Key Eng. Mater. **484**, 107–116 (2011)

Field Assisted Sintering Mechanisms

U. Anselmi-Tamburini, G. Spinolo, F. Maglia, I. Tredici,
T. B. Holland and A. K. Mukherjee

Abstract Field assisted sintering studies have produced a wealth of data about the densification behaviors of many powder systems. However, the sheer volume of work has not met with sufficient mechanistic descriptions of the processes in metal or ceramic systems. This fact has, and is, limiting the acceptance and widespread use of this promising technique in larger than laboratory scale manufacturing. We describe here the nature of the influences of electric fields and/or currents, changes in heating rate, and the effects of applied pressures upon ceramic and metal systems in context of the commonly accepted stages of sintering. As many of the specific mechanisms discussed have not been directly characterized within field assisted sintering studies we focus on the established theoretical underpinnings to better understand their influence and to enable definitive future experimentation on this area of research.

1 Introduction

Understanding the basic mechanisms involved in a new technology represents a key step towards its widespread application in research and industry. A good understanding of the physical and chemical mechanisms is, in fact, absolutely essential in order to control and eventually improve the technology. FAST (SPS)

U. Anselmi-Tamburini · G. Spinolo · F. Maglia · I. Tredici
Department of Chemistry, University of Pavia, Pavia, Italy

T. B. Holland (✉) · A. K. Mukherjee
Department of Chemical Engineering and Materials Science,
University of California, Davis, USA
e-mail: tbholland@ucdavis.edu

R. H. R. Castro and K. van Benthem (eds.), *Sintering*, Engineering Materials 35,
DOI: 10.1007/978-3-642-31009-6_8, © Springer-Verlag Berlin Heidelberg 2013

represents one such example as a clear interpretation of its basic mechanisms is still lacking. During the initial years of use it was generally believed that the unique characteristics of FAST could be explained by a single mechanism, based on the presence of electric sparks or plasma. The FAST technique was therefore often referred to as spark plasma sintering (SPS). Although the evidence supporting this interpretation was insufficient, it enjoyed and still does wide support in the community. As more investigations occurred, this explanation became less convincing and other mechanisms have been suggested. This ongoing discussion produced the impression that the technique is based upon frail foundations inducing skepticism among the possible industrial users. The term FAST will be used in this chapter instead of SPS but they reflect the same technique mentioned in previous chapters as SPS.

In reality we now have a much deeper understanding of the technique and the apparent confusion is mostly the result of a wrong approach to the problem. The early claims of an active role of plasma convinced most of the early users that there was a unique simple mechanism that could justify all the experimental evidence. We now understand that this approach was probably wrong, because it did not recognize the intrinsic complexity of the process. The presence of strong electric fields along with thermal and stress gradients generate a complex scenario where several basic processes can be active at the same time. Furthermore, the high heating rates and the short processing times typically associated to this technique produce a situation that is often dominated by kinetics versus thermodynamics. This opens the possibility of intrinsically complex behaviors, often observed in far from equilibrium systems. In other words, no one simple explanation for FAST characteristics exists, but there exists a group of phenomena that are operative, cooperatively or competitively, with proportionally different contributions at each stage of the sintering process. With this in mind we believe it is useful for the sintering community to systematically present and discuss these basic processes that might be active in FAST while accounting for each of their roles in relation to the experimental conditions and sample characteristics. Some of these processes have been already widely discussed in the FAST literature, while others will be discussed here for the first time. Specifically, this chapter will discuss aspects of arc and spark discharge, electromigration, electrotransport and polarization, pressure and stress gradients, thermodiffusion, and heating rates.

2 Arc and Spark Discharge

The presence of plasma in FAST apparati and its role on the sintering and reactivity of the processed powders was first described by Tokita [1, 2]. His papers profoundly impacted the FAST community and have been referenced for years as the only source of information about the FAST mechanism. In his papers, Tokita suggested that the intense electric flow present in the apparatus might induce the formation of electric sparks between the particles of the green pellet, generating plasma clouds and localized temperature increases. Local melting, vaporization and sputtering phenomena would then be expected, producing a substantial increase in material transfer producing rapid formation of necks. Further, it was suggested that the localized plasma can produce a general increase in the surface diffusivity deriving from the removal of impurities and, in the case of metals, from the ablation of the superficial oxide layer.

However, direct experimental evidence was never provided for this explanation. Reports of plasma discharges in the SPS or in experimental setups mimicking it have been presented, but they are scanty [3, 4] and limited to very specific materials and configurations. A recent investigation by Hulbert et al., on the other hand, could not find any evidence supporting the presence of plasma [5, 6]. Such controversy is not surprising: plasma generation and stability represent a very complex topic. Its application to a system presenting complex geometries and chemical heterogeneities, such as the one present in a powder bed, does not allow any firm quantitative conclusion.

In general terms three different classes of vacuum discharge should be considered: arcs, sparks and glow discharges [7–9]. The occurrence of each depends on a complex combination of physical and geometrical parameters such as: gas pressure, gas composition, applied voltage, discharge current, morphology and chemical nature of the surfaces. The term spark discharge is generally used for discontinuous processes characterized by transient high currents (in the kA range) and generated by high voltage pulses, often in the kilovolt range. Arcs, on the other hand, are continuous phenomena characterized by high discharge current, typically 10 A or greater, associated to a low voltage, typically in the range of few tens of Volts. Finally glow discharges present relatively low currents, 1 A or less, and relatively high excitation voltages (300 V or more) [7–9].

Some of these processes do not seem to be compatible with the experimental conditions present in the FAST apparatus. FAST systems typically use relatively small applied voltages in the range of a few volts. This may rule out the possibility of spark or glow discharges that are associated with triggering voltages in the range of hundreds or thousands of volts. Arc discharges, on the other hand, could in principle be sustained under typical FAST conditions, but only in the case of metallic samples, as non-conducting samples cannot sustain the high currents associated with these phenomena. However, as we will see in a following section, dielectric material polarization might provide the conditions by which the formation of plasma may occur. With externally applied fields of several V/m, it is possible to reach local field strengths of hundreds or even thousands of V/m.

In an attempt to obtain direct experimental evidence of discharge phenomena occurrences in FAST, Hulbert et al. [5, 6] have used a complex approach involving the use of electrical and optical techniques. Firstly, one end of a high temperature fiber optic probe was embedded in the powder charge inside an FAST graphite die, while the other end of the fiber was connected to a high sensitivity spectrometer in the attempt to detect any light emission deriving from plasma discharge phenomena occurring in the powder bed during the sintering process. The experiment was performed using both conductive and non-conductive powders. In an extreme

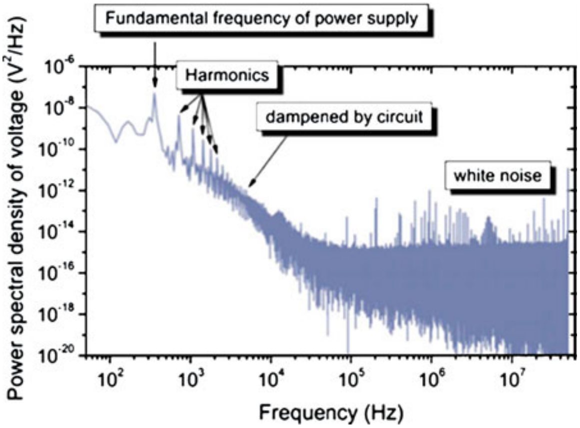

Fig. 1 An FFT plot of one duty cycle of the SPS process. This plot is for the SPS of 325 mesh 99.9 % pure Al powder after a temperature of 100 °C was reached using a heating rate of 100 °C/min. The plot is representative of all FFT data collected [5]

case, the contact between the plungers and the body of the graphite die were coated with boron nitride in order to force all the current to flow through the sample. No evidence of light emission was observed in any of the experiments they performed, based on heating cycles reaching temperatures as high as 650 °C. In a different kind of experiment two electrodes were imbedded in the powder bed and connected to a high resolution oscilloscope characterized by an analog bandwidth of 1 GHz and a sampling rate of 5×10^9 samples per second. The result of this analysis is particularly important because discharge processes produce a distinctive high frequency electromagnetic pattern that should be easily observed by an FFT analysis of the collected signal. Instead, the experimental results (Fig. 1) did not present any significant features, besides the components deriving from the pulsed power supply with its harmonics. In the high frequency region only white noise was observed.

In addition to the experimental observations, Hulbert et al. have discussed another relevant point, based on basic plasma physics arguments, that has been generally overlooked in the FAST literature: in order to ignite and maintain an electrical discharge a minimum number of charge carriers are required. Since the volume concentration of ions or free electrons is never extremely high, it is then difficult to produce electric discharges in vacuum across very short distances. This critical distance is usually identified with the Debye length. For usual conditions (low vacuum) the Debye length is around 100 μm, a distance far larger than the typical distance between grains in a green pellet.

The arguments presented by Hulbert et al. seem to rule out the possibility of a significant presence of plasma discharges in FAST apparatus. However, due to the complexity of the physics underlying this topic, the argument will probably continue to be discussed in the FAST community. It will be almost impossible to prove the absence of plasma in any possible combination of the experimental conditions allowed by the technique. However, unless some relevant positive proof is presented, it becomes more and more difficult to justify all the typical characteristics of the FAST densification behaviors only on the basis of the presence of plasma discharges.

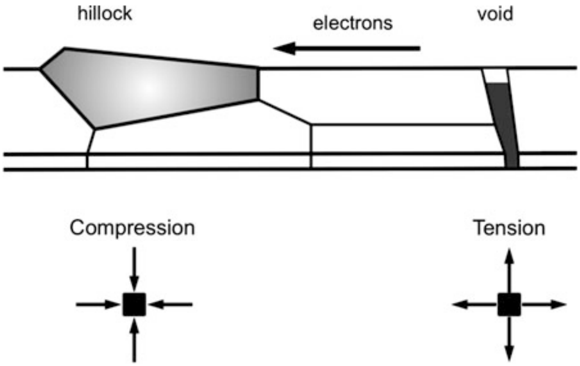

Fig. 2 Effect of atomic diffusion induced by electromigration on a thin metal line (from [16] redrawn)

3 Electromigration

Electromigration is a mass transport phenomenon observed mainly in metals and resulting from the momentum transfer between the conducting electrons and the metal ions. This transfer of momentum produces a migration of material in response to the very intense electronic flux. Its effects are generally observed with current densities above 1000 Acm^{-2}. Electromigration has been studied in depth by solid state physicists because it represents the main source of failure in microelectronic devices. The atomic diffusion induced by the elevated current densities can produce local depletion or accumulation of material in metallic interconnects, resulting in voids or hillock formation (see Fig. 2). The redistribution of mass results in the accumulation of vacancies, ultimately in the form of voids, and balances the mass in the growing hillocks. Electromigration in FAST processes has been discussed since the early literature, suggested by the high current fluxes involved in the technique. Again, unequivocal experimental evidence relative to the role that electromigration plays in the actual FAST process is still lacking, due also to the complex geometrical and composition situation typical of the technique.

An abundance of studies is present in literature on the theory and modeling of electromigration. Several different theoretical approaches have been proposed from the early ballistic models to the latest complex quantum-mechanical approaches [10–15]. In the following we will summarize only the basic elements of these models emphasizing the aspects of the theory that are relevant for the FAST applications.

3.1 *Brief Review of Electromigration Theory*

Electromigration can be considered as the correlation between moving components under the effect of an external driving force. In the framework of the irreversible thermodynamics, in a multi-component system the motion of the *i*th component depends on its interaction with all the other components [11, 12]. As a result the atomic flux, J_i, will be represented by:

$$J_i = \sum_J L_{ij} X_j \quad (i = 1, 2, \ldots, n) \tag{1}$$

where L_{ij} are the phenomenological coefficients correlating the flux of the ith component to the driving force X_j of the jth component. For a pure metal in an electric field the following pair of flux reactions can be rewritten:

$$J_a = -L_{aa}\nabla\mu - L_{ae}\nabla\phi \tag{2}$$

$$J_e = -L_{ea}\nabla\mu - L_{ee}\nabla\phi \tag{3}$$

where J_a is the flux of atoms and J_e is the flux of charge carriers (electrons or holes), $\nabla\mu$ the gradient of chemical potential and $E = -\nabla\phi$ the electric driving force. The L_{aa} coefficient represents the atomic mobility and L_{ee} the electronic conductivity of the metal in the absence of an applied electrical field. The off-diagonal terms L_{ae} and L_{ea} represent the correlation coefficients representing the coupling between the electronic and atomic movements. The term L_{ea} is the one responsible for the electromigration. As a result, the second term on the right hand size of Eq. (2) represents the atomic flux due to the electromigration. In a pure metal, where the diffusivity is controlled by vacancy movement, this term is generally represented in the following form [11–15]:

$$J_a^E = \frac{D_a c}{kT} Z^* eE = \frac{D_a c}{kT} Z^* e\rho j \tag{4}$$

where D_a is the atomic diffusivity, c the vacancy concentration, k the Boltzmann's constant, T the absolute temperature, e the electronic charge, E the applied electric field, ρ the resistivity and j the current density [14]. Z^* is called the effective charge of the atom and is generally considered to be composed of two elements [12]:

$$Z^* = Z_{el}^* + Z_{wd}^* \tag{5}$$

Where Z_{el}^* is the nominal valence of the metal ion once the dynamical screening of the electrons is ignored and accounts for the direct electrostatic force on the metal ion; while Z_{wd}^* accounts for the momentum exchange between the carriers and the metal ions. The term $Z_{wd}^* eE$ is generally referred to as the "*electron wind force*". The electron wind term generally dominates Eq. (5), since the direct electrostatic component is usually considered vanishing in metals. It must be noted that the magnitude and even the sign of Z_{wd}^* is related to the nature of the carrier (electrons or holes) and the nature of the metal. In some cases, for instance, it shows a negative sign; in that case a diffusion of material is observed in direction opposed to the direction of the current flow [11].

In diffusion-controlled creep, Eq. (4) is modified to include the effects of vacancy formation near the cathode and the resultant back stress this causes. Equation 6 shows this relationship [17, 18],

$$J = \frac{ND}{kT\left(Z^{*}e\rho j - \Omega\frac{d\sigma}{dx}\right)} \tag{6}$$

where N is the atomic density, ρ is resistivity, j is current density, σ is stress, and Ω represents the atomic volume. Studies of the back stress associated with Eq. (6) have found that the effective valence parameter, Z^{*}, can be found by mechanical testing means [17, 18].

The electromigration effect is strongly dependent on two other parameters: temperature and microstructure of the sample. It is evident from Eq. (4) that ignoring the temperature dependence of Z^{*}_{wd}, which is often an uncharacterized property, the material flux induced by electromigration has the same temperature dependence as a regular diffusion processes. Therefore, at the high consolidation temperatures during FAST experiments, electromigration effects are expected to become more significant.

Mass transfer induced by electromigration is very sensitive to the microstructure of the material [14]. In a perfectly homogeneous material such as a single crystal, electromigration can be observed only at the two electrodes, since material is removed at one electrode and deposited at the other electrode. In any intermediate region no modification is observed when stress buildup is disregarded, as the amounts of material flowing in and flowing out the region are identical. However, irregularities in the microstructure, such as pores, grain boundaries, inclusion and dislocations, produce local alterations to the current flux, resulting in a non-zero atomic flux divergence. When $\nabla \cdot J \neq 0$ material accumulation (when $\nabla \cdot J < 0$) or material depletion (when $\nabla \cdot J > 0$) is observed [10]. Because of this effects of electromigation are difficult to predict for materials with complex microstructures, such as powder agglomerates. In such a case material depletion or deposition can be observed at any point in the sample depending on the local flux divergence. No direct experimental observation of these effects in partially sintered microstructures has so far been reported.

Even in absence of porosity, the difference in conductivity between the bulk and the grain boundary is sufficient to produce flux divergence and hence influence the rate of material transfer. In fact, Ho and Kwok, demonstrated that in presence of grain boundaries Eq. (4) can be replaced by the following relation [11]:

$$J_b^E = \frac{D_b N_b}{kT}\frac{\delta}{d}Z^{*}eE \tag{7}$$

where N_b and D_b are the atomic density and the atomic diffusivity in the grain boundary, δ the effective grain boundary (gb) width (~ 1 nm) for mass transport and d the average grain size. As a result, even in presence of fairly large grain sizes the role of flux differences between the grain boundaries and the bulk can be profound. With a diffusivity ratio of $D_a/D_b \approx 10^{-7}$ the flux ratio for the grain size of 1 μm will be $J_b^E / J_a^E \approx 10^4$. It is important to note that when the grain size gets smaller this effect becomes even more relevant, suggesting that nanometric materials should be even more prone to material transfer induced by electromigration.

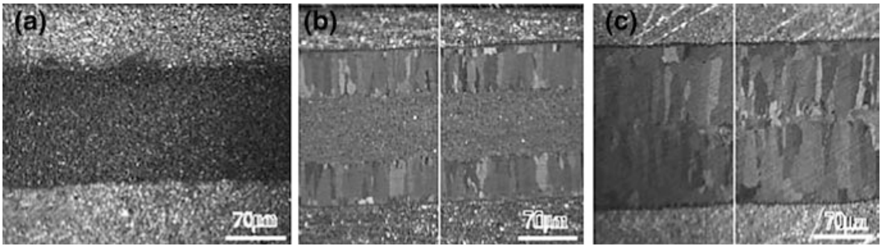

Fig. 3 Optical micrographs showing product phase formation in three-layer Al-Au-Al system annealed at 723 K for 4 h: (**a**) with no current (**b**) with a current density of 0.5093 107 A/m^2, and (**c**) with current density of 1.019 107 A/m^2 [25]

3.2 Electromigration and Solid State Reactivity

Most of the theories for electromigration were developed for pure metals. Some of them have also been extended to the case of metals containing small amounts of dissolved impurities [13], and some have been developed for metallic glass alloys. However, it has been largely proven that intense electric currents can influence solid-state chemical reactions, producing enhancement or inhibition of the kinetics of interfacial reactions. Although this topic is not generally considered part of classical electromigration, it represents the result of the same basic phenomena in the case of a heterogeneous system.

The influence of electromigration on solid state reactivity in metallic systems has been largely investigated in connection with microelectronics applications, where reactive diffusion in metal contacts represents a major problem. The general aspects of this phenomenon, however, have been investigated by a relatively small group of researchers [19–30]. A typical example of this effect is shown in Figs. 3 and 4, [26] where diffusion couples between Au and Al foils were exposed to current flux along directions perpendicular to the interface. It is evident that this flux produces a significant increase in the growth rate of the intermetallic phases together with a drastic decrease in the incubation time usually observed for the first appearance of the product layers.

In some cases the current flux may inhibit rather than enhance reactivity, or have no effect at all. In some cases, the effect appears to be independent from the direction of the current flux, while in others it has been shown to have a significant effect only when the current flux has a certain relationship with the chemical diffusion flux. These apparent inconsistencies have been interpreted recently on the basis of phenomenological models applying the electromigration quantities to heterogeneous systems [31–33]. These models indicate that the current flux can enhance or inhibit the kinetics of growth depending on a complex combination of the diffusivity of the involved atoms and of their Z^* values. Orchard and Greer [27] demonstrated that, in the case of an A-rich phase placed in contact with a B-rich phase, in order to produce an $A_\beta B$ interfacial layer, the electromigration contribution to the intermixing flux is given by

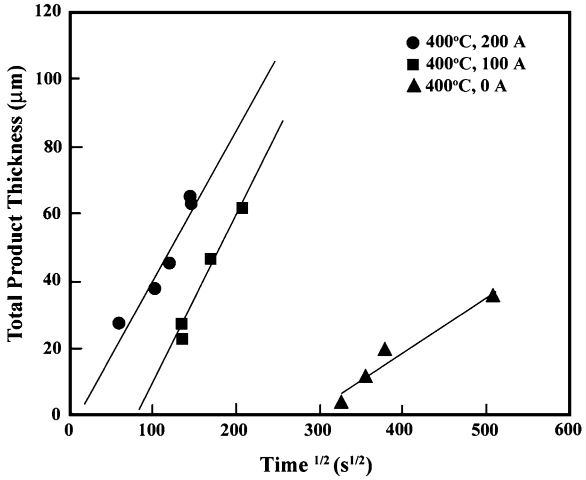

Fig. 4 Time dependence of the growth of the total product layer for Au-Al diffusion couples annealed at 400 °C at different current densities (redrawn from [26])

$$J^A_{\beta,EM} = -J^B_{\beta,EM} = \frac{C^A_\beta C^B_\beta}{C_0} Z \tag{8}$$

where $J^A_{\beta,EM}$ and $J^B_{\beta,EM}$ represent the flux of atoms of A and B (with concentrations C^A_β and C^B_β) in the product phase β and C_0 is the inverse of the atomic volume Ω. The quantity Z is given by

$$Z = \frac{E|e|}{kT}\left(Z^*_A D^*_A - Z^*_B D^*_B\right) \tag{9}$$

where Z^*_A and Z^*_B represent the effective charge for the two atoms and D^*_A and D^*_B their tracer diffusivities. It is evident that the contribution of the electromigration to the overall atomic flux, and to the growth of the interfacial product, is related to the relative values of the effective charge and of the intrinsic diffusivity of the contributing species. As a result of this, Hsu et al. [32] identified four typical situations for the influence of electromigration on a solid-state reaction:

- If one of the two species has a higher intrinsic diffusivity than the other and the electromigration has a strong influence on its mobility an enhancement in the growth of the layer thickness on the cathode side (cathode enhancement) and a suppression in the layer thickness growth on the anode side (anode suppression) must be expected when the thickness of the product layer is small.
- If the faster diffusing species is insensitive to electromigration, while the slower diffusing species is heavily influenced then cathode suppression and anode enhancement must be expected for small layer thicknesses.
- If both species have similar intrinsic diffusivities the influence of electromigration becomes crucial. In general, for thin reaction layers, a suppression in the growth rate is observed on both sides.

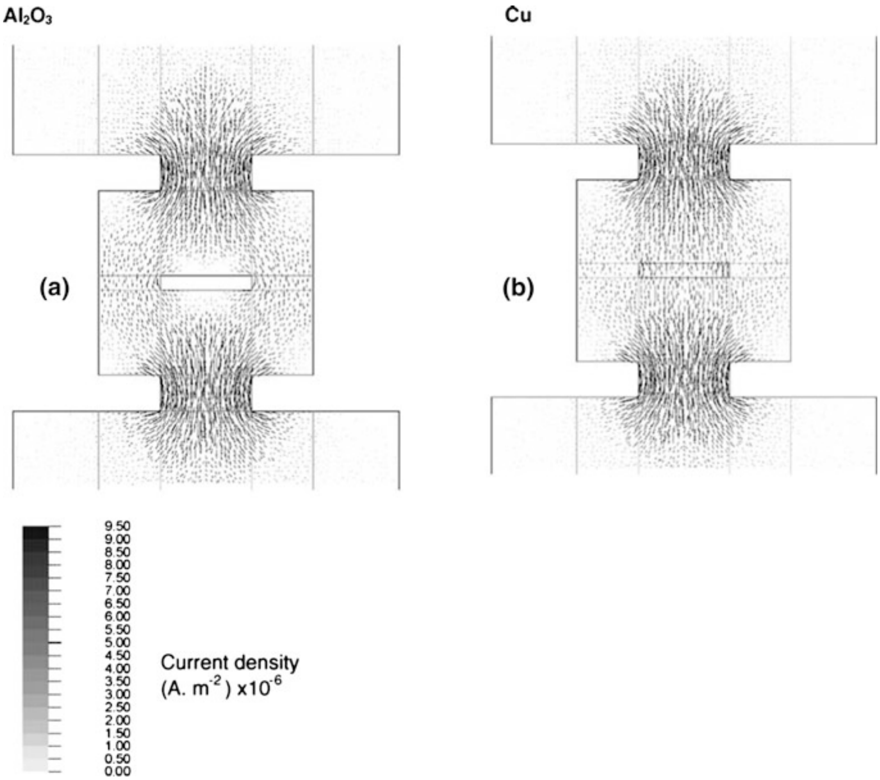

Fig. 5 Current distributions in the SPS die for alumina and copper samples. Applied voltage = 5 V [34]

- When the reaction layers are large, simultaneous cathode and anode enhancements must be expected as the electromigration becomes the dominant mass transfer mechanism.

3.3 *Electromigration in FAST*

As mentioned above, direct experimental evidence for the role of electromigration in FAST processes is limited, even though electromigration it is frequently referred to in the FAST literature.

In discussing the role of electromigration in FAST it is critical to note that the magnitude of the current must be accounted for. It is often reported that very high currents in the range of several thousand Amperes are utilized. However, in a typical geometry, such as the one reported in Fig. 5, only a fraction of the total current flows through the sample even when the sample is a highly conductive material.

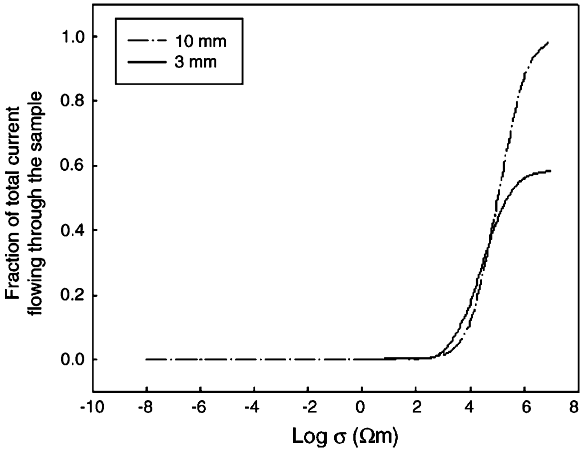

Fig. 6 Dependence of the fraction of the total current flowing through the sample on its electrical conductivity. Sample thickness: 3 and 10 mm; applied voltage = 5 V [34]

The containing die, generally made out of high density graphite, represents an alternative current path, placed in parallel with the sample itself [34]. As a result, the amount of current flowing through the sample is a complex function of the die geometry and of the sample's intrinsic electrical properties. An example of this relationship is reported in Fig. 6, where the actual fraction of the overall current flowing through the sample is reported as a function of the sample conductivity and thickness. It is evident that even for highly conductive samples, only a relatively small fraction of the overall current flows through the sample when the sample is thin. This argument is particularly relevant in the early stage of the process, when the intrinsic electrical conductivity of the pellets is always low, even in the case of metals. As a result, the significance of electromigration for FAST processes might have been over-emphasized in many cases.

A significant contribution to understanding the role of current flux during the sintering of metallic systems has been given by Frei et al. [35]. Here the authors used the classical sphere on plate geometry inside a FAST apparatus forcing all the current to flow through the sample. By applying this approach to copper, a marked influence of current on the kinetics of neck growth was demonstrated. On the other hand, the role of current on the solid state reactivity in a FAST apparatus was shown by Chen et al. [36] and Anselmi-Tamburini et al. [37] through the formation of molybdenum disilicide from elemental starting precursors using a planar diffusion-couple geometry.

4 Electrotransport and Polarization in Ionic Materials

In ionic materials applied external electric fields can produce a shift in the ionic lattice elements in the case of polarization or an enhancement of their movements in the case of electrotransport. The resulting transfer of material might eventually play a role in controlling and/or modifying the kinetic and the mechanisms of the sintering process. Very little attention in the FAST literature has been paid to this relationship to date; however, as the interest in sintering processes involving the application of electric field is increasing, more attention must be paid to this concept. In this section, some basic elements of solid state electrochemistry will be presented in the attempt to clarify the possible role(s) that a field might play during the sintering of ionic materials in general and in FAST in particular.

4.1 Electrochemical Transport and Related Phenomena

It must first be realized that in ionic conductors, as well as in mixed (ionic/electronic) conductors, the application of an electric field can produce a number of different phenomena. The first obvious outcome is represented by the buildup of chemical potential gradients that might eventually produce the decomposition of the compound (electrolysis) when the gradients exceed the stability limits of the material. Separately, or in association with this electrodic polarization, a flux of charged particles (ions, electrons or holes) through the material can occur as well. It is important to note that the possibility of developing an ionic flux (current) is related not only to the intrinsic properties of the material, but also to the nature of the contacts (electrodes) supplying the field [38]. In general four types of electrodes must be considered [38]:

- reversible electrodes (allowing the transfer of any type of carrier)
- electrodes passing only ionic currents (so-called semi-blocking ionic electrodes)
- electrodes passing only electronic currents (so-called semi-blocking electronic electrodes)
- electrodes passing neither ionic nor electronic currents (blocking electrodes)

Incidentally, the last case includes electrodes which are not in contact with the material, so this classification considers either contact and non-contact fields.

It is important to remember that in order to be reversible to ions, an electrode (a material with electronic charge carriers, electrons or holes) must take part in a heterogeneous chemical reaction of the redox kind, where a species of the redox couple is an ion of the sample, the other species of the couple belongs to the electrode phase (or to an additional phase—gas phase, for instance—which is in contact with electrode and sample), and the electrode supplies or removes the electronic carriers required for the reaction balance. At least two coupled electrodic reactions must occur at either side of the sample and both must be free of constraints to complete.

4.1.1 Diffusion Under the Influence of an External Field

First, let’s consider the effect of an applied field on the ionic diffusivity in the presence of completely reversible electrodes. The electric field produces a driving force for matter transfer in addition to chemical potential driven diffusion.

The phenomenological flux equations represented by the Fick's laws for diffusion must then include an additional term to account for the additional driving force.

This represents a particular case of the more general diffusion under the influence of an external force [42, 43]. In the presence of an external acting force F the mobility of the atomic elements will be given by u and their velocity by $F \cdot u$, with the resulting flux of matter becoming

$$J'' = c\,F\,u = c\,v \tag{10}$$

The total flux of matter in one dimension, due to diffusion and the action of an external force, will then be

$$J = -D\frac{\partial c}{\partial x} + c\,v - \nabla U \tag{11}$$

Under the assumption that D is not a function of the local concentration, the rate of change with time will be

$$\frac{\partial c}{\partial x} = D\frac{\partial^2 c}{\partial x^2} - \frac{\partial (c\,v)}{\partial x} \tag{12}$$

If the intensity of the external force is independent from x, then (10) takes the form:

$$\frac{\partial c}{\partial t} = D\frac{\partial^2 c}{\partial x^2} - v\frac{\partial c}{\partial x} \tag{13}$$

In the case of an ionic material, in the presence of an external field, the driving force is $q \cdot E$, where q is the charge of the moving species and E the electric field $-\nabla U$. Therefore, the atomic flux produced by the external driving force will then be given by

$$J_e = c\,\mu\,q\,E \tag{14}$$

This result is largely used in solid state electrochemistry as it relates the ionic flux to the applied field. The potential consequences during sintering are discussed in the following section.

4.1.2 Material Transfer under the Influence of an External Field

Although an external field produces an effect on ionic transport, the resulting ionic flow does not necessarily aid sintering or densification. In order to clarify this point let's consider the effect of a DC field on a metal oxide *MO* utilizing two *equal* non-blocking electrodes [41]. Despite the apparently simple situation, four different cases of electrotransport can be identified which produce different results on the transfer of matter.

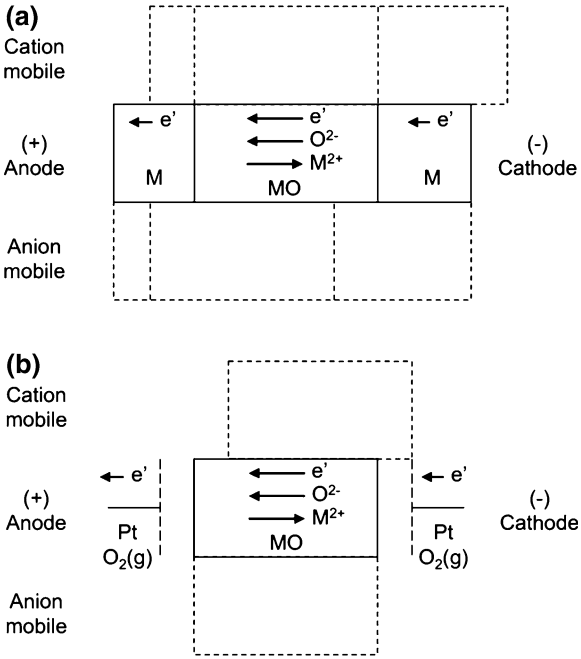

Fig. 7 Schematic of the cell-configuration change with respect to laboratory reference frame, driven by the current flowing through a mixed conductor MO between identical reversible electrodes of (**a**) metal M or (**b**) gas(O_2). Pt indicate inert-metal electrodes. Initial configuration is represented by solid lines. Upper and lower dashed lines show the effects of the current when the cationic and anionic contribution is predominant, respectively. (Redrawn from [41])

The four cases are summarized in Fig. 7 and derive from the nature of the ion (cation or anion) which is exclusively or predominantly mobile and by the nature of the processes taking place at the electrodes. First, it is important to note that the reactions taking place at the electrodes are:

$$M^{2+}(cer) + 2e^- \leftrightarrow M(ele) \tag{15}$$

$$O_2(\frac{gas}{ele}) + 4e^- \leftrightarrow 2O^{2-}(cer) \tag{16}$$

Here the right to left direction describes the oxidation processes occurring at the anode (positive electrode), while the left to right represent the reduction process occurring at the cathode. In the following the four possible situations are analyzed in more detail.

(1)Electrodes reversible to oxide anion and only the cation is mobile:

Here the cathodic process can be written as:

$$2M^{2+}(cer) + O_2(gas) + 4e^- \rightarrow 2MO \tag{17}$$

Two formula units of the solid oxide are formed on the cathode by combining the oxygen anions from reduction of the oxygen gas with the cations which move across the oxide layer. The anodic process can be analogously written as:

$$2MO \rightarrow 2M^{2+} + O_2(gas) + 4e^- \tag{18}$$

indicating that two formula units of the solid oxide are decomposed at the anode to produce oxygen gas plus mobile cations, which can move away in the oxide layer towards the cathode. The overall result of this process in quite interesting. Although no net change in the amount of ceramic phase occurs, equal amounts of ceramic phase are transferred from one electrode to the other. Therefore, the whole sample moves with respect to an external reference frame in the direction from anode to cathode, much like the case of electromigration in metal systems. This is indicated by the dashed lines in the upper part of Fig. 7b, which shows that after a while the oxide will be shifted towards the left. This transport of material towards one electrode might eventually help to densify the material on that side.

(2) Electrodes reversible to mobile oxide anions:

The cathodic reduction and the anodic oxidation reactions for for oxygen are given by the following equations:

$$O_2(gas) + 4e^- \rightarrow 2O^{2-} \tag{19}$$

$$2O^{2-} \rightarrow O_2(gas) + 4e^- \tag{20}$$

In this case, the only species that can move in the solid is oxygen. The result is a transfer of oxygen through the ceramic phase coupled with oxygen reduction at the cathode and oxidation at the anode. The net amount of the phase is again unchanged and there is no transfer of solid material, as indicated by the lower part of 7b.

(3) Electrodes reversible to the mobile cation:

Reduction of the cation at the cathode is described by

$$M^{2+}(cer) + 2e^- \rightarrow M \tag{21}$$

while the oxidation at the anode follows

$$M \rightarrow M^{2+} + 2e^- \tag{22}$$

The cation is also the only species that can diffuse through the oxide layer. This behavior is similar to case 2 in that there is a transfer of material from one electrode to the other, without a direct involvement of the oxide layer. The dimension of one metallic electrode will be reduced and the dimension of the other will increase, as shown by the dashed lines in the upper part of Fig. 7a.

(4) Electrodes reversible to the metal/cation couple, with the anion being the mobile species:

The overall cathodic process can now be written as:

$$2MO + 4e^- \rightarrow 2M + 2O^{2-} \tag{23}$$

Here two formula units of the solid oxide are decomposed at the cathode to depositing reduced metal on the electrode and producing anions, which move through the oxide layer towards the other electrode.

The anodic process can be analogously written as:

$$2M + 2O^{2-} \rightarrow 2MO + 4e^{-} \tag{24}$$

two formula units of the solid oxide are formed at the anode by combining the cations produced by oxidation of the electrodic metal with the anions which move in the oxide layer towards this electrode (lower part of Fig. 7a). As a net result, equal amounts of ceramic phase are decomposed at one electrode and deposited at the other. The total amount of the phase is unchanged (no net formation or electrolysis of the oxide occurs), but the whole sample moves from cathode to anode.

Therefore, the overall result, in two of the four cases, is that the ceramic sample undergoes a net movement with respect to the laboratory reference frame occurring from a net transfer of the oxide from one electrode to the other. In these cases, if the starting material is represented by a porous polycrystalline pellet, the externally applied electric field can produce the decomposition of disordered and porous material at one electrode and rebuild it at the other in a fully dense form. The basic requirement for this process to happen is that the same redox reaction occurs at both electrodes (in opposite directions) and that the mobile ion is different from the electrode-reversible ion. The treatment can be extended in a straightforward manner to semiconducting oxides, if due care is paid to the contribution of electrons or holes to the charge transport in the oxide. The effect then applies to many transition metal (e.g. Fe, Co, Ni) oxides where the ionic contribution to electric conductivity is due to cations, while oxygen ion conductors with fluorite structure (e.g. zirconia, ceria, bismuth oxide) are seemingly ruled out.

It must also be considered that material depletion and accumulation can be observed not only at the electrodes but in any location in the sample where nonzero atomic flux divergence ($\nabla \cdot J \neq 0$) is produced as a result of the microstructure. The process is analogous to the case discussed for electromigration above. In fact, Byeon and Hong [41] have shown how the ionic flux induced by an externally applied field can be used to produce the bonding of two single crystals of manganese-zinc ferrite. Other experimental evidence of these phenomena has been reported in the literature [41–43], although generally the topic has been largely neglected by the sintering community. It is quite possible that these phenomena might play a role in FAST processes, when the right material and the appropriate conditions are met.

4.1.3 Migration of Grain Boundaries

In ionic materials an applied electric field is also known to enhance the mobility of grain boundaries. Grain boundary movement represents an essential step in the grain growth process and is necessary to obtain full densification [44, 45]. The influence of the electric field on grain boundary mobility was thus far mostly reported for alumina [45, 46].

The interaction of grain boundaries with external electric fields derives from the presence of net charges associated with the grain boundary cores. Using absolute-reaction rate theory, Jeong and Han [45] have demonstrated that the driving force ΔG_m that causes an ionic species to jump across a grain boundary is given by:

$$\Delta G_m \cong \Delta G_d + Z_c es\left(\frac{v}{2x_D}\right) \tag{25}$$

ΔG_d is the capillary driving force in the absence of an applied field; Z_c the charge valence of the ion, v the driving force exerted by the applied bias per grain boundary, x_D is the Debye length corresponding to the thickness of the space charge region, e the elementary charge and s the jumping distance of the ion. Grain boundary migration is expected to stop when the applied voltage falls below a threshold value given by:

$$v_{th} \cong -\frac{2x_D \Delta G_d}{Z_c es} \tag{26}$$

For alumina values of −2.15 mV per grain boundary are found, which corresponds to macroscopically applied voltages to the green body of several hundreds or thousands of volts. Initially, such values may appear unreasonable for FAST/SPS applications. However, we will demonstrate further below that local field strengths in dielectric materials may indeed achieve such magnitudes. The possible role that field induced grain boundary movement can play in FAST/SPS processes has still to be clarified, but it might become relevant particularly for nanometric materials.

4.1.4 Correlation Effects in Ionic Materials

Ion movements can derive not only from a concentration gradient or direct electrostatic effects, but also by correlation with the movement of other charge carriers. An example of this is the correlation between the movement of electrons (or holes) and ions in mixed conductors characterized by an elevated electronic conductivities. In these materials an intense electronic flux can produce a flux of the lattice ions, resulting in a net transport of material across the sample. In analogy with the treatment used above for electromigration, the correlation effect between the electronic and ionic movements can be described using the following set of phenomenological equations [47, 48]:

$$\begin{aligned} J_i &= -L_{ii}\nabla\eta_i - L_{ie}\nabla\eta_1, \\ J_e &= -L_{ei}\nabla\eta_e - L_{ee}\nabla\eta_e \end{aligned} \tag{27}$$

where J_e represent the flux of mobile ions and electrons under the effect of the corresponding gradients of electrochemical potentials η_i η_e, while the off-diagonal phenomenological coefficients, following Onsager, are symmetrical $L_{ie} = L_{ei}$. It has long been a common practice to neglect these coefficients, assuming

$$L_{ei} = L_{ie} = 0 \tag{28}$$

meaning that ions and electrons move independently (equivalent to the Kohlrausch's law in electrolytic solutions). However, the work of Yoo et al. [47, 48] has shown that for several semiconducting oxides, such as FeO, CoO, and TiO_2, the relation (28) is not valid. In this case Yoo et al. [47, 48] defined the charge-of-transport for electrons defined as

$$\alpha_e^* \equiv \frac{L_{ei}}{L_{ee}} = \left(\frac{J_i}{J_e}\right)_{\nabla\eta_i=0} \tag{29}$$

representing the number of cations dragged by an electron in the absence of any ionic driving force (i.e.$\nabla\eta_i = 0$). Remarkably, the value of this coefficient can be quite high, approximately 10^{-1}, indicating that the number of cations transferred as a result of this effect can be substantial when high electric currents are involved. Furthermore, it has been shown that in some cases $L_{ie} > L_{ii}$, so the contribution of this effect to the total ionic flux can be relevant.

Correlation effects are usually considered an exotic topic in solid-state electrochemistry and their application to sintering and densification has never been discussed. However, it is important to recognize that, when the appropriate conditions are met, it might produce a contribution to the densification comparable or even higher than the contribution coming from the ionic conductivity. Furthermore, since these processes are induced by the electronic flux, no electrochemical requirements regarding the electrodic reactions are involved. That means that in principle they can be observed in any ionic materials characterized by a high enough electronic conductivity.

4.1.5 Influence of Applied Fields on Reactivity Between Ionic Materials

Electric fields can also modify the reactivity of ionic materials significantly. This represents a topic of particular interest in this overview, since FAST is often used to perform reactive sintering processes.

The influence of electric fields on the solid state reactivity of ionic materials is not surprising, since the reactivity in ionic materials is defined by the diffusivity of the component ions. The rate of growth of a product phase can be enhanced or reduced in the presence of an external electric field, depending on the details of the reaction mechanisms and the experimental conditions. The problem has been investigated extensively, particularly in the case of the formation of spinels starting from the oxides [49–54]. Fig. 8 shows a spinel formation reaction in presence or absence of an external electric field [43]. The reactions at the two phase boundaries that drive the motion of the interfaces are the following

Phase boundary	Reaction	
$AO - AB_2O_4$	$4AO + 2B^{3+} \rightarrow AB_2O_4 + 2A^{2+}$	(30)
$AB_2O_4 - B_2O_3$	$4B_2O_3 + 2A^{2+} \rightarrow 3AB_2O_4 + 2B^{3+}$	(31)

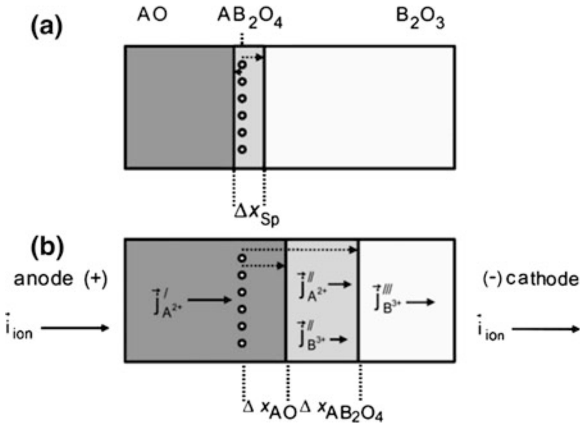

Fig. 8 Spinel formation $AO + B_2O_3 = AB_2O_4$. (**a**) only driven by chemical diffusion and (**b**) in an external electrical field [54]

In the absence of an external applied field, the reaction proceeds through the counter-diffusion of the two cations across the original interface, as the oxygen ions are virtually immobile. Two situations occur in the presence of an external electric field. If the ionic current induced by the external field is directed towards B_2O_3, the total growth rate is increased and the spinel layer grows towards the cathode. If, on the other hand, the ionic current is directed towards AO, the growth process stops at a constant thickness, due to the competition between the atomic flux produced by the electric and the chemical driving forces. A formal theory of this process has been developed by Schmalzried and Smolin [50].

4.2 Dielectric Polarization

As mentioned earlier, FAST/SPS apparatuses apply relatively low electric fields, usually in the range of few volts per meter. However, very little attention has been paid to the fact that an externally applied field can be enhanced locally as a result of the electronic properties of a dielectric material. Since the local field has a significant influence not only on the possible presence of plasma discharge but also in defining local defect equilibria and ionic movements, it represents a topic of great interest when the field assisted sintering of dielectric materials is considered [55].

In general, five different mechanisms of polarization of dielectric materials are considered [56]:

- **Electronic polarization.** This is active in all dielectric materials and is due to the displacement of the electronic clouds against the nuclei. This polarization is approximately proportional to the volume of the electronic cloud, so it is higher for larger atoms.

- **Ionic Polarization.** This is observed in ionic materials and is due to the displacement between the positive and negative sublattices under the effect of the electric field.
- **Orientation polarization.** This is observed in materials containing molecules characterized by permanent dipoles. It derives from the alignment of such permanent dipoles under the external electric field.
- **Space charge polarization.** This is observed when there is a partial mobility in the charge carrier that produces spatial dishomogeneity in the charge distribution.
- **Domain wall polarization.** This is relevant only in the case of ferroelectric materials and is related to the movement of the domain wall that separate regions of different oriented polarization.

The total polarization of a dielectric material results from all the active contributions. Modeling the intergranular electric field in a powder bed is a quite complex task. In the approximation of string of spheres the local intensity of the electric field has been calculated using either a semi-analytical [57] or a purely numerical approach [55]. In the case of spheres connected by a neck, only a numerical approach is viable due to the complexity of the geometry [55]. Furthermore, in the presence of moving charges, the resulting local fields are not prone to analytic solutions.

In a dielectric material the intensity of the externally applied electric field is altered due the charge generated by the polarization process. The field intensity is defined by [58]:

$$\nabla \cdot E = \frac{1}{\varepsilon_0}\left(\rho + \rho_p\right) \tag{32}$$

where ρ_p is the electric charge due to the polarization and ρ represent the other electric charges eventually present. ρ_p is connected to the polarization vector (***P***) through the relation:

$$-\nabla \cdot P = \rho_p \tag{33}$$

Now, in a dielectric material. the polarization is proportional to the electric field

$$P = \varepsilon_0 \chi_e E \tag{34}$$

where χ_e is the electric susceptibility:

$$\varepsilon_r = 1 + \chi_e = \frac{\varepsilon}{\varepsilon_0} \tag{35}$$

From (29) and (30) derives:

$$-\nabla \cdot (\varepsilon_0 E + P) = \rho \tag{36}$$

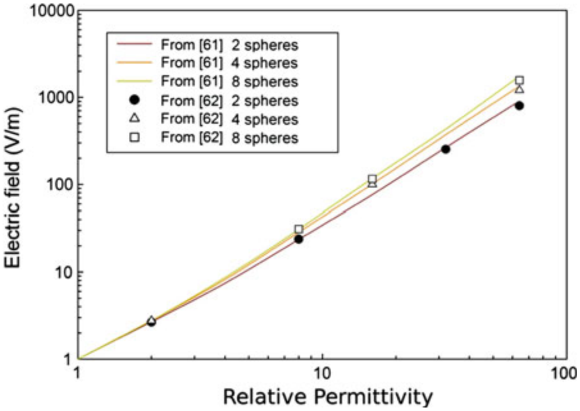

Fig. 9 Electric field at the contact point between a sequence of 2, 4 and 8 spheres exposed to an external uniform field of 1 V/m [57], [59]

It is common practice to define $D = \varepsilon_0 E + P$ as the *electric displacement*. The use of $\boldsymbol{D}$ allows the definition of a relationship between the field and the distribution of the *free charge:*

$$\nabla \cdot D = \rho \tag{37}$$

The field calculations are usually done using the relation (35). In the case of dielectric particles, assuming no free charges and a non-contacting external electric field, the electric field distribution can be solved numerically using the following equation:

$$\nabla \cdot D = 0 \tag{38}$$

From (31) and (34) the displacement is related to the electric field by:

$$\begin{aligned} D &= \varepsilon_0 (1 + \chi_e) E \\ &= \varepsilon_0 \varepsilon_r E \\ &= \varepsilon E \end{aligned} \tag{39}$$

Solving for the electric displacement numerically allows derivation of the field and polarization distributions without any need to consider complex equations involving dipole distributions. Some examples for results of these calculations are reported in Fig. 9.

For Fig. 9 the maximum local electric field was calculated at the point of the contact between adjacent spheres with an externally applied field of 1 V·m^{-1}. Different numbers of spheres were arranged in a line parallel to the direction of the applied field and the resulting local field strengths are reported as a function of the dielectric constant of the material. It is evident that for all geometries the local field can be increased three orders of magnitude when the material is characterized by a high dielectric constant. That means that, in the very early stages of the FAST

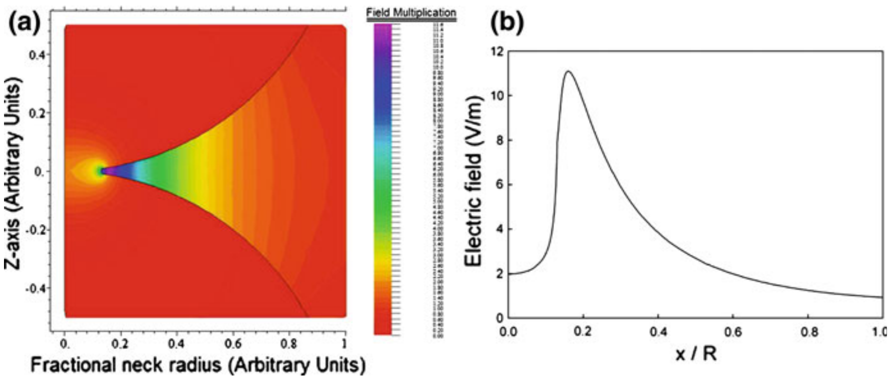

Fig. 10 (**a**) Electric field strength in the region surrounding the neck between two spheres of dielectric material. The neck radius corresponds to 14 % of the particle radius [55]. (**b**) Electric field strength along a line starting from the center of the neck and extending radially for the geometry shown in (**a**) [55]

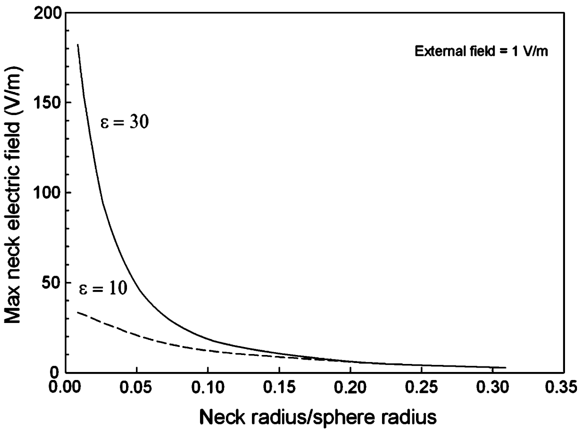

Fig. 11 Maximum field strength in the region around the neck as a function of the ratio between the neck and the spheres radius for two different values of the dielectric constant [55]

process, extremely high local electric fields can be experienced by the particles at their points of contact even if the applied electric field is quite low. It is interesting to note that this amplification effect remains active even when the necks start to grow.

Fig. 10 shows the electric field intensity distribution in the region close to the neck connecting two spheres of dielectric material in the case of a neck dimension that is 14 % of the sphere radius. The intensity of the field in this region decreases with the growth of the neck diameter, but remains significant even for a neck radius that is 14–15 % of the sphere radius as seen in Fig. 11. This is generally considered typical for the transition from early stages to intermediate stages of sintering, and can be assumed to be consistent with the case of high green densities achieved during high pressure sintering or pre-greening. These results suggest that polarization effects might play a relevant role in the sintering of dielectric material under the effect of an external electric field.

It must be noted that polarization effects can play a relevant role also in the early stage of the sintering of metallic powders, since the passivating oxide shell often has dielectric characteristics. Although the layer is generally very thin it can produce a significant local amplification of the externally applied electric field, as suggested by the calculations of Techaumant and Takuma [57, 60]. This point has never been considered in relation with FAST but it surely deserves more attention, as a local field amplification can enhance dielectric breakdown phenomena through the oxide layer, with a resulting relevant influence of the beginning of the sintering process.

4.3 Concluding Remarks on Electrotransport and Related Phenomena

Electrotransport processes are different in several important aspects from the diffusion controlled processes that are active in conventional sintering. Independently of geometry and boundary conditions, a diffusion controlled process shows a specific dependence on time and space coordinates that are generally defined by the $x/t^{1/2}$ ratio in one dimension, a kind of fingerprint of the underlying nature of random walk. On the contrary, field controlled transport shows a constant speed, corresponding to a constant x/t ratio in one dimension. On relatively small length scales processes controlled by electrotransport are therefore comparatively slower than if they are controlled by diffusion (and vice versa). Another significant difference is obviously that electrotransport is driven by an externally set field and therefore can be tuned at will; it is possible to produce an enhancement in the transport or reduce/suppress an unwanted process.

The role that an externally applied electric field might play varies significantly according to the particular stage of the sintering process. In the early stages it might enhance or facilitate the formation of necks and enhance the mobility that sustains their growth, while in the late stages it might enhance bulk mobility, mobility along the grain boundaries, or produce grain boundaries movements. This would and does have a profound effect on the grain growth which defines and controls the final stage of densification of powder samples. Our understanding of these processes is still mostly limited to the general principles and experimental analogies, and as such there is a general lack of experimental evidences clarifying the role that the electric field might actually play for densifying different materials in different experimental conditions. This is a point that needs to be clarified as the interest towards field enhanced techniques is growing rapidly.

5 Pressure Effects and FAST/SPS Processing

In typical FAST/SPS experiments sintering pressures are less than 200 MPa due to the necessity of using conductive die materials, usually represented by high-grade graphite. Experiments in which higher pressures are used uniformly use multi-die plunger setups with SiC plungers being the highest load bearing feature. Consolidation pressures of up to 1 GPa have been achieved with this setup, with the sample dimension being, at the largest, 5 mm. This has limited the use of high pressure to experiments in which no current or field effect is expected to interact with the samples to date, however this limitation is expected to be removed by the use of other die/plunger materials such as: WC/Co, and/or pure WC. Here will be useful to review some of the basic principles of pressure-assisted sintering and then relate what is currently understood about the interactions with an applied field.

5.1 Basic Principles of Pressure Assisted Sintering

The following discussion will exclusively focus on uniaxial pressures utilized in FAST operation. As much of the literature available concerns hot isostatic pressing, some account of the nature of the stresses found in FAST is useful.

When discussing the effects of pressure on the densification behavior we must first discern between the intrinsic and external stresses on the system. In the absence of an externally applied pressure the intrinsic stress state is often calculated using the Laplace equation, shown in Eq. (41).

$$\sigma_{Laplace} = \frac{2\gamma_{sv}}{R} \tag{40}$$

where σ is the stress, γ_{sv} is the surface energy of the particle, and R is the particle radius. Convex surfaces, in which the radius of curvature is inside the mass, are by convention given positive, tensile stress values. While concave surfaces develop opposite stresses. Once a neck forms the Laplace equation is insufficient due to the presence of a negatively (convex) curved neck surface with an interface energy between the grains, γ_{ss}. Once the pores attain equilibrium, i.e. spherical shape in the later stages the sintering stress changes slightly. Raj [61] has demonstrated a more broadly applicable stress associated with both interfaces, shown in Eq. (42).

$$\sigma_{Raj} = \frac{2\gamma_{ss}}{D} + \frac{4\gamma_{sv}}{D_p} \tag{41}$$

where D is the grain size of the sample and D_{p} is the pore size.

FAST processing almost exclusively uses uniaxial pressing which results in a state of stress that is both hydrostatic and deviatoric. The hydrostatic stress largely contributes to the change in the solid–vapor surface energy (γ_{sv}) as shown in Eq. (42) [62],

$$\frac{dV_s}{dt} = (1 - V_s)B\left(g\frac{\gamma_{sv}}{d_p} + P_E\right) \tag{42}$$

where dV_s/dt is the densification rate $(1 - V_s)$ pore fraction remaining, B reflects mostly diffusion related processes, d_p is pore diameter, g is a geometric term, and finally P_E is the effective pressure. The deviatoric stress provides shear stresses to reorganize powders through pore collapse in agglomerates or non-ideal packing, cleans surfaces by shearing removal of oxides and other surface contaminations, and provides for plastic flow of the densifying porous media in the later stages of densification. In nanometric powders, it is often assumed that the intrinsic stress is driven largely by the surface energy of the curved pores.

During the course of densification the actual local pressure levels must be accounted for in porous media. Assuming that the powder particles are perfectly spherical, and before the formation of a neck, the area over which the load is applied approaches zero, resulting in extremely high stress amplification. As densification proceeds the neck size increases, while through plastic or diffusional flow stress accommodation mechanisms and the level of stress is reduced accordingly. Once the final stage of sintering is achieved, at which point closed porosity occurs, the "effective" stress is lessened by the gas pressure occurring in closed pores. In uniaxial hot pressing it is found that the presence of the deviatoric stress provides an increase in pore coordination (N_c) up to approximately 14 for initial powder packing. This decreases as a function of density (V_s), and is well represented by German's equation:

$$N_c = 14 - 10.4(1 - V_s)^{0.38} \tag{43}$$

This relationship assumes that the particles are spherical, make spherical contacts, and ideal packing occurs. So, in addition to the stress changes inherent in growing necks, one must account for the concomitant changes in coordination that occur across the stages of sintering. The relationship of the externally applied pressure, σ_e, to the average contact force between particles, f, is,

$$f = \frac{4\pi R^2}{N_c V_s}\sigma_e \tag{44}$$

where R is the particle radius. Therefore, prior to pore closure, the effective pressure, σ_{eff}, at each particle would be

$$\sigma_{eff} = \frac{4\pi R^2}{a N_c V_s}\sigma_e + \sigma_{Laplace/Raj} \tag{45}$$

where a is the area of the forming neck. $\sigma_{Laplace/Raj}$ reflects either the intrinsic stress from Eqs. (41) ($\sigma_{Laplace}$) or (42) (σ_{Raj}).

The densification rate will change as the effective pressure decreases with the increasing levels of density. At stress levels above those of the temperature compensated yield stresses, the densification is rate independent and immediate. As the pressure levels diminish with higher density, and grain growth, the pressure effects become dominated by rate dependent creep and/or diffusion mechanisms.

5.2 Energetics of Pressure Sintering

The influence of pressure upon the thermodynamics and kinetics of densification is often oversimplified in the FAST literature. This largely stems from the low pressures involved in most experiments. Increasingly higher levels of pressure (up to 1GP) are being utilized. It is largely unresolved whether there exists an interaction between the applied field and the pressure, particularly in materials other than alkali-halides and fast-ion conductors. In the following we will discuss possible interactions applied fields and pressures.

In the presence of an applied pressure, p, the Gibbs free energy of activation for the diffusion process changes in accordance with the hydrostatic component of stress.

$$\Delta G = \Delta E - T\Delta S + p\Delta V \tag{46}$$

ΔE is the activation energy of diffusion associated with the internal energy change and $\Delta V = (\partial \Delta G/\partial p)_T$ is the activation volume of diffusion. Inspection of Eq. (46) reveals how the activation enthalpy is modified by the change in pressure.

$$\Delta H = \Delta E + p\Delta V \tag{47}$$

Considering the Arrhenius-type equation for diffusivity and the differential of Eq. (47) with respect to pressure results in Eq. (48) for the activation volume ΔV.

$$\Delta V = -k_b T\left(\frac{\delta \ln D}{\delta P}\right)_T + k_b T\left(\frac{\delta \ln f a^2 v^0}{\delta P}\right) \tag{48}$$

f is the correlation coefficient for diffusion, a is the lattice parameter of the crystal, and v^0 is the jump frequency. The first term in Eq. (48) typically dominates the activation volume while the second term represents small fractions of the molecular volume. ΔV is considered the *effective* activation volume combining the diffusivities of the various individual diffusion mechanisms. Activation volumes are experimentally determined by measuring the changes in ionic conductivity (σ_{DC}) as a function of applied pressure, resulting in a conductivity-dependent activation volume, V_σ. For such analysis, only the dominant part of Eq. (48) is used for a reasonable approximation:

$$\Delta V_\sigma \approx -k_b T\left(\frac{\delta \ln \sigma_{DC}}{\delta P}\right) \tag{49}$$

The effective activation volume is a weighted average of the activation volumes of the operative mechanisms currently contributing to material flow. Therefore, it is sensitive to changes in mechanism, e.g., when a transition from single vacancy to di-vacancy dominated diffusion occurs.

The pressures alone used during FAST are not sufficient to contribute to significant increases in the diffusivity. A synergistic interaction between the applied fields, particularly in the case of stronger field strengths, may however generate more suitable "hydrostatic pressures" for FAST applications. Ita and Cohen [63] modeled the pressure affected diffusivity in MgO over a wide range of pressures up to 140 GPa and found that the free energies of migration of Mg or O vacancies were largely insensitive to applied pressures while the formation of vacancy pairs (Schottky defects) had a measurable response. However, changes in activation energy were of the order of 10^{-19} J, which is insignificant compared to pressure ranges achievable during SPS. They find that the commonly used approximation for incorporating pressure effects is reasonably accurate. By normalizing the experimental temperature with that of the pressure dependent melting temperature, Eq. (50) was found to be accurate within the constraints of the pressure/melting interaction [63, 64].

$$D(P,T) = D_0 \exp\left(\frac{-gT_m(P)}{RT}\right) \tag{50}$$

For common amounts of pressure during FAST processing, the melting temperature of most materials depends weakly on the current pressure. Hence, in the absence of a synergistic operation with applied fields, pressures during SPS directly are deviatoric and cause time-dependent deformation mechanisms such as creep.

5.3 *Field Effects and Pressure*

The application of an electric field and/or current to samples during the pressure sintering process is of particular interest to the FAST community. Often it is discussed under the term electroplasticity, though the term covers a range of behaviors including the time-dependent deformation of fully dense materials as well. Here we relate the relevant contributions of applied fields to the plastic deformation of conductive and non-conductive samples at each stage of sintering.

5.3.1 Conductive Materials

The effect on the strain-rate during creep tests on metals has been suggested by Conrad [65] to have a minimum critical DC current density of 10^3 A/cm^2 or greater. Above this value an increase in creep rates of five orders of magnitude can be found. These increases are not expected to be related to the interaction of fields with dislocation motion as several in situ observations [66, 67] of the critical current density for dislocation motion are above 10^5 A/cm^2. Conrad suggests that only the thermal component of flow stress is affected by the current density and that the rate controlling mechanism is unchanged. It is important to distinguish between the applied field strength and the applied current as both have been found to contribute to strain-rate changes in metals. An applied, external field has been found to enhance **or** retard creep rates at homologous temperatures higher than $\sim 0.5T_\mathrm{m}$ where grain boundary diffusion dominates.

The particular nature of how the current can interact with the creep behavior is important in the understanding of the effects of sintering of these powders in the presence of a strong electric current. The effect on the modulus of the material, M, was found by Mizubayashi et al. [68] to differ under high current densities according to Eq. (51) [68]

$$M = \frac{Z^{*} e \phi}{\alpha i_d S} \tag{51}$$

where Z^{*} is the effective valence parameter of the total contributing diffusive species, e is the elementary charge number, φ is the applied electric field, S is the area over which the force acts, α is a proportionality constant, and finally i_d is the current density. Therefore in the early stages of sintering the contribution of the field then can be seen to lower the modulus, thus increasing the effective strain imparted by the elevated stress levels from small contact areas as discussed above. Unfortunately the effective valence parameters and proportionality are not commonly available for many systems.

5.3.2 Non Conductive Materials

In ceramic materials the mechanical response to an applied field is less well understood. Primarily, the bulk of the work devoted to the interactions of an applied field and pressure is on alkali halides such as NaCl. The use of applied fields with strengths of 13 kV/cm has been shown by Zuev et al. [69] to increase the dislocation velocities, with the concomitant lowering of the flow stress, in single crystals of NaCl, while Yang and Conrad [70, 71] have found that applied fields with an order of magnitude lesser strength show decreases in flow stress in proportion with the applied field strengths. The decreases were found to occur with and without contacting electrodes [72], are independent of the field direction, had no effect on strain rate sensitivity, and were insensitive to grain size changes in the 30–2000 μm range. All tests were performed in the creep regime consistent with power-law, dislocation-mediated deformation. Since the non-contacting and contacting electrode results do not vary, it is clear that the role of a field in the plastic accommodation mechanism is not consistent with the nature of electromigration, but it is the result of the interaction with the applied field itself. Dislocations in alkali halides have been known to have net charges associated with them since the early 1950 and 1960s, and it is reasonable to expect that an applied field will then produce a net force upon the length of the dislocation line of appropriate orientation. The force per unit length of a dislocation is balanced by the charge of the dislocation per unit length oriented appropriately in the field as shown in Eq. 52,

$$\tau \cdot \vec{b} = qE \cos\theta \tag{52}$$

where q is the charge per unit length of the dislocation in the halide, E is the field strength, τ is the applied stress, $\vec{b}$ is the Burger's vectors, and θ is the angle between the Burger's vector and applied field. A more thorough discussion of the specifics of dislocation charges in ionic materials may be found in [73]. Conrad notes that a further influence of the field may be in the redistribution of charged defects within the crystal which would have an influence similar to that of increasing the Peierl's force discussed in most dislocation theory.

6 Heating Rate Effects

Elevated heating rates have long been known to benefit densification behaviors in numerous material systems [74–78]. Early studies on heating rate in typical hot-pressing experiments on large grained powders showed strong effects in moving from 10 to 50 °C/min, so naturally it has been assumed that the same increases in densification rates and decreased final grain sizes would extend to FAST processes where heating rates can achieve up to 1500 °C/min. Unfortunately the picture has not been particularly clear for the powder systems usually studied in FAST. It is therefore beneficial to first understand the contributions of elevated heating rates during sintering and/or densification in theory before attempting to determine the role heating plays in and of itself during FAST densification.

6.1 Kinetics and Driving Force During Sintering

Olevsky et.al. [77] have suggested a more comprehensive model by which the contributions of heating rate may be understood. The bulk of their arguments are outside the scope of this chapter, but a general and somewhat simplified description of heating rate contributions that are consistent with their model is useful. The main contribution of heating rate to the densification behavior derives from the time spent at temperatures where non-densifying mass flow mechanisms are dominant. During heating to a given target temperature, often chosen to be approximately 0.7–0.75T_m, the powders proceed through several mass flow regimes from the lowest activation energy to highest: surface diffusion, grain boundary diffusion, power-law creep, and finally volume diffusion. Surface diffusion is non-densifying since the mass transfer is wholly confined to the surface of the neck regions and does not result in lessening of the distance between powder particle centers.

However, Olevsky et. al. argue that surface diffusion reshapes pores to have larger radii of curvatures and therefore lessened driving force for removal of the pores. This process is called pore spheroidization. If the time spent in the surface diffusion dominated regime (0.25–0.4T_m) is minimized, the microstructure may then achieve both high driving forces *and* fast, densifying kinetic mechanisms to provide fully dense microstructures. During the final stage of densification, less grain growth is necessary to achieve the full density. As one would expect the contribution is very dependent upon the starting grain size of the powders. Using

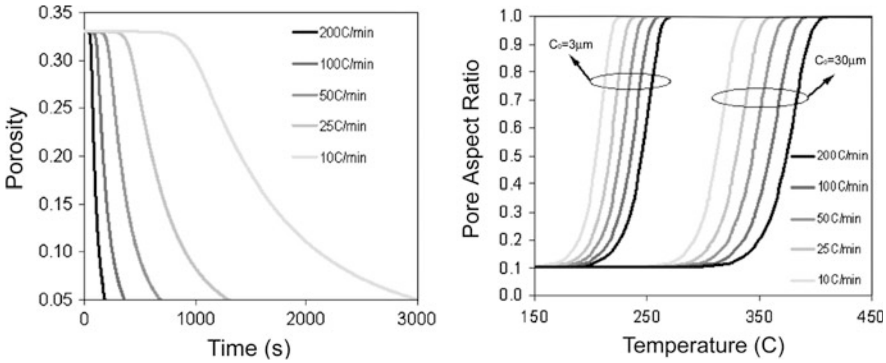

Fig. 12 Pore spheroidization in aluminum powders for starting grain sizes of 3 and 30 μm. [77]

aluminum as a model material Olevsky et.al. find that the rate of pore spheroidization is less sensitive to heating rate as starting grain size is diminished (Fig. 12). Qualitatively similar results were found by Zhou et.al. [79], Zhao et.al. [80] and Shen et.al. [81] in FAST experiments with heating rate.

6.2 Reactive Sintering

In reactive sintering the heating rate can be utilized to modify the temperatures at which a reaction may occur. Phase transformation, such as glass de-vitrification or other 1st order reactions, temperatures are elevated for increasing heating rates. This is due to the Kissinger effect [85] (Eq. 53), which describes that for a temperature-dependent reaction the onset of that reaction will vary in accordance with the applied isothermal heating rate.

$$\ln\left[\frac{A\dot{T}}{T^2}\right] = B - \frac{\Delta H_{rxn}}{k_b T} \tag{53}$$

In the equation above A and B are given material constants, and $\dot{T}$ is the heating rate. In some cases this may be useful for increasing the driving force for the reaction and its nucleation rate. Very little work exists in the FAST literature related to Kissinger experiments, however.

6.3 Thermodiffusion

Thermodiffusion (also known as Soret, Ludwig-Soret, Thermomigration, or Thermotransport) can be considered a subset of effects associated with heating rates as it relates the occurrence of increased driving forces occurring from the presence of thermal gradients. In principle it is an application of the process of non-equilibrium or irreversible thermodynamics. In terms of flux discussed earlier in this chapter, thermodiffusion is the natural result of the off-diagonal terms found in the flux/force matrix from Eq. (1), where Q represents heat flow and M represents mass flow in one a single dimension x.

$$J_Q = -L_{QQ}\frac{1}{T}\frac{dT}{dx} - L_{QM}T\frac{d}{dx}\left(\frac{\mu}{T}\right) \tag{54}$$

$$J_M = -L_{MQ}\frac{1}{T}\frac{dT}{dx} - L_{MM}T\frac{d}{dx}\left(\frac{\mu}{T}\right) \tag{55}$$

Equations (54) and (55) completely describe the relationship between the mass and heat flow in the presence of a temperature gradient. Typically, thermotransport is represented only in the case of the steady state mass flow where J_M is zero. Thus algebraically the steady state relationship for thermotransport can be represented as

$$d\left(\frac{\mu}{T}\right) = -\frac{L_{MQ}}{L_{MM}}\frac{dT}{T^2} \tag{56}$$

where the complete differential $d(\mu/T)$ using the thermodynamic relationships from Eq. 46 becomes,

$$d\left(\frac{\mu}{T}\right) = \frac{\overline{V}dP}{T} - \frac{\overline{H}dT}{T^2} \tag{57}$$

Set equal to one another equations. Eqs. (56) and (57) are typically represented as:

$$\frac{\overline{V}dP}{T} = -Q^*\frac{dT}{T^2} \tag{58}$$

where Q^* is the heat of transport of the moving species. Q^* then represents a difference in the energy of the moving species and the partial molar enthalpy of the region from which it has diffused. Or more succinctly stated, it is the apparent amount of heat the diffusing species carries per atom. Thermotransport it is also applicable for the determination of vacancy motion in the presence of a thermal gradient. In the presence of a thermal gradient, vacancies will be distributed in accordance with the thermal gradient while the overall concentration of vacancies is maintained at an equilibrium value. This concept was first proposed by Shockley [83] and demonstrated experimentally in Zn by Shewmon [84]. In determining the flux of vacancies it is then only necessary to set the flux of atoms equal to an opposite flux of vacancies along with the Onsager reciprocity relationship (microscopic reversibility produces off-diagonal terms that are identical i.e. $L_{ik} = L_{ki}$). It is readily found then that the flux of vacancies, J_v, becomes

$$J_v = -Dn\left[\nabla C_v - \frac{Q^* C_v \nabla T}{k_b T^2}\right] \tag{59}$$

Fig. 13 Relative magnitudes of densification rate contributions of surface tensions, power-law creep, and thermotransport for (**a**) fine grain and (**b**) large grain sizes [78]

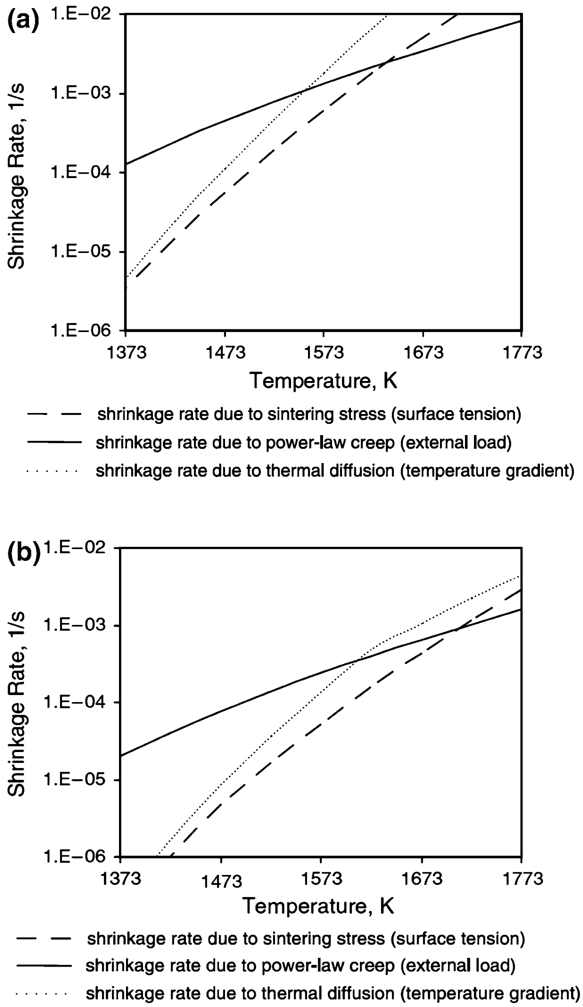

where n is the number of atoms per unit volume, D is the self-diffusion coefficient of the diffusing species, ΔC_v is the vacancy concentration gradient, and ΔT is the temperature gradient. Olevsky et al. [78] note a particularly important point to understand about Eq. 59: the temperature gradient has two distinct contributions. The first term reflects the vacancy distribution as a function of the temperature gradient, and the second describes the specific effect of thermotransport in crystalline solids. The details of how this is related to sintering at elevated heating rates or in the presence of the natural thermal gradients developed in FAST are outside the scope of this chapter, but are well described in a paper by Olevsky on the subject. Overall, their model suggests that at high heating rates thermotransport may contribute significantly to the densification rates of non-conductive materials primarily and is increasingly active as grain sizes are lowered as shown in Fig. 13.

7 Summary

It is shown that the prediction of the consolidation performance of the FAST technique is complicated by a myriad of influences. The incorporation of thermotransport into models of densification in non-conductive materials, or conductive materials in which a non-conductive layer is present, is necessary. The current best models assume that vacancy concentrations from thermotransport are linearly independent of fields and/or stresses (Laplacian or applied), and as such may underestimate the role of this mechanism in FAST/SPS applications.

Acknowledgments T. B. Holland and A. K. Mukherjee would like to thank the Office of Naval Research Program Manager, Dr. Lawrence Kabacoff, for his support (ONR Grant #N00014-10-1-0632).

References

1. Tokita, M.: Proceedings of NEDO International Symposium on Functionally Graded Materials, Kyoto, 1999
2. Tokita, M.: J. Soc. Powder Technol. Jpn. **30**, 790 (1993)
3. Omori, M.: Mater. Sci. Eng. A **287**, 183–188 (2000)
4. Yanagisawa, O., Kuramoto, H., Matsugi, K., Komatsu, M.: Mater. Sci. Eng. A **350**, 184–189 (2003)
5. Hulbert, D.M., Anders, A., Dudina, D.V., Andersson, J., Jiang, D., Unuvar, C., Anselmi-Tamburini, U., Lavernia, E.J., Mukherjee, A.K.: J. Appl. Phys. **104** (3), 033305–033307 (2008)
6. Hulbert, D.M., Anders, A., Andersson, J., Lavernia, E.J., Mukherjee, A.K.: Scripta Mater. **60**, 835–838 (2009)
7. Smirnov, B.M.: Plasma Processes and Plasma Kinetics. Wiley-VCH, Weinheim (2007)
8. Anders, A.: Arcs: From Fractal Spots to Energetic Condensation. Springer, New York (2008)
9. Chapman, B.: Glow Discharge Process: Sputtering and Plasma Etching. Wiley, New York (1980)
10. Tan, C.M., Roy, A.: Mater. Sci. Eng. R **58**, 1–75 (2007)
11. Ho, P.S., Kwok, T.: Rep. Prog. Phys. **52**, 301–348 (1989)
12. Tu, K.N.: Phys. Rev. B **45**, 1409 (1992)
13. Ho, P.S.: Phys. Rev. B **8**, 4534 (1973)
14. Pierce, D.G., Brusius, P.G.: Microelectron. Reliab. **37**, 1053–1072 (1997)
15. de Orio, R.L., Ceric, H., Selberherr, S.: Microelectron. Reliab. **50**, 775–789 (2010)
16. Kraft, O., Sanchez Jr, J.E., Bauer, M., Arzt, E.: J. Mater. Res. **12**, 2027–2037 (1997)
17. Blech, I.A., Herring, C.: Appl. Phys. Lett. **29**, 131 (1976)
18. Blech, I.A., Tai, K.L.: Appl. Phys. Lett. **30**, 387–389 (1977)
19. Chen, S.W., Chen, C.M.: JOM **55**, 62–67 (2003)
20. Yamanaka, K., Tsukada, Y., Suganuma, K.: Scripta Mater. **55**, 867–870 (2006)
21. Liu, W.-C., Chen, S.-W., Chen, C.-M.: J. Electron. Mater. **27**, L6–L9 (1998)
22. Chen, S.-W., Chen, C.-M., Liu, W.-C.: J. Electron. Mater. **27**, 1193–1199 (1998)
23. Chen, C.-M., Chen, S.-W.: J. Electron. Mater. **28**, 902–906 (1999)
24. Chen, C.-M., Chen, S.-W.: J. Electron. Mater. **29**, 1222–1228 (2000)
25. Bertolino, N., Garay, J., Anselmi-Tamburini, U., Munir, Z.A.: Scripta Mater. **44**, 737–742 (2001)
26. Bertolino, N., Garay, J., Anselmi-Tamburini, U., Munir, Z.A.: Philos. Mag. B **82**, 969–985 (2002)

27. Garay, J.E., Anselmi-Tamburini, U., Munir, Z.A.: Acta Mater. **51**, 4487–4495 (2003)
28. Friedman, J.R., Garay, J.E., Anselmi-Tamburini, U., Munir, Z.A.: Intermetallics **12**, 589–597 (2004)
29 Kumar, A., He, M., Chen, Z., Teo, P.S.: Thin Solid Films **462–463**, 413–418 (2004)
30 Gan, H., Tu, K.N.: J. Appl. Phys. **97**, 063514 (2005)
31 Orchard, H.T., Greer, A.L.: Appl. Phys. Lett. **86**, 1–3 (2005)
32. Hsu, C.-M., Wong, D. S.-H, Chen, S.-W.: J. Appl. Phys. **102,** (2007)
33. Leo, P., Rasetti, A.: J. Electron. Mater. **39**, 2687–2695 (2010)
34. Anselmi-Tamburini, U., Gennari, S., Garay, J.E., Munir, Z.A.: Mater. Sci. Eng. A **394**, 139–148 (2005)
35. Frei, J.M., Anselmi-Tamburini, U., Munir, Z.A.: J. Appl. Phys. **101**, (2007)
36. Chen, W., Anselmi-Tamburini, U., Garay, J.E., Groza, J.R., Munir, Z.A.: Mater. Sci. Eng. A **394**, 132–138 (2005)
37. Anselmi-Tamburini, U., Garay, J.E., Munir, Z.A.: Mater. Sci. Eng. A **407**, 24–30 (2005)
38. Kroger, F. A., The Chemistry of Imperfect Crystals. p. 131. North-Holland Publ. Co and Wiley, New York(1964)
39. Jost, W.: Diffusion in Solids, Liquids, Gases. Academic Press, London (1952)
40. Mehrer, H.: Diffusion in Solids: Fundamentals, Methods, Materials, Diffusion-Controlled Processes, 1st ed. 2007. Corr. 2nd ed. Springer, New York (2007)
41. Byeon, S.C., Hong, K.S.: Mater. Sci. Eng. A **287**, 159–170 (2000)
42. Yoo, H.-I., Lee, K.-C.: J. Electrochem. Soc. **145**, 4243–4247 (1998)
43. Yoo, H.-I., Lee, C.-E., De Souza, R.A., Martin, E.M.: Equal mobility of constituent cations in $BaTiO_3$. Appl. Phys. Lett. **92**, (2008)
44. Lange, F.F., Kellett, B.J.: J. Am. Ceram. Soc. **72**, 735–741 (1989)
45. Jeong, J.-W., Han, J.-H., Kim, D.-Y.: J. Am. Ceram. Soc. **83**, 915–918 (2000)
46. Choi, J.-I., Han, J.-H., Kim, D.-Y.: J. Am. Ceram. Soc. **86**, 640–643 (2003)
47. Yoo, H.-I., Lee, J.-H., Martin, M., Janek, J., Schmalzried, H.: Solid State Ionics **67**, 317–322 (1994)
48. Yoo, H.-I., Lee, D.-K.: Solid State Ionics **179**, 837–841 (2008)
49. Brown, I.W.M., Mackenzie, K.J.D.: J. Mater. Sci. **17**, 3663–3671 (1982)
50. Schmalzried, H., Smolin, S.: Phys. Chem. Chem. Phys. **102**, 1740–1746 (1998)
51. Johnson, M.T., Schmalzried, H., Carter, C.B.: Solid State Ionics **101–103**, 1327–1333 (1997)
52. Johnson, M.T., Carter, C.B., Schmalzried, H.: J. Am. Ceram. Soc. **83**, 1768–1772 (2000)
53. Korte, C., Ravishankar, N., Carter, C.B., Schmalzried, H.: Solid State Ionics **148**, 111–121 (2002)
54. Korte, C., Zakharov, N.D., Hesse, D.: Phys. Chem. Chem. Phys. **5**, 5530 (2003)
55. Holland, T.B., Anselmi-Tamburini, U., Quach, D.V., Tran, T.B., Mukherjee, A.K.: Effects of local Joule heating during the field assisted sintering of ionic ceramics. J. Eur. Ceram. Soc. (2012, in press)
56. Kittel, C.: Introduction to Solid State Physics. Wiley, New York (1996)
57. Techaumnat, B.,Takuma, T.: IEEE Trans. Dielectr. Electr. Insul. **10**, 623–633 (2003)
58. Cheng, D.K.: Field and Wave Electromagnetics. Addison-Wesley, Boston (1983)
59. Holland, T.B., Tran, T.B., Quach, D.V.: J. Eur. Ceram. Soc., http://dx.doi.org/10.1016/j.jeurceramsoc.2012.03.012 (2012)
60. Techaumant, B., Takuma, T.: IEEE Trans. Magnet. **41**, 1388–1391 (2005)
61. Raj, R.: J. Am. Ceram. Soc. **70**, C210 (1987)
62. German, R.M.: Sintering Theory and Practice. John Wiley and Sons Inc., New York (1996)
63. Ita, J., Cohen, R.E.: Phys. Rev. Lett. **79,** 3198–3201 (1997)
64. Sammis, C.G., Smith, J.C., Schubert, G.: J. Geophys. Res. **86**, 10707–10718 (1981)
65. Conrad, H.: Electroplasticity in metals and ceramics. Mater. Sci. Eng. A **287**, 276–287 (2000)
66. Livesay, B., Donlin, N., Garrison, A., Harris, H., Hubbard, J.: Dislocation based mechanisms in electromigration," International Reliability Physics Symposium, IEEE, pp. 217–227 (1992)
67. Vdovin, E., Yu Kasumov, A.: Sov. Phys. Solid State **30**, 180 (1988)

68. Mizubayashi, H., Kameyama, N., Hao, T., Tanimoto, H., Phys. Rev. B **64**, (2001)
69. Zuev, L., Gromov, V., Alexankina, O.: Sov. Phys. Crystallogr. **19**, 553 (1975)
70. Di, Y., Conrad, H.: Mater. Sci. Engr. A **225**, 173 (1997)
71. Di, Y., Conrad, H.: Br. Ceram. Soc. Trans. **97**, 263 (1999)
72. Di, Y., Conrad, H.: Am. Ceram. Soc. **80**, 1389 (1998)
73. Hirth J.P., Lothe, J.: Theory of Dislocations. p. 857, John Wiley and Sons, Inc., (1982)
74. Zhou, Y., Hirao, K., Yamauchi, Y., Kanzaki, S.: Scripta Mater. **48**, 1631–1636 (2003)
75. Chu, M.Y., Rahaman, M.N., Jonghe, L.C., Brook, R.J.: J. Am. Ceram. Soc. **74**, 1217–1225 (1991)
76. Zaspalis, V.T., Sklari, S., Kolenbrander, M.: J. Magn. Magn. Mater. **310**, 28–36 (2007)
77. Olevsky, E.A., Kandukuri, S., Froyen, L.: J. Appl. Phys. **102**, 114913 (2007)
78. Olevsky, E.A., Froyen, L.: J. Am. Ceram. Soc. **92**, S122–S132 (2009)
79. Zhou, Y., Hirao, K., Yamauchi, Y., Kanzaki, S.: Scr. Mater. **48**, 1631 (2003)
80. Zhao, J., Holland, T., Unuvar, C., Munir, Z.A.: Int. J. Refract. Met. Hard Mater. (2008)
81. Shen, Z., Johnsson, M., Zhao, Z., Nygren, M.: J. Am. Ceram. Soc. **85**, 1921 (2002)
82. Kissinger, H.E.: J. Res. Nat. Bur. Stand. **57**, 217 (1956)
83. Shockley, W.: Phys. Rev. **91**, 1563–1564 (1953)
84. Shewmon, P.: J. Chem. Phys. **29**(1032), 1958 (1958)
85. Di, Y., Conrad, H.: Acta Mater. **46**, 1998 (1963)

Effects of Applied Stress and Heating Rate in Field Assisted Sintering

Olivier Guillon

Abstract In the previous chapters we have mainly described the effects of the electrical field on the densification behavior when using Field Assisted Sintering. In addition to those effects, Field Assisted Sintering also offers the possibility of applying a mechanical pressure as well as high heating rates during sintering. The result is a significant change in the sintering process. That is, we have gone through the description of conventional sintering in the initial chapters of this book, and there is a great temptation to use that theory directly to understand SPS. But comparing free sintering and SPS is like comparing the performances of two ways of transportation such as bicycle and motorcycle. The first one relies on a natural driving force (the rider's muscles), the second one gets further energy from the attached engine. The translation movement obtained through rotation of wheels is the same but kinetics and possibly final destination are not! Therefore, the present chapter aims at reviewing the separate contributions of applied stress and heating rate on the densification behavior and microstructure development of oxide ceramics. Carefully-designed experiments coupled with physical understanding enable us to figure out the real advantages and drawbacks of this technique as well as to extend its possibilities.

O. Guillon (✉)
Friedrich-Schiller-Universität Jena, Institute of Materials Science and Technology,
Löbdergraben 32, 07743 Jena, Germany
e-mail: olivier.guillon@uni-jena.de

R. H. R. Castro and K. van Benthem (eds.), *Sintering*, Engineering Materials 35,
DOI: 10.1007/978-3-642-31009-6_9,

1 Effect of Applied Stress

1.1 Theoretical Framework

We have seen that sintering is a thermally activated process whose driving force is provided by the surface curvature of particles. This leads to the reduction of the total free energy in the system. However, for some materials/powders, full densification may be difficult to reach and an additional driving force for sintering provided by externally applied mechanical pressure may be required.

A mechanical stress modifies the densification behavior in the following ways [1, 2]: At a minimum it enhances the existing densification mechanisms already present in free sintering (such as diffusion through grain boundaries or lattice, viscous flow) while not affecting the non-densifying mechanisms (such as surface diffusion, evaporation/condensation). It can also activate new mechanisms, such as plastic deformation or grain boundary sliding. The useful “deformation mechanism maps” have been established showing the controlling densification mechanism based on the temperature, pressure conditions and grain size [3].

Different types of pressure-assisted sintering can be listed. First, sinter-forging describes the case where the specimen is free to deform radially under a uniaxial pressure in the order of magnitude of the sintering stress [4]. The sintering stress (or sintering potential) is related to grain size (or particle size in the case of amorphous materials), pore size, surface energy and grain boundary energy [2, 5]. Submicron oxide powders exhibit sintering stress in the MPa range, as shown for alumina [6], or even higher in case of nanocrystalline compacts with a fine porosity.

Second, in hot pressing (HP) and SPS, the powder is confined in a die, pressed between two punches and in general the effective stress is significantly larger than the sintering stress. Finally, hot isostatic pressing (HIP) involves hydrostatic pressure, transmitted through a fluid at high temperature.

Creep equations describing the deformation of dense materials at high temperature were adapted for the intermediate and final stage of sintering by transforming creep rate into densification rate and by taking into account the porous nature of the sintering body [7, 8]. However, these equations are only an approximation of the densification in HP or SPS. Modified versions could include pore separation as realistic length scale for diffusion for example. They were also embedded in a set of constitutive equations relating strain rates and stresses [9, 10]. Still, this continuum mechanical description is useful to identify the main mechanisms during SPS and HP and is described in the following paragraph.

By using a die, the lateral shrinkage of the sample remains negligible and densification takes place only along the thickness direction. As large strains are observed, the use of true strain ε_z should be preferred to the engineering strain:

$$\varepsilon_z = \ln\left(\frac{h}{h_0}\right) \tag{1}$$

where h is the instantaneous sample height and h_0 is the initial height of the green body. Instantaneous density ρ can be computed from the following equation:

$$\rho = \rho_0 \exp(-\varepsilon_z) \tag{2}$$

where ρ_0 is the initial sample density.

By neglecting the intrinsic sintering stress, the normalized densification rate (equal to the opposite of the true strain rate) can be described by the following general equation [1]:

$$\frac{1}{\rho}\frac{d\rho}{dt} = -\dot{\varepsilon}_z = \frac{HD}{G^m kT}(\phi p_a)^n \tag{3}$$

where H is a numerical constant (including Burgers vector and shear modulus when dislocation motion is active). The diffusion coefficient of the rate-controlling species D is given by:

$$D = D_0 \exp\left(\frac{-E_a}{RT}\right) \tag{4}$$

where D_0 is a pre-exponential factor, E_a is the activation energy, R is the gas constant, G is the grain size, k is the Boltzmann constant, T is the absolute temperature.

The product ϕ (stress intensification factor) times p_a (uniaxial applied stress) is called effective stress. The stress exponent n and grain size exponent m depend on the sintering mechanism. When dislocation motion is active, the effective stress may be further normalized by the effective shear modulus at high temperature [11]. For that purpose, the influence of the relative density on the Young's modulus and Poisson's ratio has to be known [12].

The stress intensification factor ϕ describes how the macroscopic applied stress is magnified at the microscopic scale in a porous body. For a low density body, the contact area between particles where forces are transmitted is small and stresses are locally higher than the macroscopic applied stress. For a dense material, ϕ is equal to 1. Various expressions for the stress intensification factor are available from the literature [1]. For example, when a macroscopic stress of 50 MPa is applied onto an alumina compact of 80 % relative density (assuming an initial green density of 55 %), it may result in an effective stress ranging from 90 MPa [13], 175 MPa [14, 15] to 250 MPa [16]. It is recommended to consider several expressions for ϕ; depending on the material and density range investigated, they may however lead to the same conclusion [17, 18].

Typical values for stress and grain size exponents are given in Table 1. The dominant sintering mechanism can thus be determined when knowing n and m. In the case of pure crystalline oxides, sintering by viscous flow (proper to amorphous materials) may be ruled out. A mechanical stress has a stronger effect on densification rate when dislocation motion is involved than for diffusion controlled densification, due to the higher value of the stress exponent. On the other hand,

Table 1 Possible densification mechanisms and related exponent values occurring in SPS and HP [1]

Densification mechanism	Stress exponent n	Grain size exponent m
Viscous flow	1	0
Lattice diffusion	1	2
Grain boundary diffusion	1	3
Liquid phase sintering	1	3
Grain boundary sliding	1–2	1
Dislocation-induced plasticity	≥3	0

reduction of grain size plays a major role by increasing densification rates controlled by lattice and grain boundary diffusion processes, whereas plasticity is independent of grain size. In the case of liquid phase sintering, the diffusion coefficient for the solute in the liquid replaces the grain boundary coefficient [19]. Particle rearrangement possible during the first stage of sintering is not well described theoretically; therefore no exponent values are available.

The following procedure can be adopted to identify exponent's n and m. With negligible grain growth and temperature kept constant, the stress exponent n can be calculated from:

$$\ln\left(\frac{1}{\rho}\frac{d\rho}{dt}\right) \propto n\ln(\phi p_a)(\mathrm{G}\ \&\ \mathrm{T\ fixed}) \tag{5}$$

To calculate the grain size exponent m, the effective stress$(\phi p_a)$and temperature T are assumed to be constant, giving:

$$\ln\left(\frac{1}{\rho}\frac{d\rho}{dt}\right) \propto -m\ln G\,(\mathrm{T}\ \&(\phi p_a)\mathrm{fixed}) \tag{6}$$

Finally, to calculate the activation energy of the diffusion coefficient, grain size has to be fixed:

$$\ln\left(\frac{\dot{\rho}}{\rho}\frac{T}{(\phi p_a)^n}\right) \propto -E_a/RT \tag{7}$$

Particular attention has to be paid to the activation energy: identification of the densification mechanism only based on this value may be hazardous [20], especially when determined from non-isothermal conditions. This will be highlighted in Sect. 1.3.

1.2 Experimental Conditions

In order to properly identify sintering mechanisms in SPS, clear experimental conditions are required. Comparison with HP under the same parameters is a secure way to highlight any difference between the processes; though performing them is not as simple as it may first appear.

First, the mechanical load should be calibrated with a load cell placed between the punches. From a practical point of view, a minimal compressive load is required during SPS in order to maintain electrical contact and to overcome the friction of the hydraulic system. In addition, a uniaxial compressive stress is assumed in Eq. 3. The stress state in the sample was estimated by Finite Element Modeling [21]. If the mismatch in coefficients of thermal expansion α between sample and die is small (as for alumina and graphite, $\alpha \sim 6 - 8 \times 10^{-6}\ \mathrm{K}^{-1}$), only the vertical stress is significant in the sample. Otherwise, the stress state is no longer uniaxial and its hydrostatic part increases. It is important to note that in these simulations the sample was considered as a dense elastic body and its densification behavior was neglected. In reality, densifying bodies are viscous at the sintering temperature and thermal conductivity increases with density [22, 23]. The implementation of reasonable constitutive laws for sintering may have marked effects on the calculated stress field.

Second, the sample shrinkage is not directly accessible. The total displacement measured with a typical resolution of 1–10 μm by LVDT sensor or optical level gage includes several elastic and thermal strains (including those related to punches and pressing tool). For that purpose, a dense dummy sample following the same schedule as the sample can be used. By subtracting this signal from the sample curves, the sample shrinkage can be deduced.

Third, temperature measurement is a crucial issue. The temperature seen by the sample is the most important and not what is shown on the control panel. Thermocouples and pyrometers are standard. Depending on the pyrometer type, measurement is only possible above 450–600 °C. A combination of thermocouple and pyrometer is therefore required fro measuring over the whole working range. Transparent window of the furnace should be regularly checked and cleaned to guarantee measurement reproducibility.

In the case of HP, the heat is transferred first from the heating elements to the pressing tool by radiation in vacuum and then transmitted to the sample by conduction. This means that the outer surface of the die is hotter than the sample. In addition, tools for HP are usually larger than for SPS as shown in Fig. 1. This limits the standard heating rates to ~25 °C/min. On the opposite in SPS, as the current flows directly through the punches and die, an electrically conductive path must be provided to the current. Otherwise no heating would be possible [25]. High heating rates are possible thanks to the more compact design of the pressing tool. This induces large temperature gradients. Finite Element Analysis and experiments showed that the best location to perform pyrometric measurements is to focus above the center of the sample (axial measurement). The temperature of the outer surface of the die (radial measurement) can be decreased by some 20–200 °C depending on specimen and heating conditions [26, 28, 29]). Consequently it is believed that a part of the literature results claiming lower synthesis temperatures in SPS are due to inaccurate temperature measurements. The effect of tool geometry and temperature control on the macroscopic densification curve is

Fig. 1 Schematics of standard pressing tools for SPS and HP experiments, showing temperature measurement: P pyrometer; T thermocouple [24]

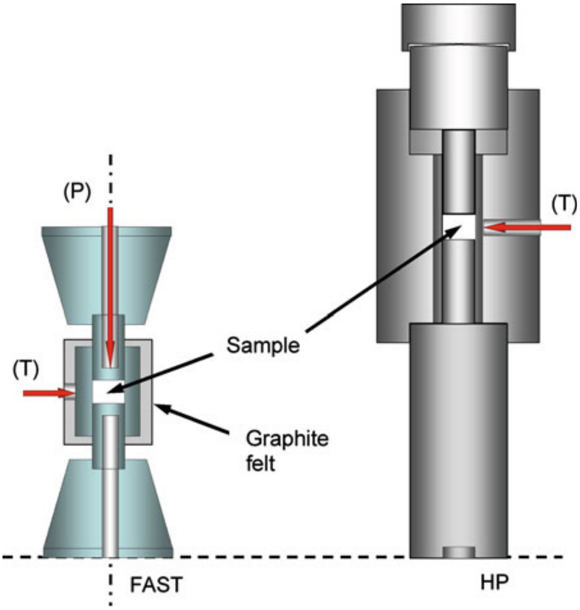

highlighted in Fig. 2. This explains why comparison between different SPS apparatus may be difficult [30].

Finally, the best calibration method remains a proper temperature measurement of the sample itself. This can involve the introduction of a thermocouple in the powder or the tracking of intrinsic/extrinsic phase transformations in silicon nitride [17, 27, 31].

1.3 Review: Densification Mechanism

Direct comparison between HP and SPS was performed on pure submicron alumina (150 nm initial particle sizes), keeping identical sample geometry, heating schedule (10 K/min), applied pressure and atmosphere (vacuum). Curves fit together if all experimental conditions are really the same, but different tool geometry or temperature control may induce discrepancies, as shown in Fig. 2. Nevertheless, the formalism described in Sect. 1.1 was applied to identify the main densification mechanism. Only isothermal data points were taken into account; pressure and final temperature were varied.

For both processes, densification of submicron alumina is controlled by grain boundary diffusion, with same stress and grain size exponents as well as activation energy of $\sim$440 kJ/mol [17, 32]. This is in accord with existing literature on HP [8, 33]. It is the same mechanism as in free sintering or sinter-forging [34]: pressure increases the vacancy gradient along the grain boundary, which raises

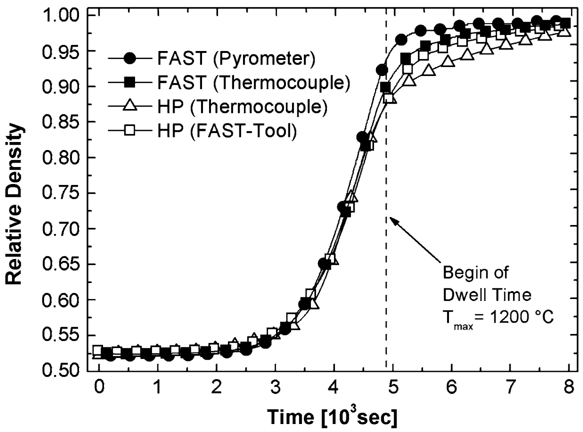

Fig. 2 Densification curves for submicron alumina obtained in SPS (with pyrometer from 450 °C or thermocouple control from room temperature) and HP experiments (with thermocouple control from room temperature, standard or SPS tool). Heating schedule are exactly the same above 450 °C; pressure is constant and equal to 50 MPa [24]

matter flux and necking rate between particles. The mechanically-induced strain rate is thus proportional to the stress. If plastic deformation exists, it is not significant and identical in HP and SPS. When co-doped with CaO and TiO_2, α-alumina may densify by grain-boundary sliding accommodated by grain-boundary diffusion [35].

Similar results have been found for ionic conductor cubic zirconia [36] and pure semi-conductor zinc oxide [18]. Nevertheless, depending on the material properties and the applied stress, different densification mechanisms may be dominant. For $MgAl_2O_4$ spinel sintered at 1175 °C under constant applied 80 MPa, a stress exponent value of 4 points to climb-controlled dislocation creep at low density (below 75 %) whereas for lower effective stress (higher densities) diffusional process controls densification [37]. In nanocrystalline Y_2O_3 under macroscopic 100 MPa [38], grain boundary diffusion of Y^{3+} controls densification and grain growth. Plastic deformation is possible above 1400 °C (however with negligible creep rates which cannot account for densification).

Calculations show that the ratio between the fraction of current flowing through an alumina sample and that flowing through the surrounding graphite die is expected to be smaller than 10^{-7} [39]. Only materials with specific electrical resistivity comparable or lower than that of graphite ($\sim 10^{-5}$ Ωm) are expected to be heated by direct Joule effect. By mixing an electrically conductive phase (such as TiN, TiB_2, TiC, ZrB_2…) to an insulating oxide powder, densification rate may be enhanced as soon as a percolation path exists [40, 41]. The role of an electrically conductive liquid phase has not been considered yet. Moreover, no presence of plasma or sparks could be detected by in situ fast voltage measurements or Atomic Emission Spectroscopy, whatever the material may be [42]. Even if there are plasma and discharges, they apparently do not contribute to a better densification of oxide ceramics by SPS compared to HP. Mechanical pressure along with temperature seem to be the most important parameters.

No separate densification mechanisms induced by the electric field or current could be evidenced in SPS for oxide ceramics. This explains why a pure zinc oxide

Fig. 3 Schematic representation of the electrical potential across a 3YSZ sample at 1000 °C highlighting the differences between “flash” sintering and SPS conditions (courtesy of S. Schwarz)

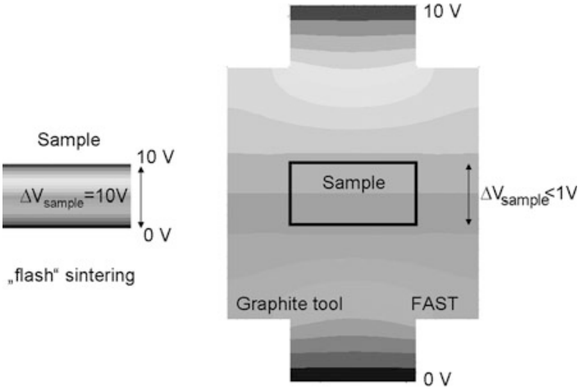

sample wrapped in insulating alumina felt densifies as well as a similar sample for which the possibility of current flow is not prohibited [18]. However, AC and DC electric fields have potential effects on the deformation behavior of oxide ceramics [43]. An electric field of a few V/cm may already reduce grain growth and increase the sintering rate of ionic conductor 3Y-TZP [44, 45], whereas surface diffusion remains unchanged [46]. Interactions between grain boundaries and electric field may be complex and multiple. They can affect grain boundary mobility as well as the driving force for grain growth. When the electric field reaches a certain level, an avalanche phenomenon takes place (“flash sintering”) leading to full densification of zirconia in a few seconds [47]. It is believed that Joule heating becomes so important that the temperature inside the sample is several hundreds of °C higher than the furnace (which remains as low as 850 °C). Considerable current densities of several A/cm^2 are met. Such conditions are not to be found in standard SPS equipments, because of the low voltage (5–15 V) available with commercial equipments and the possibility for the electric current to follow an easier path through the surrounding graphite. This means that a sample in SPS is only subjected to a small fraction of the total voltage applied to the rams, as highlighted in Fig. 3.

Furthermore, carbon contamination of oxide ceramics by the punches, quantified by Secondary Ion Mass Spectrometry [36], X-Ray Photoelectron Spectroscopy [18], Energy-dispersive X-ray Spectroscopy in SEM [48] seems to be negligible beyond a few microns inside the specimen. Even carbon initially present in the spinel powder disappeared after densification by SPS [49], which contrasts with 0.06 vol % carbon particles found in a dense spinel, sintered from another powder under different conditions [35]. A better electrical conductivity of insulating materials due to the percolation of carbon can nevertheless be excluded. Eventual darkening of the sample is also due to the formation of oxygen vacancies in a reducing environment acting as color centers [50]. Non-stoichiometry disappears after annealing in an oxygen-rich atmosphere.

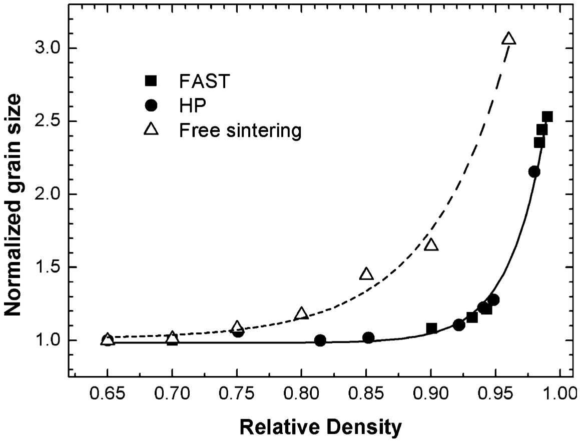

Fig. 4 Sintering trajectory for alumina processed by SPS and HP at a heating rate of 10 K/min heating rate and under 50 MPa [17]

1.4 Review: Grain Growth Behavior

Mechanical pressure promotes the densification mechanisms while leaving coarsening ones (like surface diffusion, evaporation/condensation) unchanged. As shown in Fig. 4 for alumina, SPS modifies the sintering trajectory to a significant extent when compared to free sintering of the same powder. However, no difference can be seen between HP and SPS, as they follow the same path as function of density [17, 36, 51, 52]. It is also clear that even if grain growth is delayed and reduced under pressure, it is not totally suppressed. The final grain size can be several times larger than the initial particle size. This effect is expected to be particularly marked for agglomerated nanopowders. A finer starting particle size may even lead to a larger grain size than a coarser one at full density [36]. The general importance of good green packing in ceramic processing to limit grain growth is also valid for SPS.

For nanocrystalline YAG, grain coalescence may take place below 1400 °C by grain rotation and sliding [53]. Crystallites may align to form lower-angle grain boundaries, which triggers grain boundary migration and end up into larger clusters. At higher temperature and larger grain size, rapid grain growth may only be driven by grain boundary curvature. For pure ZnO, there was no difference in microstructure between a sample electrically insulated from the pressing tool and one for which the possibility of having a current flow was not prohibited [18]. In the case of doped ZnO [54], a small fraction of the current may flow through the sample at high temperature. The electrical resistance of the sample is ~5 Ω at 750 °C (instead of 250 Ω for pure ZnO) whereas the tool resistance lies in the mΩ range. Microstructure seems to be affected by this additional current flow but further detailed investigations are necessary to clear this point.

Grain anisometry and preferential orientation should remain limited as long as exaggerated coarsening and abnormal grain growth do not take place, as already shown for HP [55]. Sometimes the pressure is only applied at high temperature.

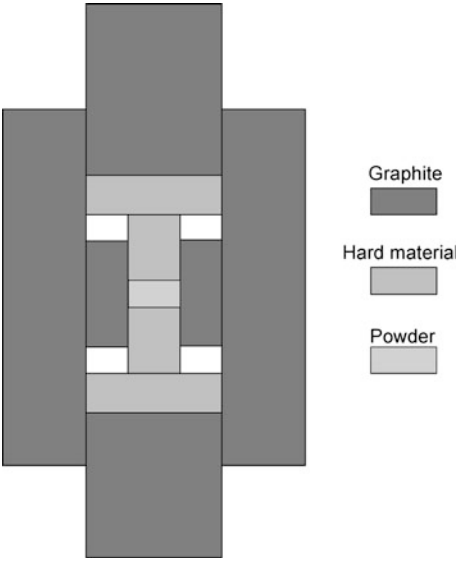

Fig. 5 Schematic representation of a high pressure tool in SPS. The hard material is typically SiC. Modified from [59]

In that case, the earlier the more beneficial it is for microstructure homogenization and smaller grain size [56]. A two-step increasing pressure scheme may also improve the uniformity of the grain size over the whole sample [57].

1.5 High Pressure Experiments

The synthesis of dense nanostructured bulk materials is particularly challenging, due to the onset of grain growth in the early stage of sintering [58]. The level of pressure available in standard SPS equipment is limited by the weak properties of the graphite pressing tool (typical fracture strength under compression between 80 and 150 MPa). This may not be enough to retain small grain size at high relative density.

The simplest way to increase the stress applied onto the specimen while overcoming the limitations of the loading system is to reduce its cross-section. A tool-in-tool design using silicon carbide and tungsten carbide parts as insert elements as described in Fig. 5 has been proposed and already tested with success [59]. The required binder-less hard materials with very good high temperature fracture strength and fracture toughness can be manufactured by SPS [60]. If electrical conductivity through the punch is desired, WC, TiB_2 etc. may be chosen. Pressures up to 1 GPa can then be achieved, but the sample diameter typically reduces to ~5 mm. This size may be large enough to measure optical and electrical properties, but not mechanical ones. Equipment up scaling or development of another technique is required to get larger parts.

Tetragonal and cubic yttria-doped zirconia [61, 62], pure and Sm-doped ceria [59], LSGM electrolyte [63], hydroxyapatite [64] and alumina [65] have been obtained under such high pressure conditions (between 250 and 800 MPa). High pressure SPS enables the fabrication of new bulk materials, as dense undoped tetragonal zirconia [66]. Starting with a particle size of 16 nm, a density of >95 % was reached after sintering at 850 °C under 790 MPa. The metastable tetragonal phase can then be stabilized at room temperature as the final grain size remains smaller than 50 nm.

Under high pressure conditions (typically >250 MPa), the final grain size is in general 2–3 times larger than the initial crystallite size and lies between ~15 and 100 nm. It hardly depends on the high pressure level but follows a standard parabolic law as function of isothermal dwell time [62]. This means that densification and coarsening are decoupled: high pressure leads to a rapid densification at low temperature, which significantly reduces grain growth kinetics.

The role of high pressure is twofold. First, at low temperature, it may already break powder agglomerates and induce particle rearrangement. This increases particle packing and reduces pore size, allowing homogeneous subsequent densification and grain growth. For example, isostatic pressing of yttria-doped zirconia nanopowder under 3 GPa leads to a green density of 60 %, whereas a pressure of 40 MPa to only 25 % [67]. Second, at higher temperature, additional densification mechanisms may be active, including plastic deformation, as the yield stress decreases with temperature [53], or power-law creep [16, 68]. As shown on single crystals, dislocation-related plasticity can be observed in yttria-stabilized cubic zirconia under 400 MPa at 800 °C [69]. These mechanisms are different from lower pressure/high temperature conditions (Sect. 1.3). From a rational point of view, no differences between high pressure HP and SPS and additional effects of electric current/field are expected under those conditions, but this needs to be checked experimentally.

2 Effect of Heating Rate

Besides pressure, one definite advantage of SPS is the possibility of achieving higher heating rates than HP, reducing considerably heating cycles. The idea of "fast firing" is not new and was proposed already 30 years ago [70, 71]. When the densification process has higher activation energy than the coarsening mechanism, reaching rapidly high sintering temperature can be beneficial to enhance densification rate while retarding grain growth. Activation energies of diffusion mechanisms for oxides are usually found in the following order: $E_{\text{surface}} < E_{\text{grain boundary}} < E_{\text{lattice}}$. This means that surface diffusion responsible for neck growth without densification is dominant at lower temperatures. At the earliest stage of sintering, the neck radius is at its smallest. If necks grow too much through surface diffusion, densification kinetics through grain-boundary diffusion is reduced, especially for fine powders [70]. The curvature radius of the pore tip increases due

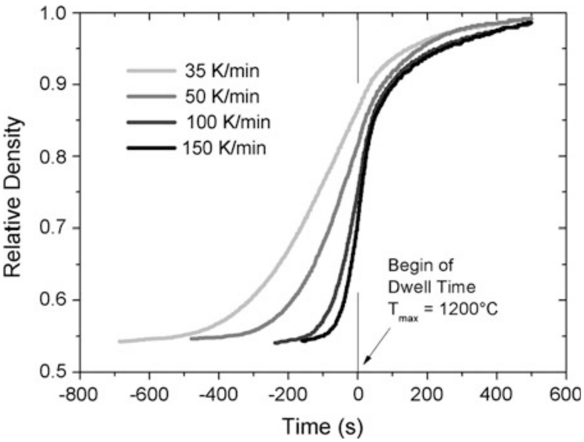

Fig. 6 Densification curves of submicron alumina sintered by SPS as a function of time for different heating rates, under a constant applied stress of 50 MPa [74]

to the mass distribution along the pore surface which leads to pore spheroidization and slows down the grain boundary diffusion [10]. By applying high heating rates, the time window for which surface diffusion is dominant is shorter. On the other hand, for glass systems undergoing crystallization, high heating rate may be beneficial in delaying the onset of crystallization detrimental to densification.

The effect of heating rate has already been investigated for free sintering under constant heating rate [72, 73]. A general observation is that by increasing the heating rate, the achieved density at a given temperature is typically smaller, but the same density can be reached when temperature is increased. The question to be solved here is if similar behavior is observed in SPS experiments or if additional phenomena appear in conjunction with high heating rates.

Representative densification curves for alumina at heating rates up to 150 K/min are plotted in Fig. 6. As for free sintering, specimens sintered at a lower heating rate have a higher density when reaching the isothermal step, but all samples are fully sintered at the end of the holding time (relative density ~99 %). Furthermore, the strain rates measured under applied load are significantly larger than in the free sintering case, which legitimates the assumption for using Eq. 3. For example, the densification rate of the same powder is almost zero for a freely sintered sample at 1200 °C with a heating rate of 30 °C/min and a density of 86 % [34]. This density is reached at the beginning of the isothermal time with a heating rate of 35 °C/min in the SPS set-up, where still significant densification occurs.

In addition, the slope of the density curves as function of the temperature [17], or in a more refined way, the derivative of the densification rate with respect to temperature is independent of the heating rate for a given density (Fig. 7). This is exactly what was observed for free sintering between 0.5 and 15 °C/min on zinc oxide [72] or alumina [75]. This means that no change in densification mechanism takes place under these conditions. Final grain volume of the dense material is expected to decrease linearly with the inverse of the heating rate.

Fig. 7 Normalized temperature derivative of density as a function of density for submicron alumina sintered by SPS for different heating rates (derived from Fig. 6)

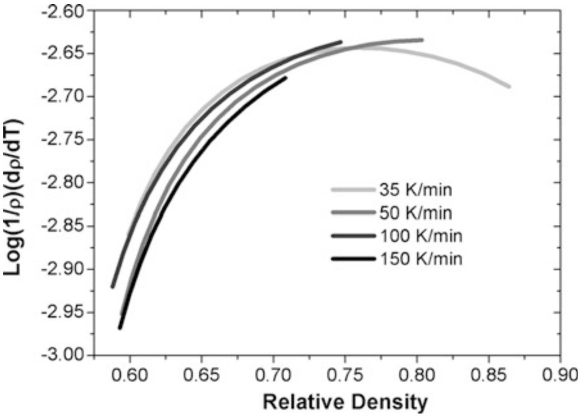

The Master Sintering Curve (MSC) approach has been derived from a free sintering model [76] and has proved to be effective in predicting densification whatever the heating schedule may be [77]. It can be extended to HP or SPS [74, 78]. By separating terms related to temperature T from all others in Eq. 3, it is possible by integrating over time to define the function Θ:

$$\frac{k}{HD_0 p_a^n}\int_{\rho_0}^{\rho}\frac{G^m}{\rho\phi^n}d\rho=\int_0^t\frac{1}{T}\exp\left(-\frac{E_a}{RT}\right)dt\equiv\Theta(t,T) \tag{8}$$

The plot of density ρ versus Θ is defined as the MSC, which can be fitted using a sigmoidal function. A unique MSC can be obtained if the applied pressure is constant, only one diffusion mechanism is dominant during sintering and the microstructure is function only of density. Usually, constant heating rate experiments are carried out for a given specimen type (raw powder and processing parameters should be kept identical) and the activation energy can be found by optimizing the mean square residual between all curves.

As shown in Fig. 8, a global apparent activation energy value of 290 kJ/mol is significantly lower than the one found for the same powder from isothermal or constant heating rate experiments [79]. Reasons for these discrepancies may be the neglected role of surface diffusion at low temperature and temperature heterogeneity within the specimen [80]. MSC has to be understood as an engineering tool to empirically describe densification from room temperature until the end of the firing cycle. That's why it should not be used to identify the densification mechanism by considering the activation energy value alone.

In some cases, when higher heating rates with short dwell times at the maximum temperature are used, another behavior can be observed, as exemplified in Fig. 9. For submicron alumina heated at temperatures below 1200 °C, it appears that a heating rate of 300 °C/min induces a higher density from the beginning of sintering at 1000 °C. A difference of up to 15 % in relative density can be observed with a sample heated at 50 °C/min, without marked grain growth [81].

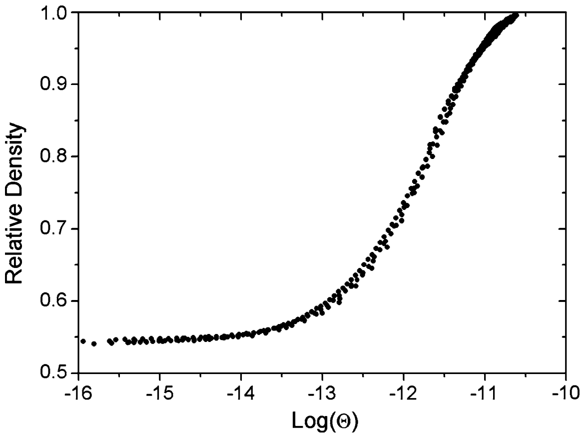

Fig. 8 Master Sintering Curve, determined from the data of Fig. 6 including isothermal step with apparent activation energy of 290 kJ/mol [74]

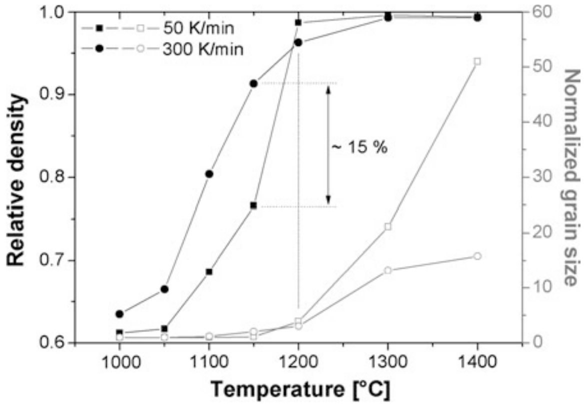

Fig. 9 Effect of heating rate on density (*full symbols*) and grain size (*open symbols*) as a function of temperature for submicron alumina [81]

Similar trends were observed on nanocrystalline alumina/zirconia composites with heating rates between 200 °C/min and 500 °C/min [82]. For nanocrystalline zinc oxide, an increase of heating rate from 50 °C/min to 100 °C/min lead to a significant increase in density at the end of the heating ramp but also during the dwell time [83]. Unfortunately, too few experimental data are available. Interrupted experiments may be affected by the accuracy of the temperature control, sample and tool geometry and may lead to contradictory results. That's why when possible the complete densification curves should be analyzed, not only the final density as unique data point for comparison between heating rates.

This new behavior contrasts nonetheless with what has been rationalized for lower heating rates (below ~250 °C/min for alumina for example). In addition, transient heating for example due to uncontrolled heating rate before pyrometer control in SPS has proven to be efficient in enhancing the sinterability of ultrafine alumina and zinc oxide [17, 18]. This rapid temperature overshoot up to ~600 °C leads to a higher total interparticle contact area in the partially sintered samples, characterized by higher Young's modulus or thermal diffusivity measured by the laser flash method [17, 84].

Several effects can lead to these surprising results: local or macroscopic temperature gradients inducing thermal stresses or/and thermal diffusion, or change in the nature of grain boundaries. First, one explanation is based on thermal heterogeneity within the sample. Due to high heating rates, thermal homogeneity in the sample may be difficult to guarantee. Gradients between the cooler and less dense core of the sample and the hotter outer surface already sintered and under tension may develop [85]. Thermal diffusion due to Ludwig-Soret effect may appear due to temperature gradients at the macroscopic or microscopic scale [86]. The second idea is supported by recent experimental results: submicron alumina green body placed in a reaction chamber, heated at ~1600 °C/min and rapidly cooled got a density above 99 % with hardly any grain growth [87, 88]. Post-sintering annealing at 1200 °C for up to 20 h did not modify grain size, but increased wear resistance by reducing grain pull-out. Along with TEM images, it is postulated that very fast sintering leads to thicker and looser non-equilibrium grain boundaries, which may enhance the effective grain boundary diffusion coefficient [88] or decrease their energy, reducing the driving force for grain boundary motion and consequent grain growth. Complementary studies on other materials would be welcome to be able to generalize (or not) these findings.

Furthermore, independent of the sintering method, for all heating rates considered ranging from a fraction of degree up to several hundreds K/min, almost fully dense samples which were quickly heated possess a reduced final grain size compared to their slow-heated counterparts [62, 72, 79, 89] although some exceptions may be possible. In general, caution is required when comparing grain sizes of almost dense materials, as the sintering trajectory usually gets much steeper for relative densities above 98 % (see Fig. 3) and it is a statistical measurement with a confidence interval whose reliability depends much on the quality of the micrographs and the number of grains taken into account. Nevertheless, as shown in Fig. 8 at temperatures between 1200 and 1400 °C and almost full density, grain size is decreased by a factor of 3 when the heating rate is increased from 50 to 300 °C/min. Drastic grain size reduction was also observed on alumina when heating from 50 °C/min to 700 °C/min [90]. As grain growth requires time at high temperature for which grain boundary mobility is enhanced, the shorter the time the sintering body has to be held at maximum temperature, the more coarsening is expected to be suppressed.

Finally, when really dense ceramics are required (for example to obtain transparent ceramics it is necessary to eliminate residual porosity levels below 0.05 %), a low heating rate comparable to HP coupled with longer dwell times may be more effective [91, 92]. It was shown that a slower heating allows more time for microstructure homogenization, leading to finer single pores located at multiple grain junctions. Pore pinning of the grain boundaries might be the reason for reduced grain growth. However, this represents a special case for which rapid heating may not be advantageous.

3 Summary

The experimental identification of real mechanisms occurring during SPS makes it possible to better understand and utilize in a more efficient and rational way this sintering technology, which was seen until recently as a “black box”. It was in particular shown in this chapter that under the same conditions (tool geometry and materials, temperature schedule, pressure), there are no significant differences between HP and SPS for different oxides, at least as long as the sintering material offers a too high resistive path against current flow compared to the pressing tool. If it becomes electrically conductive (intrinsically or extrinsically through reducing atmosphere, doping, or addition of a second conducting phase above the percolation threshold) then direct heating of the sample and current-induced phenomena such as electromigration may be possible. Otherwise no additional effects of the low electrical field or current were found on both densification and grain growth. The sintering trajectory (grain size as a function of relative density) is the same for HP and SPS. By increasing the mechanical pressure, dislocation motion may be triggered, and densification rate is strongly increased whereas the temperature required to get dense materials with a grain size below 100 nm is reduced.

By varying the heating rates, different behaviors are found. For moderate heating rates (typically between 1 and 250 °C/min, standard value for the SPS technology), the densification behavior may be described by conventional approaches such as the MSC. In contrast and depending on the material considered, higher heating rates seem to enhance significantly densification while further reducing grain growth. This new response may result from temperature and stress gradients as well as out-of-equilibrium grain boundaries. By increasing the heating rate, the final grain size is usually decreased, as the time spent at high temperature is reduced. But if complete elimination of porosity is required, a low heating rate comparable to HP may be better to get transparent ceramics with homogeneous microstructure and reduced grain growth during dwell time. Definitely more fundamental work is required in this field.

References

1. Rahaman, M.N.: Ceramic Processing and Sintering, 2nd ed. Marcel Dekker, Inc., New York (2003)
2. Olevsky, E.A.: Mater. Sci. Eng. R **23**(2), 41–100 (1998)
3. Ashby, M.F.: Acta Metall. **20**(7), 887–897 (1972)
4. Bordia, R.K., Scherer, G.W.: Acta Metall. **36**(9), 2393–2397 (1988)
5. Raj, R.J.: Am. Ceram. Soc. **70**(9), C210–C211 (1987)
6. Zuo, R.Z., Aulbach, E., Rodel, J.: Acta Mater. **51**(15), 4563–4574 (2003)
7. Coble, R.L.J.J.: Appl. Phys. **41**(12), 4798–4807 (1970)
8. Coble, R.L., Ellis, J.S.J.: Am. Ceram. Soc. **46**(9), 438–441 (1963)
9. Olevsky, E., Froyen, L.: Scripta Mater. **55**(12), 1175–1178 (2006)

10. Olevsky, E.A., Kandukuri, S., Froyen, L.: J. Appl. Phys. **102**(11), 114913 (2007)
11. Bernard-Granger, G., Guizard, C.: Acta Mater. **55**(10), 3493–3504 (2007)
12. Roberts, A.P., Garboczi, E.J.J.: Am. Ceram. Soc. **83**(12), 3041–3048 (2000)
13. Montes, J.M., Cuevas, F.G., Cintas, J.: Comp. Mater. Sci. **36**(3), 329–337 (2006)
14. Beere, W.J.: Mater. Sci. **10**(8), 1434–1440 (1975)
15. Vieira, J.M., Brook, R.J.J.: Am. Ceram. Soc. **67**(4), 245–249 (1984)
16. Helle, A.S., Easterling, K.E., Ashby, M.F.: Acta Metall. **33**(12), 2163–2174 (1985)
17. Langer, J., Hoffmann, M.J., Guillon, O.: Acta Mater. **57**(18), 5454–5465 (2009)
18. Langer, J., Hoffmann, M.J., Guillon, O.J.: Am. Ceram. Soc. **94**(8), 2344–2353 (2011)
19. Bowen, L.J., Weston, R.J., Carruthers, T.G., Brook, R.J.J.: Mater. Sci. **13**(2), 341–350 (1978)
20. Xu, J., Casolco, S.R., Garay, J.E.J.: Am. Ceram. Soc. **92**(7), 1506–1513 (2009)
21. Wang, X., Casolco, S.R., Xu, G., Garay, J.E.: Acta Mater. **55**(10), 3611–3622 (2007)
22. McWilliams, B., Zavaliangos, A.J.: Mater. Sci. **43**(14), 5031–5035 (2008)
23. Camacho-Montes, H., Elvia Garcia-Casillas, P., Rodriguez-Ramos, R., Elena Fuentes-Montero, M., Edmundo Fuentes-Cobas, L.: J. Am. Ceram. Soc. **91**(3), 836–845 (2008)
24. Langer, J.: Thesis:Vergleich der durch das elektrische Feld aktivierten Sintertechnologie mit dem Heißpressverfahren anhand von Oxidkeramiken. (2010)
25. Carney, C.M., Mah, T.-I.J.: Am. Ceram. Soc. **91**(10), 3448–3450 (2008)
26. Vanmeensel, K., Laptev, A., Hennicke, J., Vleugels, J., Van der Biest, O.: Acta Mater. **53**(16), 4379–4388 (2005)
27. Raethel, J., Herrmann, M., Beckert, W.J.: Eur. Ceram. Soc. **29**(8), 1419–1425 (2009)
28. Zavaliangos, A., Zhang, J., Krammer, M., Groza, J.R.: Mater. Sci. Eng. A-Struct. **379**(1–2), 218–228 (2004)
29. Anselmi-Tamburini, U., Gennari, S., Garay, J.E., Munir, Z.A.: Mater. Sci. Eng. A-Struct. **394**(1–2), 139–148 (2005)
30. Langer, J., Quach, D.V., Groza, J.R., Guillon, O.: Inter. J. Appl. Ceram. Tec. **8**(6), 1459–1467 (2011)
31. Zhang, D.M., Zhang, L.M., Guo, J.K., Tuan, W.H.J.: Am. Ceram. Soc. **89**(2), 680–683 (2006)
32. Aman, Y., Garnier, V., Djurado, E.J.: Am. Ceram. Soc. **94**(9), 2825–2833 (2011)
33. Vasilos, T., Spriggs, R.M.J.: Am. Ceram. Soc. **46**(10), 493–496 (1963)
34. Zuo, R.Z., Rodel, H.: Acta Mater. **52**(10), 3059–3067 (2004)
35. Bernard-Granger, G., Guizard, C.J.: Mater. Res. **24**(1), 179–186 (2009)
36. Langer, J., Hoffmann, M.J., Guillon, O.J.: Am. Ceram. Soc. **94**(1), 24–31 (2011)
37. Morita, K., Kim, B.-N., Yoshida, H., Hiraga, K.: Scripta Mater. **63**(6), 565–568 (2010)
38. Chaim, R., Shlayer, A., Estournes, C.J.: Eur. Ceram. Soc. **29**(1), 91–98 (2009)
39. Herrmann, M., Weise, B., Sempf, K., Bales, A., Raethel, J., Schulz, I.: In: Field Assisted Sintering of Ceramic Materials, Workshop FhG IFAM Dresden 2006. (2006)
40. Vanmeensel, K., Laptev, A., Van der Biest, O., Vleugels, J.J.: Eur. Ceram. Soc. **27**(2–3), 979–985 (2007)
41. Vanmeensel, K., Laptev, A., Van der Biest, O., Vleugels, J.: Acta Mater. **55**(5), 1801–1811 (2007)
42. Hulbert, D.M., Anders, A., Dudina, D.V., Andersson, J., Jiang, D., Unuvar, C., Anselmi-Tamburini, U., Lavernia, E.J., Mukherjee, A.K.J.: J. Appl. Phys. **104** (3), 033305 (2008)
43. Antolovich, S.D., Conrad, H.: Mater. Manufact. Proc. **19**(4), 587–610 (2004)
44. Ghosh, S., Chokshi, A.H., Lee, P., Raj, R.J.: Am. Ceram. Soc. **92**(8), 1856–1859 (2009)
45. Yang, D., Conrad, H.: Scripta Mater. **63**(3), 328–331 (2010)
46. Cologna, M., Raj, R.J.: Am. Ceram. Soc. **94**(2), 391–395 (2011)
47. Cologna, M., Rashkova, B., Raj, R.J.: Am. Ceram. Soc. **93**(11), 3556–3559 (2010)
48. Anselmi-Tamburini, U., Garay, J.E., Munir, Z.A., Tacca, A., Maglia, F., Chiodelli, G., Spinolo, G.J.: Mater. Res. **19**(11), 3263–3269 (2004)
49. Kim, B.-N., Morita, K., Lim, J.-H., Hiraga, K., Yoshida, H.J.: Am. Ceram. Soc. **93**(8), 2158–2160 (2010)
50. Casolco, S.R., Xu, J., Garay, J.E.: Scripta Mater. **58**(6), 516–519 (2008)
51. Bernard-Granger, G., Monchalin, N., Guizard, C.: Mater. Lett. **62**(30), 4555–4558 (2008)

52. Bernard-Granger, G., Addad, A., Fantozzi, G., Bonnefont, G., Guizard, C., Vernat, D.: Acta Mater. **58**(9), 3390–3399 (2010)
53. Chaim, R.: Mater. Sci. Eng. A-Struct. **443**(1–2), 25–32 (2007)
54. Misawa, T., Shikatani, N., Kawakami, Y., Enjoji, T., Ohtsu, Y., Fujita, H.J.: Mater. Sci. **44**(6), 1641–1651 (2009)
55. Roy, J.F., Descemond, M., Brodhag, C., Thevenot, F.J.: Eur. Ceram. Soc. **11**(4), 325–333 (1993)
56. Chaim, R., Shen, Z.J.: Mater. Sci. **43**(14), 5023–5027 (2008)
57. Wang, C., Wang, X., Zhao, Z.J.: Eur. Ceram. Soc. **31**(1–2), 231–235 (2011)
58. Fang, Z.Z., Wang, H.: Sintering of ultrafine and nanosized particles. In: Fang, Z.Z. (ed.) Sintering of Advanced Materials, Woodhead Publishing, Cambridge (2010)
59. Anselmi-Tamburini, U., Garay, J.E., Munir, Z.A.: Scripta Mater. **54**(5), 823–828 (2006)
60. Zhao, J., Holland, T., Unuvar, C., Munir, Z.A.: Int. J. Refract. Met. Hard Mater. **27**(1), 130–139 (2009)
61. Anselmi-Tamburini, U., Woolman, J.N., Munir, Z.A.: Adv. Funct. Mater. **17**(16), 3267–3273 (2007)
62. Quach, D.V., Avila-Paredes, H., Kim, S., Martin, M., Munir, Z.A.: Acta Mater. **58**(15), 5022–5030 (2010)
63. Maglia, F., Anselmi-Tamburini, U., Chiodelli, G., Camurlu, H.E., Dapiaggi, M., Munir, Z.A.: Solid State Ionics **180**(1), 36–40 (2009)
64. Eriksson, M., Liu, Y., Hu, J., Gao, L., Nygren, M., Shen, Z.J.: Eur. Ceram. Soc. **31**(9), 1533–1540 (2011)
65. Grasso, S., Kim, B.-N., Hu, C., Maizza, G., Sakka, Y.J.: Am. Ceram. Soc. **93**(9), 2460–2462 (2010)
66. Maglia, F., Dapiaggi, M., Tredici, I., Maroni, B., Anselmi-Tamburini, U.J.: Am. Ceram. Soc. **93**(7), 2092–2097 (2010)
67. Gao, L., Li, W., Wang, H.Z., Zhou, J.X., Chao, Z.J., Zai, Q.Z.J.: Eur. Ceram. Soc. **21**(2), 135–138 (2001)
68. Chaim, R., Margulis, M.: Mater. Sci. Eng. A-Struct. **407**(1–2), 180–187 (2005)
69. Baufeld, B., Bartsch, M., Messerschmidt, U., Baither, D.: Acta Metall. Mater. **43**(5), 1925–1933 (1995)
70. Harmer, M., Roberts, E.W., Brook, R.J.: Trans. J. British. Ceram. Soc. **78**(1), 22–25 (1979)
71. Harmer, M.P., Brook, R.J.: Trans. J. British. Ceram. Soc. **80**(5), 147–148 (1981)
72. Chu, M.Y., Rahaman, M.N., Dejonghe, L.C., Brook, R.J.J.: Am. Ceram. Soc. **74**(6), 1217–1225 (1991)
73. Su, H.H., Johnson, D.L.J.: Am. Ceram. Soc. **79**(12), 3211–3217 (1996)
74. Guillon, O., Langer, J.J.: Mater. Sci. **45**(19), 5191–5195 (2010)
75. Lance, D., Valdivieso, F., Goeuriot, P.J.: Eur. Ceram. Soc. **24**(9), 2749–2761 (2004)
76. Hansen, J.D., Rusin, R.P., Teng, M.H., Johnson, D.L.J.: Am. Ceram. Soc. **75**(5), 1129–1135 (1992)
77. Diantonio, C.B., Ewsuk, K.G.: Master sintering curve and its application in sintering of electronic ceramics. In: Fang, Z.Z. (ed.) Sintering of Advanced Materials, Woodhead Publishing, Cambridge (2010)
78. An, K., Johnson, D.L.J.: Mater. Sci. **37**(21), 4555–4559 (2002)
79. Aminzare, M., Golestani-fard, F., Guillon, O., Mazaheri, M., Rezaie, H.R.: Mater. Sci. Eng. A-Struct. **527**(16–17), 3807–3812 (2010)
80. Raether, F., Horn, P.S.J.: Eur. Ceram. Soc. **29**(11), 2225–2234 (2009)
81. Zhou, Y., Hirao, K., Yamauchi, Y., Kanzaki, S.J.: Eur. Ceram. Soc. **24**(12), 3465–3470 (2004)
82. Zhan, G.D., Kuntz, J., Wan, J., Garay, J., Mukherjee, A.K.J.: Am. Ceram. Soc. **86**(1), 200–202 (2003)
83. Schwarz, S., Thron, A., Rufner, J., Van Benthem, K., Guillon, O.: Effect of high heating rate on the densification of nanocrystalline ZnO. J. Am. Ceram. Soc. (2012)
84. Stanciu, L., Quach, D., Faconti, C., Groza, J.R.J.: Am. Ceram. Soc. **90**(9), 2716–2722 (2007)

85. Garcia, D.E., Seidel, J., Janssen, R., Claussen, N.J.: Eur. Ceram. Soc. **15**(10), 935–938 (1995)
86. Olevsky, E.A., Froyen, L.J.: Am. Ceram. Soc. **92**(1), S122–S132 (2009)
87. Meng, F., Fu, Z., Zhang, J., Wang, H., Wang, W., Wang, Y., Zhang, Q.J.: Am. Ceram. Soc. **90**(4), 1262–1264 (2007)
88. Zhang, J., Meng, F., Todd, R.I., Fu, Z.: Scripta Mater. **62**(9), 658–661 (2010)
89. Shen, Z.J., Johnsson, M., Zhao, Z., Nygren, M.J.: Am. Ceram. Soc. **85**(8), 1921–1927 (2002)
90. Stanciu, L.A., Kodash, V.Y., Groza, J.R.: Metall. Mater. Trans. A **32**(10), 2633–2638 (2001)
91. Kim, B.-N., Hiraga, K., Morita, K., Yoshida, H.J.: Eur. Ceram. Soc. **29**(2), 323–327 (2009)
92. Morita, K., Kim, B.-N., Hiraga, K., Yoshida, H.J.: Mater. Res. **24**(9), 2863–2872 (2009)

Characterization of Microstructures Before, During and After Densification

Klaus van Benthem

Abstract The microstructural characterization of materials is a critical step to understand structure–property relationships in sintered materials. Altering the processing parameters during sintering can lead to variations of the materials microstructure and, hence, their macroscopic properties. This chapter reviews experimental techniques for the atomic resolution characterization of microstructural defects. Emphasis is given to a variety of electron microscopy techniques and how these can be used to gain a more fundamental understanding of sintering behavior, such as defect segregation and grain growth. The recent advent of novel in situ electron microscopy techniques has enabled the atomic-scale investigation of densification mechanisms and their kinetics that occur during sintering. A review of available techniques is presented and first experimental results are discussed.

1 Introduction

A microstructure is considered the ensemble of all defect structures in the absence of thermodynamic equilibrium. The macroscopic properties of a material are determined by the materials microstructure and, therefore, the embedded defects. Microstructural characterization must hence be carried out with high spatial resolution to assess grain sizes, textures, grain boundary structures, local chemical compositions and segregation behaviors including point defect concentrations.

K. van Benthem (✉)
Department of Chemical Engineering and Materials Science,
University of California, 1 Shields Ave, Davis,
CA 95616, USA
e-mail: benthem@ucdavis.edu

R. H. R. Castro and K. van Benthem (eds.), *Sintering*, Engineering Materials 35,
DOI: 10.1007/978-3-642-31009-6_10, © Springer-Verlag Berlin Heidelberg 2013

Electron microscopy techniques provide the means to carry out such experiments with spatial resolution limits reaching well below 1 Å and single atom sensitivities [1, 2]. Many studies reported in the literature provide information about microstructural details and their correlation to macroscopic materials properties. The synthesis of dense microstructures through sintering is typically investigated through systematic variations of processing parameters (chemical composition, temperature, pressure, etc.) and the subsequent microstructural characterization using X-ray diffraction and electron microscopy. More recently, in situ experimental capabilities have become a useful tool to study sintering kinetics.

In this chapter, microstructural characterization techniques from the field of electron microcopy are reviewed. The goal of this exercise is to provide the reader with an introductory knowledge and review about experimental capabilities for structural and compositional characterization with high spatial resolution and sensitivity. The first part of the text is dedicated to a review of exemplary studies that targeted segregation of dopant atoms in individual powder particles before sintering as well as in fully dense microstructures. The second part of the text will review more recent in situ transmission electron microscopy studies that were designed to investigate fundamental mechanisms during sintering.

2 Microstructural Characterization

Experimental techniques that are heavily used for microstructural characterizations are X-ray, neutron and electron diffraction as well as optical and electron microscopy. Diffraction techniques provide detailed but integrated information about the investigated microstructure, including crystals structures and orientations as well as grain sizes. Due to the small wavelength of fast electrons combined with the ability to focus charged particles, electron microscopy techniques provide superior spatial resolution for microstructure characterization which can be combined with chemical composition profiling or selected area electron diffraction. As this chapter exclusively concentrates on electron microscopy techniques, it is important to recognize that other techniques such as X-ray and neutron diffraction can provide complementary information and should be used as additional tools to gain a more complete understanding of microstructural evolution during sintering.

Figure 1 provides a sketch of the possible interactions of the beam electrons with sample. Signals that leave the sample on the same side from which it is impacted by the electron beam include secondary electrons (SE), backscattered electrons (BSE), X-rays, etc. Such signals are recorded in a scanning electron microscope (SEM) and provide information about surface topography as well as chemical composition. Another technique is transmission electron microscopy (TEM), which analyses the scattered electrons that have penetrated the sample. Elastically scattered electrons are used to determine the atomic structure of the sample through either imaging or diffraction, while inelastically scattered electrons

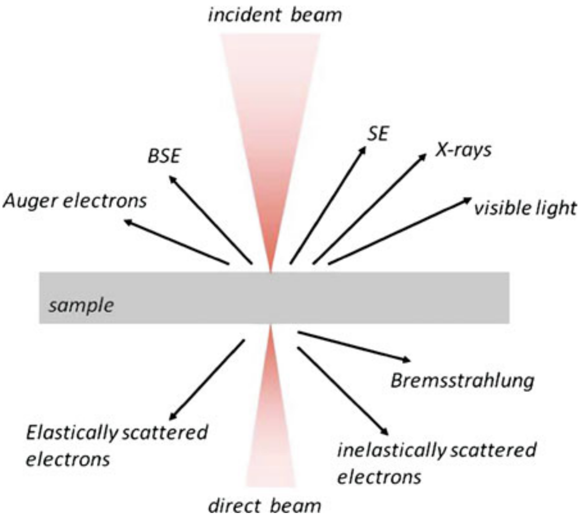

Fig. 1 Sketch of the possible interactions of the incident electron beam with the sample

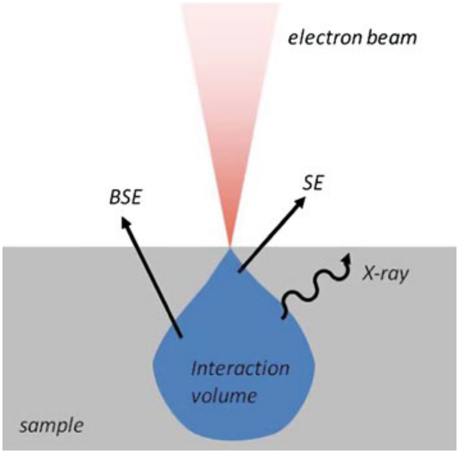

Fig. 2 Interaction volume of the electron beam with the sample in SEM. The electron range is a function of the sample material and the kinetic energy of the incident electron beam

can provide spectroscopic information to determine chemical compositions or electronic structures.

2.1 Scanning Electron Microscopy

Scanning electron microscopy (SEM) represents an efficient way to characterize materials microstructures in terms of grain size distributions, texture and local chemical compositions. In an SEM instrument a focused electron probe is scanned across the surface of a specimen while several signals that are generated due to the

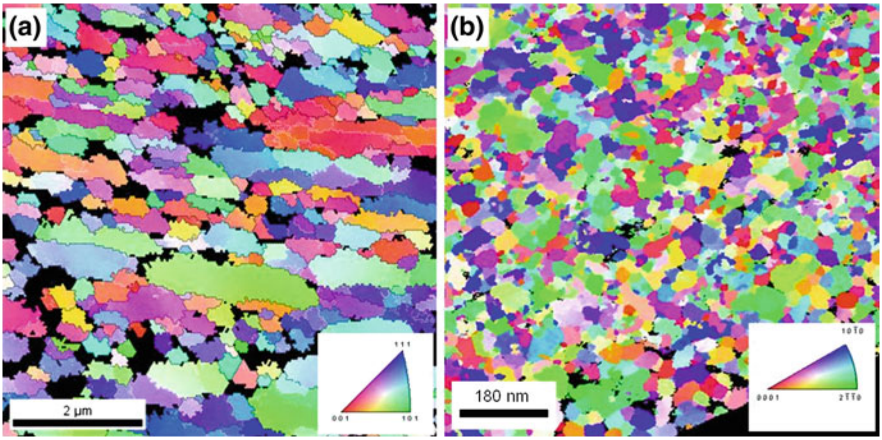

Fig. 3 Orientation images for an Mg–Al alloy (**a**) and for ZnO (**b**) recorded by EBSD inside an SEM and by electron diffraction in a conventional TEM instrument, respectively. Figure **a** is courtesy of Dr. Troy Topping (UC Davis) [4]

electron beam-specimen interaction are recorded as a function of probe position. The most commonly utilized signals include SE, BSE, electron-beam-induced current (EBIC), characteristic X-rays, etc. The resolution limits for SEM is determined not only by the diameter of the electron probe, but also by the interaction volume of the electron beam with the specimen material. Figure 2 shows a sketch of the typical geometry of the interaction volume, which is determined by how far the electrons can penetrate into the material because of their kinetic energy.

The SE mode is sensitive to the sample surface topography due to enhanced emission from edges and small particles as well as the dependence of SE yield on the tilt angle with respect to the incident electron beam [3]. By convention SE and BSE are distinguished by their kinetic energy below and above 50 eV, respectively. Since SEs are collected from volumes close to the sample surface the SE mode typically provides higher spatial resolution than obtained during BSE imaging. In contrast, BSE signals can originate from the entire interaction volume displayed in Fig. 2. The backscattering coefficient depends on the mean atomic number of the material. Hence, with an appropriate detector, BSE images provide chemical contrast while topographical contrast is suppressed [3].

The interaction cross-section for electron backscattering also depends on the relative orientation between the specimen and the incident electron beam [3]. Hence, local diffraction patterns of the sample can be recorded with an imaging camera as the BSE detector. This technique is called electron back scatter diffraction (EBSD) and is commonly utilized for orientation imaging to determine texturing of the investigated microstructure. As an example, Fig. 3a shows an SEM image of a cryomilled and subsequently quasi-isostatically forged ultrafine grained plate of an Al–Mg alloy (AA 5083) [4]. Intensities in the SEM image were color coded according to the orientation of the individual grains as displayed by the inverse pole figure for the [001] direction. Black intensities represent pores. The average grain size was around 320 nm. Few grains with sizes below 100 nm were detected.

The smallest detectable grain sizes with EBSD are typically around 80–100 nm due to overlapping grains within the interaction volume considering the angle between the EBSD detector and the optical axis of the SEM. Hence, the investigation of texture formation becomes unfeasible for microstructures with smaller grain sizes. An alternative approach is to determine orientation relationships from diffraction patterns that were recorded with electrons that have transmitted the sample.

Figure 3b shows an example for hexagonal ZnO that was consolidated using electric field assisted sintering and revealed an average grain size around 40 nm. In this case, the smallest detectable grain size is not limited by the experimental geometry since such experiments are carried out in a TEM with an on-axis detector for the acquisition of diffraction patterns. Several different TEM techniques will be reviewed in the following section. Excellent introductory texts about scanning electron microscopy can be found in the textbooks by Goldstein [2] and Reimer [3].

2.2 Transmission Electron Microscopy

In TEM electrons of the primary beam that were scattered by the specimen are recorded after they have transmitted the electron transparent sample. Specimen preparation is often challenging since sample thicknesses similar to the mean free path length for electron scattering are required. The most frequently used techniques to obtain typical specimen thicknesses below 100 nm include cutting, grinding, dimpling, and subsequent ion-thinning [5] as well as tripod polishing [6], ultramicrotomy [7, 8], electrolytic polishing [9], and focused ion beam sectioning [10–12]. Good reviews about TEM specimen preparation can be found in the textbook by Reimer [13] and several other articles [5, 14, 15]. In the following conventional TEM and scanning transmission electron microscopy (STEM) techniques will be briefly reviewed to provide an overview of their capabilities for microstructural characterization. For the advanced reader, the section about reciprocity outlines that TEM and STEM techniques are optically equivalent.

2.2.1 Conventional TEM

Conventional TEM uses a parallel illumination of the specimen, which is accomplished by a series of condenser lenses. For the coherent electron beam conditions in TEM, contrast is mainly achieved through the use of apertures in the back focal plane of the objective lens to select or interfere diffracted beams, referred to respectively as diffraction contrast or phase contrast imaging [1, 16].

TEM techniques that rely on the formation of image contrast through diffraction of a coherent beam include dark field, bright field and weak-beam imaging and are effective tools to analyze specimen thickness, bending effects and strain effects and are ideally suited to determine burgers vectors of dislocations [1, 16]. High resolution transmission electron microscopy (HRTEM) uses the interference of multiple scattered electron beams to analyze the relative phase relationships that provides information about the location of lattice planes. The intensity of a scattered electron beam $g(r)$ is commonly described in reciprocal space as $G(u)$ in terms of the contrast transfer function $H(u)$ and the Fourier transform of a function describing the specimen $F(u)$ [1].

$$G(u) = H(u)F(u) = A(u)E(u)B(u)F(u) \qquad (1)$$

In this formalism the contrast transfer function $H(u)$ describes how information (here: image contrast in frequency space) is transferred from the scattering event in the specimen to the microscope detector. $H(u)$ consists of the product of an aperture function $A(u)$, an envelope damping function $E(u)$, and the aberration function $B(u)$:

$$B(u) = \exp(i\pi\Delta f \lambda u^2 + \frac{1}{2} i\pi C_S \lambda^3 u^4 + \mathit{higher\,order\,terms}) \qquad (2)$$

In Eq. 2, Δf is the defocus of the objective lens, λ is the wavelength of the primary electron, and C_s is the spherical aberration of the objective lens. As the name suggests, the aperture function $A(u)$ represents the all scattering angle-limiting apertures of the microscope. $E(u)$ describes beam coherency, chromatic aberrations, environmental impacts, etc. As can be inferred from the equation above, contrast in HRTEM images depends on the actual imaging conditions, such as specimen thickness (implicit in $F(u)$), defocus of the objective lens and other higher-order lens aberrations. Due to the coherent nature of the scattered intensity, a variation of these parameters can change the interference conditions and hence alter image contrast. For these reasons atomic resolution HRTEM micrographs with phase contrast typically require image simulations for a quantitative interpretation of the observed contrast.

2.2.2 Scanning Transmission Electron Microscopy

In STEM mode a fine electron probe is focused onto and rastered across the specimen. Scattered electrons transmitted by the specimen are collected serially as a function of probe position. Focusing of the electron beam is typically achieved through a combination of a set of condenser lenses and the objective lens. The maximum angle under which electrons contribute to the electron probe are determined by the objective aperture and scanning is controlled by a set of scan coils. Electrons scattered into high-angles are recorded with an annular detector. The cross-section for electrons scattered into high angles over a large angular range is roughly proportional to the squared atomic number of the scattering element [1, 16]. For relatively large scattering angles, coherent effects between atomic columns average out. The scattering process itself can thus be considered purely incoherent, which bypasses the phase problem that complicates interpretation of conventional high resolution TEM using phase contrast imaging. High angle annular dark field (HAADF) imaging is often referred to as *Z*-contrast imaging due to the atomic number dependence of the scattering cross-section. Consequently, the HAADF technique is most sensitive to heavy elements, and images provide a high degree of chemical information in addition to structural details [17].

Those electrons scattered into small angles can be collected "*on-axis*" by a bright field detector, or they can be analyzed with respect to their kinetic energy to form electron energy-loss spectra to investigate inelastic scattering events [18]. In addition, secondary electron detectors, energy-dispersive X-ray detectors, cathodoluminescence detectors, etc. can also be attached to the microscope. Consequently, STEM provides the simultaneous acquisition of multiple different image and spectroscopy signals while scanning the electron probe across the specimen or pointing it directly onto different defect structures, such as, for instance, point defects, grain boundaries or heterophase interfaces [17].

2.2.3 Theorem of Reciprocity

Figure 4 shows a sketch of the electron ray diagrams for TEM and STEM operation modes and compares the essential optical elements in both instruments for one picture element, i.e. image pixel. According to the principle of reciprocity [19], which was formulated for light optics by Stokes, Lorentz, Helmholtz and other during the 19th century, the TEM ray diagram is equivalent to that for bright-field STEM when opposite directions of electron propagation are considered [16]. The principle of reciprocity in the context of electron wave optics is based on time-reversal symmetry of the electron propagation process. In Fig. 4, diaphragms passed by the electron beam before interactions with the sample are denoted by angles α, while post-specimen angles a labeled β. Hence, the TEM condenser aperture α_{TEM} is optically equivalent with the STEM collector aperture β_{STEM} which restricts the respective maximum scattering angle. Similarly, the objective apertures remain identical, i.e. $\beta_{\mathrm{TEM}} = \alpha_{\mathrm{STEM}}$.

In the more common combined TEM/STEM instrument the probe-forming aperture during STEM operation is the same aperture as used for the condenser aperture in TEM mode. The only difference between the two operating modes is that in TEM all image pixels are acquired simultaneously by using parallel illumination of the specimen, while in STEM mode image pixels are recorded serially by scanning the highly converged electron probe. As a consequence it is important to recognize that when identical apertures $\alpha_{\mathrm{TEM}} = \beta_{\mathrm{STEM}}$ and $\beta_{\mathrm{TEM}} = \alpha_{\mathrm{STEM}}$ are used, and provided that β_{TEM} is incoherently and β_{STEM} is coherently illuminated,

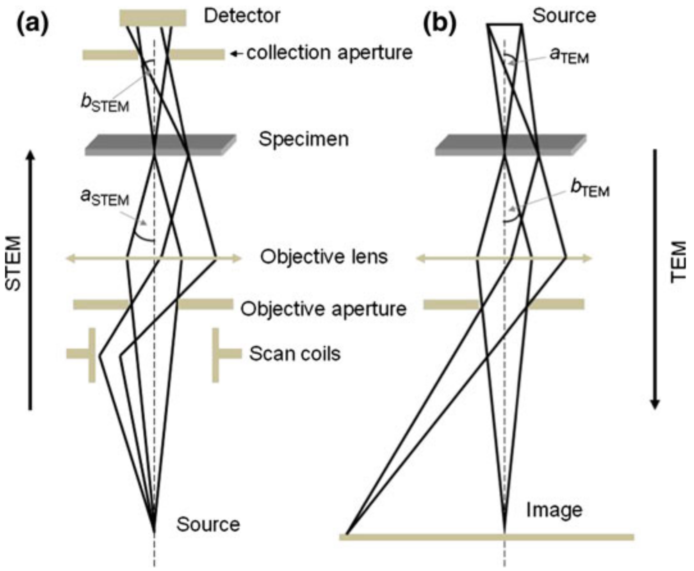

Fig. 4 Theorem of reciprocity between **a** STEM and **b** TEM. The electron ray diagrams illustrate that due to time reversal symmetry of the optical pathway, STEM and TEM imaging are equivalent to each other (after Reimer [16])

then the principle of reciprocity results in identical image contrast for bright field STEM and bright field TEM [16].

2.2.4 Resolution

The resolving power of electron microscopes is typically determined by the wavelength of the fast electrons, but is practically smaller by a factor of 50 due to environmental and instrumental instabilities as well as lens aberrations. To increase the spatial resolution, aberration correctors have recently been developed to overcome limitations due to lens imperfections. Ideal lenses focus a point source to a single image point, as illustrated in Fig. 5a. Scherzer however first recognized that every rotationally symmetric lens will always suffer from both spherical and chromatic aberrations [20]. Spherical aberrations cause electrons traveling at higher angles off the optical axis to be focused more strongly than those at smaller angles (cf. Fig. 5b). Chromatic aberrations describe the spread in focus of a lens dependent on the kinetic energy spread of the electron wave (Fig. 5c). Consequently, both types of lens aberrations lead to a blurring of the electron beam in the back focal plane and, hence, a degradation of the spatial resolution.

In general, a lens aberration causes an error in the optical path length between the actual wave front and a perfect sphere. For thin samples only the imaginary part of $B(\underline{u}) = 2\sin X(u)$ contributes to the image intensity [1]. The aberration

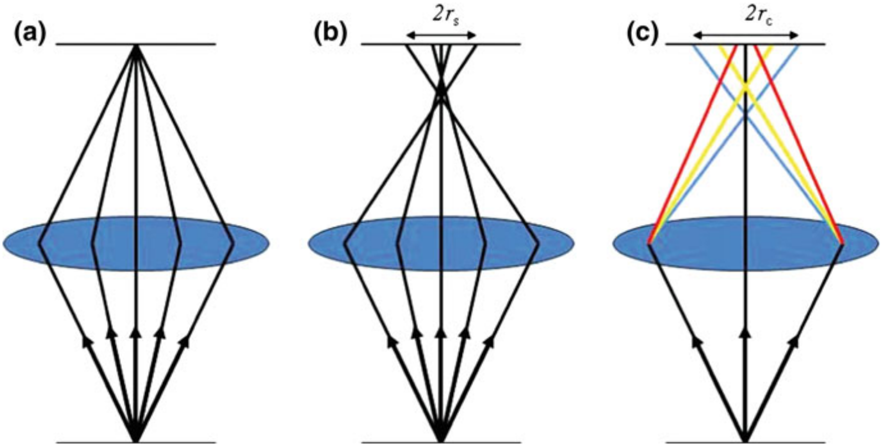

Fig. 5 Schematic drawings illustrating major lens aberrations. **a** A perfect round lens focuses a point source to a single image point. **b** Geometric aberrations such as the spherical aberration focus electrons that penetrate the lens with different angles to different focal points. The chromatic aberration **c** focuses the electron beam at different positions according to the electrons kinetic energy

function in real space $X(\theta)$ is hence commonly expressed as a Taylor expansion in the scattering angle θ. When ignoring all non-rotationally symmetric aberrations the aberration function $X(\theta)$ becomes

$$\mathrm{X}(\theta) = \frac{1}{2}\Delta f\theta^2 + \frac{1}{4}C_3\theta^4 + \frac{1}{6}C_5\theta^6 + \frac{1}{8}C_7\theta^8 + \ldots, \tag{3}$$

where $\mathrm{C}_3 = \mathrm{C}_\mathrm{s}$, C_5, and C_7 are the coefficients of third-, fifth-, and seventh-order spherical aberrations, respectively. For round magnetic lenses these coefficients are all positive and have dimensions of length. At first, the order of the aberration coefficients seems counter-intuitive to Eq. (3). However, geometric aberrations lead the electron rays at different angles towards different focus points along the optical axis, causing a lateral displacement in the Gaussian focal plane. The lateral displacements are proportional to the gradient of the aberration function $X(\theta)$. Therefore, C_s is often referred to as a third-order spherical aberration. For non-round aberrations such as astigmatism similar notations as those in Eq. (3) can be used by introducing the dependence on the azimuthal angle. The description of general lens imperfection to fifth order would need 25 aberration coefficients to be included in the expression of the aberration function [21, 22]. Most of these coefficients are small in round lenses and can be kept small by suitable lens designs and microscope column alignments.

The underlying principle used by aberration correctors is to generate an identical but negative aberration coefficient which cancels out with the one introduced by the actual lens itself. The fundamental strategy to achieve this has been laid out by Scherzer in 1947 who proposed to break rotational symmetry to eliminate spherical and chromatic aberrations [23]. Non-round optical elements, so-called multipole lenses, were built to facilitate aberration correction for round lenses [21, 22, 24, 25]. For the correction of aberrations generated by the image forming lenses in HRTEM mode, round-lens-hexapole based optics are used [24–26]. However, for STEM aberration correction, the probe forming lenses are typically carried out by similar optical elements or, alternatively, by a combination of quadrupole-octupole lenses [21, 22]. The two different designs each have certain advantages and disadvantages when compared to each other with respect to the remaining residual aberrations and geometries. An in-depth discussion of the respective topics is well beyond the scope of this review. Since the first installation of aberration correctors, it has become common practice to use the optical elements in the corrector to counter-balance the resolution limiting higher-order terms in Eq. 3 by specific non-zero lower-order lens aberrations to obtain the highest possible resolution limits. Sub-Ångström resolution was obtained for both HRTEM and STEM imaging modes [17, 25–30] with recent developments pushing resolution limits beyond 0.5 Å [27, 31]. A significant benefit of aberration correction for the characterization of, for instance, grain boundary structures in as-sintered microstructures, is that STEM imaging becomes sensitive to the detection of single dopant or impurity atoms [17, 27, 32–37]. Furthermore, a drastically decreased depth of field provides means for the three-dimensional localization of isolated atoms within the volume of respective TEM samples [27, 38–43].

2.3 In Situ Electron Microscopy

In situ TEM is one of the fastest moving developments in the electron microscopy and materials sciences communities. Novel TEM instruments and dedicated sample holders are available, which enable characterizing materials under conditions that were previously not available for TEM experiments, such as gas [44–46] and liquid phases [47], ultra-fast heating [46, 48, 49], electrical fields and currents [50], mechanical stress [51, 52], etc. Continuous image acquisition through video recording therefore makes it feasible to characterize the evolution of defect structures. Typical time constants are determined by the rate of image acquisition, which ranges from about 100 ms in TEM and HRTEM modes to several seconds for recording STEM micrographs. However, the recent development of dynamical transmission electron microscopy (DTEM) enables temporal resolutions of the order of nanoseconds or better [53–57].

The availability of heating holders as well as the feasibility for the application of electrical fields or currents to SEM and TEM samples provides means to study mechanisms of materials transport on the nanoscale and under conditions that are relevant for the consolidation of materials during sintering experiments. Further below, a select number of recently published studies are reviewed that report how in situ TEM experiments were utilized to assess sintering mechanisms of nanometric powder particles.

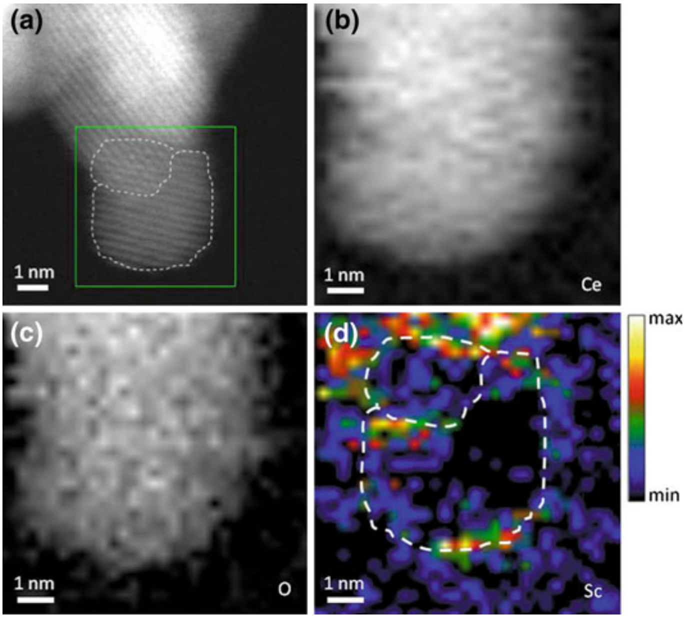

Fig. 6 **a** HAADF image of Sc-doped CeO_2 particles that served as a survey image during EELS data acquisition from the area marked in *green*. **b**, **c** and **d** show elemental distribution maps for cerium, oxygen and scandium, respectively. The *dashed lines* in (**d**) mark the circumference of the particles. False colors were used for better representation of intensities [58]

2.4 Segregation in Nanoparticles

The sintering behavior of nanopowders is critically influenced by the surface properties of the individual nanoparticles. For example, the surface energy of nanoparticles depends on their heterogeneous composition with respect to the segregation of dopant elements to the free surface. As a consequence, neck formation in green pressed powders will strongly depend on the surface excess of dopant elements in the particles, which can also control the particle sizes. As an example, Fig. 6a shows a high-angle annular dark-field STEM image recorded from Sc-doped CeO_2 nano-powder with an average particle size around 5 nm. Electron energy-loss spectroscopy (EELS) data was recorded to analyze the chemical composition and distribution of Sc atoms. Figures 6b–d show elemental distribution maps for Ce, O and Sc, respectively. EELS analysis clearly reveals that scandium atoms segregate to near surface areas of the particles and agglomerate with concentrations twice as high as compared to the volume of the particles. These experimental observations suggest that neck formation during stage I of sintering will be strongly affected by the increased dopant segregation and, hence, will be altered compared to pure CeO_2.

Doping of CeO_2 with Sc leads to the formation of one oxygen vacancy for each Sc atom to maintain charge neutrality. Nuclear magnetic resonance spectroscopy has shown that oxygen vacancies close to the surface region of Sc-doped CeO_2 are nearly immobile [58]. It was therefore concluded that oxygen transport along the grain boundaries in fully dense Sc-doped CeO_2 microstructures is hindered by immobile vacancies, so that nanogranular solid electrolytes of CeO_2 will likely be characterized by diminished oxygen conductivities compared to those with larger grain sizes.

The study of Sc-doped CeO_2 reviewed above exemplifies that segregation in nanoparticles can be significant and may alter the sinterability of these powders due to alterations of the corresponding surface energies. STEM-EELS experiments represent an efficient tool to characterize such behavior. For geometrical reasons, however, STEM-EELS results always provide information that is projected onto the plane perpendicular to the optical axis of the TEM. 3D electron tomography combined with energy-filtered TEM imaging [59] is capable to recover the full three-dimensional distribution of dopant elements on the particles' surface. The current resolution limits for such techniques is around 1 nm in all three directions in space.

3 Anisotropic Grain Growth in Si_3N_4

This section will review two case studies in which atomic resolution electron microscopy was utilized to provide a detailed mechanistic description of anisotropic grain growth during sintering of Si_3N_4 ceramics. The application of ceramic microstructures as structural materials is often limited due to their brittleness, i.e. relatively low fracture resistance. A significant improvement in the fracture toughness of Si_3N_4-based ceramics is attained by so-called self-reinforced microstructures, i.e. the dispersion of high aspect ratio β-Si_3N_4 grains embedded in a fine grained matrix [60]. Such wisker-like microstructural features as shown in Fig. 7 can bridge cracks or cause pull-out and crack deflection with the effect that more energy is dissipated during crack propagation. As a result the material becomes tougher, especially when combined with strong interfacial bonding [61].

Si_3N_4 ceramic microstructures are characterized by grains with high aspect ratios, i.e., elongated hexagonal prisms. Figure 7 shows a typical SEM micrograph of such a microstructure with Si_3N_4 grains in dark contrast and bright contrast representing a secondary phase that contains the sintering additives such as SiO_2 and rare earth (RE) oxides. The formation of elongated grains in Si_3N_4 ceramics is caused by anisotropic grain growth in which the c-axis growth rates exceed those normal to the prism faces [62]. It was found that the anisotropic grain growth during sintering is correlated with the type and concentration of the RE dopants. Relatively fast grain growth in the *c*-direction is diffusion controlled while the slower growth along any of the other directions is reaction limited by the segregation of dopants to the prism surfaces.

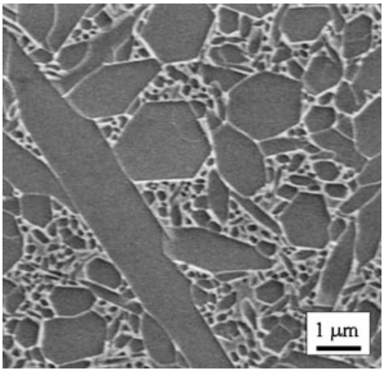

Fig. 7 BSE-SEM micrograph recorded form La-doped and liquid-phase sintered Si_3N_4. The bright contrasts show the amorphous secondary phase containing the RE dopant atoms

Only through the advent of aberration correctors for STEM imaging, beam current densities and achievable spatial resolutions became sufficient to directly image and hence determine the segregation behavior of RE atoms. Figure 8a shows a high resolution HAADF STEM image of an intergranular film (IGF) between two adjacent grains in La_2O_3-doped Si_3N_4. The grain to the right of the IGF is viewed in <0001> zone-axis orientation, i.e. the <0001> direction of the crystal is parallel to the optical axis of the TEM instrument. The prismatic (10-10) grain boundary plane is in an “edge-on” condition, while the grain on the left is in <01–11> zone-axis orientation. Due to the Z-contrast imaging conditions, the bright contrast of the IGF indicates La atom segregation to the grain boundary. Closer inspection of the image intensities in Fig. 8b however reveals that La atoms are decorating the grain surface at specific adsorption sites. Using calculations of differential binding energies, the authors of this study therefore concluded that the relative suppression in grain growth along the direction normal to the prism planes is caused by the formation of strong La-Si bonds at the grain surfaces that hinders the reaction for further growth, i.e. attachment of silicon [34, 63]. Winkelman et’al. have subsequently shown that the adsorption sites for RE atoms on the grain surface are correlated with their ionic sizes [64].

Figure 9a shows an HAADF-STEM image of the interface between a Si_3N_4 grain in <0001> zone-axis orientation and an amorphous triple pocket in Gd-doped Si_3N_4. Bright intensities at the interface represent columns of segregated Gd atoms. Two distinct adsorption sites for Gd (labeled A and B) were determined. However, at least three parallel layers of segregated Gd ions can be observed as they extend into the amorphous phase. Quantitative EELS analysis (Fig. 9b) confirmed the formation of Gd layers parallel to the interface plane. The interplanar spacing between the segregants is identical to that in bulk Si_3N_4 in the same direction. These observations indicate a structural and chemical gradient rather than an atomically abrupt crystalline/amorphous interface [65].

After illuminating the sample with the electron beam for 32 s, the outermost layer of Gd atoms was no longer visible due to the onset of electron beam damage inside the triple pocket (see Fig. 10). After an additional 32 s. most of the middle layer could also no longer be identified. After 96 s a lower intensity from sites

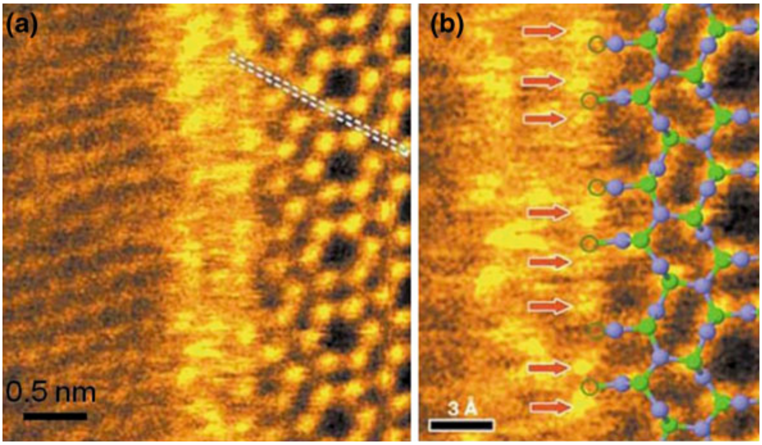

Fig. 8 HAADF-STEM micrographs of an intergranular film in La-doped Si_3N_4. La atoms are observed as the bright spots (denoted by *arrows*) at the edge of the IGF. The positions of La atoms are shifted from expected positions labeled by *open green circles*. From [34]

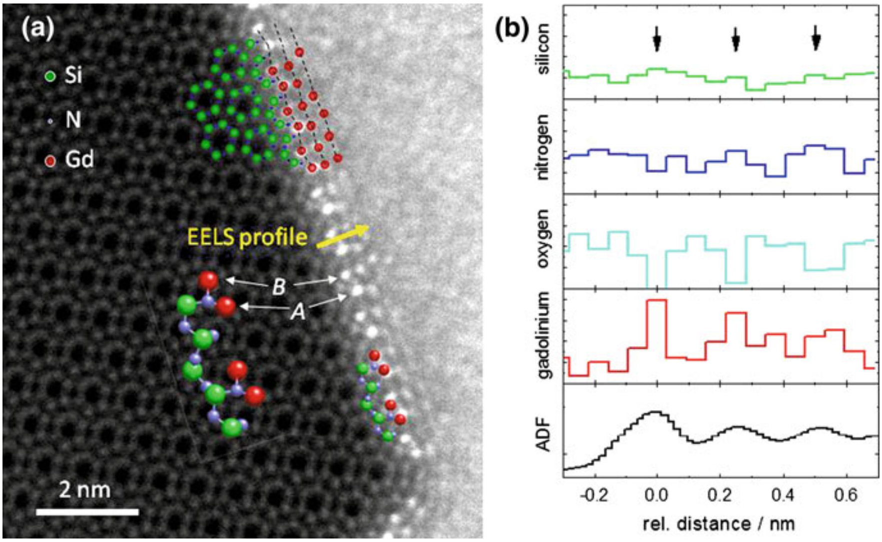

Fig. 9 HAADF-STEM image of an amorphous/crystalline interface in fully densified Gd-doped Si_3N_4 (**a**). At least three layers of segregated Gd atoms decorate the interface with adsorption sites labeled A and B on the Si_3N_4 prisamtic plane. **b** shows integrated EELS intensities for silicon, nitrogen, oxygen and Gd in comparison to the ADF intensities extracted along the *arrow* in panel (**a**). From [65]

labeled *B* indicated a decreasing population of Gd atoms at these weaker binding sites, with no observable change at the higher populated (more strongly bound) adsorption sites labeled *A*. After $T = 160$ s bright contrast in the HAADF image

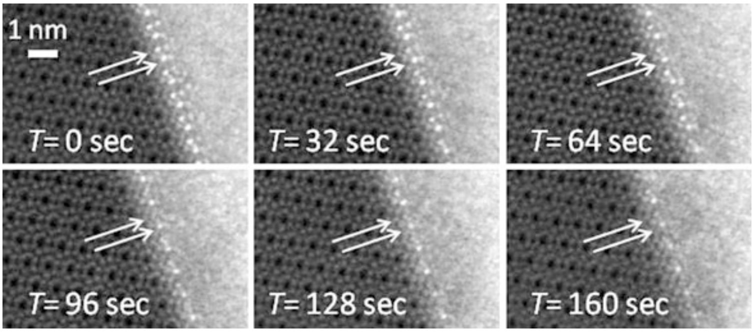

Fig. 10 Time series of HAADF-STEM images recorded from the amorphous/crystalline interface shown in Fig. 9. The *arrows* mark the two different adsorption sites for Gd atoms. Figure adapted from [65]

Fig. 11 Sketch of a possible interface configuration of two adjacent grains of Si3N4 and an IGF with a typical thickness of 1 nm and formed by the three experimentally observed layers of segregated Gd atoms

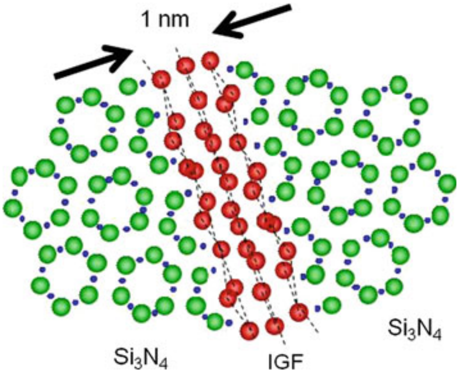

remains only on adsorption sites *A* while the bright contrasts at positions B have completely vanished [63]. Figure 10 shows HAADF micrographs extracted from the corresponding movie file. The qualitative experimental observations of relative binding energies were confirmed by calculations binding energies for different adsorption sites [63].

In summary, the identification of adsorption sites for RE dopant elements in Si_3N_4 ceramics provides detailed mechanistic insights to the observed anisotropic grain growth behavior. The investigation of the crystalline/amorphous interface between the grains and the triple pockets demonstrates a high level of atomic ordering along the interface normal. The adsorption sites of RE elements from the triple pockets were found to be identical with those within the IGFs. The formation of a roughly 1 nm thick IGF from two crystalline/amorphous interfaces may therefore suggest a high degree of structural ordering across the IGF as sketched in Fig. 11.

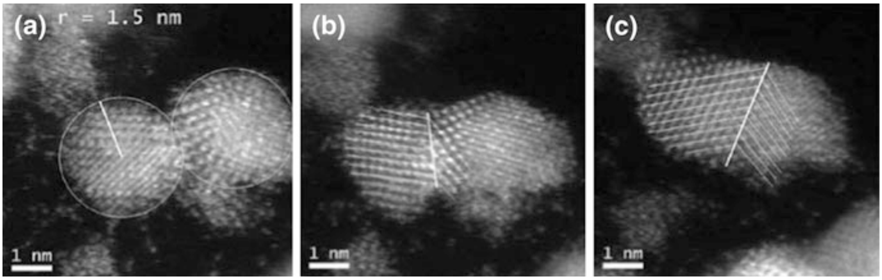

Fig. 12 HAADF-STEM images of Pt particles illustrating how (**a**) particle radii and (**b**, **c**) grain boundary diameters were measured to subsequently determine diffusion coefficients. Images are courtesy of M.A. Asoro et'al. and are reproduced from [66]

4 Thermal Sintering in TEM

Asoro et'al. [66] have used aberration-corrected in situ STEM imaging at room temperature to investigate the coalescence of Pt nanoparticles with a mean diameter of 2.8 nm. Figure 12 shows a sequence of three HAADF STEM images that were acquired in intervals of 20 s with an acquisition time of 15 s/frame. In Fig. 12a two Pt particles can clearly be distinguished from each other. Due to the atomic resolution imaging conditions, a number of single Pd atoms dispersed on the amorphous carbon support film are visible in the vicinity of the particles. After about 35 s the particles start coalescing and form a significant neck between each other (Fig. 12b). Eventually the particles form a dense volume with a separating grain boundary. The lengths of grain boundary planes measured from Fig. 12b, c are 1.9 nm and 2.8 nm, respectively [66]. The driving force for the observed coalescence of Pt particles is the surface curvature of the ultra-small particles. Considering a surface energy of 2.28 J/m^2 [67] and surface diffusion being the dominating mass transport mechanism for this experiment, Asoro et'al. were able to determine surface diffusivities from the as-measured particle and neck sizes. For room temperature, the resulting diffusion coefficients range between 1.5×10^{-20} cm^2/s and 7.2×10^{-20} cm^2/s, which is in reasonable agreement with extrapolated high temperature data available in the literature [68]. The relatively large range of the diffusivity data is likely based on heating of the sample due to electron beam irradiation as well as electron beam damaging due to the high beam current densities after aberration correction.

Matsuno and co-workers [69] have studied the consolidation of Ni nanoparticles through in situ annealing of powder particles during simultaneous atomic resolution observation with TEM. Nickel nanoparticles with diameters around 20 nm were drop-casted on TEM specimen grids that were covered with thin membranes of either amorphous carbon or silicon carbide. Figure 13 shows an HRTEM micrograph of soft agglomerates of the nickel particles suspended on carbon. Heating of the particles between 200 and 500 °C lead to coalescence of the particles and grain boundary formation was video captured by in situ HRTEM. The contact angles

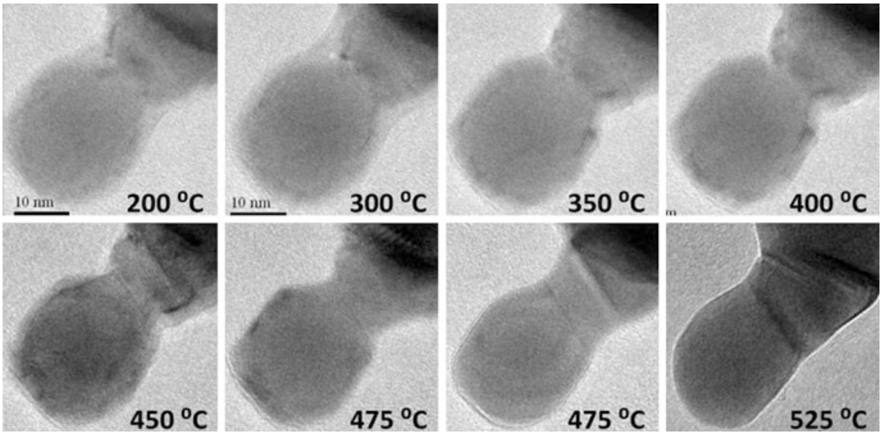

Fig. 13 Series of in situ HRTEM micrographs recorded during the heating of an agglomerate of Ni particles with a diameter of roughly 20 nm. Images were reproduced with permission from [69]

between two adjacent particles were measured as a function of temperature and time during the annealing experiment. The contact angle between the two observed particles remained mostly constant until a temperature of roughly 450 °C was reached and rapid neck formation and subsequent consolidation occurred.

A constant dihedral angle above 500 °C indicates that thermodynamic equilibrium was achieved. From such measurements the corresponding interface energy of the as-formed grain boundary can be determined, provided the surface energy of nanometric nickel was previously determined, e.g., by drop solution calorimetry.

Figure 14 shows that each particle is covered with a roughly 2 nm thick layer. EELS line profiles acquired across the individual particles have revealed that these layers were comprised of nickel oxide that passivates the particles. During the in situ thermal annealing experiments the oxide layers start to disappear at temperatures around 350 °C and are fully removed from the particles' surfaces before coalescence occurs. To clarify whether the amorphous carbon support film influences the observed reduction of nickel oxide, in situ annealing experiments were repeated under identical conditions with particles suspended on SiN films. Coalescence of particles was observed similar to that reported in Fig. 13. However, the NiO layers were preserved to temperatures as high as 700 °C. These observations demonstrate that the presence of carbon lowers the reduction reaction of nickel oxides to metallic Ni, which subsequently enables coalescence of the particles. The reduction temperature in the presence of SiC is also lower than that for bulk materials, which is most likely an effect of the nanometric size of the particles rather than due to defect chemistry. Calculations of the expected reaction temperatures for reduction of NiO to metallic Ni with the corresponding oxidation of carbon to gaseous CO or CO_2 are in good agreement with the observed temperatures during the in situ TEM experiments. It is therefore concluded that the

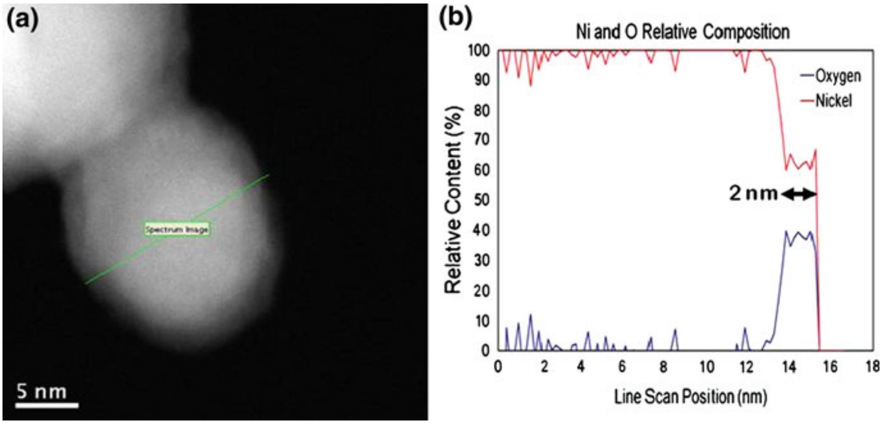

Fig. 14 **a** HAADF-STEM survey image of a Ni nanoparticle for the acquisition of spatially resolved EELS line profiles of the O K and Ni $L_{2,3}$ absorption edges. **b** shows the integrated EELS intensities recorded along the *green line* shown in **a**. Figure from [69]

availability of carbon during (field-assisted) sintering promotes a cleaning of the oxide from the surfaces of the metal particles and, therefore, aids in lowering the sintering temperatures and accelerates densification.

Until further experiments are carried out, it remains unclear, however, whether the carbon from the graphitic dies utilized during electric field assisted sintering can cause such behavior. Alternatively, carbon contamination of the powder particles or the binder utilized during green pressing may result in carbon-assisted acceleration of sintering.

5 Current-Assisted Sintering in the TEM

In a recent study, Holland et'al. exposed nanometric Ni powders (particle diameters around 120 nm) to electrical currents during simultaneous observation with in situ transmission electron microscopy [50]. Results were obtained by contacting two particles using a scanning tunneling microscope mounted onto a TEM specimen holder (Nanofactory STM-TEM specimen holder). An increasing negative electrical bias (DC) was applied to the STM tip, which generates current flow from the tip across the contacting particles to the specimen grid (see Fig. 15).

Figure 16 shows three TEM micrographs and the corresponding selected area diffraction (SAD) patterns for the initial particle configuration before (Fig. 16a), during (Fig. 16b) and after the sintering experiment (Fig. 16c). The SAD patterns demonstrate mass transfer and possible relative particle rotation during the *first* sintering stage. After a total annealing time of approximately 145 s at –10 V rapid densification of the particle agglomerate was observed. Image analysis reveals

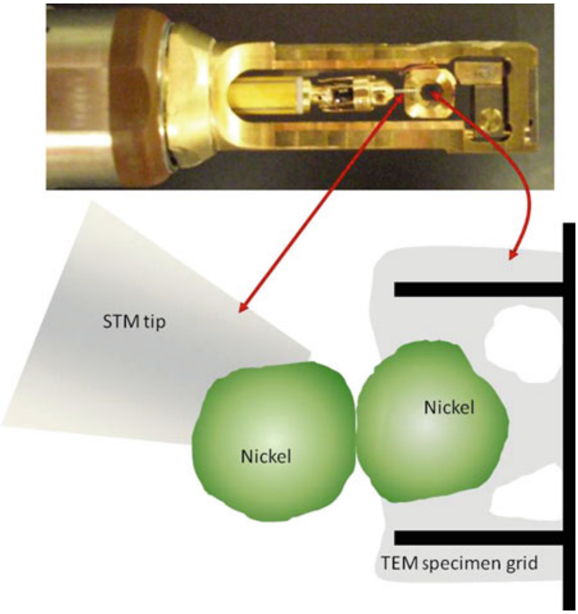

Fig. 15 Sketch of the geometry during in situ STM-TEM experiments. Ni particles were drop-casted on the specimen grid. The picture displays the utilized Nanofactory STM-TEM sample holder

poly-crystallinity with grain boundaries and no apparent inter-connected porosity (Fig. 16c), suggesting that densification of the particle agglomerate has occurred in the absence of any external heating. The formation of necks between adjacent particles was indirectly detected through the observation of “hillocks” in the current vs. time plots during the holding intervals (Fig. 16e, f). Initial neck formation forms a small metallic contact between particles and thus leads to a temporary increase of the observed current, which is then limited and subsequently decreased by the constriction resistance through Joule heating. The attendant increase in local Joule heating precedes rapid densification of the nickel particles (Fig. 16f).

Similar consolidation mechanisms were observed for Ni particles with diameters of 20 nm. However, the onset of neck formation and rapid consolidation was significantly delayed and only occurred at significantly higher applied voltages above 14 V. Figure 17 shows a TEM image of a “chain” of nickel particles between larger particle agglomerates on the TEM sample and the STM tip, respectively. Figure 17 also shows the measured electrical current across this chain of particles as a function of time for a constant tip bias of –18 V. The stepwise increase of the current indicates a time-dependent dielectric breakdown behavior as it is commonly observed for high-*k* dielectric films in semiconductor devices [70–73]. Multiple soft breakdown events and subsequent neck formation eventually lead to rapid consolidation similar to the observations described above. EELS characterization of the particles before electrical annealing revealed that the particles were surrounded by a nickel oxide surface layer with a thickness of roughly 2.5 nm. Oxide layers between

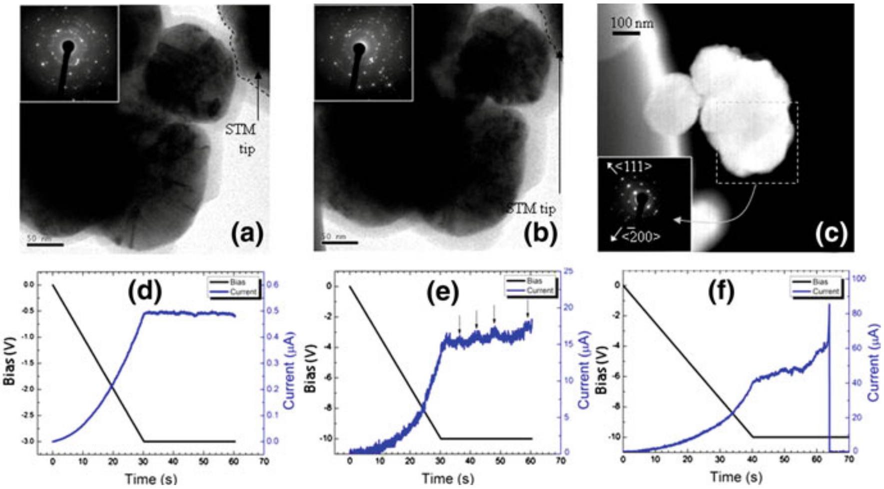

Fig. 16 TEM images and corresponding SAD patterns of nickel particles **a** before and **b** during annealing for 1 min at –10 V. The STM tip for electrical contacting is visible in the upper right corners. **c** HAADF STEM image of the as-sintered particle agglomerate. The selected area diffraction pattern was taken with TEM from the marked area. (**d**, **f**) are show the corresponding applied bias and as-measured current as functions of time. Figures modified from [50]

Fig. 17 The measured current through the chain of particles (inset) as function of time indicates typical time-dependent dielectric breakdown behavior of the surface oxide

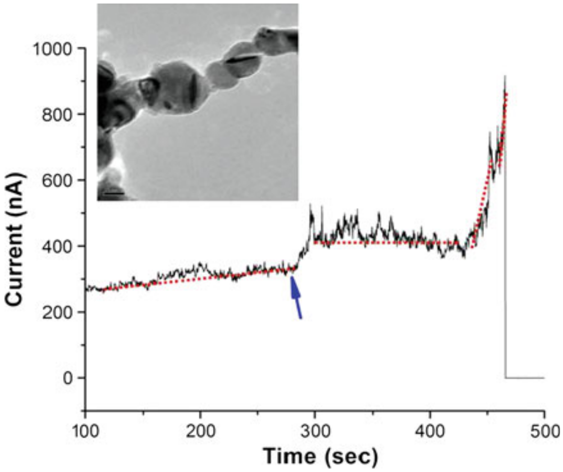

Ni particles should play no significant role in the rate of sintering assuming volume diffusion of metal atoms through the oxide [74]. The observations however suggest that (soft) dielectric breakdown is necessary before the applied current can lead to materials transport.

The results demonstrate that it is feasible to investigate electric field effects on individual nanoparticles and their subsequent consolidation by STM-TEM experiments. Current densities across individual particles and their contact areas and dielectric breakdown mechanisms that limit consolidation of typically conducting particles can be assessed on the atomic length-scale to derive effective mechanisms during all three stages of sintering.

6 Summary and Conclusions

Microstructural characterization is critical to understand structure–property relationships for specific materials systems. The availability of atomic resolution imaging and spectroscopy through electron microscopy techniques provides the means to systematically investigate the evolution of microstructures as a function of the processing, i.e., sintering conditions. Traditionally, SEM and TEM techniques were applied to either individual powder particles or readily consolidated microstructures. Detailed information about grain sizes and their distribution, texture formation, segregation behavior of dopants and impurities, atomic arrangements in grain boundary cores, and corresponding bonding configurations are accessible. However, more recently, in situ TEM and SEM techniques offer the capabilities to expose nano-sized particles to a variety of different environments, such as high heating rates, electrical fields and currents, mechanical stress, etc., as well as combinations of the above. Such experiments therefore allow the systematic investigation of atomic-scale mechanisms that lead to densification during assisted sintering experiments. It must, however, be noted that "in situ TEM sintering experiments" in fact do not represent sintering in the classical sense due to the geometric constrains of the TEM samples (2-dimensional distribution of powder particles). Instead, such techniques can enable the systematic investigation of specific and individual mechanisms that occur during sintering, for instance, heating rates or electrical currents across a contact area between two nanoparticles. To date, such experiments are feasible as demonstrated above, although they remain mostly unexplored territory.

Acknowledgments Discussions with Drs. T.B. Holland, A.K. Mukherjee, Z.A. Munir, J. Groza (UC Davis) and S. Schwartz and O. Guillon (TU Darmstadt) are gratefully acknowledged. Help provided by Dr. T. LaGrange (LLNL) for the acquisition of orientation images by TEM was invaluable. The author recognizes his graduate and undergraduate students for their diligent work on the presented projects, specifically Ms. C.S. Bonifacio, Mr. H. Ghadialy, Ms. M. Matsuno, Mr. J. Rufner, and Mr. A. Thron. This work was funded partially by UC Davis start-up funds and a CAREER award from the US National Science Foundation (DMR-0955638).

References

1. Williams, D.B., Carter, C.B.: Transmission Electron Microscopy A Textbook for Materials Science, 2nd edn. Springer, New York (2009)
2. Goldstein, J., Newbury, D.E., Joy, D.C., Lyman, C., Echlin, P.E., Lifshin, E., Sawyer, L., Michael, J.: Scanning Electron Microscopy and X-ray Microanalysis, 3rd edn. Kluwer Academic/Plenum Publishers, New York (2003)
3. Reimer, L.: Scanning Electron Microscopy, Springer-Verlag, Berlin p. 457. (1985)
4. Topping, T., Ahn, B., Li, Y., Nutt, S., Lavernia, E.: Metall. Mater. Trans. A **43**, 505–519 (2012)
5. Strecker, A., Bader, U., Kelsch, M., Salzberger, U., Sycha, M., Gao, M., Richter, G., van Benthem, K.: Zeitschrift fur Metallkunde **94**(3), 290–297 (2003)
6. Anderson, R., Klepeis, S.J.: In A new tripod polisher method for preparing TEM specimens of particles and fibers, Mater. Res. Soc., Pittsburgh, PA, USA., 1997; Anderson, R. M.; Walck, S. D., Eds. Mater. Res. Soc., Pittsburgh, PA, USA., 1997; pp193–199
7. Wei, L.-Y., Li, T.: Microsc. Res. Tech. **36**, 380–381 (1997)
8. Getter, M.E., Ornstein, L.: Phys. Tech. Biol. Res. **3**, 627 (1956)
9. Heidenreich, R.D.J.: Appl. Phys. **20**, 993 (1949)
10. Giannuzzi, L.A., Stevie, F.A.: Introduction to Focused Ion Beams: Instrumentation, Theory, Techniques and Practice. Springer Verlag, New York (2004)
11. Giannuzzi, L.A., Stevie, F.A.: Micron **30**(3), 197–204 (1999)
12. Volkert, C.A., Minor, A.M.: MRS Bull. **32**(5), 389–395 (2007)
13. Reimer, L.: Elektronenmikroskopische Untersuchungs-und Präparationsmethoden. Springer-Verlag, Berlin (1959)
14. Strecker, A., Mayer, J., Baretzky, B., Eigenthaler, U., Gemming, T., Schweinfest, R., Ruhle, M.: J. Electron Microsc. **48**(3), 235–244 (1999)
15. Strecker, A., Salzberger, U., Mayer, J.: Prakt. Metallogr. **30**, 482 (1993)
16. Reimer, L.: Transmission Electron Microscopy, 2nd edn. Springer, Berlin (1997)
17. Varela, M., Lupini, A.R., van Benthem, K., Borisevich, A.Y., Chisholm, M.F., Shibata, N., Abe, E., Pennycook, S.J.: Annu. Rev. Mater. Res. **35**, 539–569 (2005)
18. Egerton, R.F.: Electron Energy Loss Spectroscopy in the Electron Microscope, 2nd edn. Plenum Press, New York (1996)
19. Potton, R.J.: Rep. Prog. Phys. **67**(5), 717–754 (2004)
20. Scherzer, O.: Zeit. Phys. **101**, 593–603 (1936)
21. Dellby, N., Krivanek, O.L., Nellist, P.D., Batson, P.E., Lupini, A.R.: J. Electron Microsc. **50**, 177–185 (2001)
22. Krivanek, O.L., Dellby, N., Lupini, A.R.: Ultramicroscopy **78**, 1–11 (1999)
23. Scherzer, O.: Optik **2**(2), 114–132 (1947)
24. Rose, H.: Optik **85**(1), 19–24 (1990)
25. Haider, M., Rose, H., Uhlemann, S., Schwan, E., Kabius, B., Urban, K.: Ultramicroscopy **75**(1), 53–60 (1998)
26. O'Keefe, M.A., Allard, L.F., Blom, D.A.: J. Electron Microsc. **54**(3), 169–180 (2005)
27. Kisielowski, C., Freitag, B., Bischoff, M., et al.: Microsc. Microanal. **14**(5), 469–477 (2008)
28. Pennycook, S.J., Chisholm, M.F., Lupini, A.R., Varela, M., van Benthem, K., Borisevich, A.Y., Oxley, M.P., Luo, W., Pantelides, S.T.: Materials Applications of Aberration-Corrected Scanning Transmission Electron Microscopy. In Advances in Imaging and Electron Physics. Elsevier Academic Press Inc, San Diego **153**, pp.327–384 (2008)
29. Nellist, P.D., Chisholm, M.F., Dellby, N., et al.: Science **305**(5691), 1741–1741 (2004)
30. Peng, Y.P., Oxley, M.P., Lupini, A.R., et al.: In Spatial resolution and information transfer in scanning transmission electron microscopy. Microscopy and Microanalysis **14**, 36–47 (2008)
31. Krivanek, O.L., Chisholm, M.F., Nicolosi, V., et al.: Nature **464**(7288), 571–574 (2010)
32. Oh, S.H., van Benthem, K., Molina, S.I., et al.: Nano Lett. **8**(4), 1016–1019 (2008)
33. Shibata, N., Painter, G.S., Satet, R.L., et al.: Phys. Rev. B: Condens. Matter **72**(14), 4 (2005)

34. Shibata, N., Pennycook, S.J., Gosnell, T.R., et al.: Nature **428**(6984), 730–733 (2004)
35. van Benthem, K., Contescu, C.I., Pennycook, S.J., Gallego, N.C.: Single Pd Atoms in Activated Carbon Fibers for Hydrogen Storage. Carbon **49**(12), 4059–4063 (2009)
36. Varela, M., Findlay, S.D., Lupini, A.R., et al. Phys. Rev. Lett. **92**(9), 095502 (2004)
37. Wang, S.W., Borisevich, A.Y., Rashkeev, S.N., et al.: Nat. Mater. **3**(4), 274–274 (2004)
38. Borisevich, A.Y., Lupini, A.R., Pennycook, S.J.: Proc. Natl. Acad. Sci. U S A **103**(9), 3044–3048 (2006)
39. Borisevich, A.Y., Lupini, A.R., Travaglini, S., Pennycook, S.J.: J. Electron Microsc. **55**(1), 7–12 (2006)
40. van Benthem, K., Lupini, A.R., Kim, M., Baik, H.S., Doh, S., Lee, J.H., Oxley, M.P., Findlay, S.D., Allen, L.J., Luck, J.T., Pennycook, S.J.: Appl. Phys. Lett. **87**(3), 3 (2005)
41. van Benthem, K., Lupini, A.R., Oxley, M.P., Findlay, S.D., Allen, L.J., Pennycook, S.J.: Ultramicroscopy **106**(11–12), 1062–1068 (2006)
42. Raj, R., Cologna, M., Francis, J.S.C.: J. Am. Ceram. Soc. **94**(7), 1941–1965 (2011)
43. Cologna, M., Raj, R.: J. Am. Ceram. Soc. **94**(2), 391–395 (2011)
44. Kodambaka, S., Hannon, J.B., Tromp, R.M., Ross, F.M.: Nano Lett. **6**(6), 1292–1296 (2006)
45. Sharma, R.: J. Mater. Res. **20**(7), 1695–1707 (2005)
46. Kamino, T., Yaguchi, T., Konno, M., et al.: J. Electron Microsc. **54**(6), 497–503 (2005)
47. de Jonge, N., Peckys, D.B., Kremers, G.J., Piston, D.W.: Proc. Natl. Acad. Sci. U S A **106**(7), 2159–2164 (2009)
48. Allard, L.F., Bigelow, W.C., Jose-Yacaman, M., et al.: Microsc. Res. Tech. **72**(3), 208–215 (2009)
49. Allard, L.F., Bigelow, W.C., Nackashi, D.P., Damiano, J., Mick, S.E.: Microsc. Microanal. **14**(2), 792–793 (2008)
50. Holland, T.B., Thron, A.M., Bonifacio, C.S., Mukherjee, A.K., van Benthem, K.: Appl. Phys. Lett. **96**(24), 243106 (2010)
51. Minor, A.M., Morris, J.W., Stach, E.A.: Appl. Phys. Lett. **79**(11), 1625–1627 (2001)
52. Stach, E.A., Freeman, T., Minor, A.M., et al.: Microsc. Microanal. **7**(6), 507–517 (2001)
53. Kim, J.S., LaGrange, T., Reed, B.W., et al.: Science **321**(5895), 1472–1475 (2008)
54. LaGrange, T., Campbell, G.H., Reed, B., et al.: Ultramicroscopy **108**(11), 1441–1449 (2008)
55. Reed, B.W., Armstrong, M.R., Browning, N.D., Campbell, G.H., Evans, J.E., LaGrange, T., Masiel, D.J.: Microsc. Microanal. **15**(4), 272–281 (2009)
56. Lobastov, V.A., Srinivasan, R., Zewail, A.H.: Proc. Natl. Acad. Sci. U S A **102**(20), 7069–7073 (2005)
57. Park, H.S., Baskin, J.S., Kwon, O.-H., Zewail, A.H.: Nano Lett. **7**(9), 2545–2551 (2007)
58. Kim, S., Jain, P., Avila-Paredes, H.J., Thron, A., van Benthem, K., Sen, S.: J. Mater. Chem. **20**(19), 3855–3858 (2010)
59. Midgley, P.A., Weyland, M.: Ultramicroscopy **96**(3–4), 413–431 (2003)
60. Lange, F.F.: J. Am. Ceram. Soc. **56**(10), 518–522 (1973)
61. Sun, E.Y., Becher, P.F., Hsueh, C.H., et al.: Acta Mater. **47**(9), 2777–2785 (1999)
62. Kramer, M., Hoffmann, M.J., Petzow, G.: J. Am. Ceram. Soc. **76**(11), 2778–2784 (1993)
63. Painter, G.S., Averill, F.W., Becher, P.F., Shibata, N., van Benthem, K., Pennycook, S.J.: Phys. Rev. B: Condens. Matter **78**(21), 9 (2008)
64. Winkelman, G.B., Dwyer, C., Hudson, T.S., et al.: Philos. Mag. Lett. **84**(12), 755–762 (2004)
65. van Benthem, K., Painter, G.S., Averill, F.W., et al.: Appl. Phys. Lett. **92**(16), 163110 (2008)
66. Asoro, M.A., Kovar, D., Shao-Horn, Y., et al.: Nanotechnology **21**(2), 025701 (2010)
67. Jones, R.D., Rowlands, D., Rossiter, P.L.: Scripta Metall. **5**(10), 915–919 (1971)
68. Marcos, M.L., González Velasco, J.: Chem. Phys. Lett. **283**(5–6), 391–394 (1998)
69. Matsuno, M., Bonifacio, C.S., Holland, T.B., Van Benthem, K.: (in preparation) *(*2011)
70. Waser, R.: Nanoelectronics and Information Technology: Advanced Electronic Materials and Novel Devices, 2nd edn., p. 1002. Wiley, New York (2005)
71. Bonifacio, C.S., Thron, A.M., Bersuker, G., van Benthem, K.: Microsc. Microanal. **16**(S2), 1298–1299 (2010)

72. Bersuker, G., Heh, D., Park, H., Khanal, P., Larcher, L., Padovani, A., Lenahan, P.M., Ryan, J.T., Lee, B.H., Tseng, H., Jammy, R.: In Breakdown in the metal/high-k gate stack: Identifying the “weak link” in the multilayer dielectric. In: International Electron Devices Meeting (IEDM) Technical Digest, 2008, pp. 791–794 (2008)
73. Bonifacio, C.S., van Benthem, K.: J. Appl. Phys. (2012) submitted
74. Munir, Z.A.: J. Mater. Sci. **14**(11), 2733–2740 (1979)